# TURBULENT DIFFUSION IN UNIFORMLY SHEARED FLOW

by
Christina M. Vanderwel

Thesis submitted to the
Faculty of Graduate and Postdoctoral Studies
in partial fulfillment of the requirements
for the Doctorate in Philosophy degree in Mechanical Engineering

Ottawa-Carleton Institute for Mechanical and Aerospace Engineering
Faculty of Engineering
University of Ottawa

## Abstract

The objective of this thesis research is to further the understanding of turbulent diffusion by experimentally studying the turbulent diffusion of a plume of dye released in uniformly sheared flow generated in a water tunnel. The flow studied was nearly homogeneous but strongly anisotropic and had a turbulent Reynolds number of 150. Maps of the turbulent velocity and dye concentration were measured simultaneously using stereoscopic particle image velocimetry and planar laser-induced fluorescence. A thorough analysis of the planar laser-induced fluorescence technique was performed; several previously unconsidered sources of error were identified and corrections were proposed. The measured evolutions of the mixed velocity-concentration statistics of the plume were compared with previous studies. The turbulent scalar flux vector was related to the mean concentration gradient through a first-order gradient transport model and, for the first time in an experimental flow, all components of the turbulent diffusivity tensor were measured directly. The turbulent diffusivity tensor was found to be highly anisotropic and its streamwise component appeared to be countergradient. The relative diffusion of the plume was also investigated and the evolution of the mean square particle separation was found to be consistent with Richardson-Obukhov scaling, with a value of Richardson's constant equal to 0.35. The fine structure of the concentration field and the mixed velocity-concentration statistics were also documented. Because of the high level of intermittency of the present plume, the scalar probability density function was strongly non-Gaussian and the conditional expectations of the velocity components and the scalar dissipation, conditioned upon the scalar value, were distinctly non-linear. Lastly, the role of coherent structures on scalar diffusion was investigated and a conditional eddy analysis demonstrated that hairpin vortices were associated closely with large scalar flux events.

## Acknowledgements

My most sincere thanks go to my advisor and mentor, Dr. Stavros Tavoularis. I would also like to thank the staff of the University of Ottawa Mechanical Engineering Machine Shop, especially Mike Burns, Stan Weedmark, and Leo Denner, and recognize my fellow students, especially George Choueiri, Laura Brown, Amir Behnamian, Steffen Pentelow, and Michael Robert, for all their support throughout my studies. I also gratefully acknowledge the financial support of the University of Ottawa and the Natural Sciences and Engineering Research Council of Canada.

# Table of Contents

## List of Figures

## List of Tables

## Nomenclature

| | |
|---|---|
| $A, A'$ | amplitude of the mean and r.m.s. concentration profiles |
| $a, a_i, a_{cal}$ | calibration coefficient |
| $B$ | constant for calculating the Taylor microscale |
| $b, b'$ | fitting constants |
| $C$ | concentration |
| $C_2$ | Kolmogorov constant |
| $C_a$ | apparent concentration |
| $C_{cal}$ | calibration concentration |
| $C_m$ | measured concentration |
| $C_p$ | peak concentration |
| $C_P$ | conditional concentration |
| $C_S$ | source concentration |
| $c$ | concentration fluctuation / fitting constant |
| $D$ | scalar turbulent diffusivity / molecular diffusivity |
| $D_{ij}$ | turbulent diffusivity tensor |
| $d_p$ | particle diameter |
| $E, E_0$ | camera response |
| $f_c$ | scalar pdf |
| $g$ | Richardson's constant / offset between the laser and plume |
| $h$ | depth of water in the test section / numerical coefficient |
| $I, I_{fr}, I_0, I_{ab}$ | radiant power flux |
| $J$ | flux |
| $K_i$ | apparent diffusivities |
| $k$ | turbulent kinetic energy |
| $L$ | representative lengthscale |
| $L_{\alpha\alpha,\beta}$ | integral length scale |

| | |
|---|---|
| $m$ | total injected mass |
| $\dot{m}$ | injected mass flow rate |
| $m_{ij}$ | turbulence anisotropy |
| $n$ | exponent in a power law |
| $P$ | pressure |
| $Q$ | volume flow rate |
| $q(s)$ | the distance-neighbour function |
| $R$ | autocorrelation coefficient |
| $Re$ | Reynolds number |
| $Re_{\lambda_{11}}$ | Reynolds number based on the Taylor microscale |
| $Re_x$ | Reynolds number based on the downstream position |
| $r$ | radius / separation distance |
| $r_0$ | initial separation distance |
| $S^*$ | shear-rate parameter |
| $S$ | alternative shear-rate parameter |
| $Sc$ | Schmidt number |
| $Sc_T$ | turbulent Schmidt number |
| $s$ | distance between particle pairs / line of sight vector |
| $T_L$ | Lagrangian timescale |
| $t$ | time |
| $t_B$ | Batchelor timescale |
| $t_s$ | time scale of the shear |
| $t_u$ | eddy lifetime |
| $U_c$ | mean centreline velocity |
| $U_g$ | terminal velocity |
| $U_i$ | velocity |
| $u_i$ | velocity fluctuation |
| $u_i'$ | root-mean squared velocity fluctuation |

| | |
|---|---|
| $w, w_T$ | widths |
| $X$ | average displacement in single particle dispersion |
| $x_i$ | components of the position vector in the test section |
| $x_0$ | virtual origin |
| $y_i$ | alternative coordinate system |

**Greek symbols**

| | |
|---|---|
| $\alpha$ | magnification factor |
| $\gamma$ | molecular diffusivity |
| $\gamma_c$ | scalar intermittency factor |
| $\delta$ | boundary layer thickness in the turbulent boundary layer |
| $\delta_{ij}$ | Kronecker delta |
| $\epsilon$ | rate of dissipation of turbulent kinetic energy / dye absorptivity |
| $\epsilon_c$ | scalar dissipation |
| $\eta$ | Kolmogorov microscale |
| $\eta_B$ | Batchelor microscale |
| $\theta$ | angle |
| $\lambda_{11}$ | Taylor microscale |
| $\mu$ | dynamic viscosity of the fluid |
| $\mu_i, \mu_i'$ | coordinates of the mean plume axis |
| $\nu$ | kinematic viscosity of the fluid |
| $\nu_T$ | turbulent viscosity |
| $\rho$ | density of the fluid |
| $\rho_p$ | density of particles |
| $\sigma$ | absolute plume width |
| $\sigma'$ | half widths of the r.m.s. concentration maps |
| $\sigma_L$ | standard deviation of the laser intensity profile |
| $\sigma_M$ | standard deviation of meandering |

$\sigma_P$ standard deviation of the idealized plume concentration profile

$\sigma_Q$ standard deviation of the distance-neighour function

$\sigma_R$ relative plume width

$\tau_{ij}$ Lagrangian timescale

$\tau_S$ time constant of settling particles

$\phi$ quantum efficiency

$\psi$ scalar space variable

### Acronyms

**2D** two-dimensional

**3D** three-dimensional

**DNS** direct numerical simulation

**LDV** laser Doppler velocimetry

**pdf** probability density function

**PIV** particle image velocimetry

**PLIF** planar laser induce fluorescence

**PPIV** planar particle image velocimetry

**r.m.s.** root mean square

**SPIV** stereo particle image velocimetry

**USF** uniformly sheared flow

# Chapter 1

# Introduction

## 1.1 Turbulent diffusion

Turbulent diffusion is the process of spreading and mixing of admixtures by turbulent motions. It is the essential mechanism that drives dispersal of pollutants in the environment, mixing in industrial processes, and chemical reactions in diverse systems. Examples of natural flows of interest include the diffusion of smoke from wildfires, volcanic ash from volcanic eruptions, and the spreading of pollen by the wind. Other examples of turbulent diffusion in environmental flows apply to anthropogenic pollutions, such as smoke and smog in the atmosphere (as in figure 1.1) and oil spills in waterways. Turbulent diffusion also plays a prominent role in many industrial processes, as for example in combustion engines and furnaces, whose efficiency depends strongly on it (Bilger, 1989), and in many other kinds of chemical and ionic reactions (Calef & Deutch, 1983).

Figure 1.1: A plume of smoke emitted in the atmosphere from a smokestack at the University of Ottawa (photo taken February 24, 2014 by the author).

Although turbulent diffusion has been studied extensively for a long time, its analysis for engineering purposes is still based on crude models and is primarily concerned with the prediction of the mean concentration of the admixture (Roberts & Webster, 2002). Taylor's (1921) foundational theory of absolute diffusion considered the one-dimensional motion of an individual fluid particle released from a fixed point in isotropic turbulence. He defined the rate of dispersion as the rate of growth of the variance of an ensemble of particle displacements; he demonstrated that the rate of dispersion would be zero at the moment of particle release, would initially increase linearly with dispersion time, and would eventually reach an asymptote which would depend only on the turbulence properties. This theoretical analysis was expanded to three-dimensional isotropic turbulence by Batchelor (1949) and to homogeneous turbulent shear flows by Riley & Corrsin (1974) and Tavoularis & Corrsin (1985).

Around the same time Taylor proposed his theory of absolute diffusion, Richardson (1926) developed his foundational theory on relative dispersion, which attempts to quantify the temporal evolution of the separation distance of pairs of fluid particles in turbulent flows. The variance of an ensemble of particle pair separations is analogous to the width of a cloud of contaminants relative to its centre of mass, as opposed to relative to its point of origin as in Taylor's absolute diffusion framework. Richardson's celebrated four-thirds law states that the rate of change of the variance of particle pair separations would behave universally, depending on the variance to the power of 4/3.

Examples of investigations of turbulent diffusion in the environment include early observations of anti-aircraft shell-bursts (Roberts, 1923; Sutton, 1932) and plumes of lycopodium spores released in the atmosphere (Hay & Pasquill, 1959) and dyes released in a lake (Csanady, 1963). These studies investigated the rate of dispersion of the scalar in the absolute and relative frameworks proposed by Taylor and Richardson; however, in actual turbulent flows such as those, the turbulent properties are generally inhomogeneous and the evolution of the rate of dispersion cannot be described entirely by these simplified models.

Results obtained in the controlled environment of a laboratory are useful for isolating the complicating effects encountered in many environmental and industrial flows

and obtaining reproducible measurements. Models of the turbulence properties may be developed in these simplified environments and then applied to the analysis of more complicated flows. The simplest case of turbulent mixing is when the substance is passive, which means that it does not affect the velocity field. Examples of passive scalars include the concentration of non-reacting neutrally-buoyant solutions and the temperature of the fluid under such conditions that buoyancy effects are negligible. Previous relevant laboratory studies of passive scalar diffusion include investigations of diffusion behind two-dimensional line sources in grid turbulence (Warhaft, 1984; Anand & Pope, 1985; Stapountzis *et al.*, 1986), in uniformly sheared flow (Tavoularis & Corrsin, 1981; Karnik & Tavoularis, 1989), and in channel flow (Lepore & Mydlarski, 2011), as well as point sources in uniformly sheared flow (Nakamura *et al.*, 1986) and in channel flows (Webster *et al.*, 2003; Rahman & Webster, 2005). Uniformly sheared flow (USF) is a canonical turbulent shear flow that is characterized by a uniform mean velocity gradient perpendicular to the mean flow direction. It has many of the characteristics of turbulent boundary layers and channel flows, such as the strong anisotropy of the Reynolds stresses and the presence of large-scale coherent structures; however, unlike other shear flows, it is free of the effects of boundaries and inhomogeneity, thus being suitable for testing diffusion models, which often assume homogeneity of the flow field. Models of the turbulence properties can therefore be more easily developed and validated in this simplified and consistent environment and then applied to the analysis of more complicated flows.

## 1.2 Objectives

The general objective of this thesis is to study experimentally the turbulent diffusion of a passive scalar in a plume emitted from a point source in a uniformly sheared flow. The general goals of the study are to document the turbulent velocity and concentration statistics of the flow in order to further investigate and refine existing theories and models of turbulent diffusion.

The specific objectives of this research are:

(a) To investigate the ensemble-averaged properties of the velocity and concentration fields in the plume in an absolute reference frame; to investigate the rate of growth of the plume width compared with Taylor's diffusion model; to apply a first-order gradient transport model to relate the scalar fluxes with the scalar gradient and to measure all nine components of the turbulent diffusivity tensor.

(b) To investigate the relative dispersion of the plume, test the applicability of Richardson's four-thirds law within the inertial subrange, and measure Richardson's constant under these specific experimental conditions.

(c) To measure the properties of the fine structure of the concentration field, and properties appearing in the balance equation of the scalar pdf, including the scalar pdf, the scalar derivatives, and conditional expectations of the velocity components, conditioned on the scalar value.

(d) To investigate the effect of the dominant coherent structures in the flow on the instantaneous concentration field and turbulent diffusion.

The results from this study are expected to contribute to the fundamental understanding of turbulent diffusion and also serve as benchmarks for validating theoretical and computational models of turbulent diffusion.

### 1.3 Methodology

The experiments investigated the turbulent diffusion of a point source plume of dye in uniformly sheared flow generated in a water tunnel. Measurements of the turbulent velocity and concentration fields in cross-sections of the plume were obtained simultaneously with the use of stereoscopic particle image velocimetry and planar laser induced fluorescence. This is the first time that simultaneous two-dimensional maps of the velocity and concentration have been obtained in USF, as opposed to previous studies, which reported point measurements obtained by LDV, hot-wires, cold-wires, and thermistors in wind tunnels.

## 1.4 Organization of the thesis

This thesis is prepared in the form of a manuscript-based thesis. A general background and literature review is provided in Chapter 2. Chapter 3 contains a description of the apparatus and experimental procedures used in the experiments. Chapter 4 consists of the following manuscript detailing the uncertainty analysis of the PLIF technique, which explores several sources of error not previously considered in the literature:

> Vanderwel C. and Tavoularis S. (2014) "On the accuracy of PLIF measurements in slender plumes, Experiments in Fluids, Vol. 55, Issue 8, 1801, Published August 10, 2014.

The main results are presented in Chapters 5-7, each of which explores a different facet of turbulent diffusion. Chapter 5 addresses the absolute diffusion of the plume and contains the following manuscript:

> Vanderwel, C. and Tavoularis, S. (2014), "Measurements of turbulent diffusion in uniformly sheared flow, Journal of Fluid Mechanics, Vol. 754, pp. 488-514, Published August 7, 2014.

Chapter 6 addresses the relative dispersion of the plume and reproduces the article

> Vanderwel, C. and Tavoularis, S. (2014), "Relative dispersion of a passive scalar plume in turbulent shear flow", Physical Review E., Vol. 89, pg. 041005R, Published April 24, 2014.

Chapter 7 reports measurements of the fine structure of the plume, presented in the form of the manuscript

> Vanderwel, C. and Tavoularis, S. (2014), "The fine structure of a slender scalar plume in sheared turbulence", Presented at the iTi (interdisciplinary Turbulence initiative) Conference on Turbulence, Bertinoro, Italy, September 21-24, 2014. Also under review for publication in Progress in Turbulence VI, Springer Verlag.

Chapter 8 explores the role of coherent structures on the turbulent diffusion of the plume and is presented in the form of the manuscript

Vanderwel, C. and Tavoularis, S. (2015), "Scalar dispersion by coherent structures", Under review for the Ninth International Symposium on Turbulence and Shear Flow Phenomena (TSFP9), Melbourne, Australia, June 30 - July 3, 2015.

Finally, a summary of the main results of this thesis is presented in Chapter 9, with a list of the novel contributions of this work and recommendations for directions for future work. Details of the refurbishment of the water tunnel are presented in Appendix A. Additional maps of the evolutions of some of the measured turbulent properties of the plume that were not included in the manuscripts are presented in Appendix B.

# Chapter 2

# Background and Literature Review

## 2.1 Introduction to turbulent flows

### 2.1.1 General background

In fluid dynamics, flows are generally classified to be laminar, turbulent, or transitional. Laminar flows are characterized by smooth motions, whereas turbulent flows exhibit random fluctuations. The random fluctuations experienced by turbulent flows are conventionally studied by decomposing the flow velocity, $U_i$ where $i = \{1, 2, 3\}$, into a mean $\overline{U_i}$ and a fluctuation $u_i$ as $U_i = \overline{U_i} + u_i$. This is referred to as Reynolds decomposition. The standard deviation of the velocity fluctuations in the direction $i$ is denoted as $u_i' \equiv \sqrt{\overline{u_i{}^2}}$. The turbulent kinetic energy per unit mass is $k \equiv \frac{1}{2}\left(\overline{u_1{}^2} + \overline{u_2{}^2} + \overline{u_3{}^2}\right)$. The rate of dissipation of turbulent kinetic energy by viscous actions is denoted by $\epsilon$. The Reynolds number,

$$\mathrm{Re} = \frac{\overline{U_1} L}{\nu}, \tag{2.1}$$

where $\overline{U_1}$ is the mean streamwise velocity, $L$ is a representative lengthscale in the flow, and $\nu$ is the kinematic viscosity, is a measure of the relative importance of "inertial" forces with respect to viscous forces. Flows at relatively large Reynolds numbers are normally turbulent. The turbulence Reynolds number,

$$Re_{\lambda_{11}} = \frac{u_1' \, \lambda_{11}}{\nu}, \tag{2.2}$$

where $\lambda_{11}$ is a turbulence lengthscale, to be introduced in the next section, is representative of the ratio between turbulent eddy viscosity and laminar viscosity.

### 2.1.2 The lengthscales of turbulence

Turbulent motions ("eddies") have a wide range of time, length, and amplitude scales. Eddies obtain energy from the free-stream and transport energy down to eddies with

smaller scales. The scale of the largest (energy containing) eddies usually correspond to the external dimensions of the flow. The integral lengthscale $L_{\alpha\alpha,\beta}$ is defined as the the integral of the spatial autocorrelation of the velocity as (Pope, 2000)

$$L_{\alpha\alpha,\beta} = \int_0^\infty \frac{\overline{u_\alpha(x_\beta)u_\alpha(x_\beta + \mathrm{d}x_\beta)}}{\overline{u_\alpha^2(x_\beta)}}\mathrm{d}x_\beta. \tag{2.3}$$

The smallest scales of the flow, representing motions that are strongly affected by viscous forces, are characterized by the Kolmogorov lengthscale (Pope, 2000)

$$\eta = \left(\frac{\nu^3}{\epsilon}\right)^{1/4}. \tag{2.4}$$

An intermediate length scale is the Taylor microscale (Tennekes & Lumley, 1972)

$$\lambda_{11} = \sqrt{\frac{\overline{u_1^2}}{\overline{(\partial u_1/\partial x_1)^2}}}. \tag{2.5}$$

### 2.1.3 Uniformly sheared flow

Uniformly sheared flow (USF) is a statistically simple shear flow that can be generated approximately experimentally. Ideally, the mean streamwise velocity varies linearly with the transverse position as

$$\overline{U_1} = \frac{\mathrm{d}\overline{U_1}}{\mathrm{d}x_2}x_2 \tag{2.6}$$

$$\overline{U_2} = 0 \tag{2.7}$$

$$\overline{U_3} = 0 \tag{2.8}$$

where the shear rate $\mathrm{d}\overline{U_1}/\mathrm{d}x_2$ is constant throughout the flow. The Reynolds stresses are homogeneous in cross-planes, but develop in the streamwise direction. The shear is a source of turbulent kinetic energy, countering the turbulence dissipation, and making this flow self-sustaining by causing the turbulence stresses to grow downstream.

Uniformly sheared flow shares many similarities with the outer regions of turbulent boundary layers and therefore can be used as a tool to gain insight into turbulent boundary layer flows. Like turbulent boundary layers, the turbulence stresses

are strongly anisotropic, as indicated by non-zero values of the components of the anisotropy tensor, which is defined as

$$m_{ij} = \frac{\overline{u_i u_j}}{2k} - \frac{1}{3}\delta_{ij}. \tag{2.9}$$

The shear-rate parameter, which is defined as

$$S^* = \frac{t_u}{t_s} = \frac{d\langle U_1 \rangle}{dx_2}\frac{(2k)}{\epsilon}, \tag{2.10}$$

is the ratio of the turbulence timescale to the timescale of the mean shear and so it represents the relative strength of the turbulent activity compared to the production of turbulent kinetic energy by mean shear. Whereas the values of $m_{ij}$ and $S^*$ vary across a turbulent boundary layer, they are uniform in USF. De Souza *et al.* (1995) point out that the majority of experimental studies of USF have $S^* \approx 11$ and $m_{12} \approx 0.15$, which are comparable to corresponding values in the outer regions of turbulent boundary layers.

A thorough review of previous studies of USF was presented in the author's Master's thesis (Vanderwel, 2010). Of direct relevance to the current work are the following studies:

- Tavoularis & Corrsin (1981), who used hot-wire anemometry in a wind tunnel to study the turbulence properties of USF as well as the properties of a scalar field generated by a superimposed uniform mean temperature gradient.

- Rogers & Moin (1987), who studied the structure of homogeneous shear flow using direct numerical simulation (DNS) and identified hairpin vortices in the flow.

- Tavoularis & Karnik (1989), who used hot-wire anemometry to document the effect of the shear value on USF in a wind tunnel

- Karnik & Tavoularis (1989), who studied experimentally the properties of a line source plume superimposed in USF.

- De Souza *et al.* (1995), who studied the Reynolds stress anisotropy of USF using LDV in a high speed wind tunnel.

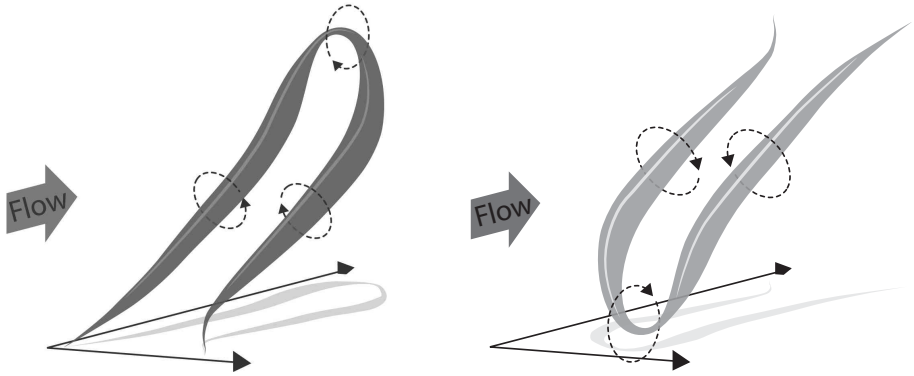


Figure 2.1: Sketches of a typical upright (left) and inverted (right) hairpin vortex, prevalent in USF (Vanderwel, 2010).

- Ferchichi & Tavoularis (2000), who documented the effect of the turbulent Reynolds number on the fine structure of USF.
- Vanderwel & Tavoularis (2011), who studied USF in a water tunnel using particle image velocimetry, and documented the prevalence of hairpin vortices in the flow.

Both DNS and experimental studies have demonstrated that USF contains coherent structures similar to those observed in the outer regions of turbulent boundary layers. Vanderwel (2010) identified the shape of the predominant structures as hairpin-shaped vortices, which unlike in turbulent boundary layer flow, appeared both in upright and inverted orientations, as sketched in figure 2.1. It is hypothesized that the presence of the wall in turbulent boundary layer flow acts to suppress the development of inverted structures, whereas this effect is not present in USF. Apart from this difference, the coherent vortices in USF have similar characteristics to those in turbulent boundary layers; they were observed within relatively strong shear layers, which separated regions of fluid with nearly uniform velocity, and were observed in small groups. These experimental results are in conformity with previous DNS studies; Lee *et al.* (1990) observed streamwise streaky structures in USF similar to the streaks formed in turbulent boundary layers by hairpin vortices and Rogers & Moin (1987) revealed upright and inverted hairpin vortices scattered within homogeneously sheared flow.

## 2.2 Turbulent diffusion

### 2.2.1 Introduction to diffusion

Diffusion describes the transport of a scalar property in a fluid from a region of high concentration to a region of low concentration. The concentration of a substance mixed with the fluid or the temperature of the fluid are both examples of scalar properties, which may be considered passive if they do not affect the velocity field of the flow.

The flux $J_i$ of a substance with concentration $C$ along the direction $x_i$ by molecular diffusion is described by Fick's law,

$$J_i = -\gamma \frac{dC}{dx_i}, \tag{2.11}$$

where $\gamma$ is an empirical constant called the molecular diffusivity. For fluids in motion, the concentration of a substance is also transported (or advected) with the fluid motion and is governed by the advection-diffusion equation,

$$\frac{\partial C}{\partial t} + U_j \frac{\partial C}{\partial x_j} = \gamma \frac{\partial^2 C}{\partial x_j \partial x_j}. \tag{2.12}$$

This equation does not apply to flows with buoyancy effects or any other body forces, nor for reacting substances, and therefore only applies to passive scalars. For passive scalars, this equation is decoupled from the Navier-Stokes equations. The first term, $\partial C/\partial t$, is the time rate of change of the concentration, the second term, $U_j \frac{\partial C}{\partial x_j}$, represents the rate of transport of the species by the flow, and the third term represents the rate of transport of the species through molecular diffusion.

In a turbulent flow, the smallest scales of the scalar field, representing the scales at which diffusion is dominated by molecular diffusion, are represented by the Batchelor scale, $\eta_B$. The ratio of $\eta_B$ to the Kolmogorov lengthscale, $\eta$, which represents the smallest scales of the velocity field, is equal to the square root of the Schmidt number $\mathrm{Sc} \equiv \nu/\gamma$, which is a measure of the relative rates of momentum transport by viscosity and scalar transport by molecular diffusivity. As $\mathrm{Sc} > 1$ for most substances, the scalar field typically exhibits much finer fluctuations than the size of the smallest eddies in the flow.

### 2.2.2 Governing equations of turbulent diffusion

For turbulent flows, with the use of Reynolds decomposition, one may separate the turbulent variables into their mean and fluctuating components as $U_i = \overline{U_i} + u_i$ and $C = \overline{C} + c$. Applying this decomposition to equation 2.12 produces turbulent transport equations for passive scalars. The balance equation for the mean scalar is (Pope, 2000)

$$\frac{\partial \overline{C}}{\partial t} + \overline{U_j}\frac{\partial \overline{C}}{\partial x_j} = \frac{\partial}{\partial x_j}\left(\gamma \frac{\partial \overline{C}}{\partial x_j} - \overline{cu_j}\right). \tag{2.13}$$

The term $-\overline{cu_j}$ is called the turbulent scalar flux vector. The presence of this term in the mean scalar equation introduces three additional unknowns, namely $\overline{cu_1}$, $\overline{cu_2}$, and $\overline{cu_3}$. One type of closure is possible by the use of a model for the turbulent mass flux vector in terms of $\overline{C}$. The most commonly used model is the first-order gradient transport model (Arya, 1999)

$$-\overline{cu_i} = D_{ij}\frac{\partial \overline{C}}{\partial x_j}, \tag{2.14}$$

where $D_{ij}$ is the turbulent, or "eddy", diffusivity tensor, which has nine components, the values of which depend on the turbulent field. The gradient transport model is based on the assumptions that the macroscopic characteristic lengthscale of the scalar is much greater than that of the transporting mechanism (*i.e.*, the turbulence) and that the flow properties are approximately homogeneous over the turbulence lengthscale (Corrsin, 1974). Despite the fact that these assumptions are not satisfied in most cases of interest, the gradient transport model is known to provide fairly accurate predictions in a variety of situations (Sreenivasan *et al.*, 1982). Application of (2.14) requires empirical knowledge of all nine components of $D_{ij}$. Nevertheless, measurements of these components are quite scarce, due to the difficulty of measuring simultaneously the local magnitudes and directions of both the mean concentration gradient and the turbulent mass flux vector.

A balance equation for the scalar variance may be derived as (Pope, 2000)

$$\frac{\partial \overline{c^2}}{\partial t} + \overline{U_j}\frac{\partial \overline{c^2}}{\partial x_j} = -2\overline{cu_j}\frac{\partial \overline{C}}{\partial x_j} - \frac{\partial \overline{c^2 u_j}}{\partial x_j} + \gamma\frac{\partial^2 \overline{c^2}}{\partial x_j \partial x_j} - 2\gamma\overline{\frac{\partial c}{\partial x_j}\frac{\partial c}{\partial x_j}}. \tag{2.15}$$

The term $-2\overline{cu_j}\frac{\partial \overline{C}}{\partial x_j}$ represents the rate of production of scalar fluctuations. The term

$-2\gamma\overline{\frac{\partial c}{\partial x_j}\frac{\partial c}{\partial x_j}}$ represents the rate of destruction of scalar fluctuations by molecular motions and is commonly written as $-2\epsilon_c$, where $\epsilon_c$ is referred to as the scalar dissipation rate. The remaining two terms on the right hand side of the equation represent the rate of transport of scalar fluctuations by turbulence and molecular diffusion, respectively. The values of the scalar variance $\overline{c^2}$, the turbulent flux vector $\overline{cu_j}$, and the scalar dissipation rate $\epsilon_c$, are of particular importance in many problems (Warhaft, 2000). Measurements of the various terms in the governing equations, their trends, and their relative importance help us gain insight into the fundamental mechanisms of turbulent transport. Such measurements can also be used for developing and testing theoretical and numerical models and for validating computer simulations.

### 2.2.3 Balance equation for the scalar pdf

A balance equation for the probability density function (pdf) of the scalar, $f_c$, is often used in the study of reactive flows, including combustion. This equation is (Ferchichi & Tavoularis, 2002)

$$\frac{\partial f_c}{\partial t}+\overline{U_j}\frac{\partial f_c}{\partial x_j}=-\frac{\partial(\overline{u_j|\psi}\ f_c)}{\partial x_j}-\frac{\partial\overline{cu_j}}{\partial x_j}\frac{\partial f_c}{\partial\psi}+\frac{\partial\overline{C}}{\partial x_j}\frac{\partial(\overline{u_j|\psi}\ f_c)}{\partial\psi}-\frac{\partial^2(\overline{\epsilon_c|\psi}\ f_c)}{\partial\psi^2}+\gamma\frac{\partial^2 f_c}{\partial x_j\partial x_j}, \quad (2.16)$$

where $\psi$ denotes the sample-space variable. This equation contains the conditional expectations of the velocity fluctuations and the scalar dissipation conditioned on the scalar value, denoted as $\overline{u_j|\psi}$ and $\overline{\epsilon_c|\psi}$, respectively. In homogeneous scalar fields with jointly-Gaussian velocity and scalar fluctuations, these conditional expectations would be linear functions of the scalar value, however, this may not be the case for inhomogeneous scalar fields. For this reason, measurements of the scalar pdf and the conditional expectations of the velocity and scalar dissipation in a variety of flows and scalar fields are necessary for the development of accurate models of terms in the scalar pdf equation. As the scalar dissipation is related to the scalar derivatives, conditional expectations of the scalar derivatives would also be of interest.

### 2.2.4 The absolute diffusion of scalar plumes

The study of turbulent diffusion originated with the work of Taylor (1921), who considered the one-dimensional motion of an individual fluid particle released from a

fixed point in stationary isotropic turbulent flow, neglecting molecular diffusion. He demonstrated that the variance of an ensemble of particle displacements following time $t$ from their release should depend only on the turbulence properties as

$$\overline{X^2}(t) = 2\overline{v^2}\int_0^t (t-\xi)R(\xi)d\xi, \tag{2.17}$$

where $v$ represents the Lagrangian velocity fluctuations and $R(\xi)$ is the Lagrangian correlation coefficient. Taylor further identified two regimes of diffusion which would occur in the limits of short $t$ and long $t$, known as the turbulent convection and turbulent diffusion regimes (Anand & Pope, 1985). In these regimes, (2.17) would be simplified as, respectively,

$$\overline{X^2}(t) \approx \overline{v^2}t^2, \quad \text{for} \quad t \ll \mathcal{T}, \tag{2.18}$$

$$\overline{X^2}(t) \approx 2\overline{v^2}\mathcal{T}t, \quad \text{for} \quad \mathcal{T} \ll t, \tag{2.19}$$

where $\mathcal{T}$ is the Lagrangian integral timescale of the turbulence. It follows that the rate of dispersion, defined as

$$\frac{1}{2}\frac{\mathrm{d}\overline{X^2}(t)}{\mathrm{d}t} = \overline{v^2}\int_0^t R(\xi)d\xi, \tag{2.20}$$

has the following limits for the near- and far-field regimes

$$\frac{1}{2}\frac{\mathrm{d}\overline{X^2}(t)}{\mathrm{d}t} \approx \overline{v^2}t, \quad \text{for} \quad t \ll \mathcal{T}, \tag{2.21}$$

$$\frac{1}{2}\frac{\mathrm{d}\overline{X^2}(t)}{\mathrm{d}t} \approx \overline{v^2}\mathcal{T}, \quad \text{for} \quad \mathcal{T} \ll t. \tag{2.22}$$

This implies that the rate of dispersion would be zero at the moment of particle release, would initially increase linearly with dispersion time, and would eventually reach an asymptote which would depend only on the Lagrangian integral timescale of the turbulence and the variance of the Lagrangian velocity fluctuations.

The theoretical analysis of three-dimensional turbulent diffusion was first presented by Batchelor (1949), who defined a three-dimensional diffusion coefficient tensor $\frac{1}{2}\mathrm{d}\overline{X_iX_j}/\mathrm{d}t$ in terms of the mean Lagrangian displacement tensor $\overline{X_iX_j}(t)$ of a particle transported by homogeneous turbulence. He further demonstrated that, in

homogeneous, non-sheared turbulence and for a Gaussian particle displacement distribution, $\frac{1}{2}\mathrm{d}\overline{X_i X_j}/\mathrm{d}t$ would be equal to the turbulent diffusivity tensor $D_{ij}$, as defined in (2.14). Batchelor also showed that, in isotropic turbulence, $D_{ij}$ would be proportional to the identity tensor (Kronecker's delta); as in Taylor's theory, the magnitudes of the components of $D_{ij}$ would increase with dispersion time and would eventually reach asymptotes that depend only on the Lagrangian integral timescales of the turbulence, $\mathcal{T}_{ij}$, and the intensities of the Lagrangian velocity fluctuations.

Riley & Corrsin (1974) expanded Batchelor's analysis for homogeneous turbulent shear flow and noted that the normal diffusivities were unequal and that some of the cross-diffusivities were not zero. As with the theories of Taylor and Batchelor, the magnitudes of the turbulent diffusivities were shown to depend on the Lagrangian integral timescales of the turbulence, $\mathcal{T}_{ij}$, and the intensities of the Lagrangian velocity fluctuations. Corrsin (1974) suggested that the asymptotic values of the turbulent diffusivities could be estimated from Eulerian properties, as surrogates for their Lagrangian counterparts, for example as $D_{22} \approx u_2'^2 T_{11}$. Additional theoretical arguments have been made by Tavoularis & Corrsin (1985), Rogers *et al.* (1989) and Younis *et al.* (2005) to derive asymptotic expressions for the turbulent diffusivity tensor components in shear flows. These theories will be revisited in a later section.

A classical approach for measuring turbulent diffusion in the laboratory or in the environment is to relate the rate of growth of puffs and plumes generated in the turbulent flow to an apparent turbulent diffusivity. The plume generated by a continuously emitting source may be considered as the result of superposition of clouds emitted successively by an instantaneous source. For a plume of particles emitted from a point source in a turbulent flow with a uniform mean velocity $U_1$ in the $x_1$ direction, the apparent diffusivities in the two normal directions $x_2$ and $x_3$ are defined as

$$K_2 = \frac{U_1}{2}\,\frac{\mathrm{d}\sigma_2^2}{\mathrm{d}x_1}, \quad K_3 = \frac{U_1}{2}\,\frac{\mathrm{d}\sigma_3^2}{\mathrm{d}x_1}, \tag{2.23}$$

where $\sigma_2$ and $\sigma_3$ are the corresponding characteristic plume widths. If, and only if, the streamwise dispersion were negligible, the apparent plume diffusivities $K_2$ and $K_3$ would be equivalent to the diffusion coefficients $\frac{1}{2}\mathrm{d}\overline{X_2^2}/\mathrm{d}t$ and $\frac{1}{2}\mathrm{d}\overline{X_3^2}/\mathrm{d}t$ (Arya, 1999),

and thus to $D_{22}$ and $D_{33}$.

Further assuming that the two apparent turbulent diffusivities are uniform in space and equal to each other ($K_2 = K_3 = K$) leads to the well known Gaussian plume formula (Arya, 1999) for the mean concentration of a continuous plume in uniform mean flow

$$\overline{C} = \frac{Q}{4\pi K x_1} \exp\left[-U_1\left(\frac{x_2^2 + x_3^2}{4K x_1}\right)\right]. \tag{2.24}$$

According to this solution, the maximum concentration of the plume would decay as $x_1^{-1}$ and the plume width would grow as $x_1^{0.5}$. With the same assumptions, a similar solution may be obtained for uniformly sheared flow (Davidson, 2004). Maps of the mean concentrations of the scalar fields created by instantaneous and continuous point sources in USF, according to this simplified solution, are plotted in figure 2.2. For moderate values of shear, although the individual puffs created by the instantaneous point source rotate due to the shear, the profile of the plume, which is essentially the superposition of infinitely-closely released puffs (Arya, 1999), is essentially symmetric about the plume axis. As in uniform flow, this solution predicts that the maximum concentration of the continuous source plume decreases roughly as ${x_1}^{-1}$ and the plume width grows roughly as ${x_1}^{0.5}$.

Examples of investigations of turbulent diffusion in the environment include early observations of anti-aircraft shell-bursts (Roberts, 1923; Sutton, 1932) and plumes of lycopodium spores released in the atmosphere (Hay & Pasquill, 1959) and dyes released in a lake (Csanady, 1963). Examples of relevant laboratory studies include investigations of diffusion behind a line source in grid turbulence (Warhaft, 1984; Anand & Pope, 1985; Stapountzis *et al.*, 1986), a line source in uniformly sheared flow (Tavoularis & Corrsin, 1981; Karnik & Tavoularis, 1989), a line source in channel flow (Lepore & Mydlarski, 2011), a point source in uniformly sheared flow (Nakamura *et al.*, 1986), and a point source in channel flows (Webster *et al.*, 2003; Rahman & Webster, 2005). In these actual turbulent flows, the turbulent kinetic energy and lengthscale would generally evolve downstream and so would the diffusivities of superimposed scalar plumes. As a result, (2.24) would not be applicable and the plume growth rate would be expected to deviate from the previously mentioned power law.

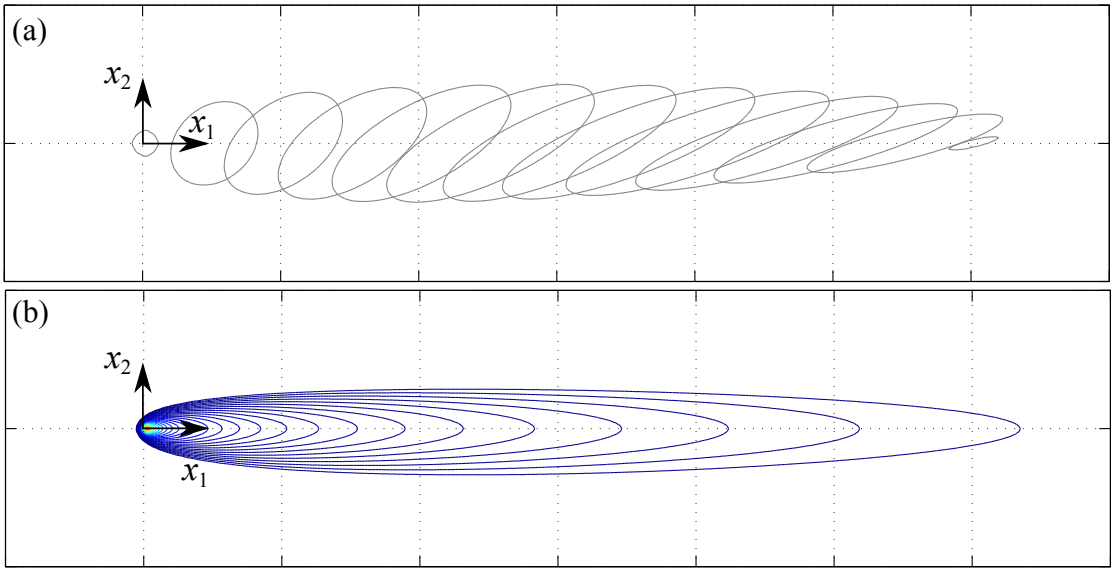


Figure 2.2: Plots of the analytical solutions for (a) the evolution of a puff in USF and (b) the mean concentration of a plume in USF, assuming a constant isotropic diffusivity.

Experimental studies of plumes in grid turbulence and shear flows have found that the plume widths followed power laws but with powers different from the theoretical value of 0.5. This discrepancy between the simplified solutions and actual turbulent flows highlights the need for further studies of turbulent diffusion and refined turbulent diffusion models.

### 2.2.5 Relative dispersion

A feature of the flow that is not considered with an absolute diffusion framework is the fact that the instantaneous plume may have a very different shape than the time-averaged plume. In many turbulent flows, and especially in the atmosphere, eddies larger than the plume create a transverse shift of the entire plume, in a process commonly referred to as meandering. As illustrated in figure 2.3, the time-averaged plume would be appear much wider than the instantaneous plume. Depending on the range of scales, a very long length of time may be required to measure the time-averaged concentration field; until the time-averaged result has converged, increasing the averaging time would have the effect of broadening and smoothing the average

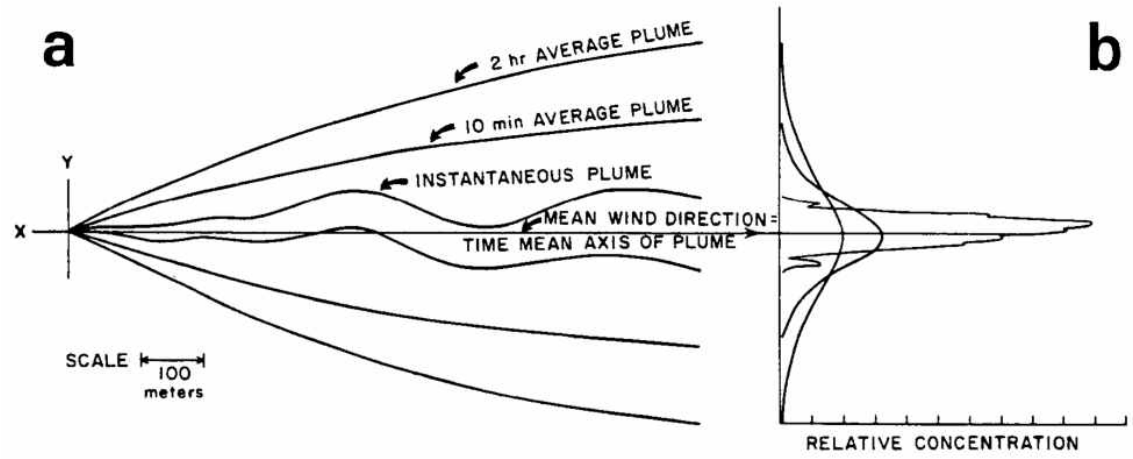


Figure 2.3: Effects of averaging time on plume shape and intensity: (a) outlines of a pollutant plume viewed from above at an instant in time, over a 10-minute period, and over a 2-hour period; (b) corresponding cross-plume relative concentration (from Slade, 1968).

plume.

Eddies of different sizes contribute to the dispersion of the plume but act on the plume differently. Large-scale eddies tend to transport the plume intact causing it to meander, but do not significantly spread the boundaries of the plume. Small-scale eddies tend to act at the plume boundary and are responsible for diffusion of the scalar into the freestream. The rate of growth of the plume boundaries would therefore be dependent on the relative size of the plume with respect to the lengthscale of the turbulence. This fundamental relationship, which was first recognized by Richardson (1926), led to the development of the framework for the analysis of relative dispersion.

Relative dispersion is concerned with the rate of spreading of the boundaries of a plume of contaminants relative to its cross-sectional centre-of-mass. This approach removes the effects of motions with scales larger than the plume width, essentially removing the effect of meandering, and focusses on the effect of the smaller eddies in the flow.

This approach can also be interpreted as studying the evolution of the separation distance, $r$, of a pair of particles in the flow, also known as two-particle dispersion. The instantaneous width of the point source plume at a given distance, $x_1$, downstream from its source would be equal to $1/\sqrt{2}$ times the root mean square separation, $\sqrt{\overline{r^2}}$,

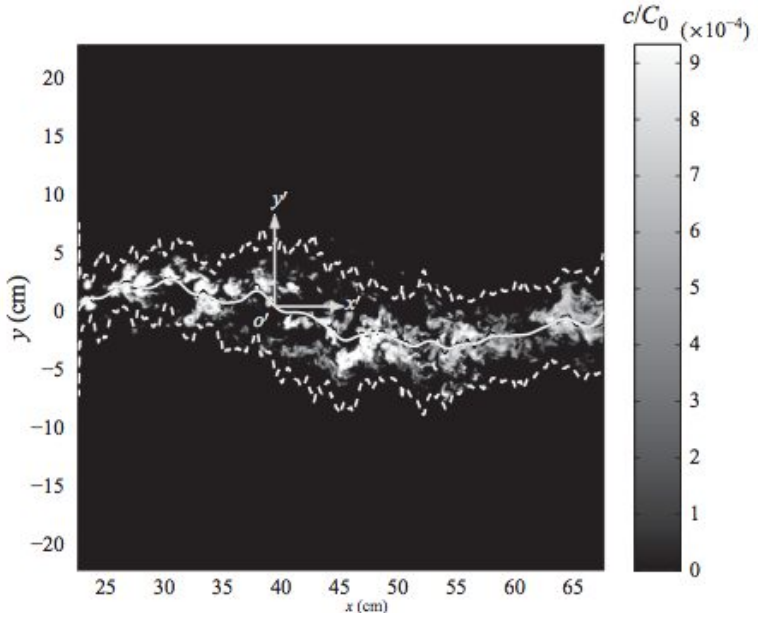


Figure 2.4: Investigation of the relative dispersion of a dye plume in channel flow by Liao & Cowen (2010); the instantaneous centre of mass of the plume is marked by a solid white line and its boundaries are marked by dashed lines.

of all particles located in the cross-section at this distance (Brier, 1950; Batchelor, 1952). The relative width of a plume can be calculated from the ensemble-average of instantaneous measurements of the plume concentration, each shifted to a common centre-of-mass. Figure 2.4 shows a representative measurement from the study of Liao & Cowen (2010), using this method to analyze the relative dispersion of a plume in channel flow.

The root mean square separation, $\sqrt{\overline{r^2}}$, may also be estimated as the standard deviation of the distance-neighbour function, $q(s)$, which is the probability that a pair of particles are separated by a distance $s$ (Liao & Cowen, 2010). In a plume, $q(s)$ can be calculated as the marginal pdf of the ensemble-averaged two-dimensional auto-correlation map of the concentration. Various theoretical predictions of the shape of $q(s)$ exist, however, experimental observations of the shape of $q(s)$ are conflicting (Salazar & Collins, 2009).

The current understanding is that there are three distinct regimes of relative dispersion, which govern the evolution of $\sqrt{\overline{r^2}}$ (Salazar & Collins, 2009):

1. **Dissipation range ($\sqrt{\overline{r^2}} \ll \eta$):** In this range, where $\sqrt{\overline{r^2}}$ is much smaller than the Kolmogorov lengthscale, $\eta$, diffusion is dominated by viscosity.

2. **Inertial range ($\eta \ll \sqrt{\overline{r^2}} \ll L_{11,1}$):** In this range, where $\sqrt{\overline{r^2}}$ is much larger than $\eta$ but smaller than the integral lengthscale of the flow, $L_{11,1}$, diffusion is dominated by eddies of size $\sim \sqrt{\overline{r^2}}$; this range can be further divided in the following subranges:

   (a) **Batchelor subrange ($t \ll t_B$):** For short times, the diffusion has some residual dependence on the initial separation, $r_0$, and $\overline{r^2}$ evolves as

   $$\overline{r^2}(t) - r_0^2 = \tfrac{11}{3} C_2 (\epsilon r_0)^{3/2} t^2. \tag{2.25}$$

   The Batchelor timescale, $t_B = (\overline{r_0^2}/\epsilon)^{1/3}$, represents the largest time for which the initial separation is important.

   (b) **Richardson-Obukhov subrange ($t_B \ll t \ll T_L$):** For intermediate times that are much smaller than the Lagrangian timescale $T_L$, the evolution of $\overline{r^2}$ depends only on the mean dissipation rate of turbulent kinetic energy, $\epsilon$, according to the law

   $$\overline{r^2}(t) - r_0^2 = g \epsilon t^3, \tag{2.26}$$

   where $g$ is a universal constant, known as Richardson's constant. This equation is a direct result of Richardson's 4/3 Law, which predicts that $\frac{1}{2} \mathrm{d}\overline{r^2}/\mathrm{d}t \propto (\overline{r^2})^{2/3}$, and Obukhov's (1941) scaling arguments, and is commonly referred to as the Richardson-Obukhov law.

3. **Diffusion range ($\sqrt{\overline{r^2}} \gg L_{11,1}$):** In this range, the particle separation is large enough for their motions to be uncorrelated. This range is equivalent to the far-field range of absolute diffusion (*i.e.*, Taylor's single particle diffusion).

In the Richardson-Obuhkov regime, the evolution of $\sqrt{\overline{r^2}}$ behaves universally and depends only on the mean dissipation rate of turbulent kinetic energy, $\epsilon$. Theoretical estimates of Richardson's constant, $g$, span the range from 0.06 to 3.52 (Sawford, 2001); however, recent experimental and numerical studies indicate that $0.5 < g < 0.6$ (Salazar & Collins, 2009).

### 2.2.6 Diffusion by coherent structures

Coherent structures are the recurring, dominant, vortical, large-scale flow patterns that are ubiquitous in turbulent flows. Previous experimental and numerical studies have shown that hairpin vortices are the predominant coherent structures in turbulent boundary layers (Adrian, 2007; Wu & Moin, 2010) as well as in other shear flows (Vanderwel & Tavoularis, 2011; Ghaemi & Scarano, 2011). The generation of such structures has been explained by the lifting and stretching of quasi-two-dimensional roller vortices. Coherent structures have been shown to be a primary mechanism for the generation of Reynolds stresses that dominate the transport of momentum, so that their control is essential for drag and noise reduction. As a corollary of Reynolds analogy, which connects heat and mass transport to momentum transport, one would expect that coherent structures should also be largely responsible for scalar transport. This connection has been demonstrated qualitatively by flow visualizations of scalar field patterns in turbulent boundary layers (Head & Bandyopadhyay, 1981; Kline *et al.*, 1967; Falco, 1977). More recently, Wu & Moin (2010) also observed hairpin vortices in isocontours of a scalar field examined by direct numerical simulations.

The effects of coherent structures on scalar transport are particularly important in the context of environmental flows. Katul *et al.* (1997) and Li & Bou-Zeid (2011) have noted that, in the atmospheric surface layer, the ejection and sweep motions that are typically associated with coherent structures are responsible for much of the land-surface evaporation, heat and momentum fluxes. Provenzale (1999) reviewed the impact of coherent vortices in quasigeostrophic flows in the ocean and the atmosphere and described how scalars seeded within vortices experience reduced dispersion compared to the free stream, and become, in a sense, islands of stability. Investigations of particle dispersion have also demonstrated that coherent structures are responsible for particle clustering, which has direct ramifications to reactive flows such as combustion as well as to droplet coalescence and the formation of clouds in the atmosphere (Shaw *et al.*, 1998; Rouson & Eaton, 2001). Better understanding of the role of coherent structures in scalar transport is also important for working towards the refinement of turbulent diffusion models to better be able to resolve their effects.

# Chapter 3

# Apparatus, Instrumentation, and Procedures

## 3.1 The water tunnel

All experiments were conducted in the recirculating water tunnel at the University of Ottawa. The test section has a free surface and three glass walls; it is 0.53 m wide, it was filled to a depth of 0.426 m, and provides continuous optical access over its 4 m length; details of the recent renovation of this facility are provided in Appendix A.1. Measurements of the quality of flow in the water tunnel are presented in Appendix A.2.

Nearly homogeneous USF was generated by a perforated plate of varying solidity and a flow separator inserted at the entrance to the test section (see figure 3.1). The spacing of the flow separator plates was $L$ = 25.4 mm. The mean velocity field and the turbulence properties in the USF were documented thoroughly with the use of laser Doppler velocimetry (LDV) and particle image velocimetry (PIV) by Vanderwel & Tavoularis (2011). The point source of the dye was approximately 2 m downstream of the exit of the flow separator at mid-depth and mid-span; the origin of the coordinate system was at this point.

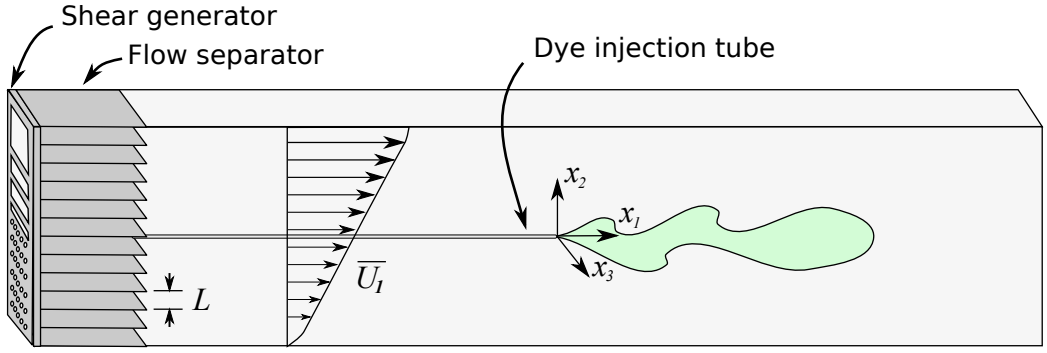


Figure 3.1: Sketch of the water tunnel test section. The origin of the coordinate system is at the injection point of the dye.

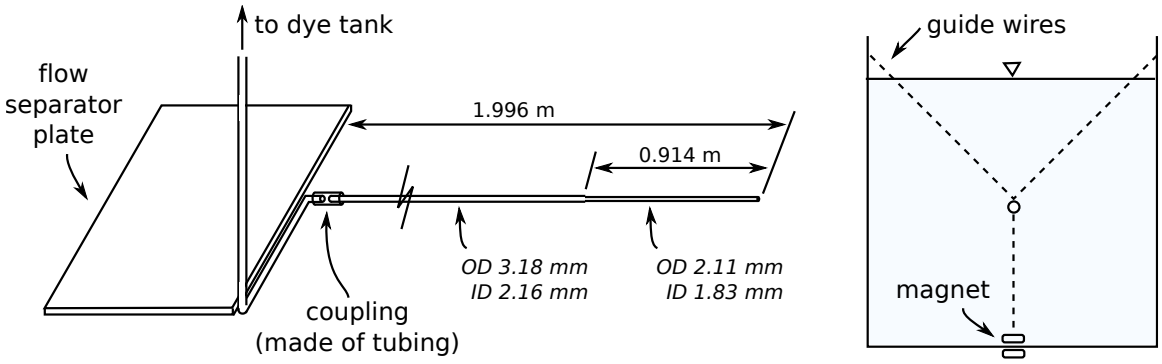


Figure 3.2: Sketch of the dye injection nozzle.

## 3.2 The dye injection system

The dye injection tubing was designed to produce as low a disturbance to the flow as possible. This system is illustrated in figure 3.2. The injection tube extended streamwise from the flow separator at the beginning of the test section and its tip was located 1996 mm from the exit of the flow separator. The upstream part of the injector was made of 1/8" stainless steel tube (OD 3.18 mm, ID 2.16 mm) and the tube tip was made of precision stainless tubing (OD 2.11 mm, ID 1.83 mm, 914 mm long). The injector was tethered in place by 50 $\mu$m thick guide wires that were suspended from the top of the channel at several downstream positions. Near the exit of the injector tip, an additional guide wire was tethered to a small magnet at the bottom of the tunnel that was kept in place by another magnet on the other side of the glass bottom. The guide wires ensured that the injector was free of any movement or vibrations. No measurable wakes of the wires were detected, as expected as their Reynolds number was 5.

In order to ensure a steady flow rate through the nozzle, the dye solution was supplied by a canister that was pressurized using compressed air controlled by a pressure regulator. The flow rate through the nozzle was $Q = 0.97$ m$\ell$/s (58 cc/min) and was regulated by a rotameter with a built-in needle valve (Matheson 605 Glass) with an uncertainty of 0.05 m$\ell$/s. The optimal flow rate through the injector was determined by comparing the velocity maps for different injection flow rates in a plane normal to the flow at a distance of $x_1/L = 5$ from the injector tip; this distance is

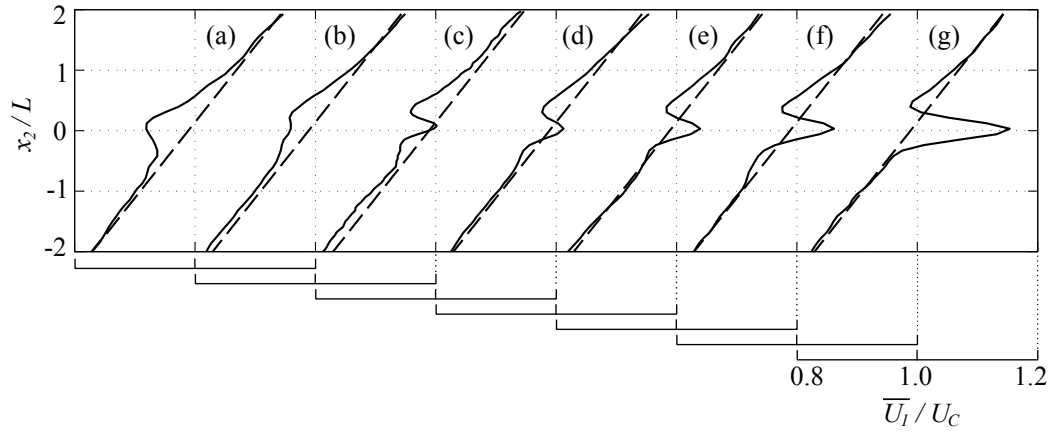


Figure 3.3: Solid lines are transverse profiles of the mean streamwise velocity at $x_1/L = 5$ and $x_3 = 0$ with injector flow rates of (a) 0, (b) 0.78, (c) 0.97, (d) 1.07, (e) 1.25, (f) 1.37, and (g) 1.68 m$\ell$/s. Dashed lines represent velocity profiles without the injector. The flow rate chosen for the present experiments was $Q = 0.97$ m$\ell$/s.

equal to approximately 70 inner tube diameters. The transverse profiles of the mean velocity measured at this location are presented in figure 3.3. The physical presence of the injection tube created a region of relative velocity deficit due to the boundary layer that grew along the tube. At the same time, injection at a velocity higher than the local value created a local momentum surplus within the injected fluid. Our objective was to adjust the injection flow rate so that the momentum surplus of the jet would compensate, as much as possible, for the momentum deficit around the injector, without introducing significant jet effects which would distort the structure of the USF. The value $Q = 0.97$ m$\ell$/s, represented by curve (c) in figure 3.3, was deemed to be the optimal one and was used for all reported results.

## 3.3 Experiment configuration

### 3.3.1 Overview of the equipment

Stereoscopic particle image velocimetry (SPIV) was used to measure velocity vector maps in cross-sections of the flow oriented both normal to and parallel to the mean flow direction. The SPIV equipment consisted of the FlowMaster system from LaVision GmbH (Ypsilanti, MI), which included a Nd:YAG pulsed laser (Solo PIV

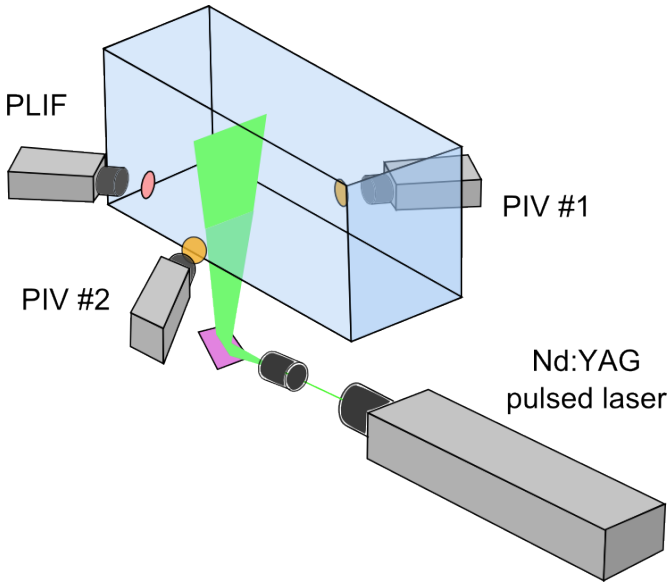


Figure 3.4: Sketch of the 3D SPIV-PLIF normal-plane experimental configuration.

120XT; New Wave Research, Fremont, CA), two LaVision Imager Pro X 4M cameras with 2048 × 2048 pixels, a programmable timing unit (Lavision PTU-9 External #1108058), and an acquisition computer. The cameras were fitted with Nikon Nikkor 50 mm f/1.8D lenses and 532 nm bandpass filters (Lavision #1108560) in order to capture only the particle images. The laser sheet was created with divergent sheet optics (Lavision #1108405) using a $f = -10$ mm divergent lens.

Measurements of scalar concentration maps in the same plane as the velocity measurements were obtained by planar laser-induced fluorescence (PLIF). The PLIF measurements were obtained with a pco.edge sCMOS camera from PCO AG (Kelheim, Germany) with 2560 × 2160 pixels, which was fitted with a Nikon Nikkor 50 mm f/1.4D lens and a 540 nm longpass filter (Lavision #1108573) in order to capture only the fluorescent light from the dye.

### 3.3.2 Configuration

The majority of measurements were obtained in the $x_2 - x_3$ plane, which is normal to the flow direction (see figure 3.4).

Liquid prisms were used to reduce the optical distortion created by the inclined view through the glass (see figure 3.5). Without using liquid prisms, the camera

image would have a horizontal astigmatism caused by looking through the glass; the left and right sides of the image would be refracted by different amounts, and thus the object plane could never be in focus. The liquid prism is fixed to the outside of the glass and has a face that was approximately normal to the camera lens axis. The large changes in refractive indices between air and glass and glass and water have an insignificant effect because the interfaces are crossed in a nearly normal direction. The use of a prism for SPIV was first suggested by Prasad & Jensen (1995). van Doorne & Westerweel (2007) also made use of such a prism, having an angle of 45 degrees. This solution is also discussed by Adrian & Westerweel (2011). The design of the liquid prisms used in the current experiments is illustrated in figures 3.5 and 3.8. They were made of machined acrylic plates, which were then glued together. A thin pane of glass (2 mm thick) was glued into a frame made by one of the acrylic plates using marine epoxy; the glass was as thin as possible to reduce optical distortions. The prism was then pushed against the glass wall of the test section and filled with distilled water. A window gasket sealed the prism against the test section.

In addition, Scheimpflug adapters were used to focus the lens on an object plane that was not normal to the camera. All three cameras were fitted with Scheimpflug adapters (LaVision, Series 3 #1108176). These adapters tilt the lens with respect to the camera CCD, which causes the object plane to be tilted in accordance with the Scheimpflug criterion, which states that the image plane, the lens plane, and the object plane must intersect. A simple ray-tracing illustration of the present configuration is presented in figure 3.6.

In order to avoid reflections in the PLIF image, a polarized filter was placed over the lens of the PIV camera that was opposite to the PLIF camera. Additionally, the lights in the room were turned off. These precautions eliminated any stray light, which could otherwise have interfered with the PLIF measurements.

### 3.3.3 The laser sheet profile

The variation of radiant power flux across the laser sheet was determined directly by illuminating a board painted with fluorescent paint and measuring the resulting

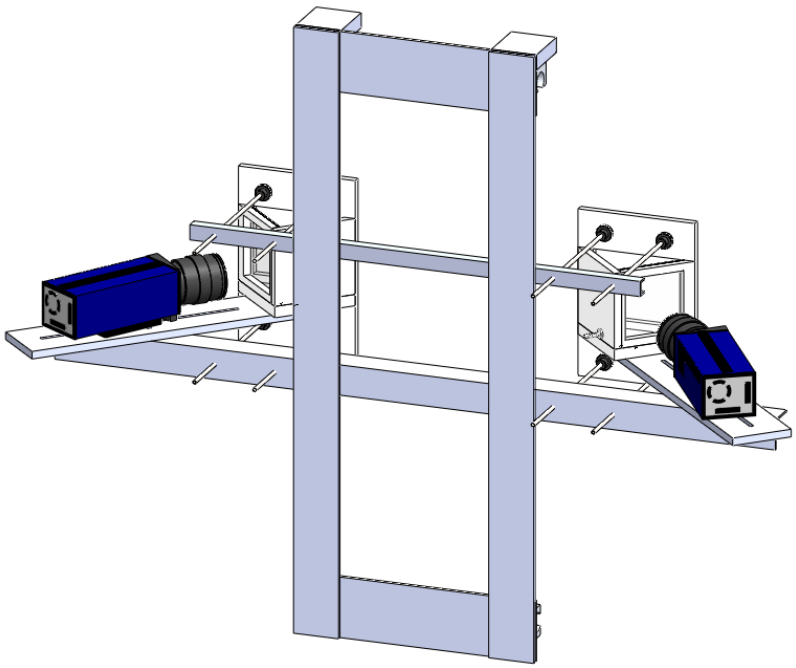

Figure 3.5: Sketch of camera cart and the liquid prisms used in the SPIV configuration. The prisms are used to reduce the optical distortions associated with viewing into a water tank at an angle.

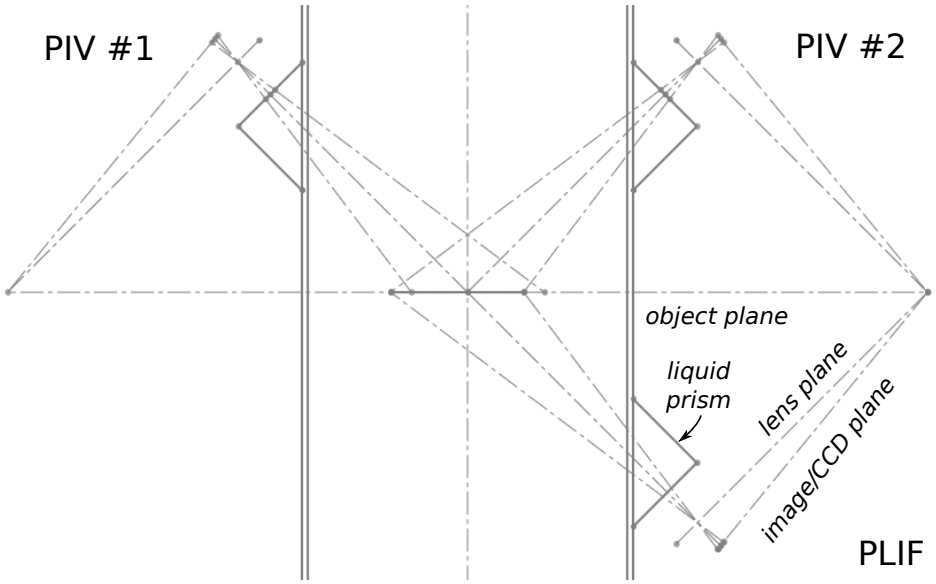


Figure 3.6: Ray-tracing of the 3D configuration, using liquid prisms and Scheimpflug adapters.

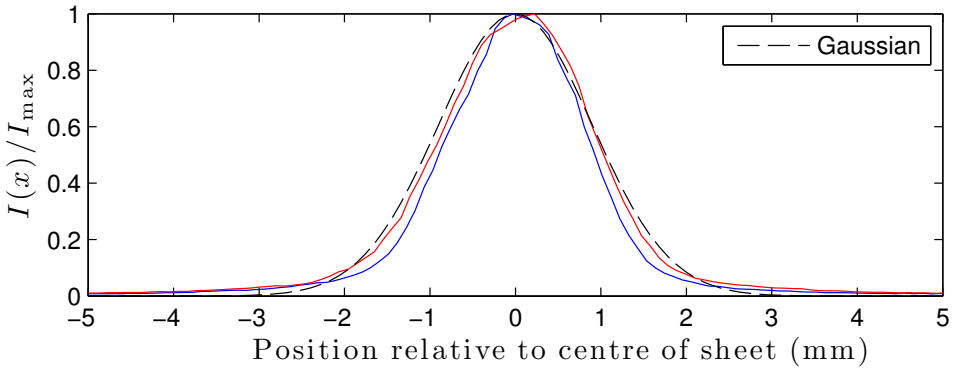


Figure 3.7: Measurements of the intensity profile of the laser sheet.

fluorescence with the camera fitted with the optical filter. The fluorescent paint was a mixture of Rhodamine 6G powder, ethanol, and clear polyurethane paint, based on a recipe provided by LaVision (Goettingen, Germany). In order to account for possibly uneven concentration on the board, images were repeated with the board rotated by 180 degrees. The radiant power flux variation, plotted in figure 3.7, was fitted well by the Gaussian function

$$\frac{I(x_3)}{I_{max}} = \exp\left[-\frac{{x_3}^2}{2{\sigma_L}^2}\right] , \tag{3.1}$$

where the characteristic halfwidth of the sheet was $\sigma_L \approx 1$ mm.

### 3.3.4 Aligning the laser sheet

Careful alignment of the laser sheet was performed to ensure that it was accurately located. The alignment was performed by placing a target on the bottom glass of the tunnel and above the free surface of the tunnel. The lower target was a piece of masking tape on the outside of the bottom glass window, and the upper target was marked on a board that was mounted above the tunnel. These targets were accurately positioned with a ruler so that they were in the centre of the tunnel. The laser sheet optics and mirror were then iteratively adjusted until both the lower and the upper targets were simultaneously illuminated by the laser sheet.

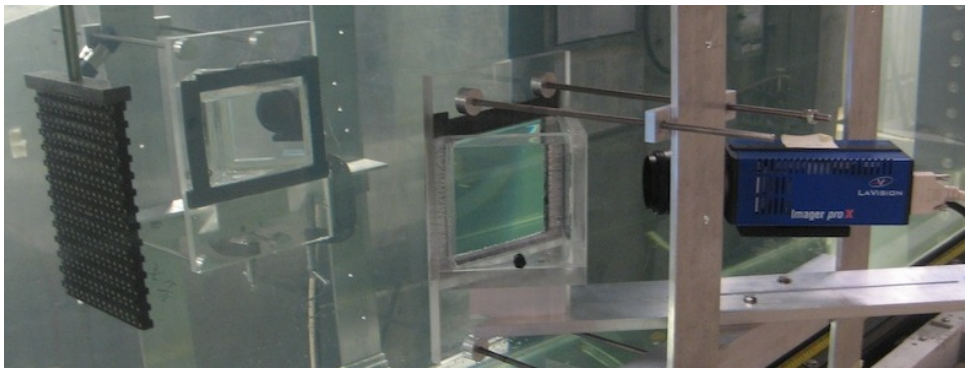


Figure 3.8: Photograph of the camera setup for SPIV using the calibration target.

### 3.3.5 Determining the image mapping functions

A calibration target mounted in the desired image plane was used to help setup the camera positions (figure 3.8). The target was 204 mm × 204 mm and contained a grid of dots equally spaced on a 15 mm × 15 mm grid on two planes separated by a distance of 3 mm. The cameras were aligned such that their fields of view were closely matched in position and scale. At this point the camera settings were also adjusted so that each foci was on the calibration plate. The spatial resolutions of the cameras were approximately 0.05 mm/pixel.

The calibration plate was aligned carefully in the desired image plane. The calibration plate was mounted on a vertical rod that was mounted above the tunnel, ensuring that the plane was vertical. To ensure that the plate was aligned with the streamwise direction $x_1$, the plate was pressed against the side wall of the tunnel as the rod was mounted securely, locking its rotation. Furthermore, the $x_3$ position of the plate was aligned in the centre of the tunnel using the same marking that was used as an upper target for aligning the laser sheet. The $x_1$ position of the plate was measured relative to the streamwise ruler mounted above the water tunnel. The $x_2$ position was positioned by eye at first, and then carefully measured by inserting a ruler in the tunnel and measuring the distance from the bottom glass.

The software created an initial image mapping function for both cameras by taking an image of the calibration plate with both cameras. The dots on the calibration plate were identified by the software and the image mapping function ensured that

these dots were coincident in both camera images. The image mapping function used a pinhole camera model and correctly estimated the focal lengths and positions of both cameras using the images of the calibration plate. The RMS fit error from this alignment was reported by the software as 0.2-0.3 pixels.

Errors due to misalignment of the laser sheet and the calibration target were corrected by the self-calibration software process. The calibration plate was removed and images of particles illuminated in the laser sheet ware captured by both cameras simultaneously and used to correct the camera mapping function. At this point, the focusing of the two cameras was fine-tuned to have the particles in the best focus. Errors due to misalignment of the laser plane and the calibration plane are manifested as translational errors and rotational errors. These errors were typically on the order of 3 pixels and ±2°, respectively. After the image mapping function was updated, the average deviation in the alignment of the two cameras was reported by the software as 3.4 pixels.

A further complication was caused by the third camera, which was calibrated on the back side of the calibration target. Because the depth of the field was so small (because of the large aperture) the calibration target had to be traversed by the width of the target so that the focal plane was exactly the same as those of the other two cameras. However, the software took into consideration that the third camera was calibrated using the reverse side of the target and automatically compensated for the thickness of the target. Therefore, because the target was actually displaced for the measurement, a z-translation of the thickness of the plate had to be input into the software for the calibration to be correct.

## 3.4 Stereo particle image velocimetry

### 3.4.1 Methodology

Particle image velocimetry measures the instantaneous velocity of the flow. In order to do so, two images of the particles in the measurement plane are taken, one shortly after the other. The velocity measurement $U$ is then calculated from the recorded displacement $\Delta X$ of the particles, the magnification factor $\alpha$ between the object plane

and camera image plane, and the time separation $\Delta t$ of the two images as

$$U = \frac{\alpha \Delta X}{\Delta t} \ . \tag{3.2}$$

Stereo particle image velocimetry uses two cameras to measure the three-dimensional displacement of the particles. Each camera determines a two-component vector field by means of eq. 3.2, which are then consolidated to determine the third velocity component.

### 3.4.2 The seeding

In the reported experiments, hollow glass spheres were used to seed the flow. Similar hollow glass spheres were also used by van Doorne & Westerweel (2007). The particles were premixed in water and injected into the flow at the entrance to the test section, ahead of the shear generating apparatus, using a injection tube that was gravity fed from a small tank located above the water tunnel reservoir.

A typical particle image is presented in figure 3.9. Adrian & Westerweel (2011) suggest an optimal value of 10 particle images per interrogation area; as can be seen in figure 3.10, the current particle images have approximately this particle density for an interrogation area of 32 × 32 pixels.

The particle dynamics can introduce error in the velocity measurement that is caused by differences between the particle velocities and the velocity of the fluid. The terminal velocity $U_g$ of small, heavy spherical particles causes a relative vertical velocity when the particle density is different from the fluid density. This velocity can be estimated by the expression provided by Raffel *et al.* (1998), where $d_p$ is the diameter of the particle, $\rho_P$ and $\rho$ are the densities of the particles and the fluid respectively, and $\mu$ is the viscosity of the fluid.

$$U_g = d_p^2 \frac{(\rho_P - \rho)}{18\mu} g \tag{3.3}$$

Tracer particles are also subject to drag when there is a relative motion between the particle and the fluid. The time constant of the particle-fluid interaction $\tau_S$ is given by Tavoularis (2005) as

$$\tau_S = \frac{\rho_P d_p^2}{18\mu} \left( 1 + \frac{1}{2\rho_P/\rho_f} \right). \tag{3.4}$$

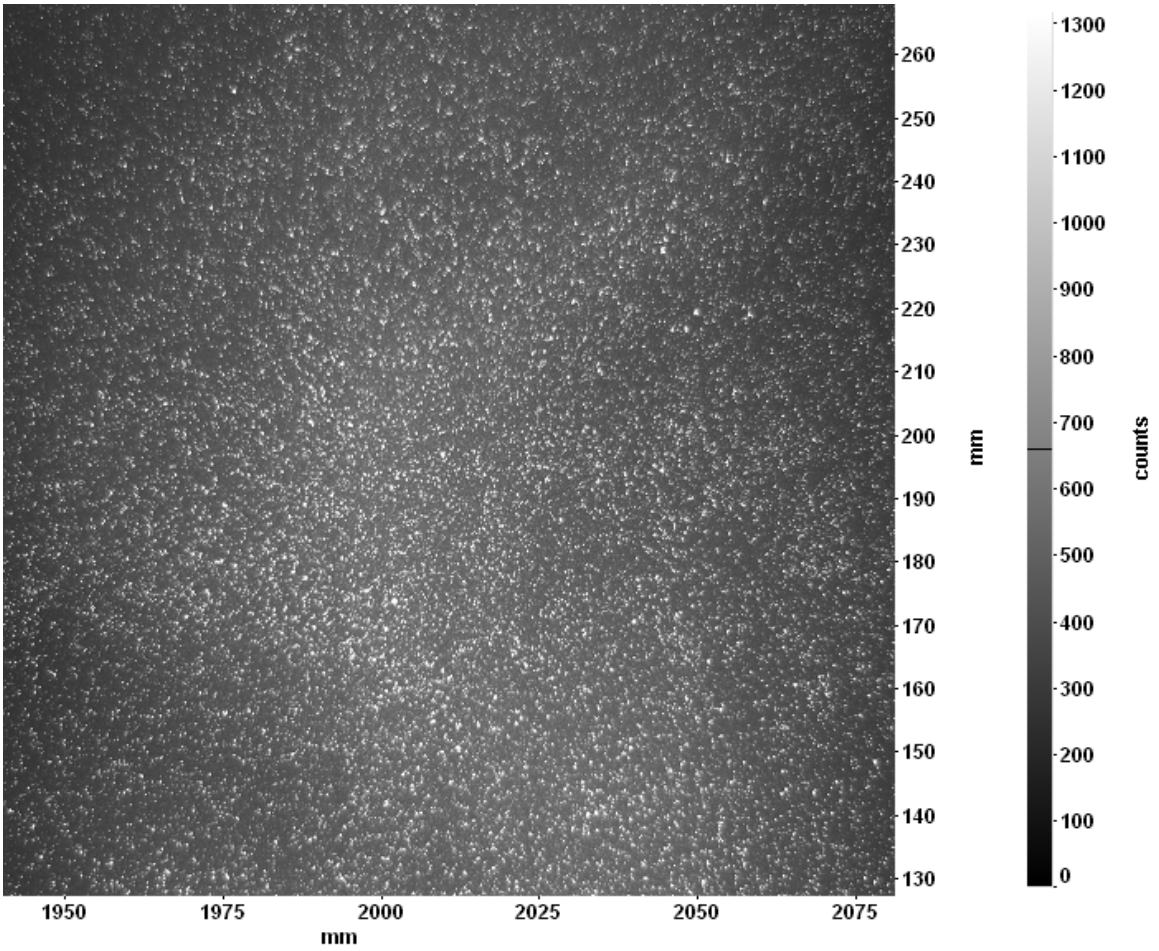


Figure 3.9: A typical particle image from the current experiments.

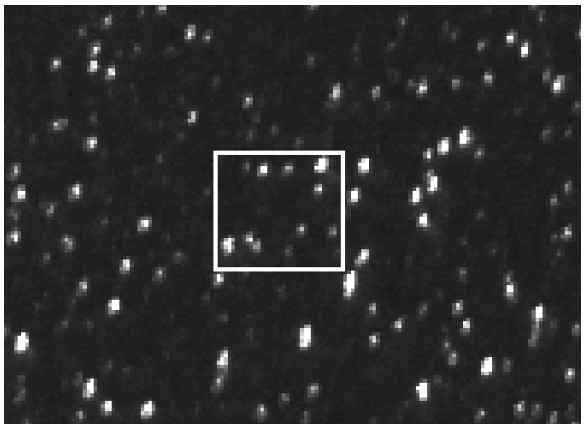

Figure 3.10: A zoomed-in portion of a typical particle image from the current experiment. A 32 × 32 pixel area corresponding to the size of the interrogation area is indicated by the white square.

| Particle Type | $\rho_P$ (g/cm$^3$) | $d_P$ ($\mu$m) | $U_g$ (m/s) | $\tau_S$ ($\mu$s) |
|---|---|---|---|---|
| Silicon Carbide | 3.21 | 2 | $5.4 \times 10^{-6}$ | 0.9 |
| Hollow Glass Spheres | 1.1 | 12 | $8.8 \times 10^{-6}$ | 14.4 |
| Background Contaminants | 5.2 | 5 | $64 \times 10^{-6}$ | 8.9 |

Table 3.1: Dynamic properties of various particle tracers.

The properties of the hollow glass spheres are presented in table 3.1, compared with the properties of silicon carbide particles, which are also commonly used as seed particles, and the properties of possible background contamination that may have been present in the flow. The worst of this contamination was from rust particles, which had an estimated density of 5.2 g/cm$^3$ (ferric oxide), and had an estimated maximum diameter of 5 $\mu$m, which was the pore size of the water filter used on the water channel. Because $U_g$ and $\tau_S$ are small for each of these kinds of particles, they would all follow the flow quite well and have negligible contribution to the measurement uncertainty. The hollow glass spheres do not follow the flow quite as well as the silicon carbide particles, but reflect much more light because of their larger diameter, which was why they were chosen for seeding the present experiments.

### 3.4.3 PIV parameters and processing

PIV measurements were performed using the DaVis 7 software from LaVision. The present measurements used a time separation of $\Delta t = 1500$ $\mu$s, resulting in an average particle separation of 4 pixels. Measurements were taken at 2 Hz.

The cross-sectional profile of the laser intensity had approximately the shape of a Gaussian distribution with a standard deviation of 1 mm. During the interval between the two pulses, a particle travelling with the centreline flow velocity of 0.18 m/s would be displaced by a streamwise distance of 0.27 mm, which satisfies well the SPIV requirement of being much smaller than the laser sheet thickness.

Because some of the fluorescence intensity is apparent in the spectral range captured by the PIV camera, the images benefited from a pre-processing step. Prior to processing the PIV images, the image intensity was filtered in order to normalize the local intensity relative to a scale length of 4 pixels. This successfully made the

particles stand out, even when the local intensity of the region was high due to the presence of fluorescent dye.

These images were then processed using a multi-pass routine starting with an interrogation window of 64 × 64 pixels, and then decreasing to 32 × 32 pixels with 50% overlap. The resulting resolution of the velocity maps was approximately one vector per 1.15 mm × 1.15 mm flow area. Vectors with too few particles within the interrogation volume were deleted. The vector fields were then post-processed, smoothing the results using low-pass filter with a 3 × 3 window, and filling up all the empty spaces.

The vector fields that were produced were of good quality, following the criteria outlined by Adrian & Westerweel (2011):

- There were no obviously erroneous vectors.

- Pixel locking was not a significant effect. Pixel locking affects the resolution of the velocity measurement. To test if pixel locking is significant, a histogram of the velocity magnitudes was plotted (figure 3.11). These histograms showed that the resolution of the velocity measurement was correct to at least 4 decimal places; the histogram with bin widths at 5 decimal places begins to show variation in the frequencies of neighbouring bins, indicating insufficient resolution.

- The fraction of valid interrogation data was greater than 95%. From the same data used to estimate the pixel locking effect, less than 1% of vectors were deleted because of insufficient particles within the interrogation zone.

### 3.4.4 Uncertainty estimates

Methods for estimating the uncertainty involved in PIV are discussed by the Specialist Committee on Uncertainty Analysis of 25th ITTC (2008) and by Adrian & Westerweel (2011). Errors can affect the particle displacement $\Delta X$, the magnification factor $\alpha$, and the time separation $\Delta t$, used in the calculation of the velocity vectors $U$ by each camera (eq. 3.2). Errors affecting each of these factors are discussed in the following

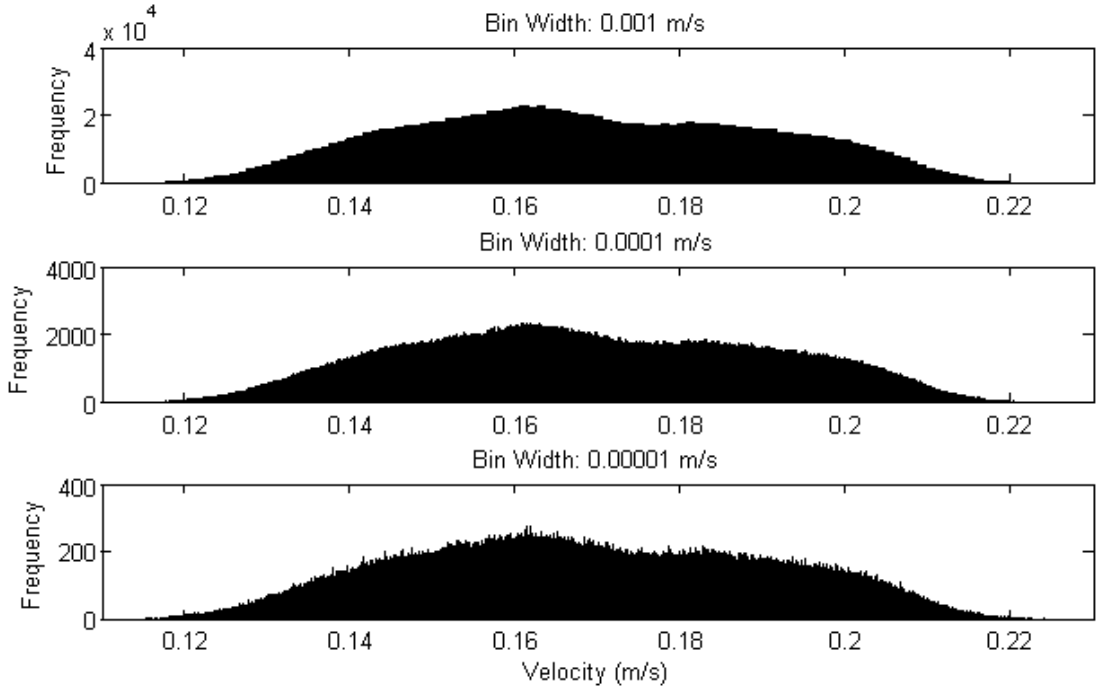


Figure 3.11: Histograms of the streamwise velocity from 100 measurements taken at the same location. These histograms show that pixel locking is not significant and scatter in the velocity measurement is only effects the 5 decimal place.

paragraphs. Note that for the present experiments, nominal values of these factors are $\alpha = 0.05$ mm/pixel, $\Delta t = 1500$ $\mu$s, $\Delta X = 4$ pixels.

**Magnification** $\alpha$ The magnification ratio, $\alpha$, defined as the ratio between the image size in pixels and the true length on the measurement plane in millimetres, is determined by calibration with a LaVision calibration plate (type #22), followed by self-calibration by the DaVis software using simultaneous images of particles in the measurement plane by both cameras. As described in section 3.3.5, the final average deviation in the alignment of the two cameras is 3.4 pixels. The total size of the CCD is 2048 pixels, so a misalignment of 3.4 pixels would translate to a bias error of $3.4/2048 = 0.2\%$. This is in line with the recommendation of Adrian & Westerweel (2011) who suggest that the uncertainty in the magnification should be able to be optimized to approximately 0.3%.

**Time separation of pulses** $\Delta t$ The time separation of the two pulses is triggered and recorded by the timing unit, which has an uncertainty of 5 ns, according to the LaVision manual. Furthermore, the duration of the two pulses contributes an uncertainty of $2 \times 5$ ns as the particle may be captured at any point during the pulse. These combined uncertainties result in a precision of 0.0001% from the total average time separation of 1500 $\mu$s, which is entirely negligible.

**Displacement of particles** $\Delta X$ Uncertainty in the measurement of the displacement of the particles can be caused by the finite thickness of the laser sheet, during the recording of the particle images to the camera, or during the cross-correlation calculations. Factors contributing to these processes are:

- The correlation process is not perfect and contributes to the uncertainty of the calculated particle displacement. The Specialist Committee on Uncertainty Analysis of 25th ITTC (2008) and Adrian & Westerweel (2011) agree that an average random error of 0.1-0.2 pixels would be due to the potential mismatching of particles. This leads to a fractional precision of 5%.

- An additional systematic error is due to the discretisation of particles into discrete pixels, referred to as 'pixel-locking'. Measurements of this effect in section 3.4.3 indicated that this effect was negligible.

- The ability of the particles to follow the flow was previously discussed in section 3.4.2. While the seed particles were found to follow the flow well, foreign particles up to a diameter of 5 $\mu$m would exhibit a terminal velocity of $64 \times 10^{-6}$ m/s, which corresponds to a precision uncertainty of about 0.05% which is entirely negligible.

**Error in the velocity components** Using the previously found uncertainties, the uncertainty of the two-component velocity fields determined by each camera can be determined as

$$\frac{\delta U}{|U|} = \sqrt{\left(\frac{\delta\alpha}{\alpha}\right)^2 + \left(\frac{\delta(\Delta t)}{\Delta t}\right)^2 + \left(\frac{\delta(\Delta X)}{\Delta X}\right)^2}\,. \tag{3.5}$$

This leads to a velocity bias limit at about 0.2% and a precision limit at about 5%, for a total velocity uncertainty in the instantaneous velocity measurements of about 5%. The low-pass smoothing filter that was applied to the vector field during processing drastically decreases high-frequency random errors, thus further decreasing the precision uncertainty.

The uncertainty in each of the three velocity components in the SPIV setup can be determined as functions of the general velocity uncertainty in the 2D system as (Lavision GmbH, 2012)

$$\delta U_1 = \delta U_{2C} \frac{\sqrt{\cos^2\theta_1 + \cos^2\theta_2}}{|\sin^2(\theta_1 - \theta_2)|}, \tag{3.6}$$

$$\delta U_2 = \delta U_{2C} \frac{1}{\sqrt{2}}, \tag{3.7}$$

$$\delta U_3 = \delta U_{2C} \frac{\sqrt{\sin^2\theta_1 + \sin^2\theta_2}}{|\sin^2(\theta_1 - \theta_2)|}, \tag{3.8}$$

where $\theta_1$ and $\theta_2$ are the angles at which the two cameras viewed the measurement plane. In the current configuration, $\theta_1 = +45°$ and $\theta_2 = -45°$, which leads to $\delta U_1$ and $\delta U_3$ being equal to $\delta U_{2C}$, while $\delta U_2$ is reduced by $1/\sqrt{2}$ compared to $\delta U_{2C}$. Therefore,

the overall velocity uncertainty in the SPIV configuration is essentially the same as in the two-component configuration.

By averaging a large amount of velocity measurements, the precision limit may be reduced. The uncertainty in the mean value is reduced by $1/\sqrt{N}$, where N is the number of samples Tavoularis (2005). For all time-averaged measurements a minimum of 500 samples were used, which drastically reduces the precision uncertainty of the mean velocity to about 0.2%.

In addition to the velocity uncertainty, the PIV also fails to capture the small motions of the turbulent flow due to the resolution of the measurements. The resolution of the vector field is approximately one vector per 1.15 mm × 1.15 mm flow area. Any motions smaller than this scale cannot be resolved. However, considering that the Kolmogorov length scale of this flow was $\eta \approx 0.6$ mm, velocity changes between measurement points would be relatively small.

# Chapter 4

## On the accuracy of PLIF measurements in slender plumes

This chapter addresses the methodology and uncertainty of the planar laser-induced fluorescence technique as applied to concentration measurements of a slender dye plume. The results are presented in the form of the manuscript

> Vanderwel C. and Tavoularis S. (2014) "On the accuracy of PLIF measurements in slender plumes, Experiments in Fluids, Vol. 55, Issue 8, 1801,

which was published on August 10, 2014. This manuscript explains the procedure for concentration measurements in the present experiments and includes a thorough analysis of the uncertainty of the PLIF technique. In particular, we identified two previously unconsidered sources of error contributed by non-uniformity of the concentration across the laser sheet and by secondary fluorescence. We proposed new methods to evaluate and correct for these sources of error and demonstrated that the corrected concentration measurements accurately determined the injected dye mass flow rate in the far field.

Exp Fluids (2014) 55:1801
DOI 10.1007/s00348-014-1801-x

RESEARCH ARTICLE

# On the accuracy of PLIF measurements in slender plumes

**Christina Vanderwel · Stavros Tavoularis**

Received: 20 May 2014 / Revised: 18 July 2014 / Accepted: 24 July 2014


**Abstract** The purpose of this article was to assess the measurement uncertainty of the planar laser-induced fluorescence (PLIF) method and, as much as possible, to devise corrections for predictable biases. More specifically, we considered the measurement of concentration maps in cross sections parallel to and normal to the axis of a slender plume containing Rhodamine 6G as a passive scalar tracer and transported by a turbulent shear flow. In addition to previously examined sources of error related to PLIF, we also investigated several unexplored ones. First, we demonstrated that errors would arise if the laser sheet thickness was comparable to or larger than the thickness of the instantaneous plume. We then investigated the effect of secondary fluorescence, which was attributed to absorption and re-emission of primary fluorescence by dye both within and outside the laser sheet. We found that, if uncorrected, this effect would contaminate the calibration as well as the instantaneous concentration measurements of the plume, and proposed methods for the correction of these errors and for identifying the instantaneous boundaries of the in-sheet dye regions.

## 1 Introduction

Planar laser-induced fluorescence (PLIF) is a popular method of studying the mixing and dispersion of passive scalars in turbulent flows. It consists of injecting an aqueous solution of fluorescent dye into water flow, illuminating a thin layer of the water with a laser sheet and recording its image, and constructing planar maps of dye concentration from the recorded maps of light intensity. PLIF is an attractive experimental technique, as it is non-intrusive, quantitative, and capable of providing two-dimensional scalar concentration maps. In addition, it can be fairly easily combined with other optical methods that can provide simultaneous measurements of flow velocity and temperature.

PLIF has been applied successfully by numerous previous investigators, some of whom addressed various aspects of its uncertainty. For example, the uncertainty of PLIF image processing algorithms was discussed, among others, by Walker (1987), Ferrier et al. (1993), Karasso and Mungal (1997), Cowen et al. (2001), Melton and Lipp (2003), Webster et al. (2003), Shan et al. (2004), Crimaldi (2008), and Sarathi et al. (2012). However, the requirements of uncertainty analysis in different studies have been quite diverse, depending on the objective and scope of the experiment, the flow conditions, the experimental configuration, and other factors. In some studies, PLIF was used only qualitatively, for the purpose of detecting a scalar interface, without concern for quantifying concentration. In other studies, the experimental conditions were such that uncertainty that could be possibly introduced by some sources was essentially negligible. For these reasons, a general PLIF uncertainty analysis is still lacking, with several potential sources of uncertainty remaining unexplored.

Motivation for the work presented in this article arose during an experimental investigation of the diffusion of a slender passive scalar plume in turbulent flow, for which dye concentration measurements were collected on planes both parallel with and normal to the flow direction. The

C. Vanderwel · S. Tavoularis
Department of Mechanical Engineering, University of Ottawa, Ottawa, ON, Canada

Published online: 10 August 2014

experimental setup and PLIF methodology are described in Sect. 2, whereas some results have been presented in other articles (Vanderwel and Tavoularis 2013, 2014a). In the course of these experiments, we first evaluated the concentration uncertainty introduced by sources discussed in the literature, but we also identified additional uncertainty sources and effects that have not been previously discussed, although intrinsic to the PLIF methodology.

The following section provides a brief description of the experimental facility, the properties of the dye used, and its illumination and recording methodology. In Sect. 3, we present an idealized method for concentration measurement, which neglects the effects of concentration non-uniformity, light attenuation, and secondary fluorescence. We then discuss each of these effects in turn in Sects. 4–6, providing limits of concentration non-uniformity level to avoid substantial errors and correction procedures for the effects of light attenuation and secondary fluorescence. In Sect. 7, we present a method for identifying and discarding out-of-sheet dye, whereas in Sect. 8, we describe our method for concentration measurement that takes into consideration several corrections. Lastly, in Sect. 9, we present a test of the accuracy of the PLIF measurements in a slender turbulent plume.

## 2 The experimental facility, the dye, and the PLIF instrumentation

### 2.1 The flow field

The experiments were conducted in a recirculating water tunnel, having a test section with a free surface, a width of 0.53 m, a length of about 4 m, and filled to a height of 0.46 m from the bottom. Uniformly sheared flow (USF), with a linear mean velocity variation, approximately homogeneous turbulence on a transverse plane, and Reynolds stresses that grew exponentially in the streamwise direction, was generated in the test section with the use of a shear generator. Details about the turbulent field have been presented previously by Vanderwel and Tavoularis (2011). Velocity measurements at the specific conditions of the present experiments were taken using stereoscopic particle image velocimetry (SPIV). A neutrally buoyant aqueous solution of fluorescent dye was injected isokinetically into the flow through a fine tube having an inner diameter of 1.83 mm and a wall thickness of 0.15 mm, at a point approximately 2 m downstream of the shear generator, where the turbulence structure was fully developed (see Fig. 1). The undisturbed mean velocity at the point of dye injection was $U_C = 0.18$ m/s, the mean shear was $\mathrm{d}\overline{U}_1/\mathrm{d}x_2 = 0.5\ \mathrm{s}^{-1}$, and the turbulent Reynolds number

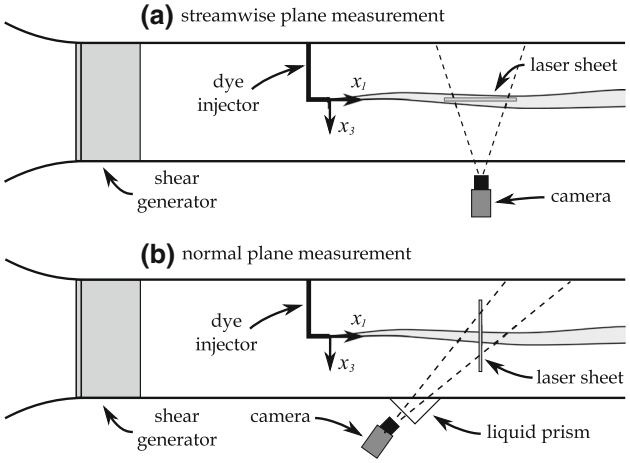


**Fig. 1** *Top view* of the apparatus in the **a** streamwise and **b** normal-plane configurations

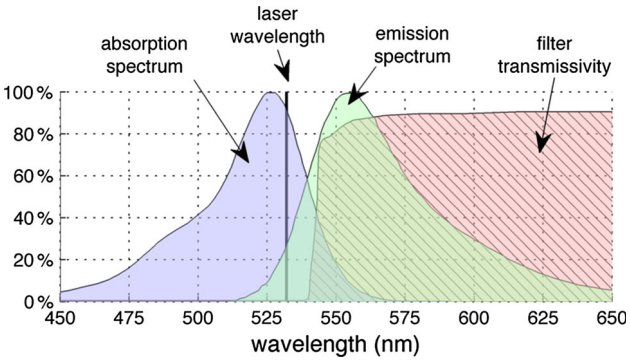


**Fig. 2** The absorption and emission spectra of Rhodamine 6G (data from Würth et al. (2012), normalized by their maximum values) and the transmission spectrum of the optical filter (data from Lavision, Goettingen, Germany) with the wavelength of the Nd:YAG laser indicated by a *solid black line*

was $Re_\lambda \approx 150$. The integral lengthscale of the turbulence was comparable to the spacing of the shear generating apparatus, which was $L = 25.4$ mm.

### 2.2 The dye

Rhodamine 6G (CAS: 989-38-8, A&C American Chemicals Ltd., Montreal, Canada) was chosen as the dye tracer for these experiments. The absorption and emission spectra of Rhodamine 6G as measured by Würth et al. (2012) for a concentration of approximately 0.4 mg/l (which is comparable to concentrations measured currently in the plume) are plotted in Fig. 2. These spectra indicate an absorption peak at 525 nm and an emission peak at 554 nm, in contrast to the values of 530 nm for the absorption peak and 560 nm for the emission peak as reported by Arcoumanis et al. (1990); however, the shapes of the spectra are known

to be sensitive to concentration and excitation wavelength, which could account for this discrepancy. The molecular diffusivity of the dye is $D = (4.0 \pm 0.3) \times 10^{-10}$ m$^2$ s$^{-1}$ (Gendron et al. 2008). Because the dye solution used was very dilute, its kinematic viscosity would be essentially equal to that of water in room temperature, namely $\nu = (1 \pm 0.05) \times 10^{-6}$ m$^2$ s$^{-1}$. Then, the Schmidt number of the dye can be estimated as $\mathrm{Sc} = \nu/D = 2{,}500 \pm 300$, which is a very large number.

Several tests were performed to determine the characteristics of the fluorescent dye under the specific conditions of the present experiments. Some tests aimed at determining a suitable dye concentration at the plume source, which had to be sufficiently high for the plume to be resolved accurately and sufficiently low for light absorption along the line of sight to be negligible. Dye solutions were prepared by mixing Rhodamine 6G powder with distilled water. Dye concentrations prepared in the laboratory were deemed to be reproducible within a precision of 0.5 %. Figure 3 is a photograph of dye solutions with different concentrations, illuminated by ceiling-mounted fluorescent tubes. At low concentrations, which were comparable to those used in the present experiments, the mixture appeared clear in laboratory lighting. Solutions with slightly higher concentrations produced some visible yellow–green fluorescence, as the room lighting emission spectrum overlaps with the dye's absorption spectrum. At higher concentrations, the fluorescence produced by the dye was quenched and the mixture had a red color, like the Rhodamine 6G powder.

The following four minor effects, which could potentially affect the accuracy of concentration measurements, were examined in advance of the main tests.

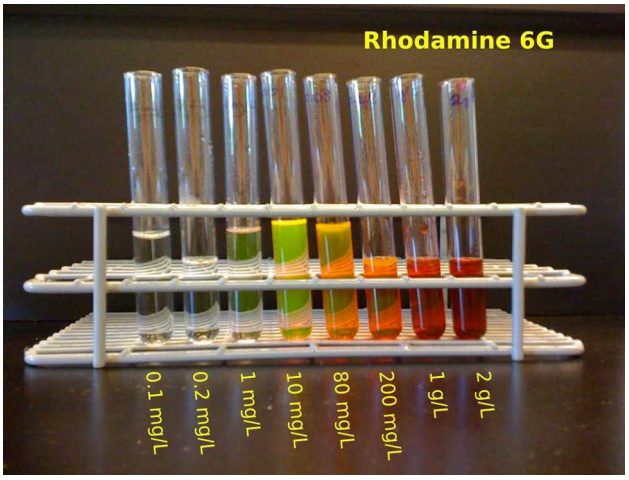


**Fig. 3** Photograph of various concentrations of Rhodamine 6G mixed with water illuminated with standard ceiling-mounted fluorescent tube lights

(a) *Effect of water chlorination* To measure the rate of Rhodamine 6G bleaching by chlorine added to the water in the water tunnel (Webster et al. 2001), we prepared a mixture of dye with a concentration of 0.1 mg/l using water from the water tunnel, which was equipped with an automated chlorination system that maintained the chlorine concentration at a nominal level of about 3 mg/l. The dye concentration of this mixture was measured until it decayed to half its initial value $C_0$. The measurements were fitted well by the exponential expression $C/C_0 = \mathrm{e}^{-t/t_b}$, where $t_b = 3{,}800$ s, corresponding to a half-life of 44 min. During the convection time of the dye in the test section, its concentration would have decayed by about 0.3 %, which is much lower than the general concentration measurement uncertainty. In fact, this chlorine bleaching effect is rather beneficial, as it reduces drastically the building-up of background concentration in the water tunnel.

(b) *Effect of pH* Rhodamine 6G is known to be insensitive to pH in the range from 2 to 12 (Anaspec).

(c) *Effect of water temperature* According to the literature (Zhu and Mullins 1992), the fluorescence of Rhodamine 6G is insensitive to temperature in the range below 120 °C, especially within the usual laboratory range.

(d) *Effect of photodecomposition* Unlike other fluorescent dyes, which are known to photobleach, Rhodamine 6G is insensitive to this effect (Arcoumanis et al. 1990; Crimaldi 2008).

### 2.3 Flow illumination and image recording

The region of interest in the flow was illuminated by a Nd:YAG pulsed laser (Solo PIV 120XT, New Wave Research Inc., Fremont, CA, USA). The standard deviation of the pulse-to-pulse power fluctuations of the laser was found to be about 3 %; this value was determined by monitoring fluorescent emissions in a tank filled with a solution of dye with a uniform concentration over a 10-min interval and following a warm-up period of about 2 min. Laser power fluctuations were deemed to have a much lesser effect on the time-averaged properties of the plume than other sources of error, to be discussed in Sect. 9.

Images of the flow were recorded using a digital sCMOS camera (pco.edge, PCO, Kelheim, Germany), which has an array of 2,160 (height) × 2,560 diodes (i.e., approximately $5.5 \times 10^6$ pixels) and a 16-bit pixel depth. The camera triggering was synchronized with the laser pulses. The laser was positioned underneath the water tunnel, and the laser sheet was reflected by a mirror upwards through the glass wall. Measurements of the concentration were taken in

cross sections of the plume in planes parallel to the streamwise direction and normal to it, as illustrated in Fig. 1. The streamwise configuration measured the dye concentration in the $(x_1, x_2)$ plane at the center of the tunnel, with the camera positioned normal to the measurement plane. Normal-plane measurements in the $(x_2, x_3)$ plane were obtained by positioning the camera at an angle of 45° to the laser sheet. A Scheimpflug adapter and a liquid prism were used to eliminate optical aberrations due to the oblique viewing angle (Prasad and Jensen 1995).

The laser emission spectrum peaked at a nominal wavelength of 532 nm, which is very close to the peak absorption wavelength of the dye. A long-pass optical filter with a cutoff wavelength of 540 nm (Part # 1108573, LaVision, Goettingen, Germany) was placed in front of the camera lens to separate the fluorescence emitted by the dye from the laser light and light scattered by the SPIV seeding particles. Furthermore, the room lights were turned off during the experiment in order to eliminate the chance that any stray light would interfere with the measurements. The transmission spectrum of the optical filter is also indicated in Fig. 2; the filter was designed to block more than 99 % of the laser light, while allowing approximately 75 % of the fluorescent light to pass through to the camera.

### 2.4 The calibration tank

The camera output, pixel by pixel, was calibrated with the use of a small tank, having internal dimensions 307 mm (width) × 154 mm (thickness) × 210 mm (height), filled with a dye solution of uniform concentration $C_{cal}$, and submerged in the water tunnel in the field of view of the camera. Depending on whether the calibration was intended for use during streamwise or normal-plane measurements, the thickness of the dyed fluid along the line of sight between the center of the tank and the camera lens would be 77 mm or 109 mm, respectively. In all cases, the distance over which the incident light travelled in the dyed fluid until it reached the center of the tank was 105 mm.

## 3 An idealized method for dye concentration measurement

The measurement of dye concentration using the PLIF method is potentially subject to several bias and precision errors. As a starting point for evaluating the uncertainty of this method, we shall first present an idealized analysis, clearly identifying all underlying assumptions that are necessary for this analysis to be accurate.

Consider an elementary volume of fluid containing fluorescent dye with a uniform concentration $C$ and illuminated by laser light with a uniform radiant power flux $I$ (measured in $\mathrm{W/m^2}$). Let the cross-sectional area of this volume be $\mathrm{d}A = \mathrm{d}y_1\mathrm{d}y_2$ and its thickness be $\mathrm{d}y_3$ (Fig. 4). The dye within the volume would emit "primary" fluorescent radiation that would be proportional to the product of the incident radiant power crossing the volume, the dye absorptivity $\varepsilon$ (measured in $\mathrm{m^{-1}(kg/m^3)^{-1}}$), and the dye quantum efficiency $\phi$, i.e., the ratio of emitted to absorbed energy (Guilbault 1990; Crimaldi 2008). In the absence of light absorption along the line of sight (see Sect. 5), the power flux of the radiation emitted by dye in this elementary volume and received by the camera lens, assumed to be far away from the illuminated region of the flow, would be

$$\mathrm{d}I_{\mathrm{fr}} = h\phi\varepsilon IC\mathrm{d}y_3\,, \tag{1}$$

where $h$ is a numerical coefficient that depends on the orientation of the camera. Now, consider that illumination extends over a layer of fluid that has a thickness $\Delta y_3$. The radiant power flux of primary fluorescence that would be received by the camera lens would be

$$I_{\mathrm{fr}} = h\phi\varepsilon\int_0^{\Delta y_3} C(y_3)I(y_3)\,\mathrm{d}y_3\,. \tag{2}$$

Assuming that the dye concentration was uniform over $\Delta y_3$, one may simplify the previous equation to

$$I_{\mathrm{fr}} = h\phi\varepsilon C\int_0^{\Delta y_3} I(y_3)\,\mathrm{d}y_3\,. \tag{3}$$

Let us further assume that the only radiation received by the camera would be the one described previously. Each diode (i.e., a single pixel) of the camera provides as output a number $E$ between 0 and $2^{16} - 1$ (i.e., 65,535). Let $E_0$ be the output of the same diode in the absence of dye in the

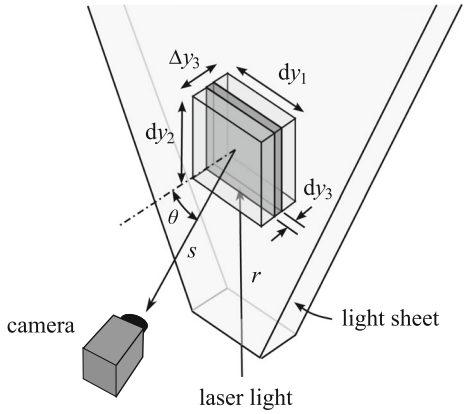


**Fig. 4** Illustration of an elementary volume of fluid containing fluorescent dye and illuminated by a laser sheet

camera field of view; $E_0$ was typically about 100 for all diodes. The voltage difference $E - E_0$ would be proportional to the radiant power flux $I_{\mathrm{fr}}$ received by that diode. This implies that the dye concentration at a point $(y_1, y_2)$ in the centerplane of the laser sheet would be related to the corresponding diode output as (Catrakis and Dimotakis 1996; Webster et al. 2003)

$$C(y_1, y_2) = \frac{[E(y_1, y_2) - E_0(y_1, y_2)]_i}{a_i(y_1, y_2)}, \quad (4)$$

where $a_i$ is a pixel-specific calibration factor and the subscript $i$ denotes idealized conditions. Under the assumption that the idealized conditions are also met during calibration, the values of $a_i$ would be determined by calibration of the camera output in a tank having uniform concentration.

The previous analysis was based on several assumptions, whose violation may potentially influence significantly the accuracy of concentration measurements in slender plumes. For the evaluation of these assumptions, three particular effects need to be addressed: a) the effect of concentration non-uniformity across the illuminated fluid volume, b) the possible attenuation of incident radiation and fluorescence emitted by dye contained in the illuminated fluid volume, and c) the effect of radiation other than primary fluorescence, which would be added to the latter to produce the camera output. The importance of these effects during calibration and during measurement will be discussed in detail in the following sections.

## 4 Effect of concentration non-uniformity across the light sheet

### 4.1 Description of the effect

Most analyses of PLIF measurements assume that the dye concentration changes sufficiently slowly for it to be constant across the light sheet produced by the laser. Although in a turbulent flow this condition can never be met exactly, in many cases, it is satisfied approximately. In the present experiments, however, the instantaneous dye plume width was particularly small and the laser sheet thickness was not minimized for PLIF needs, but rather optimized for concurrent SPIV measurements. An example of an instantaneous concentration map measured in the streamwise plane is presented in Fig. 5. The instantaneous width of the plume was typically between 1 and 5 mm, much smaller than the time-averaged plume width, but comparable to the laser sheet thickness, which was 2 mm (see the following subsection). Because calibration of the dye concentration measurement method was done using a tank filled with dye of uniform concentration, an error would occur when only part of the illuminated region during the experiment was occupied by the plume, or more generally when the concentration across the illuminated sheet was non-uniform.

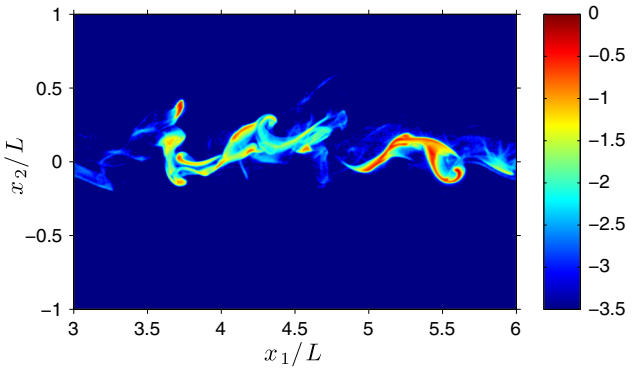


**Fig. 5** Representative instantaneous map of dye concentration (in a logarithmic scale) with the optical setup in the streamwise plane configuration (Fig. 1a)

### 4.2 The laser sheet

The variation in radiant power flux across the laser sheet was determined directly by illuminating a board painted with fluorescent paint and measuring the resulting fluorescence with the camera fitted with the optical filter. The fluorescent paint was a mixture of Rhodamine 6G powder, ethanol, and clear polyurethane paint, based on a recipe provided by LaVision (Goettingen, Germany). The radiant power flux variation was fitted well by the Gaussian function

$$I(x_3) = I_0 \exp\left[-\frac{{x_3}^2}{2{\sigma_{\mathrm{L}}}^2}\right], \quad (5)$$

where $I_0$ is the intensity on the center of the sheet and the characteristic half-width of the sheet was $\sigma_{\mathrm{L}} \approx 1$ mm.

### 4.3 Concentration error for a streamwise light sheet

Let us consider a configuration in which the laser light sheet is parallel to a streamwise plane, as in Fig. 1a. For a simplified analysis, let us first assume that the plume has a Gaussian instantaneous concentration profile in the direction $x_3$ across the laser sheet, i.e.,

$$C(x_3) = C_p \exp\left[-\frac{(x_3 - g)^2}{2{\sigma_{\mathrm{P}}}^2}\right], \quad (6)$$

where $C_p$ is the peak concentration, $g$ is the position of the peak relative to the laser sheet center and $\sigma_{\mathrm{P}}$ is the instantaneous plume half-width (see Fig. 6). The radiant power flux emitted along a line of sight when the plume overlaps with the laser sheet can be calculated by (2). The voltage output of the camera would be

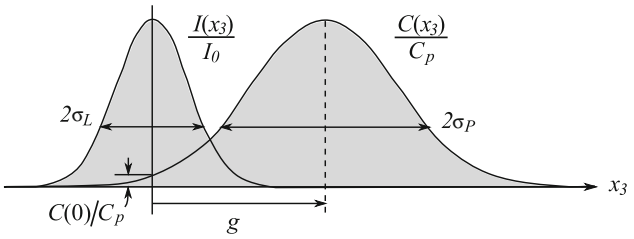


**Fig. 6** Sketch of a plume of dye with a Gaussian concentration profile and a laser sheet with a Gaussian radiant power flux variation

$$E = k\int_{-\infty}^{\infty} I(x_3)C(x_3)\mathrm{d}x_3 + E_0, \tag{7}$$

where $k$ is a constant of proportionality. However, because calibration of the camera output was performed in a tank with uniform dye, this measurement would be interpreted as if the concentration was uniform across the laser sheet with an apparent value $C_a$, namely as

$$E = kC_a\int_{-\infty}^{\infty} I(x_3)\mathrm{d}x_3 + E_0. \tag{8}$$

Equating the right-hand sides of (7) and (8), one may determine the apparent value of the concentration as

$$C_a = \frac{\int_{-\infty}^{\infty} I(x_3)C(x_3)\mathrm{d}x_3}{\int_{-\infty}^{\infty} I(x_3)\mathrm{d}x_3}, \tag{9}$$

which, in the case of Gaussian light intensity and concentration profiles, can be simplified to

$$C_a = \frac{C_p}{\sqrt{1+(\sigma_\mathrm{L}/\sigma_\mathrm{P})^2}}\exp\left[-\frac{(g/\sigma_\mathrm{P})^2}{2(1+(\sigma_\mathrm{L}/\sigma_\mathrm{P})^2)}\right]. \tag{10}$$

The apparent concentration, normalized by the actual peak value, has been plotted in Fig. 7a as a function of plume position $g/\sigma_\mathrm{P}$ for a few representative values of the ratio $\sigma_\mathrm{L}/\sigma_\mathrm{P}$. As $\sigma_\mathrm{L}/\sigma_\mathrm{P} \to 0$, $C_a \to C(0)$. It is important to note that the error $C(0) - C_a$ is positive when $g/\sigma_\mathrm{P}$ is relatively small, but becomes negative for larger values of this ratio.

A similar analysis can be made for a plume that has a rectangular concentration profile with a value $C_p$ and a width $2\sigma_\mathrm{P}$. In this case, the apparent concentration would be

$$C_\mathrm{a} = \frac{C_p}{2}\left[\mathrm{erf}\left(\frac{(\mathrm{g}/\sigma_\mathrm{P})+1}{\sqrt{2}(\sigma_\mathrm{L}/\sigma_\mathrm{P})}\right) - \mathrm{erf}\left(\frac{(\mathrm{g}/\sigma_\mathrm{P})-1}{\sqrt{2}(\sigma_\mathrm{L}/\sigma_\mathrm{P})}\right)\right]. \tag{11}$$

This relationship has been plotted in Fig. 7b as a function of $g/\sigma_\mathrm{P}$ for a few representative ratios of $\sigma_\mathrm{L}/\sigma_\mathrm{P}$. Again, as $\sigma_\mathrm{L}/\sigma_\mathrm{P} \to 0$, the apparent concentration becomes equal to the actual local concentration, and the concentration error is positive when $g/\sigma_\mathrm{P}$ is relatively small and negative for larger values of this ratio.

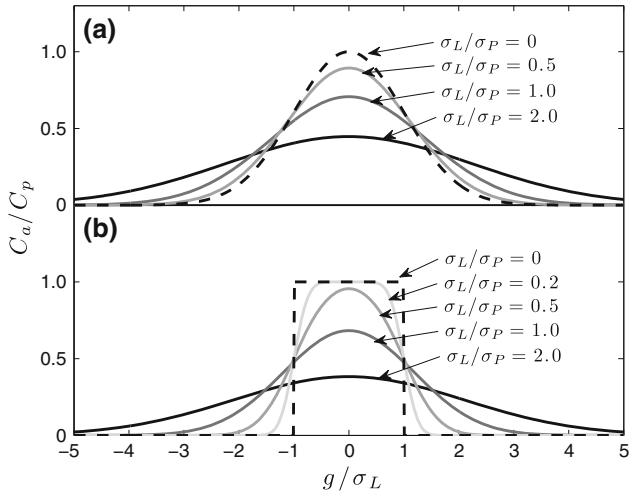


**Fig. 7** Apparent concentrations of plumes with **a** Gaussian and **b** rectangular concentration profiles, having peak concentrations $C_p$ and widths $2\sigma_\mathrm{P}$ as functions of relative positions with respect to the laser sheet centerplane for different values of $\sigma_\mathrm{L}/\sigma_\mathrm{P}$

If the shape of the instantaneous plume concentration profile was known, as for the two cases considered previously, it would have been possible to devise corrections for this effect. However, because the actual plume profiles are very complex and unpredictable, this effect is nearly impossible to quantify or correct for. Finer dye filaments would be subject to a larger error than thicker dye filaments, and this error would manifest itself inhomogeneously and intermittently. The fact, however, that the local instantaneous error would sometimes be positive and sometimes negative would result in a partial cancellation of the overall error of the average local concentration. If the distance $g$ between the plume and laser sheet centerplanes was evenly distributed, the overestimated concentration at times when $g$ was relatively large would balance, partially or even totally (for the two cases of considered plume concentration profiles), the underestimated concentration when $g$ was relatively small and the ensemble-averaged concentration would end up having a lower or no error. In practice, however, the location of the plume centerplane would follow a quasi-Gaussian rather than uniform distribution, which would introduce a bias that would underestimate the average local concentration.

The matter is further complicated by other effects, which may introduce a bias in the concentration measurement. An additional error in plume concentration would be due to the depth of field of the camera, which would cause any fluorescence produced in front of or behind the centerline of the laser sheet to be blurred over neighboring pixels. Whereas this effect would not introduce any error during calibration measurement in the tank of uniform concentration, it would likely cause an artifact that is equivalent to dye diffusion across the depth of field. All things considered, in the present

experiment, we would expect that, very near the source of the plume, where the plume was thin and did not meander significantly, the mean concentration would be underestimated, whereas further downstream, where the plume was much wider, errors would be less significant. This hypothesis will be verified in Sect. 9.

Although it may not be possible to devise accurate and general correction methods for the finite laser sheet thickness effect, it is possible to suggest a threshold for this thickness, relative to the plume width, below which the associated error may be neglected. Unlike the local concentration value, which may be either underestimated or overestimated, the apparent peak concentration $C_{\mathrm{ap}}$ would always be lower than the actual peak concentration $C_p$. The ratios of these two values for Gaussian and rectangular plumes are, respectively,

$$\frac{C_{\mathrm{ap}}}{C_p} = \frac{1}{\sqrt{1 + (\sigma_{\mathrm{L}}/\sigma_{\mathrm{P}})^2}} \tag{12}$$

and

$$\frac{C_{\mathrm{ap}}}{C_p} = \mathrm{erf}\left(\frac{\sigma_{\mathrm{P}}}{\sqrt{2}\sigma_{\mathrm{L}}}\right). \tag{13}$$

These ratios have been plotted in Fig. 8 for a range of values of $\sigma_{\mathrm{L}}/\sigma_{\mathrm{P}}$. This figure shows that the error would be entirely negligible for $\sigma_{\mathrm{L}}/\sigma_{\mathrm{P}} \leq 0.3$ and would increase to values comparable to 30 % for $\sigma_{\mathrm{L}}/\sigma_{\mathrm{P}} \approx 1$. Taking into consideration that, for the present dye, which has a very low molecular diffusivity, the instantaneous plume concentration profile would more often be rectangular-like than Gaussian-like, we may assess that, when $\sigma_L/\sigma_{\mathrm{P}} \leq 0.6$, the concentration error due to finite laser sheet thickness would not warrant specific correction and could be incorporated in the overall concentration measurement uncertainty.

### 4.4 Concentration error for a normal light sheet

In a normal-plane optical configuration, as in Fig. 1b, the thickness of the laser sheet would typically be much smaller than the streamwise extent of connected dye filaments. If the light sheet was viewed perpendicularly by the camera, one would then expect that the error due to dye non-uniformity across the laser sheet would be negligible. In the present setup, however, the camera viewing angle was oblique. With such a view, both the streamwise and the transverse intermittencies of the plume would introduce errors in the concentration measurement. Consequently, the error in this configuration could be, very roughly, comparable to the error in the streamwise viewing configuration. Measurements presented in Sect. 9 are compatible with this postulation.

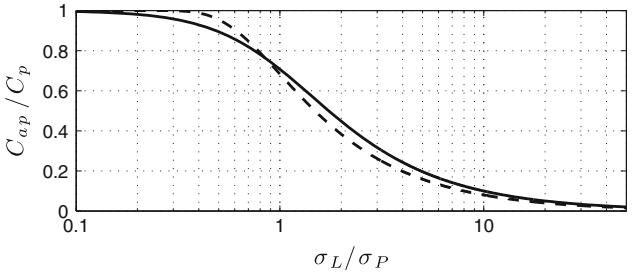


**Fig. 8** Dependence of the ratio of apparent and actual peak concentrations of plumes with Gaussian (*solid line*) and rectangular (*dashed line*) concentration profiles on $\sigma_{\mathrm{L}}/\sigma_{\mathrm{P}}$

## 5 Effect of radiation attenuation

The power flux of incident laser radiation transmitted through a fluid volume that contains an absorbing substance (dye) with a spatially varying concentration $C(r)$ along a path with a length $\Delta r$ would be attenuated according to the Beer–Lambert Law (Crimaldi 2008)

$$I_{\mathrm{ab}}(r) = I \exp\left(-\varepsilon \int_0^{\Delta r} C(r)\,\mathrm{d}r\right), \tag{14}$$

where $I$ is the power flux of the incident light in the absence of attenuation. For a uniform concentration along the light path, this would become

$$I_{\mathrm{ab}}(r) = I \exp(-\varepsilon C \Delta r). \tag{15}$$

Consequently, if one attempted to measure the local concentration $C$ while disregarding attenuation effects, one would get a lower value $C_m$ as

$$C_m = C \exp(-\varepsilon C \Delta r). \tag{16}$$

The accuracy of this relationship was tested by taking concentration measurements in the calibration tank filled with solutions having uniform concentrations in the range from 0.025 to 0.3 mg/l (Walker 1987; Ferrier et al. 1993; Karasso and Mungal 1997). The apparent concentration $C_m$ was calculated as the average of values from 150 images taken in the center of the tank, where the length of the light path inside the tank was $\Delta r = 105$ mm. The ratio $C_m/C$ is plotted versus the actual concentration in Fig. 9. The data could be fitted well (with differences having a standard deviation of 3 % of the measured concentration) by (16) with $\varepsilon = 4 \pm 1\ \mathrm{m}^{-1}(\mathrm{mg/l})^{-1}$.

Based on the previous test, we chose the concentration of dye in the tank to be $C_{\mathrm{cal}} = 0.075$ mg/l during calibration of the camera; this value was deemed to be sufficiently large to produce a strong camera output but not large enough to result in significant radiation attenuation. The mean attenuation at the center of the image with the

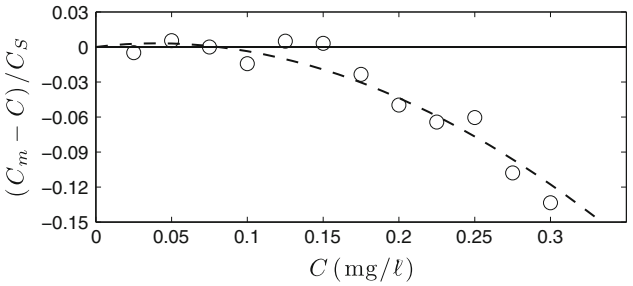


**Fig. 9** Differences between the measured and actual concentrations in the calibration tank; the *dashed line* represents the best of (16) to the data; $C_S = 0.3$ mg/l

tank filled with a dye solution having that concentration was approximately $(3 \pm 1)$ %, according to (16). The camera output during calibration was corrected for this attenuation of the incident laser light.

Equation (16) was also used to estimate the significance of light attenuation during the measurements in the plume. For the present work, the source concentration was chosen to be $C_S = 0.3$ mg/l. The maximum light attenuation, which would occur near the exit of the injection tube, was estimated to be 0.2 %, which is entirely negligible. Attenuation of the fluorescence emitted by the dye between the measurement plane and the camera lens is expected to have even less of an effect, considering that the absorptivity of the fluorescent signal is generally much lower than that at the wavelength of the laser (Lemoine et al. 1996).

## 6 Effect of secondary fluorescence

### 6.1 Evidence for and possible sources of out-of-sheet fluorescence

For the idealized analysis in Sect. 3, it was assumed that the camera would receive only fluorescence radiation emitted by dye within the laser sheet. Nevertheless, dye outside the laser sheet was also recorded by the camera, as evident in the instantaneous image of the plume cross section in the normal-plane configuration (Fig. 1b), shown in Fig. 10. Because of the oblique viewing angle, out-of-sheet dye patterns are discernible to the left and right of the dye that would be illuminated by the laser sheet. Although out-of-sheet emissions were out of focus and at least an order of magnitude lower in magnitude than the peak emission of the in-sheet dye, they could be resolved fairly vividly by the camera, which had a very wide dynamic range, and were clearly visible when plotted with a logarithmic color scale. If they remained unaccounted for, emissions from out-of-sheet dye would distort largely the shapes of the instantaneous and mean concentration maps

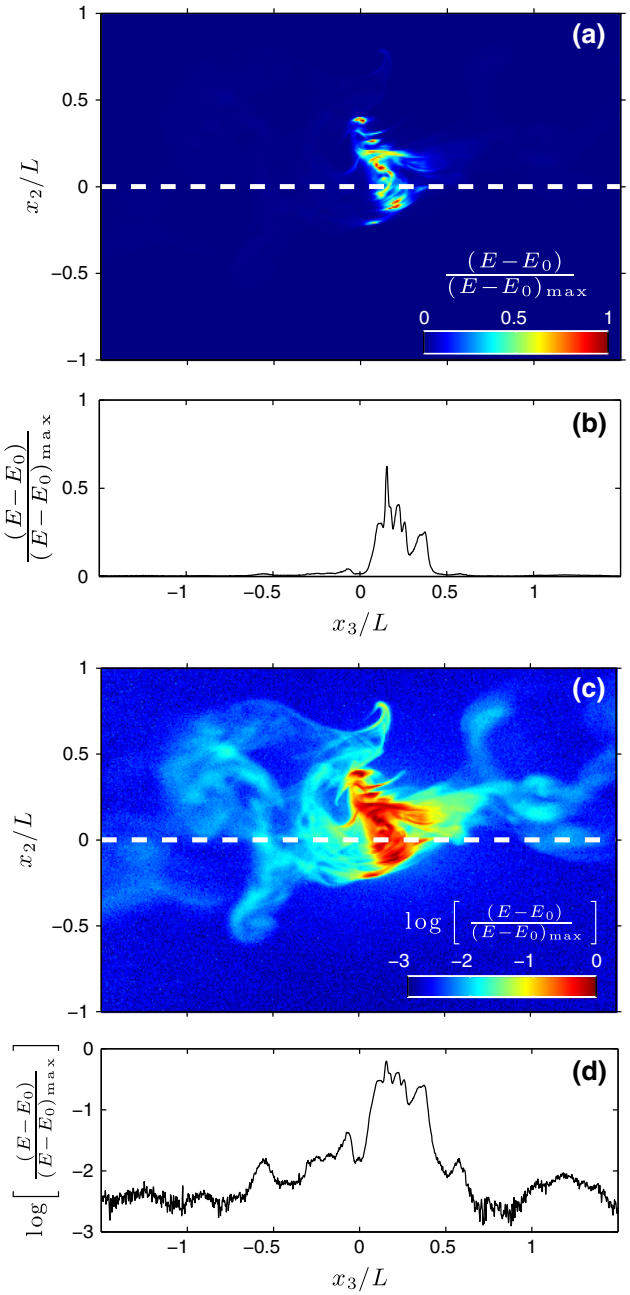


**Fig. 10** Representative instantaneous maps of the net output $E - E_0$ of the camera viewing the plume in the normal-plane configuration in **a** linear and **c** logarithmic scales. The values have been normalized by the maximum value $(E - E_0)_{\max}$ in the image. The *dashed lines* indicate the location of the profiles plotted in **b** and **d**

of the plume and would bias the measurement of the total in-sheet dye mass.

The following possible causes for the visibility of out-of-sheet dye were considered.

(a) *Ambient light* This was negligible, because the room lights were turned off during the experiments.

(b) *Laser light scattered by seed particles used for SPIV* Because of the very low number of particles in the

illuminated plane, the scattered light was also considered to be negligible.

(c) *Laser light reflected from the free surface or the glass walls* This was not deemed to be significant, as it would remain largely within the measurement plane.

(d) *Primary fluorescent emissions by dye illuminated by the laser sheet* A small part of these emissions would be reabsorbed by the out-of-sheet dye, causing it also to fluoresce, albeit weakly. This secondary absorption and emission is made possible by the partial overlap of the absorption and emission spectra of the dye, a property which is true for most of the common fluorescence dyes used for PLIF. We believe that this secondary emission is the main source of out-of-sheet emissions which contribute to the total fluorescent intensity that reaches the camera lens. Of course, secondary fluorescence would not be restricted to out-of-sheet dye, but it would also be produced by in-sheet dye.

### 6.2 Secondary fluorescence in the calibration tank

The relative effect of secondary fluorescence upon the camera output was quantified directly by the following simple test. This test was performed in the calibration tank filled with a solution of Rhodamine 6G dye having a uniform concentration $C_{\text{cal}} = 0.075$ mg/l. As shown in Fig. 11, an opaque plate was mounted inside the tank parallel to the laser sheet so that it would block the view of part of the contained dye solution. By moving this plate in a direction normal to itself, it was possible to vary the thickness of the fluid layer that would be exposed to the camera, and hence the amount of out-of-sheet fluorescence. The length of incident laser light path in the tank remained the same for all positions of the plate and so did light attenuation.

For this test, we used a portable diode laser (S3 Krypton, Wicked Lasers) with the same emission wavelength (532 nm), laser sheet thickness ($\sigma_{\text{L}} \approx 1$ mm), and laser sheet profile characteristics (see Sect. 4.2) as the Nd:YAG laser used in the plume measurements.

The outputs of an array of 400 × 100 neighboring pixels viewing the opaque plate were averaged to give the corresponding net output $E - E_0$. Although the diode laser had larger pulse-to-pulse power fluctuations than the Nd:YAG laser used for the plume measurements, in this test, the measured values were corrected for possible temporal fluctuations in the laser intensity by comparison to a simultaneous reference measurement of the net output of a diode that viewed a layer of the fluid that was not blocked by the plate but had a uniform thickness equal to the total thickness of the fluid volume within the tank (see Fig. 11).

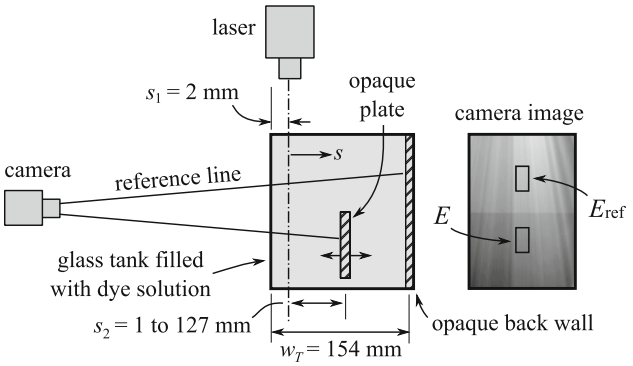


**Fig. 11** Sketch of the experiment used to measure the effect of out-of-sheet fluorescence in a tank of uniform concentration fluorescent dye

The total power flux received by the camera would be the sum of contributions of the primary fluorescence and the secondary fluorescence along the line of sight; the latter depends on the thicknesses of the two out-of-sheet dye layers in front of and behind the laser sheet, which may be made dimensionless by the laser sheet half-width $\sigma_{\text{L}}$. Therefore, one would anticipate that the net camera output would be a monotonically increasing function of the thickness of the exposed dye layer. Furthermore, one would also anticipate that the rate of increase in the net camera output would diminish with increasing thickness of the dyed fluid layer, as dye farther away from the laser sheet would emit less secondary fluorescence.

For the configuration of Fig. 11, the thickness of the dye layer in front of the laser sheet was fixed at $s_1 = 2$ mm; this was the thinnest possible layer that would not clip the primary fluorescence emitted by dye within the laser sheet. Therefore, $E - E_0$ varied only with $s_2$, which took values between 1 and 127 mm. Let $(E - E_0)_{\text{p}}$ be the hypothetical net output of the camera if there were only primary fluorescence. On condition of validation against the experimental results, one may assume that the power flux of secondary fluorescence varies as a power law of the exposed dye layer thickness. Then, for the configuration of Fig. 11, one could write the relationship

$$E - E_0 = (E - E_0)_p \left[ 1 + \underbrace{b\left(\frac{s_1}{\sigma_{\text{L}}}\right)^n}_{\substack{\text{secondary fluorescence} \\ \text{in front of sheet}}} + \underbrace{b\left(\frac{s_2}{\sigma_{\text{L}}}\right)^n}_{\substack{\text{secondary fluorescence} \\ \text{behind sheet}}} \right], \tag{17}$$

where $b$ and $n$ are empirical constants to be evaluated by curve fitting to measurements.

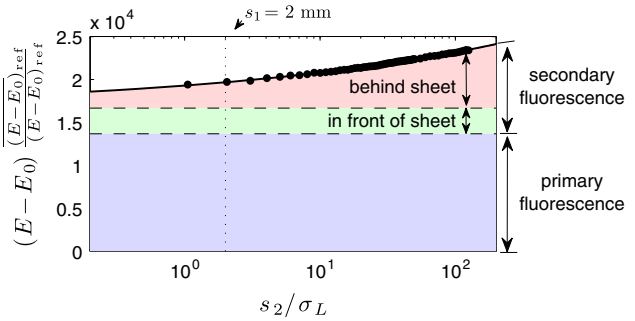


**Fig. 12** The variation in the measured power flux $(E - E_0)$ of fluorescence measured in the test described in Fig. 11 as a function of the divider position $s_2$. The *solid line* represents the fit of (17) while *shaded areas* indicate the contributions of primary fluorescence and secondary fluorescence

Measurements of $E - E_0$ as a function of $s_2/\sigma_L$ are presented in Fig. 12. These measurements were represented very well by the relationship

$$E - E_0 = c + b'\left(\frac{s_2}{\sigma_L}\right)^n, \tag{18}$$

where $c = 16{,}684$, $b' = 2{,}617$ and $n = 0.20$. Then, the two remaining constants in (17) were determined as

$$b = [c/b' - (s_1/\sigma_L)^n]^{-1} = 0.19 \tag{19}$$

and

$$(E - E_0)_p = b'/b = 13{,}678. \tag{20}$$

### 6.3 Camera calibration method

Calibration was performed in situ for each pixel of the camera and took into consideration the effects of spatial variation in the laser sheet and optics, lens vignette, and any pixel-to-pixel offsets or gain variations in the camera. Separate calibrations were performed for the streamwise plane configuration and the normal-plane configuration, as shown in Fig. 13. In both cases, the tank was filled with a solution of Rhodamine 6G dye having a uniform concentration $C_{cal} = 0.075$ mg/l and the laser sheet was centered on the centerplane of the tank. The camera output during calibration, accounting for attenuation as explained in Sect. 5, was a linear function of the concentration, having the same form as given by (4). The calibration factor of the camera could then be calculated from the camera output as

$$a_{cal}(y_1, y_2) = \frac{[E(y_1, y_2) - E_0(y_1, y_2)]_{cal}}{C_{cal}(y_1, y_2)}. \tag{21}$$

This calibration factor would be specific to a particular calibration tank configuration and would introduce an error if used for the measurement of concentration in the plume. To render this calibration procedure suitable for general use, we will reference the camera response to idealized

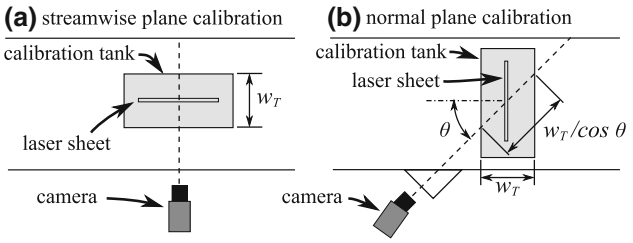


**Fig. 13** Experimental configurations during calibration

conditions, as described in Sect. 3. Under such hypothetical conditions, the net camera output for a given pixel $(y_1, y_2)$ would be $[E - E_0]_i$ and its calibration factor would be $a_i$. These parameters would be related to the corresponding actual values as

$$C_{cal} = \frac{[E - E_0]_i}{a_i} = \frac{[E - E_0]_{cal}}{a_{cal}}, \tag{22}$$

The idealized camera net output and the idealized camera calibration factors can be determined from the actual ones following corrections for the absorption of the incident laser light by dye in the tank and for secondary fluorescence. Using the corresponding corrections that were derived previously, one gets for the streamwise plane calibration

$$\frac{a_i}{a_{cal}} = \frac{[E - E_0]_i}{[E - E_0]_{cal}} = \left\{\exp(-\varepsilon C_{cal}\Delta r)\left[1 + 2b\left(\frac{w_T}{2\sigma_L}\right)^n\right]\right\}^{-1}, \tag{23}$$

and for the normal-plane calibration

$$\frac{a_i}{a_{cal}} = \frac{[E - E_0]_i}{[E - E_0]_{cal}} = \left\{\exp(-\varepsilon C_{cal}\Delta r)\left[1 + 2b\left(\frac{w_T}{2\cos\theta\sigma_L}\right)^n\right]\right\}^{-1}. \tag{24}$$

For the presently used calibration tank, the ratios of the idealized and actual camera calibration factors were 0.54 and 0.52, respectively.

## 7 Determination of the in-sheet plume boundaries

As shown in Fig. 10, camera output maps displayed out-of-sheet dye patterns that were undoubtedly produced by the emissions of dye that were upstream and downstream of the in-sheet dye. These patterns would distort grossly the detected boundaries of the plume and would bias positively the local mass flux estimate. For this reason, we devised the following method to identify and remove out-of-sheet fluorescence.

Because the fluorescence from the out-of-sheet dye is non-uniform, an edge-detection-type algorithm would be unable to discriminate between in-sheet and out-of-sheet fluorescence. Instead, we used a thresholding technique, according to which the concentrations measured by all pixels in each instantaneous image that were lower than a specified threshold would be replaced by zero values. An example of a threshold chosen specifically to remove out-of-sheet dye emissions from the same representative instantaneous concentration map in the normal-plane configuration as the one presented previously in Fig. 10 is shown in Fig. 14; the concentration contour at the value of this threshold, which has been superimposed on the concentration maps, illustrates that this approach resulted in a connected and plausible cross section of the plume. Besides being subjective, user selection of an appropriate threshold for each image would be impractical, in view of the large number of images that were analyzed. Instead, it would be more objective to determine an optimal threshold value for each ensemble of images with the use of an iterative algorithm. Another concern is that this approach would unavoidably exclude some low-concentration, in-sheet dye that, as a result of molecular diffusion, would be near the edge of the plume. To avoid significant overcompensation for this effect, one must choose a threshold that would, as much as possible, conserve the total in-sheet dye mass.

An algorithm to determine the optimal threshold for each set of images was developed, based on the histogram of the radiant intensity in the instantaneous images. This approach is similar to the one used by Prasad and Sreenivasan (1989) to determine the scalar interface of a turbulent jet. A representative histogram of an image in the present experiments is presented in logarithmic scales in Fig. 15a. This histogram had a peak at a concentration value of $0.25 \times 10^{-3} C_S$, which was the background noise level, and then extended toward higher concentration values up to a value slightly exceeding $0.1 C_S$.

This particular plot does not provide a clear indication of the appropriate threshold value. In contrast, the frequency of occurrence of each concentration value, weighted by $C/C_S$ and plotted versus $\log(C/C_S)$, allows one to determine the mass of dye within a concentration bandwidth by measuring the corresponding area under the curve. Such a plot (see Fig. 15b) clearly indicated the presence of three distinct peaks, which marked the background noise and the peak concentrations of the out-of-sheet dye and the in-sheet dye, respectively. The three peaks were separated by two local minima, which could serve for separating the three components of collected radiation intensity. To quantify objectively the equivalent dye masses that corresponded to each of these three components, we fitted the weighted histogram by the sum of

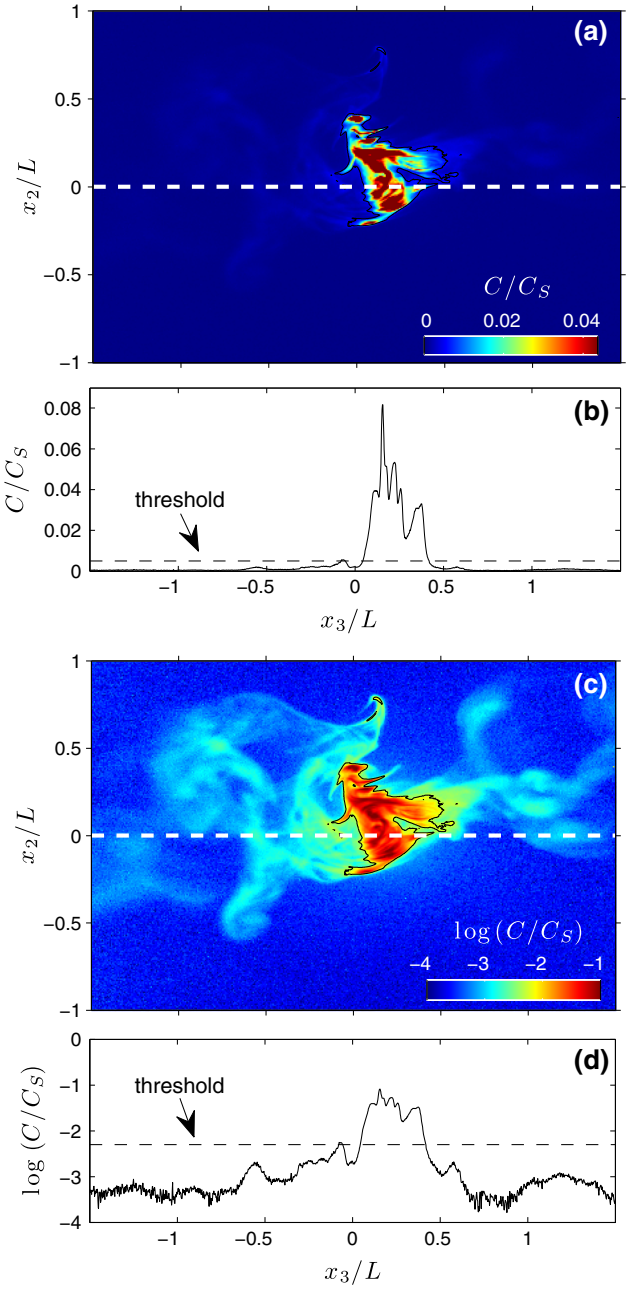


**Fig. 14** Example of an instantaneous measurement of the plume showing maps of **a** $C/C_S$ and **c** $\log(C/C_S)$. The *dashed line* indicates the location of the cross sections plotted in **b** and **d**. A *black line* indicates the contour at a threshold of $\log(C/C_S) = -2.3$; this level is also indicated by a *dotted line* in the cross-sectional plots

three skew-normal functions (Azzalini 1985) using a best-fit algorithm in MATLAB. It is interesting to note that the contribution of background noise was entirely separated from the contribution of the in-plane dye emission, which confirms the camera manufacturer's specification of negligible noise. However, the concentration bandwidths for in-sheet emissions and out-of-sheet emissions overlapped,

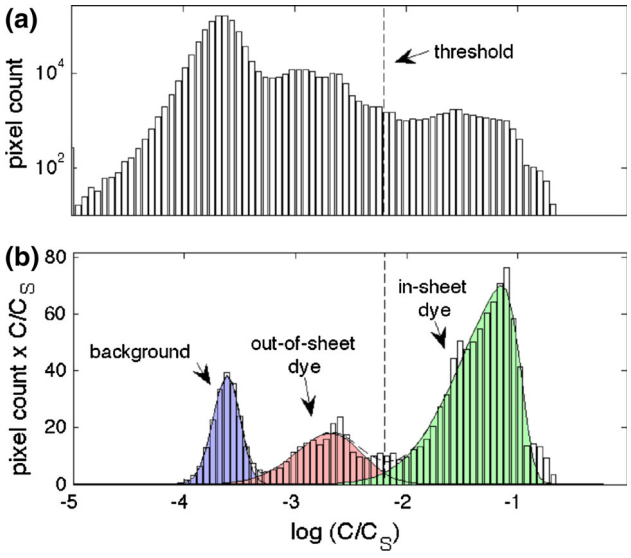


**Fig. 15** **a** Histogram of the values in the instantaneous concentration map is shown in Fig. 14c with bins uniformly spaced in the logarithmic scale and **b** the same histogram weighted by the values corresponding to the center of each bin. The weighted histogram shows three distinct regions corresponding to the in-sheet dye, the out-of-sheet dye, and the background noise; skewed Gaussian functions have been fit illustrate the three regions. A carefully chosen threshold can be used to remove the majority of the out-of-sheet dye and background, while maintaining the majority of the signal from the in-sheet dye

as expected. To separate the two contributions, we chose the threshold at a concentration value that was such that the area under the in-sheet curve below the threshold was equal to the area under the out-of-sheet curve that was above the threshold. This ensured that the mass of in-sheet dye would be conserved by the thresholding process. The computation of the optimal threshold for each instantaneous image was automated using a computer algorithm.

For the set of measurements presented in Figs. 14 and 15, the optimal thresholds determined for each instantaneous image had an average of $\log(C/C_S) = -2.3$ and a standard deviation of 0.4. Visual inspection of the resulting instantaneous in-sheet concentration maps confirmed that the plume appearance was realistic. Because the variability of the threshold for different images was relatively small, and also because some images did not contain any in-sheet dye at all, we reprocessed all images in each measurement set using the mean threshold value. This ensured that the average total mass of dye in the plume was not affected by the thresholding process, although the instantaneous mass could be somewhat distorted by the choice of suboptimal threshold; the standard deviation of this distortion was estimated to be approximately 10 % of the mean total mass of the in-sheet dye.

It is worth noting that, as the plume spread downstream, the weighted histogram peak that corresponded to the

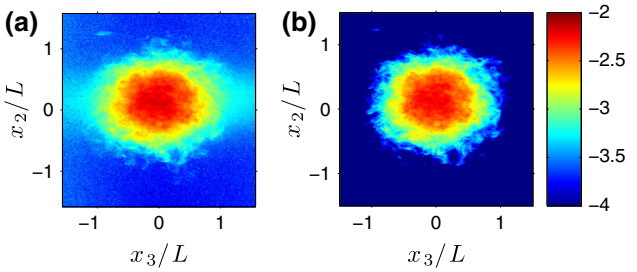


**Fig. 16** Mean concentration map ($\log(\overline{C}/C_S)$) from the same set of measurements as Fig. 14 determined **a** without and **b** with applying the thresholding correction

background noise remained at essentially the same location, whereas both other peaks were shifted toward lower values. This increased the overlaps of the areas under the three skew-normal functions, which could potentially obscure the process of threshold identification. Nevertheless, this was not a problem for any of the measurements we investigated, because all weighted histograms were represented well by the sum of three distinct skew-normal functions and the algorithm for determining the threshold remained robust throughout all our experiments.

Representative maps of the mean concentration $\overline{C}$, determined without and with the thresholding algorithm, are plotted in Fig. 16. The uncorrected map is much wider in the $x_3$ than in the $x_2$ direction, as a consequence of the fact that the vast majority of out-of-sheet fluorescence produced by the plume was viewed by the camera along the $x_3$ axis. The thresholding algorithm was effective in correcting this error and removed the halos from the flanks of the in-plane plume. It also removed the background noise. Removal of out-of-sheet fluorescence lowered the local mean concentration values by 5–8 % of the peak $\overline{C}$, thus removing the corresponding positive bias.

Out-of-sheet fluorescence had an even lower effect on the measurements of concentration fluctuations in the plume. The difference between the normalized standard deviations of the concentration $c'/C_S$, determined without and with the thresholding correction, was less than 1 % on average. The fact that the concentration fluctuation correction level is very small is a consequence of the fact that thresholding leaves unaffected large values of $C$, which are the main contributors to $c'$.

Secondary fluorescence from out-of-sheet dye also contributed to the camera output in the streamwise plane configuration. This happened even when the plume was located completely outside of the laser sheet, due to meandering. In this configuration, the value of the optimal threshold cannot be determined by analyzing the histograms of the instantaneous concentration measurements because the camera views of out-of-sheet dye and in-sheet dye were superimposed. To remove the contribution of out-

of-sheet dye that would have biased positively the mean concentration measurements, we used the same thresholding algorithm with the same values of threshold as those determined from the normal-plane measurements.

## 8 Correction method for concentration measurements in the plume

Concentration measurements in the plume would be subjected to the same sources of error as measurements in the calibration tank, as well as additional ones, which would be specific to each particular experimental configuration. The only way to apply the camera calibration procedure described in Sect. 6.3 to measurements in the plume is by referencing all results to idealized conditions (Sect. 3). The two main correctable errors that were identified during calibration were absorption of the incident laser light and secondary fluorescence. Because the present plume was very slender, absorption of the incident laser light across it would be negligible (see Sect. 5). The effect of secondary fluorescence, however, was found to be significant and required correction.

The contribution of secondary fluorescence would depend on the instantaneous thickness of the plume, on the configuration of the plume measurement, and on the location of the laser sheet with respect to the instantaneous plume axis. Close to the source, the plume thickness $w_P$ would be approximately equal to the injection tube inner diameter, which was roughly 2 mm. Away from the source, $w_P$ would be smaller than the one obtained by time averaging of the plume position, which would be subjected to the effect of meandering. A better estimate of $w_P$ would be the relative plume width (Vanderwel and Tavoularis 2014b), which was approximately 34 mm at the furthest downstream location of measurements ($x_1/L = 35$). Therefore, all along the present plume, its thickness was lower than the calibration tank width, which means that the effects of secondary fluorescence would be lesser during measurement than during calibration.

The two measurement configurations that were used in the present work are illustrated in Fig. 17a, b, for specific instances when the center of the laser sheet would be on the plume axis. In the streamwise plane configuration, the ratio of the camera net output $E - E_0$ and its hypothetical value $[E - E_0]_i$ under idealized conditions, which is equal to the ratio $a/a_i$ of the corresponding calibration factors, would be

$$\frac{a}{a_i} = \frac{[E - E_0]}{[E - E_0]_i} = \left[1 + 2b\left(\frac{w_P}{2\sigma_L}\right)^n\right]. \tag{25}$$

In the normal-plane configuration, $w_P$ would have to be replaced by $w_P/\sin\theta$. If, however, instead of being on the plume axis, the center of the laser sheet was located on the edge of the plume, the calibration factor ratio would be

$$\frac{a}{a_i} = \frac{[E - E_0]}{[E - E_0]_i} = \left[1 + b\left(\frac{w_P}{\sigma_L}\right)^n\right] \tag{26}$$

for the streamwise plane configuration and with $w_P$ replaced by $w_P/\sin\theta$ for the normal-plane configuration.

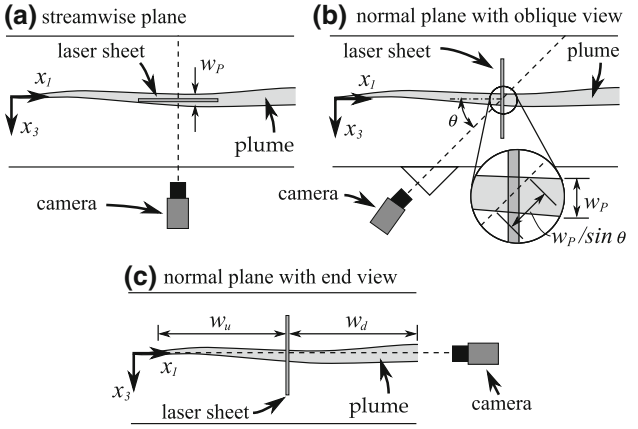


**Fig. 17** Experimental configurations during measurements in the plume

The previous discussion demonstrated that the calibration factor ratio during concentration measurements in the plume would vary from one instant to the next, as the plume position fluctuated while the laser sheet remained fixed. A maximum local value of this ratio would occur when the center of the laser sheet occupied the centerplane of the plume, while a minimum value would occur when the center of the laser sheet was at the edge of the plume; contributions from images in which the plume was completely outside the laser sheet were successfully removed by the thresholding algorithm described in Sect. 7 and so are no longer a concern. Table 1 shows the minimum and maximum values of the ratio $a/a_i$ at different locations along the plume for both configurations. A comparison of each pair of values shows that they were not very different and so it seems appropriate to chose the average of values determined from (25) and (26) for this ratio at each streamwise location. This approximation introduced an uncertainty of less than 10 % on this correction factor.

Following this analysis, it becomes evident that the dye concentration in the plume can be calculated fairly accurately from the corrected output of the camera as

$$C = \frac{E - E_0}{a} = \frac{E - E_0}{a_{\text{cal}}}\frac{a_{\text{cal}}}{a}. \tag{27}$$

where the calibration factor ratio in the tank was found in Sect. 6.3 to be $a_i/a_{cal} = 0.54$ and 0.52 for the streamwise and normal-plane configurations, respectively. Ratios of $a_{\text{cal}}/a$ are also presented in Table 1. Had the calibration

**Table 1** Calibration factor ratios for three configurations in the plume experiments

| Configuration | $x_1/L$ | $w_p/\sigma_L$ | $a/a_i$* | $a_{cal}/a$ |
|---|---|---|---|---|
| (a) | 4 | 4 | 1.34 (1.25, 1.44) | 1.37 |
| | 8 | 7 | 1.38 (1.28, 1.49) | 1.33 |
| | 11 | 10 | 1.41 (1.30, 1.52) | 1.31 |
| | 14 | 13 | 1.43 (1.32, 1.55) | 1.29 |
| | 17 | 16 | 1.45 (1.33, 1.58) | 1.27 |
| | 20 | 19 | 1.47 (1.34, 1.60) | 1.26 |
| (b) | 5 | 5 | 1.39 (1.28, 1.49) | 1.38 |
| | 12 | 11 | 1.45 (1.33, 1.57) | 1.32 |
| | 20 | 18 | 1.50 (1.36, 1.63) | 1.28 |
| | 28 | 27 | 1.54 (1.39, 1.69) | 1.24 |
| | 35 | 34 | 1.56 (1.41, 1.72) | 1.22 |
| (c) | – | – | 2.74 | 0.68 |

*Values of $a/a_i$ outside parentheses are averages, whereas those in parentheses are minimum and maximum values, respectively

coefficients for both the calibration and the plume measurements not been corrected by this procedure, the plume concentration measurements would have been biased by factors equal to $(a_{cal}/a)^{-1}$, which was typically between 0.7 and 0.8.

Besides the two previous configurations, we have also examined a third configuration that was actually possible in our facility, although not used in the present measurements. In this case, the camera would view a plane normal to the flow from a window at the downstream end of the test section (Fig. 17c). In such case, out-of-sheet dye would be present along the line of sight of the camera for long distances $w_u$ upstream and $w_d$ downstream of the laser sheet. Assuming that $w_u = w_d = 2$ m, one can estimate that the calibration factor ratio would be $a/a_{cal} = 1.48$, which means that concentration would be severely underestimated if corrections were not applied.

## 9 A test of the overall accuracy of the present concentration measurements

The accuracy of the concentration measurements in the plume was tested by comparing the measured total dye mass flow rates $\dot{m}_m$ in normal and streamwise cross sections of the plume with the mass flow rate $\dot{m}_i$ of dye released from the injection tube. The latter was estimated as

$$\dot{m}_i = C_S Q\,, \tag{28}$$

where $Q$ was the water injection volume flow rate, measured with a rotameter.

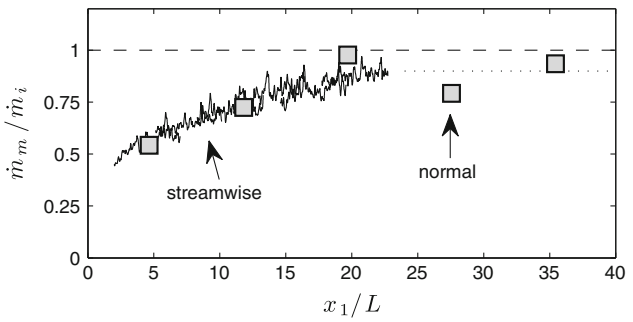


**Fig. 18** Evolution of the measured dye mass flow rate, normalized by its value at the source; the *solid line* indicates measurements in a streamwise plane, whereas squares indicate measurements in cross planes; the *dotted line* indicates the average of the data for $x_1/L \geq 20$, which was $\dot{m}_m/\dot{m}_i \approx 0.90$

The average mass flow rate of dye on transverse planes was estimated by integrating the corresponding mean concentration maps as

$$\dot{m}_m = U_c \int_{-\infty}^{\infty}\int_{-\infty}^{\infty} \overline{C}\,\mathrm{d}x_2\,\mathrm{d}x_3\,, \tag{29}$$

where $U_c$ is the mean flow velocity in the center of the channel.

The average mass flow rate of dye on streamwise planes was calculated from profiles of $\overline{C}$ in the $x_2$ direction, under the assumption that the two-dimensional $\overline{C}$ map in the $x_2 - x_3$ plane could be described by a Gaussian function as

$$\overline{C}(x_2, x_3) \propto \exp\left[-\frac{x_2^2}{2\sigma_2^2} - \frac{x_3^2}{2\sigma_3^2}\right]; \tag{30}$$

the ratio of the plume half-widths was determined from the normal-plane measurements as $\sigma_3/\sigma_2 = 1.25$ (Vanderwel and Tavoularis 2014b).

The total masses of the mean concentration maps obtained on streamwise planes in the range $2 < x_1/L < 23$ as well as on normal planes at locations $x_1/L = 5$, 12, 20, 28, and 35 are shown in Fig. 18. Both the streamwise and normal-plane measurements were corrected for the effect of out-of-sheet fluorescence, as described in Sect. 7. An observation that supports the consistency of the present analysis is that the corrected measurements in the two configurations essentially coincided, whereas there were significant differences between the corresponding uncorrected measurements.

Figure 18 clearly illustrates the fact that, near the plume source ($x_1/L = 5$), the measured mass flow rate, estimated from both streamwise and normal-plane measurements, was significantly lower than the injected mass flow rate. This discrepancy is attributed to the effect of the dye concentration non-uniformity across the laser light sheet, as described in Sect. 4, which was not accounted for in these

estimates. This explanation is supported by the following arguments. Very close to the source, the instantaneous plume cross section would have a nearly rectangular concentration profile with a characteristic width equal to the inner radius of the injection tube, i.e., $\sigma_P \approx 0.92$ mm. Then, $\sigma_L/\sigma_P \approx 1.1$ and, according to Fig. 8, the measured peak concentration would be approximately 63 % of the true value $C_S$. This estimate of bias is consistent with the measured level of underestimation of mass flow rate at $x_1/L = 5$ in Fig. 18. Away from the source ($x_1/L \gtrsim 20$), the instantaneous plume filaments had shapes closer to a Gaussian than a rectangular one and had half-widths in the range of 2 mm $\lesssim \sigma_P \lesssim 5$ mm. This corresponds to $0.2 \lesssim (\sigma_L/\sigma_P) \lesssim 0.5$, so in this region the peak concentration would be equal to 89–98 % of the true value. This statement is compatible with the observation in Fig. 18 that the error in the measured mass flow rate due to concentration non-uniformity across the light sheet became small for $x_1/L \gtrsim 20$.

Although there was visible precision uncertainty (scatter) in the measurements for $x_1/L \gtrsim 20$, these measurements fluctuated around an average $\dot{m}_m/\dot{m}_i \approx 0.90$, which may be treated as a far-field asymptotic value. The remaining 10 % discrepancy between the far-field measured dye mass flow rate and the mass flow rate at the source may be attributed to the approximations used in deriving corrections as well as the anticipated combined uncertainty of unaccounted for aspects of the PLIF method; the latter include, among others, the uncertainties of (a) injected dye concentration; (b) local velocity used for mass flow rate calculation; (c) laser power, which fluctuated with a standard deviation of 3 %; and (d) the factor $a_{cal}/a$, which depended strongly on the local plume width and could vary by 10 %. Although not perfect, the proposed methods of correction for secondary fluorescence and for out-of-sheet dye successfully drastically reduced any significant bias in the measured mass flow rate due to these effects.

In summary, one can draw the following conclusions concerning the accuracy of the present concentration measurements. All measurements have been corrected for errors due to out-of-sheet fluorescence, which is no longer a concern. They are deemed to be sufficiently accurate for $x_1/L \gtrsim 20$, where they are not subjected to significant error due to concentration non-uniformity across the laser sheet, but, for $x_1/L \lesssim 20$, the measurements would generally underestimate the true concentration due to this error, which increases with decreasing distance from the source.

## 10 Conclusions

In the previous sections, we have presented a detailed uncertainty analysis of PLIF measurements for the particular case of a slender plume in turbulent flow. In this analysis, we considered measurement planes both parallel and normal to the flow direction. In addition to uncertainties associated with the dye properties and dye attenuation, we analyzed the error that would arise when the plume width is not much larger than the laser sheet thickness and the error that would be introduced by secondary fluorescence and by out-of-sheet dye. None of these error sources has been addressed in the previous literature. We found that the error associated with a relatively large laser sheet thickness can be very significant when the plume examined is very slender and suggested that, as a rule of thumb, the laser sheet thickness should be at most 1/3 of the thickness of the thinnest filaments of dye in the plume. We found that this error would contaminate measurements in both the normal and the streamwise configurations, introducing a negative bias, which would increase with proximity to the plume source.

We also analyzed the effect of secondary fluorescence, which we attributed to absorption and re-emission of primary fluorescence. We found that this effect influenced the concentration measurement by biasing the calibration measurements and proposed a method for correcting the calibration procedure, which if uncorrected would have resulted in a bias of 20–30 %. Furthermore, we found that secondary fluorescence emitted by out-of-sheet dye contaminated measurements of instantaneous concentration maps in the plume and we also proposed a correction method, which removed a bias of 5–8 % in the mean concentration measurement. As an overall test of accuracy, we demonstrated that the corrected measurements conserved approximately the dye mass flow rate along the plume in the far-field.

**Acknowledgments** Financial support by the Natural Sciences and Engineering Research Council of Canada is gratefully acknowledged.

## References

Anaspec (Fremont, CA, USA) (2013) Rhodamine 6G fluorescence reference standard. http://www.anaspec.com/products/product.asp?id=28765. Accessed Sep 2013

Arcoumanis C, McGuirk J, Palma J (1990) On the use of fluorescent dyes for concentration measurements in water flows. Exp Fluids 10:177–180

Azzalini A (1985) A class of distributions which includes the normal ones. Scand J Stat 12(2):171–178

Catrakis H, Dimotakis P (1996) Mixing in turbulent jets: scalar measures and isosurface geometry. J Fluid Mech 317:369–406

Cowen EA, Chang KA, Liao Q (2001) A single-camera coupled PTV–LIF technique. Exp Fluids 31:63–73

Crimaldi JP (2008) Planar laser induced fluorescence in aqueous flows. Exp Fluids 44:851–863

Ferrier AJ, Funk DR, Roberts PJW (1993) Application of optical techniques to the study of plumes in stratified fluids. Dyn Atmos Oceans 20:155–183

Gendron P, Avaltroni F, Wilkinson K (2008) Diffusion coefficients of several rhodamine derivatives as determined by pulsed field gradient-nuclear magnetic resonance and fluorescence correlation spectroscopy. J Fluoresc 18(6):1093–1101

Guilbault GG (ed) (1990) Practical fluorescence, 2nd edn. Marcel Dekker, New York

Karasso P, Mungal M (1997) PLIF measurements in aqueous flows using the Nd:YAG laser. Exp Fluids 23(5):382–387

Lemoine F, Wolff M, Lebouche M (1996) Simultaneous concentration and velocity measurements using combined laser-induced fluorescence and laser doppler velocimetry: application to turbulent transport. Exp Fluids 20(5):319–327

Melton L, Lipp C (2003) Criteria for quantitative PLIF experiments using high-power lasers. Exp Fluids 35:310–316

Prasad A, Jensen K (1995) Scheimpflug stereocamera for particle image velocimetry in liquid flows. Appl Opt 34(30):7092–7099

Prasad RR, Sreenivasan KR (1989) Scalar interfaces in digital images of turbulent flows. Exp Fluids 7:259–264

Sarathi P, Gurka R, Kopp G, Sullivan P (2012) A calibration scheme for quantitative concentration measurements using simultaneous PIV and PLIF. Exp Fluids 52(1):247–259

Shan JW, Lang DB, Dimotakis PE (2004) Scalar concentration measurements in liquid-phase flows with pulsed lasers. Exp Fluids 36(2):268–273

Vanderwel C, Tavoularis S (2011) Coherent structures in uniformly sheared turbulent flow. J Fluid Mech 689:434–464

Vanderwel C, Tavoularis S (2013) Measurements of turbulent diffusion from a point source in uniformly sheared flow. In: Eighth international symposium on turbulence and shear flow phenomena (TSFP8), Poitiers, France

Vanderwel C, Tavoularis S (2014a) Measurements of turbulent diffusion in uniformly sheared flow. J Fluid Mech 754:488–514

Vanderwel C, Tavoularis S (2014b) Relative dispersion of a passive scalar plume in turbulent shear flow. Phys Rev E 89(4):041005

Walker DA (1987) A fluorescence technique for measurement of concentration in mixing liquids. J Phys E Sci Instrum 20:217–224

Webster D, Roberts P, Ra'ad L (2001) Simultaneous DPTV/PLIF measurements of a turbulent jet. Exp Fluids 30:65–72

Webster D, Rahman S, Dasi L (2003) Laser-induced fluorescence measurements of a turbulent plume. J Eng Mech ASCE 129:1130–1137

Würth C, González MG, Niessner R, Panne U, Haisch C, Genger UR (2012) Determination of the absolute fluorescence quantum yield of Rhodamine 6G with optical and photoacoustic methods-providing the basis for fluorescence quantum yield standards. Talanta 90:30–37

Zhu Y, Mullins O (1992) Temperature dependence of fluorescence of crude oils and related compounds. Energy Fuels 6(5):545–552

# Chapter 5

## Measurements of turbulent diffusion in uniformly sheared flow

This chapter addresses the absolute diffusion of a scalar plume in USF. The results are presented in the form of the manuscript

> Vanderwel, C. and Tavoularis, S. (2014), "Measurements of turbulent diffusion in uniformly sheared flow, Journal of Fluid Mechanics, Vol. 754, pp. 488-514,

which was published on August 7, 2014. Measurements of the velocity field verified that the turbulence properties were nearly homogeneous, and integral lengthscales were determined from autocorrelations of the velocity maps. The ensemble-averaged mean and standard deviations of the concentration fields were determined and the evolutions of the plume width were investigated. The mean scalar fluxes were related to the mean scalar gradients through a first-order gradient transport model and all components of the turbulent diffusivity tensor were measured directly. The measured components of the turbulent diffusivity tensor were compared with theoretical models and with the measurements of the apparent diffusivity. Estimates of the mean advective and diffusive fluxes were also analyzed and their relative balance attested to the accuracy of the results. Additional maps showing the evolutions of some ensemble-averaged properties of the plume that were not included in the manuscript are presented in Appendix B.

*J. Fluid Mech.* (2014), *vol.* 754, *pp.* 488–514.  
doi:10.1017/jfm.2014.406

# Measurements of turbulent diffusion in uniformly sheared flow

**Christina Vanderwel and Stavros Tavoularis**

Department of Mechanical Engineering, University of Ottawa, Ottawa, ON K0A 3H0, Canada

(Received 18 November 2013; revised 26 May 2014; accepted 12 July 2014)

The diffusion of a plume of dye in uniformly sheared turbulent flow in a water tunnel was investigated using simultaneous stereoscopic particle image velocimetry (SPIV) and planar laser-induced fluorescence (PLIF). Maps of the mean concentration and the turbulent concentration fluxes in planes normal to the plume axis were constructed, from which all components of the second-order turbulent diffusivity tensor were determined for the first time. Good agreement between the corresponding apparent and true diffusivities was observed. The turbulent diffusivity tensor was found to have strong off-diagonal components, whereas the streamwise component appeared to be counter-gradient. The different terms in the advection–diffusion equation were estimated from the measurements and their relative significance was discussed. All observed phenomena were explained by physical arguments and the results were compared to previous ones.

**Key words:** homogeneous turbulence, turbulent mixing

## 1. Introduction

Turbulent diffusion is the process of spreading and mixing of admixtures by turbulent motions. It is the essential mechanism that drives dispersal of pollutants in the environment, mixing in industrial processes, and chemical reactions in diverse systems. Although turbulent diffusion has been studied extensively for a long time, its analysis for engineering purposes is still based on crude models and is mostly concerned with the prediction of the mean concentration of the admixture (Roberts & Webster 2002).

The exact governing equation for the mean concentration $\overline{C}$ of an admixture released passively in a turbulent flow is the Reynolds-averaged advection–diffusion equation

$$\frac{\partial \overline{C}}{\partial t} + \underbrace{\overline{U}_i \frac{\partial \overline{C}}{\partial x_i}}_{\text{advection}} = \underbrace{\gamma \frac{\partial^2 \overline{C}}{\partial x_i \partial x_i}}_{\text{molecular diffusion}} + \underbrace{\frac{\partial(-\overline{cu}_i)}{\partial x_i}}_{\text{turbulent diffusion}}, \tag{1.1}$$

where $\overline{U}_i$ is the mean velocity vector, $\gamma$ is the molecular diffusivity, and $\overline{cu}_i$ is the concentration–velocity covariance or turbulent mass flux vector. Even if the mean velocity field were specified, this equation would be open in $\overline{C}$. One type of

closure is possible by the use of a model for the turbulent mass flux vector in terms of $\overline{C}$. The most commonly used model is the first-order gradient transport model (Arya 1999)

$$-\overline{cu_i} = D_{ij}\,\frac{\partial \overline{C}}{\partial x_j}, \tag{1.2}$$

where $D_{ij}$ is the turbulent, or 'eddy', diffusivity tensor, which has nine components, the values of which depend on the turbulent field. The gradient transport model is based on the assumptions that the macroscopic characteristic lengthscale of the scalar is much greater than that of the transporting mechanism (i.e. the turbulence) and that the flow properties are approximately homogeneous over the turbulence lengthscale (Corrsin 1975). Despite the fact that these assumptions are not satisfied in most cases of interest, the gradient transport model is known to provide fairly accurate predictions in a variety of situations (Sreenivasan, Tavoularis & Corrsin 1982). Application of (1.2) requires empirical knowledge of all nine components of $D_{ij}$. However, measurements of these components are quite scarce, due to the difficulty of measuring simultaneously the local magnitudes and directions of both the mean concentration gradient and the turbulent mass flux vector. Theoretical expressions relating $D_{ij}$ to turbulent characteristics have also been suggested; these will be discussed in following sections. Some models simplify the turbulent diffusivity tensor by assuming that it is diagonal or isotropic, but the use of such simplified models in shear flows is known to introduce additional errors.

The objective of the present work is to study turbulent diffusion in a shear flow generated in the laboratory and specifically to measure all components of the turbulent diffusivity tensor in this flow. The scalar property that has been measured is the concentration of dye in a plume released nearly passively from a thin tube in uniformly sheared flow (USF). The statistical properties of the velocity and scalar concentration fields were measured simultaneously on cross-sectional planes using stereoscopic particle image velocimetry (SPIV) and planar laser-induced fluorescence (PLIF). Thus, two-dimensional maps of the turbulent velocities and scalar concentration were obtained, as well as maps of the three concentration–velocity covariances; from these maps, the values of all components of the turbulent diffusivity tensor were determined directly by fitting (1.2) to the data. This is the first time all nine components of the turbulent diffusivity tensor have been determined together experimentally. This article will also present comparisons of the experimental results to theoretical estimates of the turbulent diffusivities.

## 2. Literature on turbulent diffusion

The study of turbulent diffusion originated with the work of Taylor (1921), who considered the one-dimensional motion of an individual fluid particle released from a fixed point in stationary isotropic turbulent flow, neglecting molecular diffusion. He demonstrated that the variance of an ensemble of particle displacements following time $t$ from their release should depend only on the turbulence properties as

$$\overline{X^2}(t) = 2\overline{v^2}\int_0^t (t-\xi)R(\xi)\mathrm{d}\xi, \tag{2.1}$$

where $v$ represents the Lagrangian velocity fluctuations and $R(\xi)$ is the Lagrangian correlation coefficient. Taylor further identified two regimes of diffusion which would occur in the limits of short $t$ and long $t$, known as the turbulent convection and

turbulent diffusion regimes (Anand & Pope 1985). In these regimes, (2.1) would be simplified as, respectively,

$$\overline{X^2}(t) \approx \overline{v^2} t^2, \quad \text{for } t \ll \mathscr{T}, \tag{2.2}$$

$$\overline{X^2}(t) \approx 2\overline{v^2}\mathscr{T} t, \quad \text{for } \mathscr{T} \ll t, \tag{2.3}$$

where $\mathscr{T}$ is the Lagrangian integral timescale of the turbulence. It follows that the rate of dispersion, defined as

$$\frac{1}{2}\frac{\mathrm{d}\overline{X^2}(t)}{\mathrm{d}t} = \overline{v^2}\int_0^t R(\xi)\mathrm{d}\xi, \tag{2.4}$$

has the following limits for the near- and far-field regimes:

$$\frac{1}{2}\frac{\mathrm{d}\overline{X^2}(t)}{\mathrm{d}t} \approx \overline{v^2} t, \quad \text{for } t \ll \mathscr{T}, \tag{2.5}$$

$$\frac{1}{2}\frac{\mathrm{d}\overline{X^2}(t)}{\mathrm{d}t} \approx \overline{v^2}\mathscr{T}, \quad \text{for } \mathscr{T} \ll t. \tag{2.6}$$

This implies that the rate of dispersion would be zero at the moment of particle release, would initially increase linearly with dispersion time, and would eventually reach an asymptote which would depend only on the Lagrangian integral timescale of the turbulence and the variance of the Lagrangian velocity fluctuations.

A theoretical analysis of three-dimensional turbulent diffusion was first presented by Batchelor (1949), who defined a three-dimensional diffusion coefficient tensor $(\mathrm{d}\overline{X_i X_j}/\mathrm{d}t)/2$ in terms of the mean Lagrangian displacement tensor $\overline{X_i X_j}(t)$ of a particle transported by homogeneous turbulence. He further demonstrated that, in homogeneous, non-sheared turbulence and for a Gaussian particle displacement distribution, $(\mathrm{d}\overline{X_i X_j}/\mathrm{d}t)/2$ would be equal to the turbulent diffusivity tensor $D_{ij}$, as defined in (1.2). Batchelor also showed that, in isotropic turbulence, $D_{ij}$ would be proportional to the identity tensor (Kronecker's delta); as in Taylor's theory, the magnitudes of the components of $D_{ij}$ would increase with dispersion time and would eventually reach asymptotes that depend only on the Lagrangian integral timescales of the turbulence $\mathscr{T}_{ij}$ and the intensities of the Lagrangian velocity fluctuations.

Riley & Corrsin (1974) expanded Batchelor's analysis for homogeneous turbulent shear flow and noted that the normal diffusivities were unequal and that some of the cross-diffusivities were not zero. As with the theories of Taylor and Batchelor, the magnitudes of the turbulent diffusivities were shown to depend on the Lagrangian integral timescales of the turbulence $\mathscr{T}_{ij}$ and the intensities of the Lagrangian velocity fluctuations. Corrsin (1975) suggested that the asymptotic values of the turbulent diffusivities could be estimated from Eulerian properties, as surrogates for their Lagrangian counterparts, for example as $D_{22} \approx u_2'^2 T_{11}$. Additional theoretical arguments have been made by Tavoularis & Corrsin (1985), Rogers, Mansour & Reynolds (1989) and Younis, Speziale & Clark (2005) to derive asymptotic expressions for the turbulent diffusivity tensor components in shear flows. These theories will be revisited in § 5.4.

A classical approach for measuring turbulent diffusion in the laboratory or in the environment is to relate the rate of growth of puffs and plumes generated in the turbulent flow to an apparent turbulent diffusivity. The plume generated by a continuously emitting source may be considered as the result of superposition of clouds emitted successively by an instantaneous source. For a plume of particles

emitted from a point source in a turbulent flow with a uniform mean velocity $U_1$ in the $x_1$ direction, the apparent diffusivities in the two normal directions $x_2$ and $x_3$ are defined as

$$K_2 = \frac{U_1}{2}\frac{\mathrm{d}\sigma_2^2}{\mathrm{d}x_1}, \quad K_3 = \frac{U_1}{2}\frac{\mathrm{d}\sigma_3^2}{\mathrm{d}x_1}, \tag{2.7a,b}$$

where $\sigma_2$ and $\sigma_3$ are the corresponding characteristic plume widths. If, and only if, the streamwise dispersion were negligible, the apparent plume diffusivities $K_2$ and $K_3$ would be equivalent to the diffusion coefficients $\frac{1}{2}\mathrm{d}\overline{X_2^2}/\mathrm{d}t$ and $\frac{1}{2}\mathrm{d}\overline{X_3^2}/\mathrm{d}t$ (Arya 1999), and thus to $D_{22}$ and $D_{33}$.

Further assuming that the two apparent turbulent diffusivities are uniform in space and equal to each other ($K_2 = K_3 = K$) leads to the well-known Gaussian plume formula (Arya 1999) for the mean concentration of a continuous plume in uniform mean flow

$$\overline{C} = \frac{Q}{4\pi K x_1}\exp\left[-U_1\left(\frac{x_2^2 + x_3^2}{4Kx_1}\right)\right]. \tag{2.8}$$

According to this solution, the maximum concentration of the plume would decay as $x_1^{-1}$ and the plume width would grow as $x_1^{0.5}$.

Examples of investigations of turbulent diffusion in the environment include early observations of anti-aircraft shell-bursts (Roberts 1923; Sutton 1932) and plumes of lycopodium spores released in the atmosphere (Hay & Pasquill 1959) and dyes released in a lake (Csanady 1963). Examples of relevant laboratory studies include investigations of diffusion behind a line source in grid turbulence (Warhaft 1984; Anand & Pope 1985; Stapountzis *et al.* 1986), a line source in USF (Tavoularis & Corrsin 1981; Karnik & Tavoularis 1989), a line source in channel flow (Lepore & Mydlarski 2011), a point source in USF (Nakamura *et al.* 1986), and a point source in channel flow (Webster, Rahman & Dasi 2003; Rahman & Webster 2005). In these actual turbulent flows, the turbulent kinetic energy and lengthscale would generally evolve downstream and so would the diffusivities of superimposed scalar plumes. As a result, (2.8) would not be applicable and the plume growth rate would be expected to deviate from the previously mentioned power law. Experimental studies of plumes in grid turbulence and shear flows have found that the plume widths followed power laws but with powers different from the theoretical value of 0.5. This discrepancy between the simplified solutions and actual turbulent flows highlights the need for further studies of turbulent diffusion and refined turbulent diffusion models.

Individual components of the turbulent diffusivity tensor, as defined by (1.2), can be calculated from measurements of corresponding mean scalar derivatives and velocity–scalar covariances. Most experimental studies that report such results have taken them at locations where the scalar gradient was nearly aligned with one of the physical mean flow axes. Tavoularis & Corrsin (1981) examined a case in which a uniform mean scalar gradient was superimposed on USF, with both gradients in the $x_2$ direction, and measured $D_{12}/D_{22} \approx -2.2$. Tavoularis & Corrsin (1985) examined a variant of this case, in which the mean scalar gradient was in the $x_3$ direction, and found $D_{33}/D_{22} \approx 1.6$. Karnik & Tavoularis (1989) studied the plume of a line source in USF, where the mean scalar gradient was nearly aligned with the $x_2$ direction and reported that $D_{12}/D_{22} \approx -2.0$ and $D_{22}/(u_2' L_{11,1}) \approx 0.1$.

The literature includes several measurements of scalar turbulent diffusivities in various inhomogeneous shear flows, as for example in turbulent jets (Lemoine, Wolff & Lebouche 1996; Borg, Bolinder & Fuchs 2001; Chang & Cowen 2002). In general, such diffusivities were determined from mean scalar and turbulent scalar flux profiles

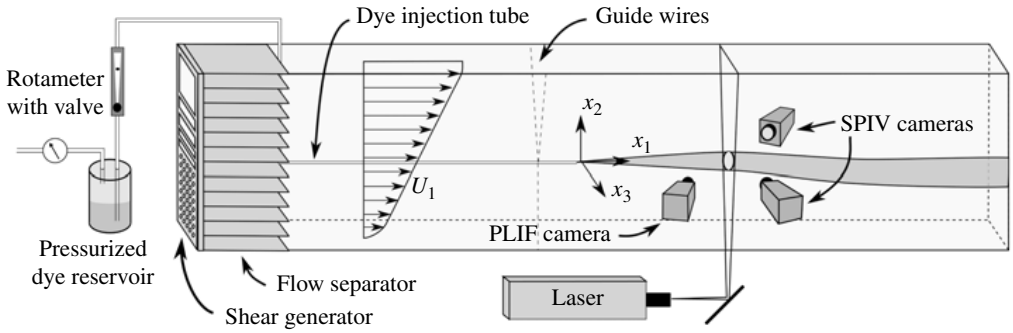


FIGURE 1. Sketch of the experimental apparatus and main instrumentation in the water tunnel test section.

in a single direction, with no consideration given to the possible three-dimensionality of the mean scalar field and the turbulence inhomogeneity. In consequence, it seems plausible that such scalar diffusivities would depend on the orientation, as well as location, of the data profiles used and, indeed, Borg *et al.* (2001) found drastically different diffusivity values in the radial and axial directions in a jet. Consequently, scalar diffusivity measurements in inhomogeneous shear flows are deemed to be specific to particular flow geometries and experimental conditions and should not be considered for general use in other turbulent flows.

A review of past literature has identified no measurements of all components of the turbulent diffusivity tensor that were taken at the same time in the same flow. The present study aims at filling this gap in the literature.

## 3. Apparatus and experimental procedures

The experiments were conducted in a free-surface, recirculating water tunnel, having a test section with a width of 0.53 m, a length of approximately 4 m, and filled to a depth of 0.46 m (figure 1). USF was generated by a perforated plate of varying solidity ('shear generator'), inserted at the entrance to the test section and followed by an array of parallel plates spaced by a distance $L = 25.4$ mm ('flow separator').

A neutrally buoyant aqueous solution of Rhodamine 6G fluorescent dye with a concentration $C_S = 0.3$ mg $l^{-1}$ was injected into the flow through a fine tube having a tip with an inner diameter of 1.83 mm and a wall thickness of 0.15 mm. To minimize its disturbance to the flow, the tube was inserted in the stream through the flow separator and was aligned with the flow section centreline so that the dye was discharged at approximately 2 m downstream of the flow separator, where the turbulence structure of the USF was fully developed. The injection tube was tethered by 50 μm thick guide wires, and was free of any movement or vibrations. The dye solution was contained in a reservoir that was pressurized by compressed air through a pressure regulator. The dye solution flow rate through the injection tube was measured by a rotameter and adjusted with a built-in needle valve so that injection created the least possible flow disturbance. The optimal flow rate was found to be $Q = 0.97 \pm 0.05$ ml $s^{-1}$ (see appendix). The dye molecular diffusivity was taken to be $\gamma = (4.0 \pm 0.3) \times 10^{-4}$ $mm^2$ $s^{-1}$ (Gendron, Avaltroni & Wilkinson 2008), which corresponds to a Schmidt number $Sc \equiv \nu/\gamma = 2500 \pm 300$. Rhodamine 6G has an absorption peak at 525 nm, which is close to the emission wavelength of the Nd:YAG laser (532 nm); it also has an emission peak at 554 nm (Würth *et al.* 2012),

which is sufficiently different from the laser emission peak for this substance to be well suited for PLIF measurements. The camera used to measure the fluorescence was fitted with an optical long-pass filter with a sharp cutoff at 540 nm, so as to be sensitive only to the fluorescence emitted by the dye and to block essentially all incident light produced by the laser and ambient light. Dye solutions were prepared by mixing Rhodamine 6G powder (A&C American Chemicals Ltd, CAS: 989-38-8, Montreal, Canada) with distilled water.

Velocity and concentration measurements were taken simultaneously in cross-sections of the flow normal to the streamwise direction, that were illuminated by a light sheet created from the output of a Nd:YAG pulsed laser. Velocity measurements were performed using a two-camera SPIV system (LaVision GmbH, FlowMaster Stereo-PIV, Göttingen, Germany). Concentration measurements were obtained using a third camera (PCO AG, pco.edge, Kelheim, Germany), which had a capacity of 5.5 MP, a pixel depth of 16 bits, and was synchronized with the SPIV system and the laser pulse triggering circuit. All cameras were fitted with Scheimpflug adapters, so that the entire measurement plane would be in focus, although viewed by the camera at an inclination. Liquid prisms were used to eliminate horizontal astigmatism that would have been introduced in the images if the cameras had viewed the flow at an inclination of 45° with respect to the glass wall (Prasad & Jensen 1995; Adrian & Westerweel 2011). The field of view of the measurements was rectangular with an approximately 120 mm vertical side and a 200 mm horizontal side. The fields of view of the three cameras were carefully aligned using a two-sided calibration target (LaVision GmbH, calibration plate no. 22), which was mounted in the image plane before the experiment. Images of the calibration plate taken with each camera were then processed by the software provided by the manufacturer (LaVision GmbH, DaVis 7.2) to create image mapping functions that ensured that the three images were coincident. The mapping functions were then fine-tuned using a self-calibration process applied to images of particles illuminated by the laser sheet taken with each camera, in order to correct for any misalignment between the laser sheet and the calibration target. Following this calibration, the average misalignment of the cameras was estimated to be 3.4 pixels, which corresponds to approximately 0.2 mm in the field of view.

Measurements were obtained in five cross-sectional planes, located at dimensionless distances from the source equal to $x_1/L = 5$, 12, 20, 28, and 35. The in-plane spatial resolutions of the measured velocity and concentration fields were, respectively, one vector per 1.15 mm × 1.15 mm flow area and one scalar sample per 0.05 mm × 0.05 mm area. The cross-sectional profile of the laser intensity had approximately the shape of a Gaussian distribution with a standard deviation of 1 mm, which, considering the 45° viewing angle, corresponds to a resolution along the line of sight of the camera of approximately 2.8 mm. The time delay between pulses for each SPIV measurement was 1500 μs. During the interval between the two pulses, a particle travelling with the centreline flow velocity of 0.18 m $s^{-1}$ would be displaced by a streamwise distance of 0.27 mm, which satisfies well the SPIV requirement of being much smaller than the laser sheet thickness. Pulse-to-pulse laser power fluctuations had a standard deviation of approximately 3 %, which was deemed to be acceptable for PLIF measurements. Concentration and velocity measurements were sampled at a rate of 2 Hz. Ensemble averages were calculated from 500 samples acquired at each of the positions $x_1/L = 5$, 12, and 20, and from 1000 samples at $x_1/L = 28$ and 35. Differences between plume widths computed by averaging 500 samples at $x_1/L = 28$ and 35 and those computed by averaging 1000 samples had a

standard deviation of 3 %, which is deemed to be sufficiently small for considering averages of 500 samples to be essentially convergent.

The concentration $C$ of dye measured by each diode (i.e. each pixel) of the camera was determined as a linear function of the radiant power flux emitted by the dye ('the fluorescence') in the plane of the laser sheet. The coefficients in this function were determined independently for each pixel of the camera from a calibration measurement in a small calibration tank, placed *in situ* and filled with a dye solution having a uniform concentration $C_{cal} = 0.075$ mg $l^{-1}$. Pixel-by-pixel calibration accounted for the effects of spatial variation in the laser sheet and optical components, lens vignette, and any pixel-to-pixel offsets or gain variations in the camera.

Concentration measurement errors and uncertainties in a slender plume using PLIF are the subject of a separate publication (Vanderwel & Tavoularis 2014*a*). In that work we quantified several hitherto disregarded sources of error, which may potentially contaminate significantly fluorescent dye concentration measurements by PLIF. One source of error is secondary fluorescence, which is the result of the absorption and re-emission of primary fluorescence by dye both within and outside the laser sheet. Secondary fluorescence was at least one, and usually two or more, orders of magnitude weaker than the primary fluorescence emitted by the dye excited by the laser sheet, but its contributions to the recorded radiation power flux were sufficient to bias both the calibration and the instantaneous concentration maps, if they had remained unaccounted for. We derived and applied novel methods to remove the effects of secondary fluorescence from the camera calibration results and the instantaneous concentration maps and also devised an effective procedure to identify the boundaries of the in-sheet dye regions in the instantaneous concentration maps. We further demonstrated that secondary fluorescence had a very weak effect on the measurement of concentration fluctuations and so we are confident that the bulk of results presented in this article are insensitive to this undesirable input. Another source of uncertainty, which applies to PLIF measurements in all flows but is exacerbated in very slender plumes, is the fact that dye concentration is not uniform along the entire thickness of the laser sheet, but part of the fluid across this sheet may sometimes contain little or no dye. This effect would bias negatively instantaneous concentration measurements that were based on calibration of the camera in a fluid with a uniform concentration. We have analysed this effect and demonstrated that such bias would be negligible for distances from the source beyond $x_1/L \approx 20$. We also found that both secondary fluorescence and dye-non-uniformity had negligible effects on the values of the plume width, lengthscales and turbulent diffusivities reported in this article.

## 4. Results

### 4.1. *The velocity field*

The USF and its turbulence structure in the same facility have been documented previously by Vanderwel & Tavoularis (2011), to be referred to as VT in the remainder of this article. New velocity measurements were taken on transverse planes at several streamwise locations in the plume. The origin of coordinates is set at the centre of the injection tube exit face (figure 1), and the term 'centreline' refers to the $x_1$ axis. The mean centreline velocity $U_c$ and the mean velocity gradient $\mathrm{d}\overline{U}_1/\mathrm{d}x_2$ in the undisturbed flow were essentially constant. Vertical profiles of the mean velocity and the velocity standard deviation in the $(x_1, x_2)$ plane are presented in figure 2. Near the exit of the dye injector, the mean and turbulent velocities were slightly disturbed; however, further downstream the mean velocity profile became nearly linear and the

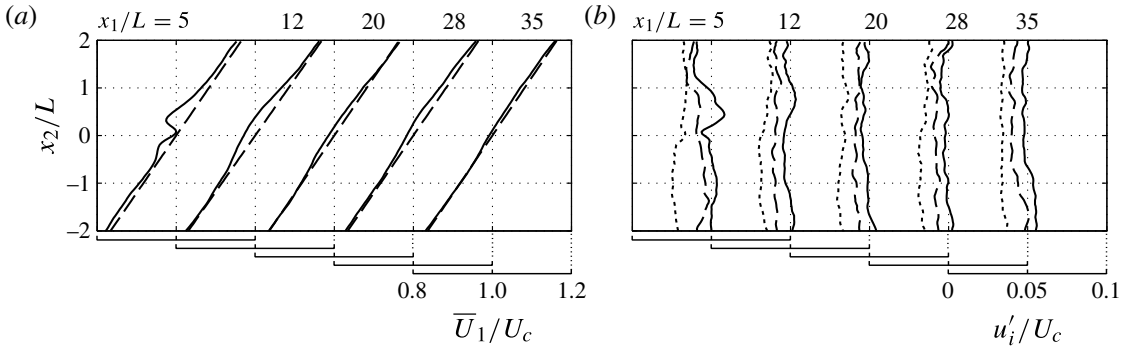


FIGURE 2. Transverse profiles of (*a*) the mean streamwise velocity in the plume (solid line), together with the linear function $U_c + x_2 \mathrm{d}\overline{U}_1/\mathrm{d}x_2$ (dashed line), and (*b*) the r.m.s. turbulent velocity components in the plume ($u_1'/U_c$: solid line, $u_2'/U_c$: dotted line, and $u_3'/U_c$: dashed line); $x_3/L = 0$.

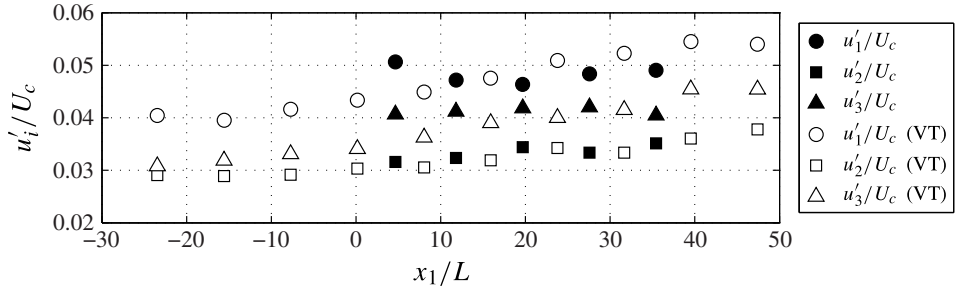


FIGURE 3. Streamwise development of the r.m.s. velocity fluctuations compared to LDV measurements from Vanderwel & Tavoularis (2011) (VT).

turbulence became nearly transversely homogeneous, in agreement with the VT results and those in other USF studies. Specifically, for $x_1/L = 20$, 28, and 35, measurements of the mean velocity deviated from the fitted lines by less than 2.5 % in the field of view and measurements of the root-mean-square (r.m.s.) turbulent velocity components had a standard deviation of approximately 5 %; these deviations are in line with the observations of VT in fully developed USF and are sufficiently small for the flow to be considered as nearly homogeneous. The streamwise evolutions of the normalized r.m.s. turbulent velocities are plotted in figure 3, together with those reported by VT at a slightly lower water tunnel speed. It is noted that the uncertainty in the VT measurements was measurably lower than the present one, because VT took averages over long time histories of laser Doppler velocimetry (LDV) signals. Near the exit of the dye injector, the turbulent velocities appear to be slightly stronger than the VT values; however, at the other locations the corresponding measurements were comparable.

The average turbulent kinetic energy $k$ was essentially the same as that measured by VT, which justifies the use of the kinetic energy dissipation rate $\epsilon$ values reported by VT for the present flow as well. In USF, the turbulent kinetic energy grows exponentially from an effective origin far upstream of the plume origin. Table 1 summarizes parameters of interest at $x_1/L = 35$. In this table, the turbulence anisotropies are defined as $m_{ij} = \overline{u_i u_j}/2k - \delta_{ij}/3$, where $\delta_{ij}$ is Kronecker's delta; $L_{11,1}$ is the streamwise integral lengthscale; $\lambda_{11}$ is the streamwise Taylor microscale,

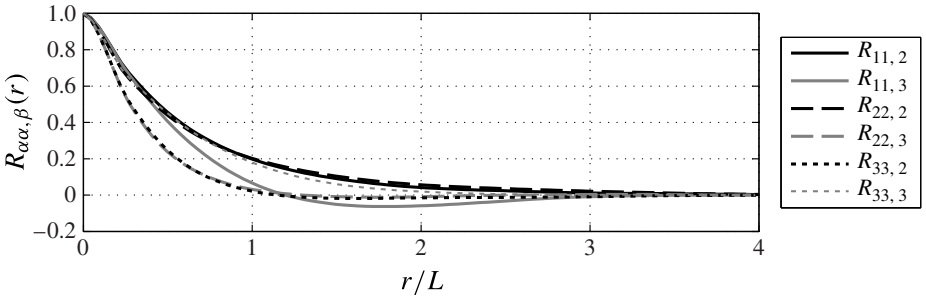


FIGURE 4. Measured autocorrelation functions on the $(x_2, x_3)$ plane, at $x_1/L = 28$.

| | |
|---|---|
| $U_c = 0.18$ m s$^{-1}$ | $\mathrm{d}\overline{U}_1/\mathrm{d}x_2 = 0.59$ s$^{-1}$ |
| $k = 86$ mm$^2$ s$^{-2}$ | $\epsilon = 7.6$ mm$^2$ s$^{-3}$ |
| $m_{11} = 0.12$ | $m_{22} = -0.12$ |
| $m_{33} = -0.01$ | $m_{12} = -0.11$ |
| $L_{11,1} = 30.5$ mm | $\lambda_{11} = 17$ mm |
| $\eta = 0.6$ mm | $\eta_B = 0.012$ mm |
| $S^* = 13.4$ | $R_{\lambda_{11}} = 150$ |
| $\nu_T = 58$ mm$^2$ s$^{-1}$ | |

TABLE 1. Measured or estimated mean and turbulence parameters at $x_1/L = 35$.

estimated as $\lambda_{11} \simeq (24\nu k/\epsilon)^{1/2}$ (de Souza, Nguyen & Tavoularis 1995); $\eta = (\nu^3/\epsilon)^{1/4}$ is the Kolmogorov microscale; $\eta_B = \eta/Sc^{1/2}$ is the Batchelor microscale; $S^* \equiv (2k/\epsilon)(\mathrm{d}\overline{U}_1/\mathrm{d}x_2)$ is the shear rate parameter; $Re_{\lambda_{11}} = u_1'\lambda_{11}/\nu$ is the turbulence Reynolds number; and $\nu_T \equiv -\overline{u_1u_2}/(\mathrm{d}\overline{U}_1/\mathrm{d}x_2)$ is the turbulent viscosity, which grew to the reported value from a value that was 41 % lower at $x_1 = 0$.

### 4.2. *Velocity integral lengthscales*

Theoretical models of turbulent diffusion make use of various integral lengthscales of the turbulent fluctuations. Previous measurements in USF have been mainly limited to the streamwise lengthscales of different velocity components, obtained from single-point laser-Doppler or hot-wire time histories with the use of Taylor's approximation (e.g. Tavoularis & Corrsin 1981; VT). However, it is the transverse lengthscale of the transverse velocity, and the corresponding spanwise scale, that are relevant to transport and diffusion, and these scales are not easily measurable by laser-Doppler and hot-wire anemometries. The current SPIV measurements provide an excellent opportunity to measure directly the transverse and spanwise velocity autocorrelation functions and integral lengthscales. The measured components of the autocorrelation function tensor, defined as

$$R_{\alpha\alpha,\beta}(r) = \frac{\overline{u_\alpha(x_\beta)u_\alpha(x_\beta + r)}}{\overline{u_\alpha^2(x_\beta)}}, \tag{4.1}$$

are presented in figure 4. These were computed from SPIV images on the $(x_2, x_3)$ plane. The corresponding integral lengthscales were calculated by integrating the corresponding autocorrelation functions up to their first zero-crossing (O'Neill *et al.* 2004). Additional lengthscales were calculated from planar PIV (PPIV) measurements

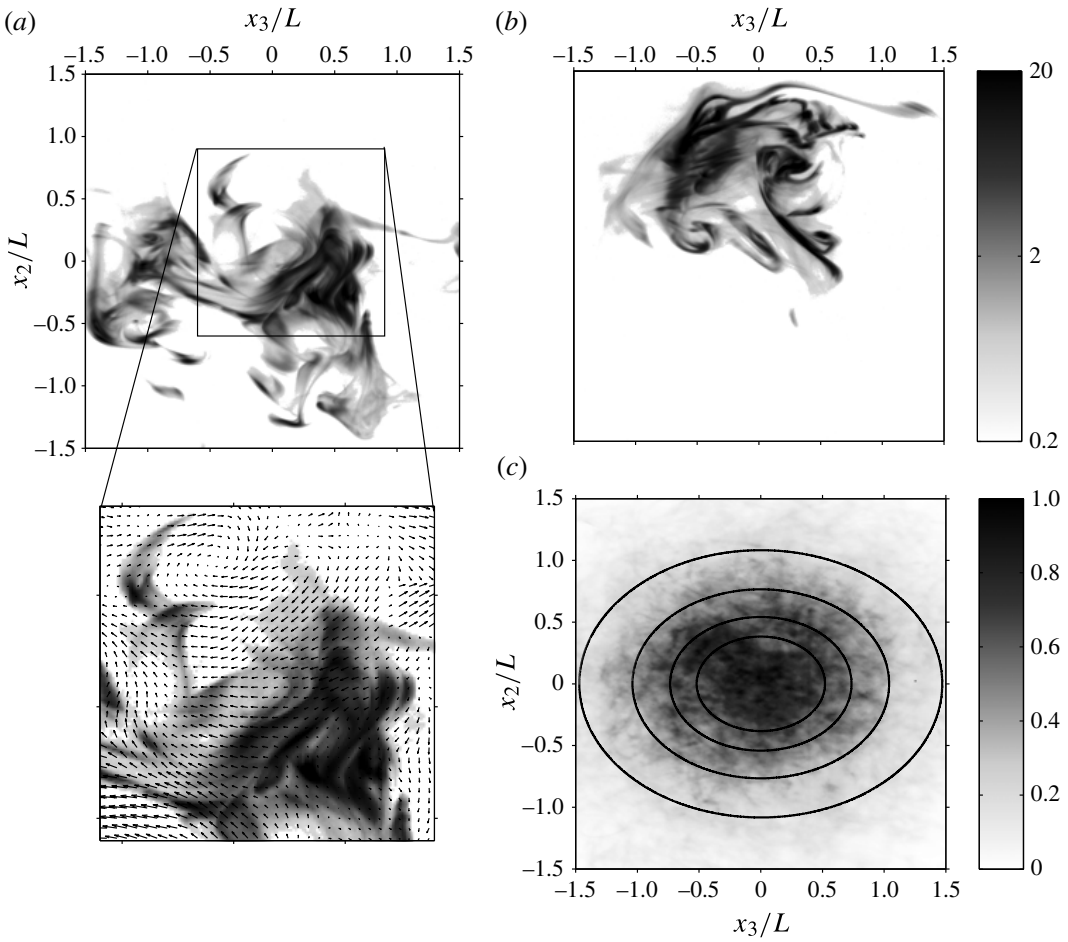


FIGURE 5. (*a*,*b*) Representative maps of the normalized instantaneous concentration $C/(C_S A)$ at $x_1/L = 28$, with a blown-up view of part of (*a*) also showing superimposed an in-plane velocity vector map; (*c*) map of the normalized mean concentration $\overline{C}/(C_S A)$, also at $x_1/L = 28$, with isocontours of the fitted two-dimensional Gaussian function indicated by ellipses.

in the ($x_1$, $x_2$) plane. The integral lengthscales were found to grow downstream; however, within the reported range of the plume, they only changed by approximately 5–10 %. The average value of $L_{11,1}$ was approximately $1.2L$, in agreement with the LDV measurements of VT. The average ratios of the measured integral lengthscales are summarized in table 2. The values of these scales demonstrate a strong anisotropy of the turbulence in the energy-containing range.

### 4.3. *The concentration field*

Two representative instantaneous concentration maps are presented in figure 5(*a*,*b*); in one case (figure 5*a*), the blown-up part also shows the in-plane velocity vector map, which, as mentioned previously, had a spatial resolution that was much lower than that of the concentration. The maps clearly show the presence of mushroom-type patterns, which are evidence of horseshoe vortices in the USF (see VT). The plume was observed to meander significantly within the field of view (Vanderwel & Tavoularis 2014*b*), with the result that large portions of the instantaneous maps had zero

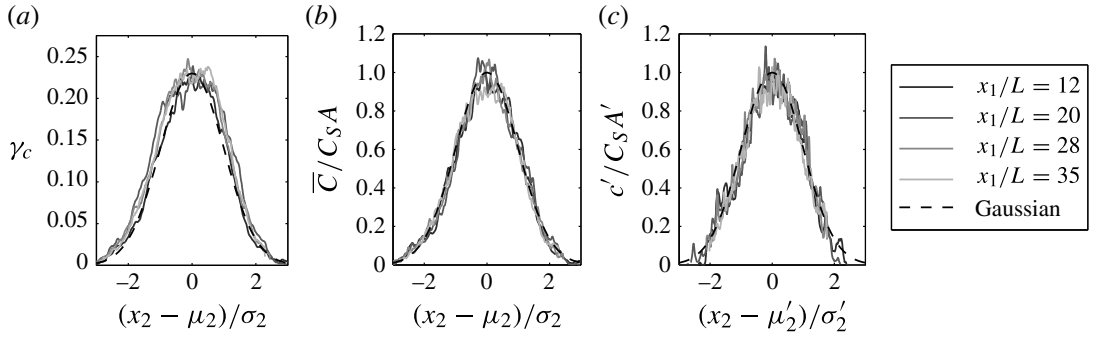


FIGURE 6. Transverse profiles of (*a*) the intermittency factor, (*b*) the normalized mean concentration, and (*c*) the normalized standard deviation of the concentration fluctuations.

| | $\frac{L_{11,2}}{L_{11,1}}$ | $\frac{L_{11,3}}{L_{11,1}}$ | $\frac{L_{22,1}}{L_{11,1}}$ | $\frac{L_{22,2}}{L_{11,1}}$ | $\frac{L_{22,3}}{L_{11,1}}$ | $\frac{L_{33,1}}{L_{11,1}}$ | $\frac{L_{33,2}}{L_{11,1}}$ | $\frac{L_{33,3}}{L_{11,1}}$ |
|---|---|---|---|---|---|---|---|---|
| SPIV | 0.54 | 0.39 | — | 0.55 | 0.31 | — | 0.30 | 0.49 |
| PPIV | 0.51 | — | 0.58 | 0.60 | — | — | — | — |

TABLE 2. Average ratios of the integral lengthscales.

concentration, whereas the areas coincident with the dye plume had relatively high concentrations that often exceeded the peak time-averaged concentration on that plane by a factor of 20. The intermittency of the local concentration can be measured by the intermittency factor $\gamma_c$, which is defined as the fraction of time during which the concentration was non-zero (Wilson, Robins & Fackrell 1985). Close to the plume source, at $x_1/L = 5$, the intermittency on the plume axis was moderate, as the peak value of $\gamma_c$ was approximately 0.4. However, for $x_1/L > 12$, the peak $\gamma_c$ remained low, at approximately 0.23; in this range, the transverse profile of the intermittency factor was self-similar and had an essentially Gaussian shape (see figure 6*a*). Strong scalar intermittency is specific to the present plume, which is relatively slender and also contains a dye with an extremely small molecular diffusivity. These specific conditions differentiate the present configuration from thermal plumes in wind tunnels (e.g. Tavoularis & Corrsin 1981; Karnik & Tavoularis 1989; Lepore & Mydlarski 2011).

The values at each pixel of all recorded instantaneous concentration maps were averaged to produce the corresponding mean concentration maps. It was found that, away from regions containing dyed water, the measured concentration was approximately $2.5 \times 10^{-4} C_S$, which was deemed to be the background concentration 'noise' level. Each mean concentration map was fitted by a two-dimensional Gaussian function

$$\frac{\overline{C}}{C_S} = A \exp\left[-\frac{(x_2-\mu_2)^2}{2\sigma_2^2} - \frac{(x_3-\mu_3)^2}{2\sigma_3^2}\right], \tag{4.2}$$

where $A$ is a dimensionless amplitude, $\mu_2$ and $\mu_3$ are the transverse and spanwise coordinates of the mean plume axis, and $\sigma_2^2$ and $\sigma_3^2$ are the corresponding second central moments of the concentration distribution; all these parameters are functions of streamwise location $x_1$. The parameters $A$, $\mu_2$, $\mu_3$, $\sigma_2$ and $\sigma_3$ were determined using the MATLAB Curve Fitting Toolbox (MathWorks, Natick, MA, USA) as those that resulted in the best fit to the mean concentrations measured at each pixel. The curve

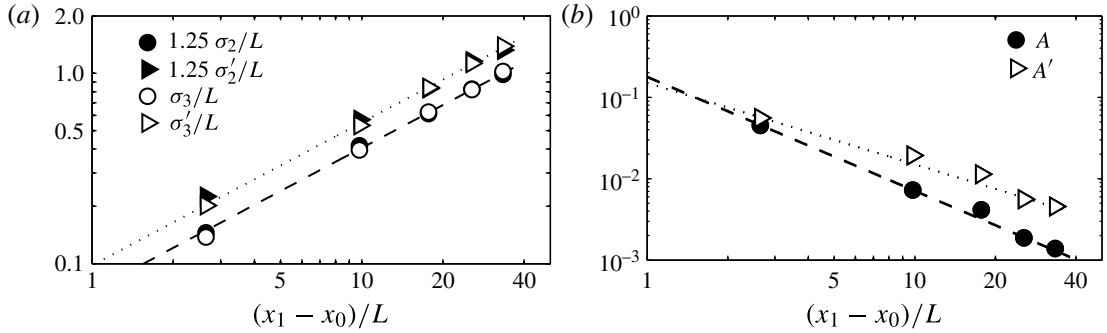


FIGURE 7. (*a*) Streamwise evolutions of the half-widths $\sigma_2$ and $\sigma_3$ of the mean concentration maps and the half-widths $\sigma_2'$ and $\sigma_3'$ of the corresponding standard deviation maps; all widths have been normalized by $L$; a dashed line indicates the power law $0.072[(x_1 - x_0)/L]^{0.75}$ and a dotted line indicates the power law $0.098[(x_1 - x_0)/L]^{0.75}$. (*b*) Streamwise evolutions of $A$ and $A'$, which are, respectively, the dimensionless amplitudes of the Gaussian fits to the mean concentration maps and the corresponding standard deviation maps; a dashed line indicates the fitted power law $A = 0.18[(x_1 - x_0)/L]^{-1.4}$ and a dotted line indicates $A' = 0.15[(x_1 - x_0)/L]^{-1.0}$; in all cases the virtual origin was $x_0 = 2.0L$.

fitting used an iterative least-squares algorithm (Trust-Region Reflective Newton) starting from the initial guesses $A = 0.01$, $\sigma_2 = 10$, $\sigma_3 = 10$, $\mu_2 = 0$, and $\mu_3 = 0$ and restricting the parameters $A$, $\sigma_2$, and $\sigma_3$ to positive values. A representative mean concentration map $\overline{C}/C_S$ is provided in figure 5(*c*), together with isocontours of the fitted two-dimensional Gaussian function. Figure 6(*b*) shows normalized transverse profiles of the mean concentration. This figure clearly shows that the concentration noise was very small compared to the peak mean value. Moreover, it is evident that the mean concentration distribution could be fitted fairly well by Gaussian functions at all measurement planes, with the possible exception of the case at $x_1/L = 5$, where the measured concentration peak slightly exceeded the Gaussian value, presumably due to persistence of injection effects.

The standard deviations $c'$ of the concentration values at each pixel of all maps recorded on each plane were also calculated and fitted by Gaussian functions as

$$\frac{c'}{C_S} = A' \exp\left[-\frac{(x_2 - \mu_2')^2}{2\sigma_2'^2} - \frac{(x_3 - \mu_3')^2}{2\sigma_3'^2}\right], \tag{4.3}$$

where the parameters $A'$, $\mu_2'$, $\mu_3'$, $\sigma_2'$ and $\sigma_3'$ were determined as those that created the best fits to the measured $c'$ at every pixel, using the same least-squares algorithm as for the mean concentration maps and starting with the same initial guesses. Transverse profiles of the normalized $c'$ are presented in figure 6(*c*), which makes it evident that Gaussian fits were fairly good at all locations.

In the following, $\sigma_2$ and $\sigma_3$ will be referred to, respectively, as the transverse and spanwise half-widths of the mean concentration map. Similarly, $\sigma_2'$ and $\sigma_3'$ will be referred to, respectively, as the transverse and spanwise half-widths of the concentration fluctuation map (i.e. of $c'$). The streamwise evolutions of the various plume half-widths are shown in figure 7(*a*). The half-widths of the fluctuation maps were greater than those of the corresponding mean maps. All half-widths grew monotonically downstream and could be fitted by power laws, with powers

equal to 0.75. The spanwise half-widths were consistently larger than the transverse ones, with $\sigma_3/\sigma_2$ and $\sigma_3'/\sigma_2' \approx 1.25$. This difference is attributed to the fact that $u_3' > u_2'$ in USF.

The fitted amplitudes $A$ and $A'$ are plotted in figure 7(*b*). Both amplitudes decreased as the plume spread, following the power laws $A = 0.18[(x_1 - x_0)/L]^{-1.4}$ and $A' = 0.15[(x_1 - x_0)/L]^{-1.0}$, with the same virtual origin of $x_0 = 2.0L$. The decrease in the mean concentration indicates that the plume is being mixed with free-stream fluid, whereas the decrease in the standard deviation indicates that the plume tends to become more homogeneous (Webster *et al.* 2003). The variation of the ratio $A'/A$ depends on the evolution of the intermittency factor, as can be demonstrated by the following idealized analysis. Consider a binary signal with values 0 and 1, as an idealized model of the concentration variation in the present plume. The probability distribution of such a signal, known as the Bernoulli distribution, has a mean equal to $\gamma_c$ and a standard deviation equal to $\sqrt{\gamma_c(1-\gamma_c)}$. For $\gamma_c < 0.5$, the standard deviation of the binary random variable would always exceed its mean, in conformity with our observation in the plume. Furthermore, as the intermittency factor decreases, the mean of the binary random variable would decrease at a faster rate than its standard deviation, which is also consistent with the increasing ratio $A'/A$ along the axis of the plume, where the peak $\gamma_c$ decreased from 0.4 to 0.23 between $x_1/L = 5$ and 12.

The estimated displacements of the transverse plume axis position $\mu_2$ and $\mu_2'$ increased gradually to a few millimetres above the $x_1$ axis far downstream of the source. In view of the slight streamline displacement due to boundary layer growth on the water tunnel bottom, the uncertainty in alignment of the measurement planes at different downstream positions and the effect of finite population of samples used for calculating these values, it would be unwise to attach much significance to this observation. For this reason, we will refrain from claiming that a systematic effect of the mean shear is to displace the plume axis in the direction of the mean velocity gradient, even slightly so. It is noted that Tavoularis & Corrsin (1981), Nakamura *et al.* (1986) and Karnik & Tavoularis (1989) reported that their plume axes drifted towards the lower velocity region of their USF; all these displacements were also relatively small. The estimated displacements of the spanwise plume axis position $\mu_3$ and $\mu_3'$ were also found to reach values of a few millimetres far downstream. In conformity with the previous discussion, we will also attribute this to uncertainties and not to a systematic asymmetry in the flow.

### 4.4. *Concentration–velocity correlations*

The covariances of the concentration and the velocity components were calculated following resampling of the SPIV measurements to the same grid as the PLIF ones. Interpolated values in the velocity field were determined by cubic spline interpolation of the values at neighbouring grid points, implemented using the scientific computation package MATLAB. As the spatial resolution of the velocity field was comparable to the Kolmogorov lengthscale of the flow, velocity changes between measurement points would be relatively small, which justifies interpolation between grid points; moreover, we found that maps of the concentration–velocity covariance were insensitive to the choice of interpolation scheme.

Because of the extremely strong concentration intermittency in the current plume, all correlation coefficients of the concentration had lower magnitudes compared with those obtained in flows with more homogeneous scalar fields. Following Wilson *et al.* (1985), we defined the mean conditional concentration $\overline{C_P}$ as the average of only

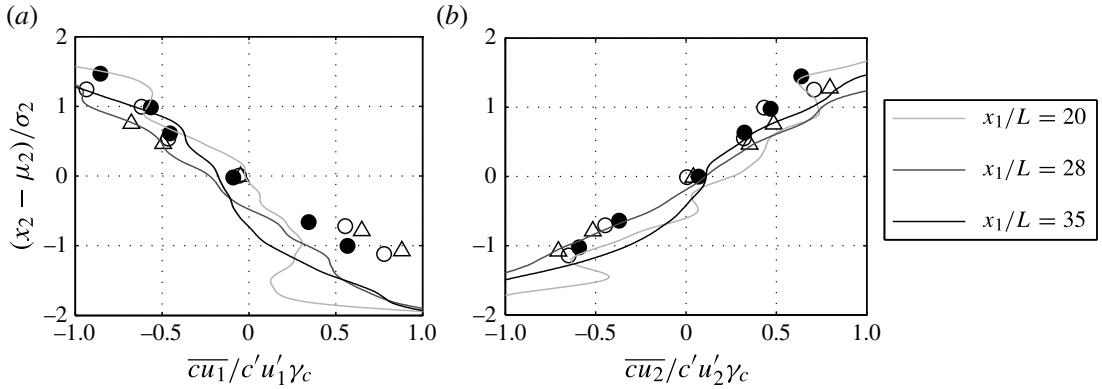


FIGURE 8. Transverse profiles of the velocity–concentration correlation coefficients corrected by the local intermittency factor $\gamma_c$, compared with corrected measurements from Karnik & Tavoularis (1989) in a thermal plume at $x_1/L=24$ (●), 48 (○), 84 (△).

non-zero values. This implies that the mean conditional concentration is related to the mean concentration as

$$\overline{C_P}=\frac{1}{\gamma_c}\overline{C}. \tag{4.4}$$

By extending this relationship to concentration fluctuations, we may estimate a conditional concentration–velocity correlation coefficient as

$$\left[\frac{\overline{cu_\alpha}}{c'u_\alpha'}\right]_P \approx \frac{1}{\gamma_c}\frac{\overline{cu_\alpha}}{c'u_\alpha'}. \tag{4.5}$$

When comparing flows with vastly different scalar intermittencies, it seems more appropriate to compare conditional rather than conventional values. Transverse profiles of the correlation coefficients $\overline{cu_\alpha}/c'u_\alpha'$, corrected by the local intermittency factor $\gamma_c$, are presented in figure 8. For $x_1/L>20$, the profiles were self-similar, and appeared to be essentially linear. Unlike conventional correlation coefficients, the conditional ones in the present plume are in good agreement with measurements in a much less intermittent thermal plume (Karnik & Tavoularis 1989), which were corrected assuming that their plume had an intermittency factor of 1 on the plume centreline, approached zero at the plume edges, and also followed a Gaussian profile. In general, $\overline{cu_1}/c'u_1'$ and $\overline{cu_2}/c'u_2'$ had opposite signs, and reversed sign near the plume axis. Lastly, we note that while the profiles of $\overline{cu_2}/c'u_2'$ were nearly symmetric, the profiles of $\overline{cu_1}/c'u_1'$ all had slightly lower magnitudes in the lower half of the plume than in the upper half; this difference is associated with the presence of counter-gradient streamwise diffusion and will be discussed in detail in § 5.5.

### 4.5. *Estimates of turbulent diffusivities*

In the present experiments, cross-sectional maps of all components of the turbulent mass flux vector $-\overline{cu_i}$ were obtained following resampling and interpolation of the SPIV measurements to the same grid as the PLIF ones. Cross-sectional maps of all components of the mean concentration gradient $\partial\overline{C}/\partial x_i$ were also independently determined by analytical differentiation of (4.2). This permitted the calculation of all nine components of the turbulent diffusivity tensor $D_{ij}$ as those values that resulted

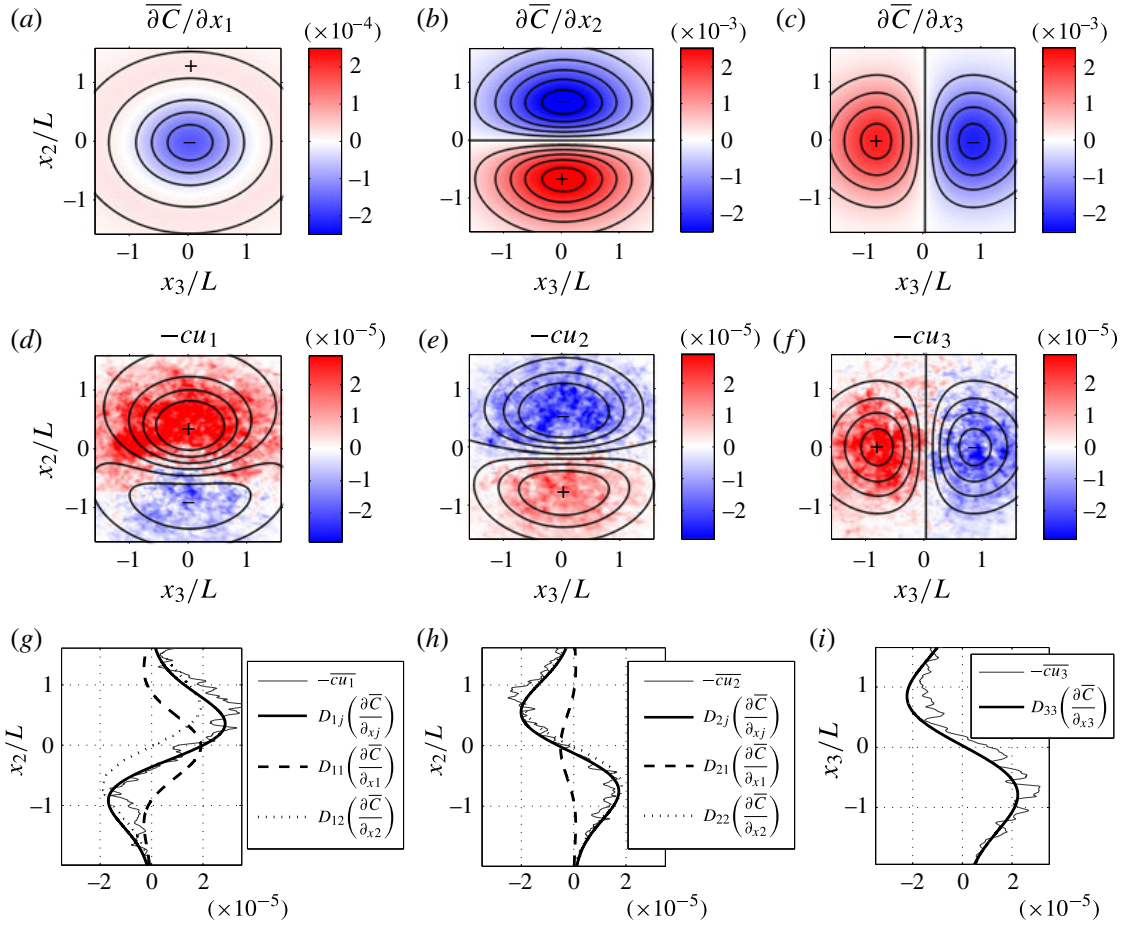


FIGURE 9. (Colour online) (*a–c*) Maps of the calculated mean concentration derivatives at $x_1/L = 28$, normalized by $C_S/L$ and (*d–f*) maps of $-\overline{cu_i}$ measurements at $x_1/L = 28$, normalized by $C_S U_c$. Black lines mark contours of the corresponding components of $D_{ij}\partial\overline{C}/\partial x_j$, also normalized by $C_S U_c$; the symbols + and − indicate regions with positive and negative values. (*g–i*) Cross-sections of the $-\overline{cu_i}$ maps with profiles of the appropriate individual terms of $D_{ij}(\partial\overline{C}/\partial x_j)$ and their sums, all normalized by $C_S U_c$.

in the best fit between the left- and right-hand sides of (1.2) over each set of corresponding maps. The cross-components $D_{13}$, $D_{23}$, $D_{31}$ and $D_{32}$ should vanish because of the symmetry of the Reynolds stress tensor and the scalar field about the $(x_1, x_3)$ plane. Moreover, preliminary calculations confirmed that the effects of these components were indeed negligible in the present flow. Consequently, these diffusivities were set to zero before calculating the other components.

Representative maps of the calculated mean scalar derivatives at $x_1/L = 28$ are presented in figure 9(*a–c*) and figure 9(*d–f*) shows representative maps of scalar flux measurements, together with contours of the corresponding components of $D_{ij}\partial\overline{C}/\partial x_j$. Figure 9(*g–i*) shows cross-sections of the scalar flux maps, together with profiles of the appropriate individual terms of $D_{ij}\partial\overline{C}/\partial x_j$ and their sums, which demonstrate that (1.2) was consistent with all measurements.

The streamwise evolution of the estimated $D_{22}$ is plotted in figure 10(*a*), whereas figure 10(*d–g*) shows the evolutions of the ratios of the remaining non-zero diffusivities and $D_{22}$. It may be seen that there is considerable uncertainty in these

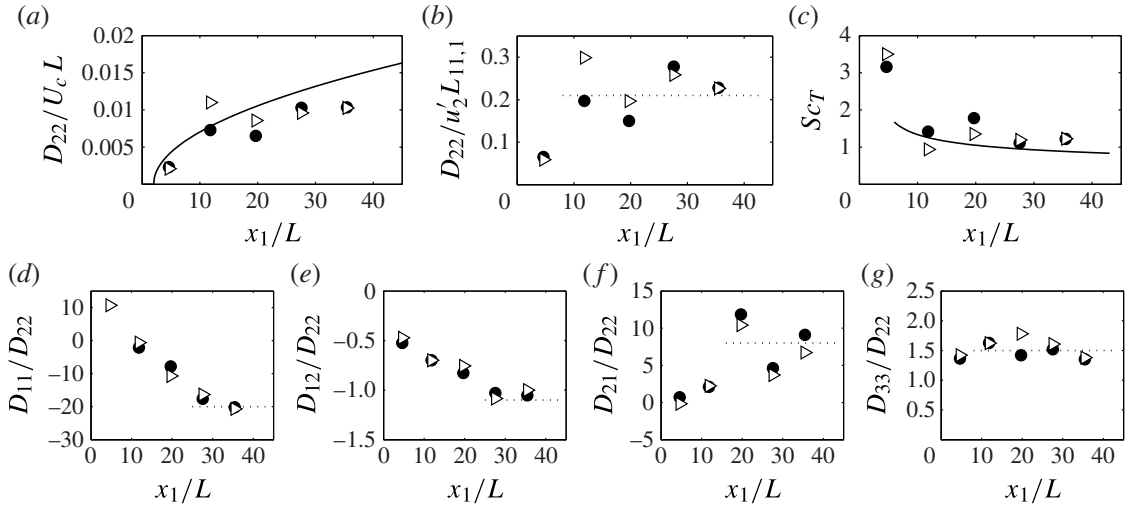


FIGURE 10. (*a*) The estimated turbulent diffusivity $D_{22}/U_cL$ (symbols) and the apparent diffusivity $K_2/U_cL$ (solid line); (*b*) $D_{22}/u_2'L_{11,1}$ (symbols) and its estimated asymptote (dotted line), with $L_{11,1} \approx L_{22,2}/0.55$; (*c*) estimates of the turbulent Schmidt number $Sc_T = \nu_T/D_{22}$ and the apparent Schmidt number $\nu_T/K_2$ (solid line); (*d–g*) ratios of the turbulent diffusivities (symbols) and their estimated asymptotes (dotted lines); ● and ▷ indicate diffusivities estimated from (1.2) and (4.6), respectively.

results, much of which is attributed to the uncertainty in the estimated streamwise scalar derivative.

Secondary estimates of the turbulent diffusivities were obtained by assuming that gradient transport also applies to third-order concentration–velocity covariances, as (Karnik & Tavoularis 1989)

$$-\overline{c^2 u_i} = D_{ij}\,\frac{\partial c'^2}{\partial x_j}, \tag{4.6}$$

and estimating maps of $\partial c'^2/\partial x_j$ by analytical differentiation of (4.3). These estimates, obtained as the best fits of maps of $-\overline{c^2 u_i}$ to sets of maps of $\partial c'^2/\partial x_j$, have also been plotted in figure 10. It can be seen that the two estimates of each diffusivity are generally close to each other, although it may be noted that the latter estimates have higher uncertainty than the former ones.

The turbulent Schmidt number $Sc_T \equiv \nu_T/D_{22}$ decreased along the plume (see figure 10*c*) and approached an asymptote of approximately 1.3 for $x_1/L \geqslant 28$. This value is somewhat larger than the value of 1.1 measured by Tavoularis & Corrsin (1981) and the conventional value near unity (Pope 2000).

The apparent diffusivities $K_2$ and $K_3$ were calculated by differentiating the power laws fitted to the corresponding half-widths, according to (2.7). This operation also provided power laws for $K_2$ and $K_3$, as, for example, $K_2/(U_cL) = 0.0025[(x_1 - x_0)/L]^{0.5}$, where, as previously, the virtual origin was set as $x_0 = 2.0L$. The apparent diffusivity ratio was $K_3/K_2 = (\sigma_3/\sigma_2)^2 = 1.56$. The evolution of the transverse apparent diffusivity $K_2/(U_cL)$, plotted in figure 10(*a*), is fairly consistent with the measured values of $D_{22}/(U_cL)$, although it tends to slightly overshoot the measurements in the far field. Similarly, the apparent Schmidt number $\nu_T/K_2$, plotted in figure 10(*c*), is consistent with the values determined using $D_{22}$. Furthermore, the ratio $K_3/K_2$ is close to

measurements of $D_{33}/D_{22}$, as shown in figure 10(*g*). These observations support the use of the apparent diffusivities $K_2$ and $K_3$ as surrogates for the turbulent diffusivities $D_{22}$ and $D_{33}$.

Taylor predicted that the turbulent diffusivity would grow to a state in which it would depend only on Lagrangian turbulence properties when $\mathscr{T} \ll t$. For a continuously released plume in steady flow, this state would be approached at a downstream distance that would be comparable to the streamwise Lagrangian integral lengthscale $\mathscr{L}_{11}$. Although we have no measurements of this lengthscale in the present flow, we can estimate it for USF as $\mathscr{L}_{11} = 2\mathscr{L}_{22}$ (Tavoularis & Corrsin 1985), where $\mathscr{L}_{22}$ is the transverse lengthscale, which in turn can be estimated as $\mathscr{L}_{22} \approx 1.3L_{22,2}/u_2'$ (Karnik & Tavoularis 1990). Using these approximations, we obtained $\mathscr{L}_{11} \approx 45L$, which is slightly higher than the current range of measurements. Nevertheless our measurements of $D_{22}/u_2'L_{11,1}$ appear to approach a constant value, in conformity with Taylor's conjecture. The value of this constant was approximately 0.21 (see figure 10*b*), which is approximately twice the value reported by Karnik & Tavoularis (1989).

When normalized by $D_{22}$, most components of the turbulent diffusivity tensor appeared to approach asymptotes far downstream of the source (figure 10*d–g*); the ratio $D_{11}/D_{22}$ (figure 10*d*) seems to be an exception, as it keeps becoming more negative with increasing downstream distance. The mean values of the ratios for $x_1/L \geqslant 28$ were

$$\frac{D_{ij}}{D_{22}} \approx \begin{bmatrix} -20 & -1.1 & 0 \\ 8 & 1.0 & 0 \\ 0 & 0 & 1.5 \end{bmatrix}. \tag{4.7}$$

The presence of non-zero cross-diffusivities and the fact that $D_{11}$, $D_{22}$ and $D_{33}$ had different values are consequences of the strong anisotropy of the turbulence in USF. The cross-diffusivities introduce effects of more than one mean scalar derivative to the each component of the scalar flux vector, a result that is also attributable to shear-generated anisotropy. One may make the following observations concerning individual scalar fluxes.

*The spanwise flux* ($-\overline{cu_3}$): This property was proportional to the spanwise mean scalar derivative. Consistent with the fact that $\overline{u_1u_3} = \overline{u_2u_3} = 0$ in USF, $D_{31} = D_{32} = 0$, so $-\overline{cu_3}$ had no contributions from the transverse and streamwise mean scalar derivatives. The ratio $D_{33}/D_{22}$ was approximately 1.5, which is sufficiently close to the values of the ratios $u_3'^2\mathscr{T}_{33}/u_2'^2\mathscr{T}_{22}$ and $K_3/K_2$ and the result reported by Tavoularis & Corrsin (1985).

*The transverse flux* ($-\overline{cu_2}$): The transverse flux had contributions from both the transverse and the streamwise mean scalar derivatives, although the contribution of the transverse derivative dominated, as illustrated in figure 9(*h*). The value of $D_{21}$ appeared to be positive, albeit within considerable uncertainty, as the term $D_{21}\partial\overline{C}/\partial x_1$ was much smaller than $D_{22}\partial\overline{C}/\partial x_2$.

*The streamwise flux* ($-\overline{cu_1}$): The streamwise flux had contributions from both the transverse and the streamwise mean scalar derivatives. As illustrated in figure 9(*g*), these contributions had, respectively, antisymmetric and symmetric profiles. The antisymmetric contribution corresponded to $D_{12}/D_{22} \approx -1.1$, which is consistent in sign but lower in magnitude than the values $-2.2$ and $-2.0$, reported, respectively, by Tavoularis & Corrsin (1981) and Karnik & Tavoularis (1989). The negative sign of $D_{12}$ is a consequence of the fact that, in USF, the

streamwise velocity fluctuations $u_1$ are negatively correlated with the transverse fluctuations $u_2$ (Tavoularis & Corrsin 1981). Because of the near symmetry of the transverse mean scalar derivative $\partial\overline{C}/\partial x_2$, its contribution to the streamwise flux was negligible along the plume axis; therefore, the non-zero values of $-cu_1$ may be attributed to the streamwise mean scalar derivative. Far downstream of the source, $-cu_1 > 0$ and $\partial\overline{C}/\partial x_1 < 0$ along the plume axis, hence $D_{11}$ was negative (i.e. counter-gradient). Although $|\partial\overline{C}/\partial x_1| \ll |\partial\overline{C}/\partial x_2|$, the term $D_{11}\partial\overline{C}/\partial x_1$ in the core of the plume was comparable in magnitude to the peak values of $D_{12}\partial\overline{C}/\partial x_2$, with the result that $D_{11}$ was an order of magnitude larger than $D_{12}$. Because $|\partial\overline{C}/\partial x_1|$ was small, the magnitude of $D_{11}$ is subject to more uncertainty than the other terms, which is why we only report the value of $D_{11}$ to one significant digit; however, the fact that estimates from both (1.2) and (4.6) are consistent attests to the accuracy of the measured diffusivities. For additional discussion concerning the complex shape of $-\overline{cu_1}$ and the negative value of $D_{11}$, see § 5.5.

## 5. Analysis of the results and discussion

### 5.1. *The plume width*

It is noted that our definition of plume width differs from those used by previous authors; Webster *et al.* (2003) defined the plume half-width as twice the standard deviation of the mean concentration profile, whereas Karnik & Tavoularis (1989) defined it as half the distance between locations with mean concentrations equal to half the peak value. Therefore, according to the present definition, the transverse half-widths of the plumes examined by Webster *et al.* and Karnik & Tavoularis would, respectively, be equal to 0.5 and 0.85 times the values reported by the corresponding authors.

The evolution of the half-widths could be fitted by power laws with an exponent of 0.75. This value is equal to the value reported by Webster *et al.*, within the range of 0.55–0.76 reported by Lepore & Mydlarski (2011), and comparable to the value 0.83 fitted by us to the data of Karnik & Tavoularis.

When comparing measurements in the present plume to those from the literature, it is also important to consider the state of growth of each plume with respect to the local size of the turbulent eddies which convect and diffuse the scalar field. The lengthscale ratio $\sigma_2/L_{22,2}$ may be chosen as a measure of relative plume growth. The streamwise evolution of this ratio in the present measurements and in the previous study by Karnik & Tavoularis (1989) is presented in figure 11. As figure 11 illustrates, our facility permitted the present plume width to grow to values that were comparable to the transverse integral lengthscale and so the entire plume may be characterized as slender. This was not the case with the plume studied by Karnik & Tavoularis (1989), which grew to measurably larger relative thicknesses.

### 5.2. *Scalar fluctuations*

All the present profiles of $c'$ (see figure 7*b*) were single-peaked, unlike some of the profiles presented by Warhaft (1984), Karnik & Tavoularis (1989), Rahman & Webster (2005), and Lepore & Mydlarski (2011), which were double-peaked. Karnik & Tavoularis attributed the presence of double peaks in the near-source profiles to the particular shape of the thermal wake of the heated ribbon used, a feature that is absent in the present experiments. The development of double peaks far downstream of the

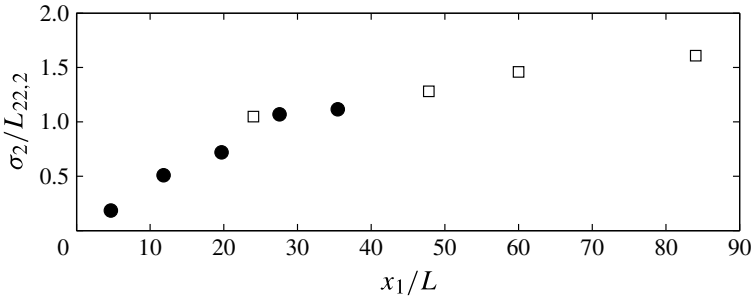


FIGURE 11. Downstream development of the ratio of the plume half-width $\sigma_2$ and the transverse turbulent integral lengthscale $L_{22,2}$: ●, present measurements; □, Karnik & Tavoularis (1989), with $L_{22,2} \approx 0.55 L_{11,1}$.

source in the previous studies was attributed to the fact that the peak production of scalar variance occurs at the inflection points of the mean concentration field, which are located on either side of the plume centreline. However, for gradient transport to be effective in producing local fluctuation peaks, the plume width must be sufficiently large with respect to the integral lengthscale of the flow. The logic behind this explanation is that, when the plume is large enough for the local scalar transport to be dominated by eddy motions that are mostly confined to the same side of the plume, scalar fluctuations would follow gradient transport and so they would peak at the two inflection points of the mean concentration gradient; on the other hand, when the plume half-width is small by comparison to the turbulent eddy mean free path, local transport would be dominated by eddy motions that sweep across much of or the entire plume and thus smooth off-axis peaks of concentration fluctuations. This argument, however, is not sufficient to explain entirely the lack of double peaks in the present plume, whose half-width grew to approximately the size of the transverse integral lengthscale. An explanation will be given in the following paragraph.

The present plume differs from the one studied by Warhaft (1984), Karnik & Tavoularis (1989), and Lepore & Mydlarski (2011) in an important aspect: the former originated from essentially a point source, whereas the latter originated from a line source and was two-dimensional on the mean. In a line-source plume, strong scalar fluctuations would be introduced mainly by transverse motions (i.e. in a direction parallel to the mean scalar gradient), whereas in a point-source plume, motions in all directions on a transverse plane may introduce strong scalar fluctuations. Therefore, if both plumes had the same ratio of $\sigma_2/L_{22,2}$, the two-dimensional plume would have a stronger tendency to be double-peaked. One may then speculate that, for a double-peak $c'$ to be manifested in a point-source plume, $\sigma_2/L_{22,2}$ would have to be much larger than its double-peaking threshold for a line-source plume. The present plume was clearly far from meeting this condition, which explains the observed single-peak pattern.

### 5.3. *Estimates of advection and diffusion*

In this section, we investigate the terms in the Reynolds-averaged advection–diffusion equation (1.1). The advection term in (1.1), which in USF is simplified to $\overline{U_1}\partial\overline{C}/\partial x_1$, was calculated by multiplying the local mean velocity by the mean streamwise concentration derivative, estimated by analytical differentiation of (4.2). The molecular

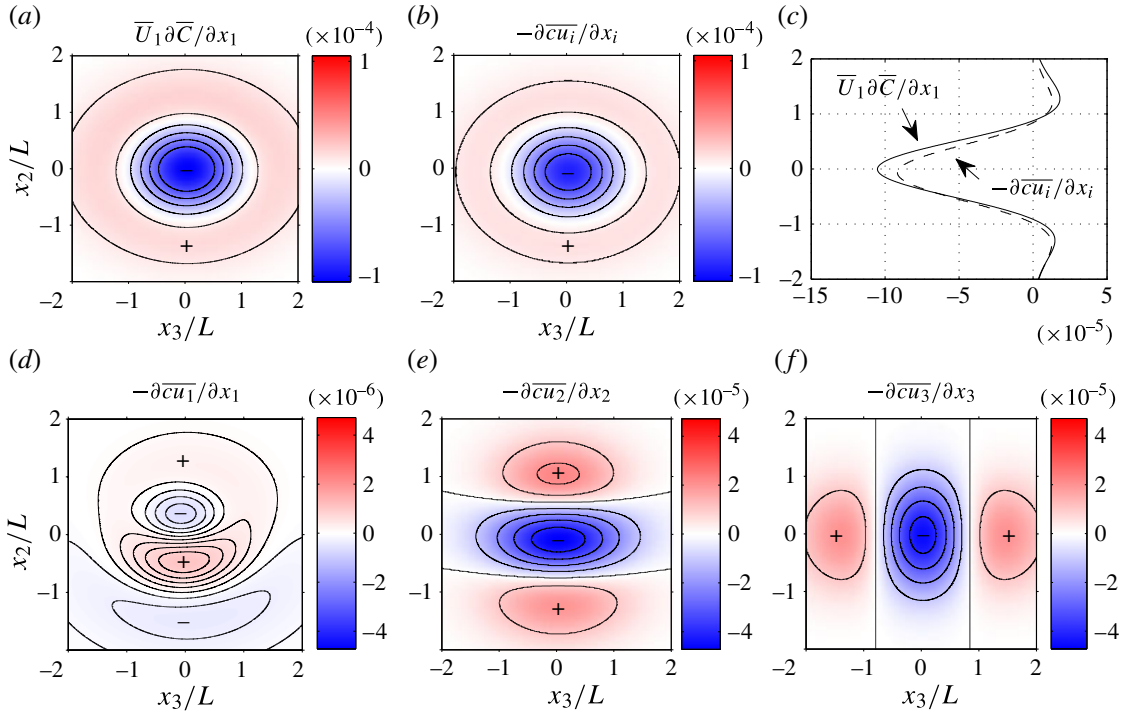


FIGURE 12. (Colour online) (*a*) Maps of the advective flux; (*b*) maps of the net diffusive flux in (1.1); (*c*) transverse profiles of the advective and net diffusive fluxes at $x_3 = 0$; (*d–f*) maps of the individual diffusive flux terms. All results were at $x_1/L = 28$; all fluxes were normalized by $C_S U_c/L$ and the symbols + and − indicate map regions with positive and negative values, respectively.

diffusion term was negligible, as the molecular diffusivity was several orders of magnitude smaller than the main turbulent diffusivity. To estimate the three turbulent diffusion terms, we first created smooth maps of $-\overline{cu_1}$, $-\overline{cu_2}$ and $-\overline{cu_3}$ using (4.2) and (1.2) and the estimated turbulent diffusivities. The streamwise diffusive flux term $-\partial\overline{cu_1}/\partial x_1$ was then determined by applying first-order central differencing to data from five measurement planes. The in-plane diffusive flux terms $-\partial\overline{cu_2}/\partial x_2$ and $-\partial\overline{cu_3}/\partial x_3$ were determined using second-order central differencing. Maps of the advection term, the three diffusive flux terms, and the net (total) diffusion term are presented in figure 12.

The estimated maps of the advection and net diffusion terms, which should ideally balance each other, are in fairly good agreement; this attests to the accuracy of our results. The net diffusion term appears to have somewhat smaller magnitude than the advection term (see figure 12*c*); this difference may be largely attributed to the uncertainty in the streamwise derivative of the mean concentration. The magnitude of this discrepancy was comparable to the one in a turbulent jet (Fukushima, Aanen & Westerweel 2000), which was also attributed to insufficient spatial resolution.

Comparing the maps of the three diffusive flux terms (figure 12*d–f*), it is evident that the spanwise term was essentially symmetric; the transverse term was slightly asymmetric, as a result of the non-zero value of $D_{21}$; the streamwise term was strongly asymmetric, in conformity with the complex shape of $-\overline{cu_1}$. The transverse and spanwise diffusive fluxes were nearly equal around the plume axis, but each became dominant off-axis, in regions in which the corresponding mean concentration

| Tavoularis & Corrsin (1985) | Rogers *et al.* (1989) |
|---|---|
| $D_{11} = \overline{u_1^2}\ \mathscr{T}_{11} + \dfrac{\mathrm{d}\overline{U_1}}{\mathrm{d}x_2}\ \overline{u_1u_2}\ \mathscr{T}_{12}^2$ | $D_{11} = \overline{u_1^2}\ \mathscr{T} - \dfrac{\mathrm{d}\overline{U_1}}{\mathrm{d}x_2}\ \overline{u_1u_2}\ \mathscr{T}^2$ |
| $D_{12} = \overline{u_1u_2}\ \mathscr{T}_{12}$ | $D_{12} = \overline{u_1u_2}\ \mathscr{T} - \dfrac{\mathrm{d}\overline{U_1}}{\mathrm{d}x_2}\ \overline{u_2^2}\ \mathscr{T}^2$ |
| $D_{21} = \overline{u_1u_2}\ \mathscr{T}_{21} + \dfrac{\mathrm{d}\overline{U_1}}{\mathrm{d}x_2}\ \overline{u_2^2}\ \mathscr{T}_{22}^2$ | $D_{21} = \overline{u_1u_2}\ \mathscr{T}$ |
| $D_{22} = \overline{u_2^2}\ \mathscr{T}_{22}$ | $D_{22} = \overline{u_2^2}\ \mathscr{T}$ |
| $D_{33} = \overline{u_3^2}\ \mathscr{T}_{33}$ | $D_{33} = \overline{u_3^2}\ \mathscr{T}$ |

Younis *et al.* (2005)

$$D_{11} = \overline{u_1^2}\left(C_2\frac{k}{\epsilon}\right) + \frac{\mathrm{d}\overline{U_1}}{\mathrm{d}x_2}\ \overline{u_1u_2}\left(2C_4\frac{k^2}{\epsilon^2}\right) + C_1\frac{k^2}{\epsilon}$$

$$D_{12} = \overline{u_1u_2}\left(C_2\frac{k}{\epsilon}\right) + \frac{\mathrm{d}\overline{U_1}}{\mathrm{d}x_2}\ \overline{u_2^2}\left(C_4\frac{k^2}{\epsilon^2}\right) + C_3\frac{k^3}{\epsilon^2}\frac{\mathrm{d}\overline{U_1}}{\mathrm{d}x_2}\overline{u_2^2}$$

$$D_{21} = \overline{u_1u_2}\left(C_2\frac{k}{\epsilon}\right) + \frac{\mathrm{d}\overline{U_1}}{\mathrm{d}x_2}\ \overline{u_2^2}\left(C_4\frac{k^2}{\epsilon^2}\right)$$

$$D_{22} = \overline{u_2^2}\left(C_2\frac{k}{\epsilon}\right) + C_1\frac{k^2}{\epsilon}$$

$$D_{33} = \overline{u_3^2}\left(C_2\frac{k}{\epsilon}\right) + C_1\frac{k^2}{\epsilon}$$

TABLE 3. Theoretical models of the turbulent diffusivities.

derivative was dominant. The streamwise diffusive flux was consistently an order of magnitude smaller than the other two and made a very small contribution (less than 5 %) to the net diffusion. This provides justification for disregarding streamwise diffusion in simplified models, even though the streamwise diffusivity $D_{11}$ is much larger than the two other normal diffusivities.

### 5.4. *Comparison of diffusivities to theoretical estimates*

Analytical models of the turbulent diffusivity tensor relevant to USF have been developed by Tavoularis & Corrsin (1985), Rogers *et al.* (1989), and Younis *et al.* (2005), to be referred to as TC, RMR and YSC, respectively. The corresponding expressions are summarized in table 3, whereas ratios of the predicted diffusivity values are compared to the present results in table 4. All models assumed that $D_{31} = D_{13} = D_{32} = D_{23} = 0$ by symmetry of the Reynolds stress tensor about the $(x_1, x_3)$ plane.

The TC model contains the Lagrangian integral timescales $\mathscr{T}_{11}$ etc. We have no measurements of these timescales in the present flow, but we used the estimates $\mathscr{T}_{22} \approx 1.3L_{22,2}/u_2'$ (Karnik & Tavoularis 1990) and $\mathscr{T}_{12} = \mathscr{T}_{21} = 4\mathscr{T}_{22}$, $\mathscr{T}_{11} = 2\mathscr{T}_{22}$, and $\mathscr{T}_{33} = \mathscr{T}_{22}$ (TC), all applicable to USF. The RMR model is very similar to the TC model; however, the former contains a constant timescale $\mathscr{T} = 2k/(C_D\epsilon)$, in which $C_D = 12.6$ for the present conditions ($C_D$ is specified by RMR as a function mainly of a Reynolds number and, weakly, of the Prandtl number). The YSC model is more

| | TC | RMR | YSC | Present |
|---|---|---|---|---|
| $D_{22}/D_{22m}$ | 3.2 | 2.3 | 3.8 | 1 |
| $D_{11}/D_{22}$ | −10.0 | 2.8 | 3.4 | −20 |
| $D_{33}/D_{22}$ | 1.6 | 1.6 | 1.9 | 1.5 |
| $D_{12}/D_{22}$ | −2.0 | −1.9 | −1.8 | −1.1 |
| $D_{21}/D_{22}$ | 0.0 | −0.5 | −1.5 | 8 |

TABLE 4. Theoretical estimates of the turbulent diffusivity ratios; $D_{22m}$ indicates the measured $D_{22}$.

complex than either of the other two models, expressing the diffusivities in terms of relationships that contain four adjustable coefficients, for which YSC recommend values.

All models predicted values of $D_{22}$ which were more than double the measured value; moreover, they all predicted values of the ratio $D_{33}/D_{22}$ that were close to the experimental one. The TC prediction of $D_{11}/D_{22}$ agreed in sign with the measured ratio although it was smaller in magnitude, whereas the two other models missed this ratio not only in magnitude, but in sign as well. All models predicted $D_{12}/D_{22}$ that had the same sign as the measured value but were more than twice as large; in this respect, the models are in fair agreement with the measurements of Tavoularis & Corrsin (1981) and Karnik & Tavoularis (1989) who found $D_{12}/D_{22}$ was −2.2 and −2.0, respectively. The RMR and YSC models predicted a negative value of $D_{21}/D_{22}$, whereas the TC model predicted a value of zero; in this respect, all models differ from the present measurements of $D_{21}/D_{22}$, which tended to be positive.

Overall, all models had comparable performances, with the notable exception that the TC model was the only one to predict correctly the sign of $D_{11}$. None of the models predicted accurately the magnitudes of the diffusivities, but predictions and measurements were of the same order of magnitude. It is noted that all models were developed and calibrated for air flows, in which the Prandtl/Schmidt numbers were of order-one, whereas the scalar field in the present experiments had a very high Schmidt number.

### 5.5. *The streamwise turbulent mass flux and the streamwise turbulent diffusivities*

The map of $-\overline{cu_1}$ (figure 9*d*) appears to be oddly complex and invites some in-depth physical scrutiny. For simplicity, let us consider the transverse profile of $-\overline{cu_1}$, shown in figure 9(*g*). We shall explain its shape by the following qualitative discussion, which makes use of gradient-transport-type arguments, but also takes into consideration the turbulence structure of USF.

If this profile were entirely the result of transverse gradient transport, it would have been antisymmetric about the plume axis. In the lower half of the plume, where $\partial\overline{C}/\partial x_2 > 0$, $c$ and $u_2$ would tend to be negatively correlated; however, in this USF, $u_2$ and $u_1$ are also negatively correlated, which implies that $c$ and $u_1$ would be positively correlated. A corresponding argument can be made for the upper half of the plume to show that $c$ and $u_1$ would be negatively correlated in this region. Using a similar argument, Tavoularis & Corrsin (1981) explained the observed sign of $\overline{cu_1}$ in USF with a uniform mean scalar gradient. This argument explains why $D_{12}$ in shear flows would have the same sign as $\overline{u_1u_2}$.

The previous argument is not sufficient to explain the variation of $-\overline{cu_1}$, because its profile is obviously not antisymmetric. Nevertheless, $-\overline{cu_1}$ can be represented

quite well by the sum of an antisymmetric part and a symmetric part. We will argue that the symmetric part may be attributed to the streamwise variation of the mean concentration and the plume growth. The supporting arguments can be best presented by considering the region near the plume axis, where the symmetric part is strongest and the antisymmetric part is weak. In this region, $\partial\overline{C}/\partial x_1 < 0$ and conventional gradient transport with a positive diffusivity $D_{11}$ would imply that $-\overline{cu_1} < 0$ as well. This is not the case, however, because the symmetric part of $-\overline{cu_1}$ is strongly positive around the plume axis, thus necessitating the use of a negative $D_{11}$. This amounts to counter-gradient transport and requires further examination.

It was mentioned previously that the present plume half-width was comparable to the transverse turbulent lengthscale $L_{22,2}$, which means that the plume was subject to strong meandering so that fluid parcels from the edges of and outside the plume would often cross its axis. The value of $-\overline{cu_1}$ would be dominated by the contributions of events having simultaneously large fluctuations of $u_1$ and large fluctuations of $c$. Large negative fluctuations of $c$ would occur if an eddy originating at the plume edge or beyond approached the plume axis, as such an eddy would transport a concentration that would be much lower than the mean near the axis. For an eddy from the edges of the plume to penetrate to the axis, it must have a strong velocity $u_2$. In USF, such eddies would typically also have strong $u_1$ with a sign opposite to that of $u_2$. Eddies from the upper edge would have $u_2 < 0$ and $u_1 > 0$, i.e. they would originate upstream of the measurement plane. On the contrary, eddies from the lower edge would have $u_2 > 0$ and $u_1 < 0$, i.e. they would originate downstream of the measurement plane. So, eddies with large $c < 0$ would sometimes be associated with $u_1 > 0$ and other times with $u_1 < 0$. How would then a net positive $-\overline{cu_1}$ be produced near the axis?

We will now demonstrate that the positive $-\overline{cu_1}$ near the plume axis is the result of plume growth in size with streamwise distance from the origin, namely the result of transverse turbulent diffusion itself. In the plume core, $\partial\overline{C}/\partial x_1 < 0$, because the peak mean concentration decays downstream; on the contrary, $\partial\overline{C}/\partial x_1 > 0$ near the edges, because the plume spreads outwards. Consequently, upstream eddies crossing the measurement plane would transport negative $c$ with a magnitude that is larger than that of downstream eddies, which also transport negative $c$; thus, the net effect of mixing would be $-\overline{cu_1} > 0$. This explains why $D_{11}$ was negative and transport was counter-gradient with respect to the gradient around the plume axis. This apparent paradox may, however, be resolved by a change of perspective: mass was actually flowing along the gradient, if one considers the gradient where it matters for $-\overline{cu_1}$, namely at the plume edges.

In the previous discussion, we invoked the fact that $u_1$ and $u_2$ are strongly correlated. In USF, this means that strong downward-bound eddies typically come from upstream and strong upward-bound eddies come from downstream, namely that the two types of eddies transport fluid from opposite edges of the plume. However, because the plume is symmetric, it makes no difference to the value of $c$ whether it comes from the upper edge or the lower one. Consequently, counter-gradient streamwise transport does not require the net Reynolds stress to be non-zero, but only that eddies with strong fluctuations in $u_1$ also have strong $u_2$, which allows them to originate outside of the plume. In other words, mean shear is not necessary for counter-gradient transport to arise, but it helps, as it organizes the motion and generates strong coherent structures, which in the case of USF are horseshoe-shaped vortices (Vanderwel & Tavoularis 2011).

We have so far focused on diffusion in the transverse direction, but there is also spanwise diffusion. In fact, Vanderwel & Tavoularis (2011) demonstrated that coherent

structures in USF are not always aligned with the transverse direction, but appear with a wide range of orientations. In the case of the present plume, strong eddies with significant spanwise velocity would still transport low-concentration fluid from the plume edges and beyond, and so they would contribute to counter-gradient transport. On the other hand, spanwise motions in two-dimensional plumes, such as those generated by a heated wire, would not encounter edges and so the range of motions that would contribute to counter-gradient transport would be severely restricted. This may explain why the transverse profiles of $-\overline{cu_1}$ measured by Karnik & Tavoularis (1987) were essentially antisymmetric and free of streamwise diffusion effects.

The scalar used here has a Schmidt number which is more than three orders of magnitude larger than the Prandtl number of air in heated-flow experiments, so it seems worthwhile to question whether this difference would play a significant role in counter-gradient transport. Molecular diffusion would reduce the contrast of concentration maps and lower concentration peaks, and so it would tend to reduce differences between concentration values in the core and the edges of the plume. Nevertheless, such effects would be present in both conventional and counter-gradient diffusion. In the absence of evidence for the opposite, one may speculate that counter-gradient diffusion is not subjected to strong Schmidt/Prandtl number effects.

To speculate whether a negative $D_{11}$ would also appear in a plume in another flow configuration, one would need to consider whether the plume width would satisfy the following conditions: first it should be sufficiently narrow in all directions by comparison to the lengthscale of the energy-containing eddies and second it should grow sufficiently fast downstream. For example, in the case of a turbulent jet transporting a scalar in its entirety, the first condition would not be satisfied and so jets with $-\overline{cu_1} > 0$ have not been reported (Fukushima *et al.* 2000; Webster, Roberts & Ra'ad 2001). We have reviewed the available literature in search of previous references to counter-gradient streamwise diffusion, but could not find any. There are, however, several references dealing with counter-gradient diffusion in the transverse direction, with which the mean scalar gradient was nearly aligned. Such phenomena have been observed in atmospheric flows (Deardorff 1966; van Dop & Verver 2001; de Roode *et al.* 2004) as well as in the laboratory (Sreenivasan *et al.* 1982; Veeravalli & Warhaft 1990; Paranthoën *et al.* 2004) and in most cases the discrepancy has been attributed to inhomogeneity.

## 6. Summary

Simultaneous concentration and velocity maps in the plume of a continuous point source in uniformly sheared turbulence have been measured. Gradient transport analysis with a turbulent diffusivity tensor described well the relationship between the measured turbulent mass flux vector and the mean concentration gradient. For the first time, all non-vanishing components of the turbulent diffusivity tensor were determined simultaneously from experimental results. The apparent diffusivities followed the same trends as the corresponding normal diffusivities on a transverse plane. Sufficiently downstream of the source, the various components of the turbulent diffusivity tensor grew at the same rates with distance from the source. Counter-gradient streamwise diffusion was reported for the first time and was attributed to the meandering and streamwise spread of the plume. Three previous theoretical models of turbulent diffusion in shear flows had some qualitative agreement with the present results, especially the model of Tavoularis & Corrsin (1985), which also predicted counter-gradient streamwise diffusion.

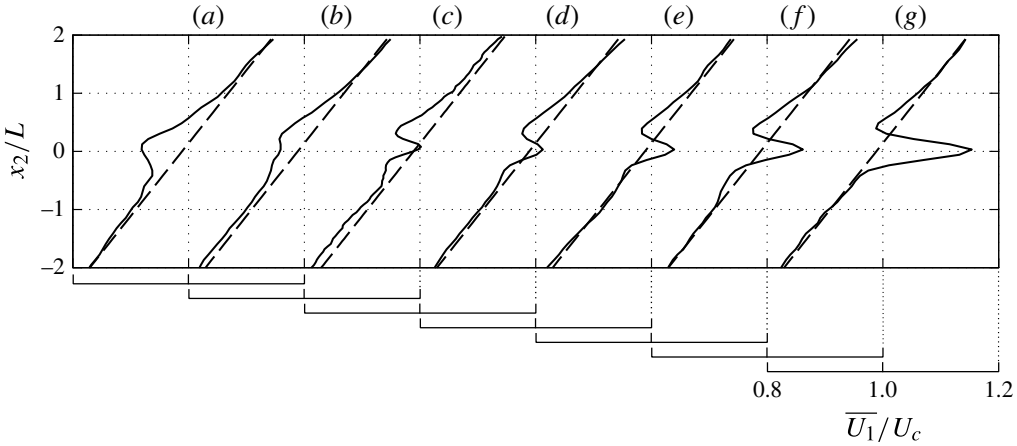


FIGURE 13. Solid lines are transverse profiles of the mean streamwise velocity at $x_1/L = 5$ and $x_3 = 0$ with injector flow rates of (*a*) 0, (*b*) 0.78, (*c*) 0.97, (*d*) 1.07, (*e*) 1.25, (*f*) 1.37, and (*g*) 1.68 ml s$^{-1}$. Dashed lines represent velocity profiles without the injector. The flow rate chosen for the present experiments was $Q = 0.97$ ml s$^{-1}$.

**Acknowledgement**

Financial support by the Natural Sciences and Engineering Research Council of Canada (NSERC) is gratefully acknowledged.

**Appendix. Determining the optimal flow rate**

The optimal flow rate through the injector was determined by comparing the velocity maps for different injection flow rates in a plane normal to the flow at a distance of $x_1/L = 5$ from the injector tip; this distance is equal to approximately 70 inner tube diameters. As representative of these velocity maps, we present transverse profiles of the mean velocity in figure 13. The physical presence of the injection tube created a region of relative velocity deficit due to the boundary layer that grew along the tube. At the same time, injection at a velocity higher than the local value created a local momentum surplus within the injected fluid. Our objective was to adjust the injection flow rate so that the momentum surplus of the jet would compensate, as much as possible, for the momentum deficit around the injector, without introducing significant jet effects which would distort the structure of the USF. The value $Q = 0.97$ ml s$^{-1}$, represented by curve (*c*) in figure 13, was deemed to be the optimal one and was used for all reported results.

REFERENCES

ADRIAN, R. J. & WESTERWEEL, J. 2011 *Particle Image Velocimetry*. Cambridge University Press.

ANAND, M. S. & POPE, S. B. 1985 Diffusion behind a line source in grid turbulence. In *Turbulent Shear Flows 4* (ed. L. J. Bradbury, F. Durst, B. E. Launder, F. W. Schmidt & J. H. Whitelaw), pp. 46–61. Springer.

ARYA, S. P. 1999 *Air Pollution Meteorology and Dispersion*. Oxford University Press.

BATCHELOR, G. K. 1949 Diffusion in a field of homogeneous turbulence. I. Eulerian analysis. *Austral. J. Chem.* **2** (4), 437–450.

BORG, A., BOLINDER, J. & FUCHS, L. 2001 Simultaneous velocity and concentration measurements in the near field of a turbulent low-pressure jet by digital particle image velocimetry–planar laser-induced fluorescence. *Exp. Fluids* **31** (2), 140–152.

CHANG, K.-A. & COWEN, E. A. 2002 Turbulent Prandtl number in neutrally buoyant turbulent round jet. *J. Engng Mech. ASCE* **128** (10), 1082–1087.

CORRSIN, S. 1975 Limitations of gradient transport models in random walks and in turbulence. *Adv. Geophys.* **18** (Part A), 25–60.

CSANADY, G. T. 1963 Turbulent diffusion in Lake Huron. *J. Fluid Mech.* **17** (3), 360–384.

DEARDORFF, J. W. 1966 The counter-gradient heat flux in the lower atmosphere and in the laboratory. *J. Atmos. Sci.* **23**, 503–506.

VAN DOP, H. & VERVER, G. 2001 Countergradient transport revisited. *J. Atmos. Sci.* **58** (15), 2240–2247.

FUKUSHIMA, C., AANEN, L. & WESTERWEEL, J. 2000 Investigation of the mixing process in an axisymmetric turbulent jet using PIV and LIF. In *Laser Techniques for Fluid Mechanics* (ed. R. J. Adrian, D. F. G. Durao, M. V. Heitor, M. Maeda, C. Tropea & J. H. Whitelaw), pp. 339–356. Springer.

GENDRON, P. O., AVALTRONI, F. & WILKINSON, K. J. 2008 Diffusion coefficients of several rhodamine derivatives as determined by pulsed field gradient–nuclear magnetic resonance and fluorescence correlation spectroscopy. *J. Fluorescence* **18** (6), 1093–1101.

HAY, J. S. & PASQUILL, F. 1959 Diffusion from a continuous source in relation to the spectrum and scale of turbulence. *Adv. Geophys.* **6**, 345–365.

KARNIK, U. & TAVOULARIS, S. 1987 Generation and manipulation of uniform shear with the use of screens. *Exp. Fluids* **5**, 247–254.

KARNIK, U. & TAVOULARIS, S. 1989 Measurements of heat diffusion from a continuous line source in a uniformly sheared turbulent flow. *J. Fluid Mech.* **202**, 233–261.

KARNIK, U. & TAVOULARIS, S. 1990 Lagrangian correlations and scales in uniformly sheared turbulence. *Phys. Fluids* A **2** (4), 587–591.

LEMOINE, F., WOLFF, M. & LEBOUCHE, M. 1996 Simultaneous concentration and velocity measurements using combined laser-induced fluorescence and laser Doppler velocimetry: application to turbulent transport. *Exp. Fluids* **20** (5), 319–327.

LEPORE, J. & MYDLARSKI, L. 2011 Lateral dispersion from a concentrated line source in turbulent channel flow. *J. Fluid Mech.* **678**, 417–450.

NAKAMURA, I., SAKAI, Y., MIYATA, M. & TSUNODA, H. 1986 Diffusion of matter from a continuous point source in uniform mean shear flows (1st report). *Bull. JSME* **29** (250), 1141–1148.

O'NEILL, P. L., NICOLAIDES, D., HONNERY, D. & SORIA, J. 2004 Autocorrelation functions and the determination of integral length with reference to experimental and numerical data. In *Proceedings of the Fifteenth Australasian Fluid Mechanics Conference. The University of Sydney, Australia, 13–17 December 2004*.

PARANTHOËN, P., GODARD, G., WEISS, F. & GONZALEZ, M. 2004 Counter gradient diffusion vs 'counter diffusion' temperature profile? *Intl J. Heat Mass Transfer* **47** (4), 819–825.

POPE, S. 2000 *Turbulent Flows*. Cambridge University Press.

PRASAD, A. K. & JENSEN, K. 1995 Scheimpflug stereocamera for particle image velocimetry in liquid flows. *Appl. Opt.* **34** (30), 7092–7099.

RAHMAN, S. & WEBSTER, D. R. 2005 The effect of bed roughness on scalar fluctuations in turbulent boundary layers. *Exp. Fluids* **38** (3), 372–384.

RILEY, J. J. & CORRSIN, S. 1974 The relation of turbulent diffusivities to Lagrangian velocity statistics for the simplest shear flow. *J. Geophys. Res.* **79** (12), 1768–1771.

ROBERTS, O. F. T. 1923 The theoretical scattering of smoke in a turbulent atmosphere. *Proc. R. Soc. Lond.* A **104** (728), 640–654.

ROBERTS, P. J. W. & WEBSTER, D. R. 2002 Turbulent diffusion. In *Environmental Fluid Mechanics: Theories and Applications* (ed. H. Shen), pp. 7–45. American Society of Civil Engineers.

ROGERS, M. M., MANSOUR, N. N. & REYNOLDS, W. C. 1989 An algebraic model for the turbulent flux of a passive scalar. *J. Fluid Mech.* **203** (1), 77–101.

DE ROODE, S. R., JONKER, H. J. J., DUYNKERKE, P. G. & STEVENS, B. 2004 Countergradient fluxes of conserved variables in the clear convective and stratocumulus-topped boundary layer: the role of the entrainment flux. *Boundary-Layer Meteorol.* **112** (1), 179–196.

DE SOUZA, F. A., NGUYEN, V. D. & TAVOULARIS, S. 1995 The structure of highly sheared turbulence. *J. Fluid Mech.* **303**, 155–167.

SREENIVASAN, K. R., TAVOULARIS, S. & CORRSIN, S. 1982 A test of gradient transport and its generalizations. In *Turbulent Shear Flows 3* (ed. L. J. S. Bradbury, F. Durst, B. E. Launder, F. W. Schmidt & J. H. Whitelaw), pp. 96–112. Springer.

STAPOUNTZIS, H., SAWFORD, B. L., HUNT, J. C. R. & BRITTER, R. E. 1986 Structure of the temperature field downwind of a line source in grid turbulence. *J. Fluid Mech.* **165**, 401–424.

SUTTON, O. G. 1932 A theory of eddy diffusion in the atmosphere. *Proc. R. Soc. Lond.* A **135** (826), 143–165.

TAVOULARIS, S. & CORRSIN, S. 1981 Experiments in nearly homogeneous turbulent shear flow with a uniform mean temperature gradient. Part 1. *J. Fluid Mech.* **104**, 311–347.

TAVOULARIS, S. & CORRSIN, S. 1985 Effects of shear on the turbulent diffusivity tensor. *Intl J. Heat Mass Transfer* **28** (1), 265–276.

TAYLOR, G. I. 1921 Diffusion by continuous movements. *Proc. Lond. Math. Soc.* **20** (2), 196–211.

VANDERWEL, C. & TAVOULARIS, S. 2011 Coherent structures in uniformly sheared turbulent flow. *J. Fluid Mech.* **689**, 434–464.

VANDERWEL, C. & TAVOULARIS, S. 2014*a* On the accuracy of PLIF measurements in slender plumes. *Exp. Fluids* (in press).

VANDERWEL, C. & TAVOULARIS, S. 2014*b* Relative dispersion of a passive scalar plume in turbulent shear flow. *Phys. Rev.* E **89** (4), 041005(R).

VEERAVALLI, S. & WARHAFT, Z. 1990 Thermal dispersion from a line source in the shearless turbulence mixing layer. *J. Fluid Mech.* **216**, 35–70.

WARHAFT, Z. 1984 The interference of thermal fields from line sources in grid turbulence. *J. Fluid Mech.* **144**, 363–387.

WEBSTER, D. R., RAHMAN, S. & DASI, L. P. 2003 Laser-induced fluorescence measurements of a turbulent plume. *J. Engng Mech. ASCE* **129**, 1130–1137.

WEBSTER, D. R., ROBERTS, P. J. W. & RA'AD, L. 2001 Simultaneous DPTV/PLIF measurements of a turbulent jet. *Exp. Fluids* **30**, 65–72.

WILSON, D. J., ROBINS, A. G. & FACKRELL, J. E. 1985 Intermittency and conditionally-averaged concentration fluctuation statistics in plumes. *Atmos. Environ.* **19** (7), 1053–1064.

WÜRTH, C., GONZÁLEZ, M. G., NIESSNER, R., PANNE, U., HAISCH, C. & GENGER, U. R. 2012 Determination of the absolute fluorescence quantum yield of Rhodamine 6G with optical and photoacoustic methods – providing the basis for fluorescence quantum yield standards. *Talanta* **90**, 30–37.

YOUNIS, B. A., SPEZIALE, C. G. & CLARK, T. T. 2005 A rational model for the turbulent scalar fluxes. *Proc. R. Soc. Lond.* A **461**, 575–594.

# Chapter 6

## Relative dispersion of a passive scalar plume in turbulent shear flow

This chapter reproduces the article

> Vanderwel, C. and Tavoularis, S. (2014), "Relative Dispersion of a Passive Scalar Plume in Turbulent Shear Flow", Phys. Rev. E 89, 041005(R),

which addresses the relative dispersion of a dye plume in USF. Relative dispersion of the passive scalar is examined in a reference frame relative to its centre-of-mass, which makes the process free of the effects of large-scale transport but preserves the effects of small-scale turbulence. The present experiments are concerned with the relative dispersion in the inertial subrange of turbulent motions. Mean relative concentration maps in cross-sections normal to the flow were determined by ensemble-averaging instantaneous concentration maps measured by means of planar laser-induced fluorescence, each shifted to a common centre of mass. The distance-neighbour functions were also determined and their shapes were compared with the analytical expressions by Richardson and by Batchelor. The mean square separation $r^2(t)$ of fluid particles was measured as the variance of the distance-neighbour function and, equivalently, as twice the second central moment of the mean relative concentration map. The streamwise evolution of $r^2(t)$ was compared with Batchelor regime scaling (${x_1}^2$) and Richardson-Obukhov regime scaling (${x_1}^3$), which are expected to prevail in the inertial range.

PHYSICAL REVIEW E **89**, 041005(R) (2014)

# Relative dispersion of a passive scalar plume in turbulent shear flow

Christina Vanderwel and Stavros Tavoularis
*Department of Mechanical Engineering, University of Ottawa, Ottawa, Ontario, Canada K1N 6N5*
(Received 23 February 2014; published 24 April 2014)

Relative dispersion of a passive scalar plume was investigated in uniformly sheared, nearly homogeneous, turbulent flow with $\mathrm{Re}_\lambda \approx 150$ using planar laser-induced fluorescence. Mean concentration maps were determined both in the laboratory frame and in a frame attached to the instantaneous center of mass of the plume cross section. The distance-neighbor function had a shape that was compatible with Richardson's expression. The mean square particle separation, two estimates of which were found to be nearly identical, had a streamwise evolution that was consistent with Richardson-Obukhov scaling with a Richardson's constant of $g = 0.35$. Batchelor scaling was also consistent with a wide range of the results.

DOI: 10.1103/PhysRevE.89.041005 PACS number(s): 47.27.tb, 47.27.Gs

Relative dispersion is concerned with the temporal evolution of the separation distance $r(t)$ of a pair of fluid particles in turbulent flows. The concept of relative dispersion was introduced by Richardson [1], who in 1926 proposed his famed four-thirds law. In this Rapid Communication, we focus on relative dispersion in the inertial subrange of turbulent motions, namely, for $\eta \ll r \ll L_{11,1}$, where $\eta$ is the Kolmogorov microscale and $L_{11,1}$ is the integral length scale of the turbulence. Within this range, relative dispersion would be dominated by eddies with sizes comparable to $r$, and the variance $\langle r^2(t)\rangle$ of separations of a large number of particle pairs can be estimated as [2]

$$\langle r^2(t)\rangle - r_0^2 = \begin{cases} \frac{11}{3} C_2 (\langle\epsilon\rangle r_0)^{2/3} t^2 & \text{for } t \ll t_B \\ g\langle\epsilon\rangle t^3 & \text{for } t_B \ll t \ll T_L. \end{cases} \quad (1)$$

In these expressions, $r_0$ is the initial pair separation, $C_2$ is the Kolmogorov constant [3,4], $\langle\epsilon\rangle$ is the mean dissipation rate, $t_B = (r_0^2/\langle\epsilon\rangle)^{1/3}$ is the Batchelor time scale, $g$ is the Richardson constant, and $T_L$ is the Lagrangian integral time scale. The range $t \ll t_B$ is known as the Batchelor regime, whereas the term Richardson-Obukhov regime signifies the range $t_B \ll t \ll T_L$. Theoretical estimates of Richardson's constant span the wide range $0.06 < g < 3.52$ [5], whereas recent experimental and numerical estimates have narrowed it down to the range $0.5 < g < 0.6$ [2].

Particle separations have been measured directly with the use of particle tracking methods [2,4,6–8]. Alternatively, mean particle separation can also be estimated from measurements of concentration in a diffusing cloud of particles relative to its center of mass [5,9–11]. A property of interest in such studies is the distance-neighbor function $q(s)$, defined as the probability density function (pdf) of the distance $s$ between particle pairs within the cloud [1,5]. $q(s)$ can be estimated as the marginal pdf of the ensemble-averaged autocorrelations of instantaneous concentration maps [12]. In the Richardson-Obukhov regime, theoretical predictions have led to the relationship $q(s) \propto e^{-s^n}$; the exponent $n$ was given as 2/3 by Richardson and as $n = 2$ by Batchelor [2], but values of $n$ from particle tracking measurements [6–8] and concentration maps [12] have so far been inconsistent. The accuracy of relative diffusion measurements in laboratory studies has improved significantly in recent years, following advances in planar laser-induced fluorescence and particle tracking techniques. Even so, the fact that most laboratory flows have been conducted at relatively low turbulence Reynolds numbers $\mathrm{Re}_\lambda$ limits their assertiveness, particularly in the light of the ongoing debate concerning the existence of the Richardson-Obukhov regime at low Reynolds numbers. Bourgoin *et al.* [4] studied the motion of particles in a closed tank stirred by counter-rotating baffled disks and observed that the evolution of $\langle r^2(t)\rangle$ was consistent with Batchelor scaling for $t \ll t_B$, but found no evidence of Richardson-Obukhov scaling for $t \gg t_B$, for values of the turbulence Reynolds number $\mathrm{Re}_\lambda$ up to 815. In contrast, Ott and Mann [7] reported evidence of Richardson-Obukhov scaling in a turbulent flow generated in a closed tank by oscillating grids at $\mathrm{Re}_\lambda \sim 100$.

The general objective of the present research was to investigate the relative dispersion of a passive scalar plume in nearly homogeneous but strongly anisotropic turbulence with a moderate Reynolds number. Specific objectives were to determine whether Richardson-Obukhov scaling applies to this flow and to estimate the shape of the distance-neighbor function and the rate of growth of the mean particle separation.

Experiments were performed in nearly homogeneous, uniformly sheared flow (USF), in a free-surface, recirculating water tunnel (see Fig. 1). A uniform velocity gradient in the $x_2$ direction was generated by a shear generator, which consisted of an array of parallel channels with a spacing $L = 25.4$ mm and varying flow obstruction. A neutrally buoyant aqueous solution of rhodamine 6G fluorescent dye was injected isokinetically into the flow through a fine tube having an inner diameter of 1.83 mm.

The turbulence structure of the USF has been documented previously [13,14]; representative values of properties of interest are presented in Table I. The initial mean particle separation, determined as the second central moment of the concentration profile at the outlet of the injection tube, was $r_0 = 0.53$ mm, which corresponded to a Batchelor time scale $t_B = (r_0^2/\langle\epsilon\rangle)^{1/3} \approx 0.14$ s. As explained in a previous article [14], the streamwise integral Lagrangian time scale was estimated as $T_L \approx 2.6 L_{22,2}/u_2' \approx 6.1$ s. Based on these values, one would expect the Richardson-Obukhov regime to extend over the diffusion time range $0.14\ \mathrm{s} \ll t \ll 6.1\ \mathrm{s}$;

 

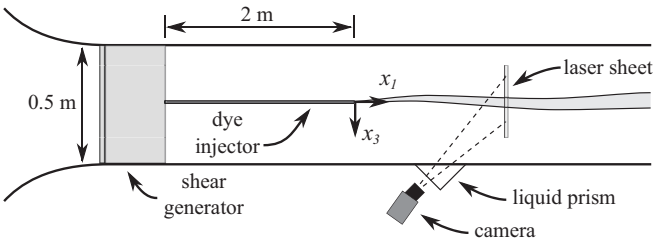


FIG. 1. Sketch of the apparatus viewed from above; the $x_2$ axis is oriented out of the page.

further employing Taylor's frozen flow approximation as $t \approx x_1/U_C$, one may estimate that the Richardson-Obhukhov regime would extend over the range of streamwise distances $1 \ll x_1/L \ll 45$, which applies to all presently reported measurements. Measurements of the concentration in cross sections of the plume normal to the flow direction were obtained via planar laser-induced fluorescence at $x_1/L =$ 5, 12, 20, 28, and 35. Normal cross sections were chosen in preference to the streamwise cross sections used in other studies [12], which cannot track the plume when it wanders out of the plane. Plume cross sections were illuminated by a light sheet created from the output of a Nd:YAG pulsed laser (New Wave Research, Solo PIV 120XT, Fremont, CA, USA) and the resulting fluorescence was recorded using a digital camera (PCO AG, pco.edge, Kelheim, Germany) which was synchronized with the laser pulses. The camera was fitted with a Scheimpflug adapter, in order to focus on the oblique measurement plane, and a liquid prism was used to eliminate the horizontal astigmatism that would have been introduced from looking through the glass wall at an angle. The concentration $C$ of dye measured by each pixel of the camera was determined as a linear function of the local radiant intensity emitted by the dye in the plane of the laser sheet. Ensemble-averaged quantities were calculated based on typically 500 independent images at each location. Additional details on the PLIF technique and its uncertainty will be the subject of a future manuscript. In summary, the uncertainty of the reported values of the plume widths and other length scales was lower than 5%.

A representative instantaneous concentration map is presented in Fig. 2(a). At this particular instant, the entire plume was located off-center and towards the top and right side of the field of view; such relatively large displacements are identified as plume wandering and are attributed to turbulent eddies with scales larger than the plume width. The plume cross section was not simply connected, but consisted of multiple elongated filaments; this action is attributed to eddies with size comparable to the plume width. Moreover, the edges of the filaments were not rounded, but showed evidence of the action of eddies with sizes much smaller than the plume width. The center of mass of the instantaneous concentration map in Fig. 2(a) is marked with a cross. Its coordinates $x_{2C}$ and $x_{3C}$ were determined from the corresponding first moments of the concentration map.

TABLE I. Representative values of flow parameters.

| |
|---|
| Shear generator spacing, $L = 25.4$ mm |
| Mean center line velocity, $U_C = 0.18$ m/s |
| Mean velocity gradient, $d\overline{U}_1/dx_2 = 0.59$ s$^{-1}$ |
| Turbulence Reynolds number, $\mathrm{Re}_\lambda = 150$ |
| Turbulent kinetic energy dissipation rate, $\langle\epsilon\rangle = 7.6$ mm$^2$ s$^{-3}$ |
| Kolmogorov microscale, $\eta = 0.6$ mm |
| Taylor microscale, $\lambda_{11} = 17$ mm |
| Eulerian integral length scale, $L_{11,1} = 30$ mm |
| Lagrangian integral time scale, $T_L = 6.1$ s |
| Dye Schmidt number, $\mathrm{Sc} = 2500$ |
| Dye source concentration, $C_S = 0.3$ mg/$\ell$ |

The map of the mean concentration $\langle C(x_2,x_3)\rangle$ in the laboratory frame is plotted in Fig. 2(b). It can be seen that the mean map extended over a much larger area than the instantaneous one, as the result of large-scale plume wandering. The joint probability density function (jpdf) of the center of mass coordinates in the instantaneous maps is presented in Fig. 2(c). A coordinate transformation of each instantaneous map to a frame centered on the instantaneous center of mass resulted in instantaneous concentration maps in a wandering frame. The ensemble average $C_R(x_2,x_3) = \langle C(x_2 - x_{2C}, x_3 - x_{3C})\rangle$ of these maps, to be referred to as the "relative" concentration map [15], is shown in Fig. 2(d). The absolute mean concentration map, the relative mean concentration map, and the jpdf of the instantaneous centers of mass could all be approximated by two-dimensional (2D) Gaussian functions, contours of which are superimposed on the maps in Fig. 2.

The half-widths of each map in the directions $x_2$ and $x_3$ were defined as the square roots of the corresponding second central moments. Following these definitions, we calculated the half-widths $\sigma_2,\sigma_3$ of the mean concentration map, $\sigma_{R2},\sigma_{R3}$ of the relative mean concentration map, and $\sigma_{M2},\sigma_{M3}$ of the jpdf of the instantaneous centers of mass. It is noted that $\sigma_3/\sigma_2 \approx \sigma_{M3}/\sigma_{M2} \approx 1.25$, which is consistent with the Reynolds stress anisotropy in USF [13]. In contrast, $\sigma_{R3}/\sigma_{R2} \approx 1.1$, which is closer to unity, in conformity with the conjecture that relative dispersion is dominated by eddies in the inertial subrange, which would be locally isotropic. The streamwise evolutions of the three mean half-widths $\sigma$, $\sigma_R$, and $\sigma_M$, computed by averaging the corresponding half-widths in the two directions, are presented in Fig. 3. The three values satisfy the relationship $\sigma^2 = \sigma_R^2 + \sigma_M^2$, in conformity with the parallel axis theorem of moments of inertia. The trends of the half-widths are in excellent agreement with the idealized trends presented by Csanady [15, Fig. 4.4a]. Within the range of reported measurements, the scale of meandering $\sigma_M$ was comparable to the relative plume width $\sigma_R$, in support of the conjecture that dye dispersion was dominated by eddies comparable in size to the width of the instantaneous plume. In the range $x_1/L \leqslant 20$, all three widths grew approximately linearly, whereas in the following range, having $20 < x_1/L \leqslant 37$, $\sigma$ and $\sigma_R$ maintained their quasilinear growth but the growth rate of $\sigma_M$ decreased monotonically, possibly tending towards a zero asymptote; the latter observation agrees with the expectation that, in the far field of the plume, $\sigma_M$ would approach an asymptotic value of the order of $L_{11,1}$ [15].

Next, we estimated the distance-neighbor functions $q(s_2)$ and $q(s_3)$ as the marginal pdfs of the ensemble-averaged

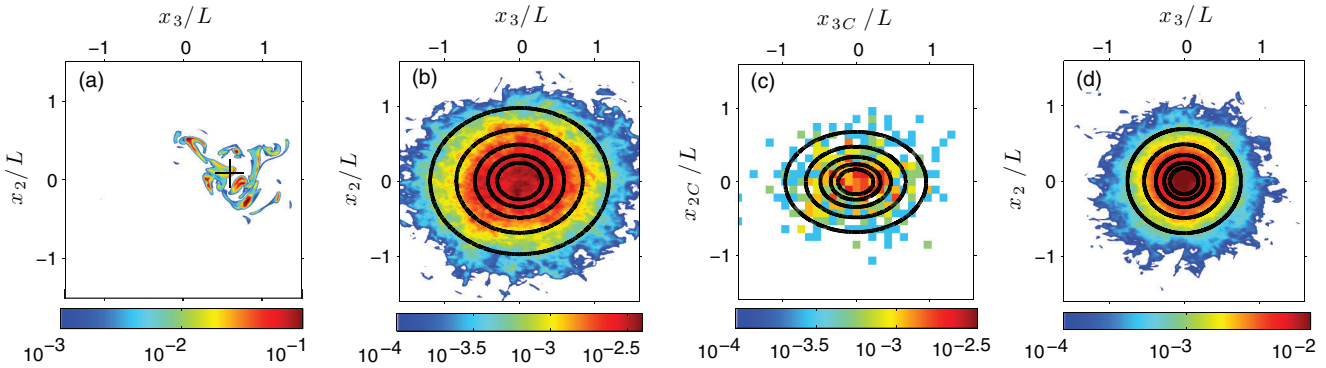


FIG. 2. (Color online) (a) A representative instantaneous concentration map with its center of mass indicated by a cross; (b) the mean concentration map in the laboratory frame; (c) the jpdf of the coordinates of the instantaneous center of mass of the plume cross section; and (d) the relative mean concentration map. All concentration values have been normalized by $C_S$; contours of fitted 2D Gaussian functions are indicated by superimposed ellipses; $x_1/L = 20$.

two-dimensional autocorrelation maps [12]:

$$\langle R(s_2,s_3)\rangle = \left\langle \frac{\iint C(x_2,x_3)C(x_2+s_2,x_3+s_3)dx_2dx_3}{\iint C^2(x_2,x_3)dx_2dx_3} \right\rangle. \quad (2)$$

Representative plots of $\langle R(s_2,s_3)\rangle$ and $q(s_2)$ are presented in Fig. 4. The half-widths $\sigma_{Q2}$ and $\sigma_{Q3}$ were defined as the square roots of the second central moments of $q(s_2)$ and $q(s_3)$. The half-width ratio was $\sigma_{Q3}/\sigma_{Q2} \approx 1.1$, which is consistent with the expectation of isotropy in the inertial subrange. The shapes of $q(s_2)$ and $q(s_3)$ at all measurement positions could be approximated by functions of the form $e^{-s^n}$. As shown in Fig. 5, the value of the exponent $n$ decreased with distance from the source. At the closest measurement position ($x_1/L = 5$), $n \approx 1.5$, and extrapolation of the data to the source is compatible with the near-field value $n = 2$, as predicted by Batchelor. Towards the end of the measurement range, however, $n$ seemed to approach the value 0.9, which is only slightly larger than Richardson's estimate of $n = 2/3$. The present evolution of $n$ has a trend that is opposite to the one observed by Liao *et al.* [12], who found that $q(s)$ resembled Richardson's pdf near the source and approached a Gaussian shape with $n = 2$ as distance from the source increased. On the other hand, the trend in Fig. 5 is in line with particle tracking results [6–8], which show that the distance-neighbor function was best described by Richardson's pdf.

The mean square particle separation $\langle r^2\rangle$ was estimated first as $2\sigma_R^2$ and secondly as $\sigma_Q^2$, where $\sigma_Q$ is defined as the average of $\sigma_{Q2}$ and $\sigma_{Q3}$ [10,12]. The two estimates, plotted together in Fig. 6, were nearly identical; standard deviations of the components of $\sigma_Q$ and $\sqrt{2}\sigma_R$ were on the average ±6% of the mean values. The particle separations were within the inertial subrange ($\eta \ll \sqrt{\langle r^2\rangle} \ll L_{11,1}$) for the entire measurement range.

The Richardson-Obukhov scaling law was fit to the measurements in the form

$$\langle r^2\rangle - r_0^2 = g\langle\epsilon\rangle\left(\frac{x_1 - x_0}{U_C}\right)^3, \quad (3)$$

where $r_0 = 0.53$ mm and the time shift $x_0/U_c$ was introduced in accordance with past practices [7,8]. The best-fit line, plotted in Fig. 6, was achieved for a virtual origin equal to $x_0 = -7.5L$ and a Richardson constant of $g = 0.35$; the latter value is within the range of theoretical estimates [5], although it is somewhat lower than other recent measurements [2]. For

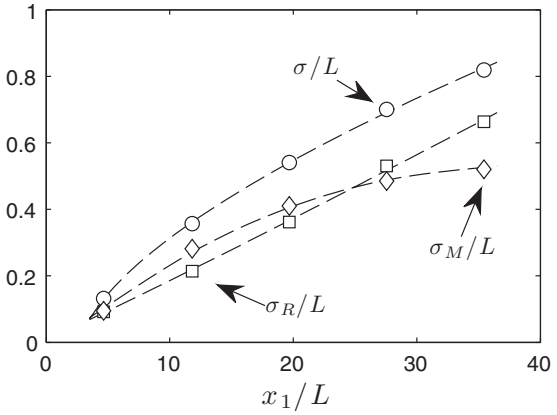


FIG. 3. (a) Evolutions of the standard deviations of the absolute mean concentration map $\sigma$, the relative mean concentration map $\sigma_R$, and the jpdf of the instantaneous centers of mass $\sigma_M$; dashed lines are included as a visual aid.

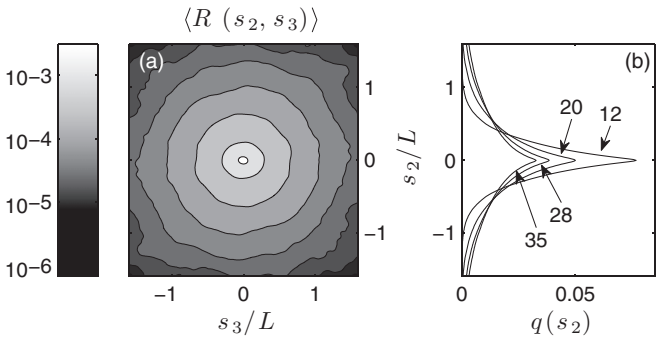


FIG. 4. (a) Map of the ensemble-averaged 2D autocorrelation map $\langle R(s_2,s_3)\rangle$ at $x_1/L = 20$ and (b) the distance-neighbor function $q(s_2)$ at $x_1/L = 12$, 20, 28, and 35.

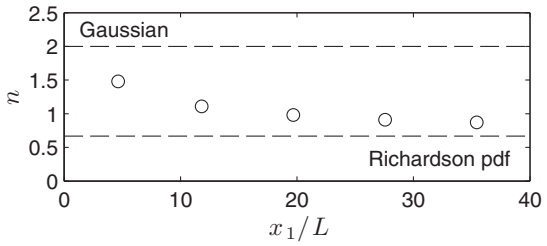


FIG. 5. Evolution of the power $n$, which describes the shape of $q(s) \propto e^{-s^n}$, versus streamwise distance $x_1$.

comparison, the Batchelor scaling law

$$\langle r^2 \rangle - r_0^2 = \frac{11}{3} C_2 \langle \epsilon \rangle^{2/3} r_0^{2/3} \left( \frac{x_1}{U_C} \right)^2, \tag{4}$$

with $C_2 = 2.13$ [3,4] and without any time shift, is also plotted in Fig. 6. It is interesting to note that this expression, which contains no adjustable parameters, was in excellent agreement with the measurements over a range that extended far beyond the Batchelor regime ($x_1/L \ll 1$); although somewhat surprising, this observation is consistent with previous studies that observed $\langle r^2 \rangle \propto t^\gamma$, with $\gamma$ in the range between 2 and 3 [2]. The apparent wide overlap of the Batchelor and Richardson-Obukhov regimes may be attributed to the moderate Reynolds number of the present flow and hence the presence of only a narrow inertial subrange [13,16], which does not permit the development of a wide and distinct Richardson-Obuhkov regime [4].

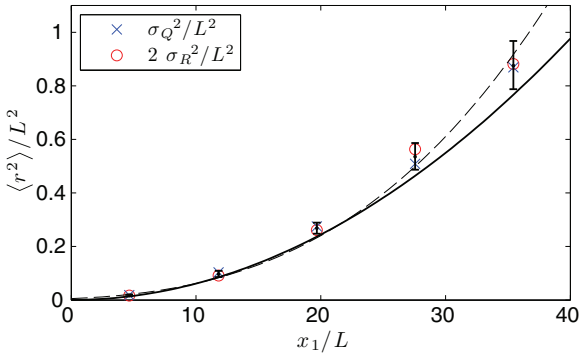


FIG. 6. (Color online) Two estimates of the streamwise evolution of the mean square particle separation; the Richardson-Obukhov scaling law is indicated by a dashed line, whereas the Batchelor scaling law is indicated by a solid line.

The main findings of this work can be summarized as follows. Estimates of particle separation in the inertial range of a scalar plume from relative mean concentration maps were essentially identical with estimates based on distance-neighbor functions. The shape of the distance-neighbor function was compatible with Richardson's expression, in line with particle tracking studies. Particle separation evolution was consistent with Richardson-Obukhov scaling with a value of Richardson's constant of $g = 0.35$. The same results were also consistent with Batchelor scaling over a range that was much wider than the Batchelor regime.

Financial support was provided by the Natural Sciences and Engineering Research Council of Canada.

[1] L. F. Richardson, Proc. R. Soc. London, Ser. A **110**, 709 (1926).
[2] J. P. L. C. Salazar and L. R. Collins, Annu. Rev. Fluid Mech. **41**, 405 (2009).
[3] K. R. Sreenivasan, Phys. Fluids **7**, 2778 (1995).
[4] M. Bourgoin, N. Ouellette, H. Xu, J. Berg, and E. Bodenschatz, Science **311**, 835 (2006).
[5] B. Sawford, Annu. Rev. Fluid Mech. **33**, 289 (2001).
[6] M.-C. Jullien, J. Paret, and P. Tabeling, Phys. Rev. Lett. **82**, 2872 (1999).
[7] S. Ott and J. Mann, J. Fluid Mech. **422**, 207 (2000).
[8] J. Berg, B. Lüthi, J. Mann, and S. Ott, Phys. Rev. E **74**, 016304 (2006).
[9] G. W. Brier, J. Meteorol. **7**, 283 (1950).
[10] G. K. Batchelor, Math. Proc. Cambridge **48**, 345 (1952).
[11] A. S. Monin and A. M. Yaglom, *Statistical Fluid Mechanics: Mechanics of Turbulence* (MIT Press, Cambridge, MA, 1975), Vol. 2.
[12] Q. Liao and E. A. Cowen, J. Fluid Mech. **661**, 412 (2010).
[13] C. Vanderwel and S. Tavoularis, J. Fluid Mech. **689**, 434 (2011).
[14] C. Vanderwel and S. Tavoularis, in Proceedings of the Eighth International Symposium on Turbulence and Shear Flow Phenomena, Poitiers, France (unpublished).
[15] G. Csanady, *Turbulent Diffusion in the Environment* (D. Reidel Publishing Company, Dordrecht, The Netherlands, 1973).
[16] M. Ferchichi and S. Tavoularis, Phys. Fluids **12**, 2942 (2000).

# Chapter 7

## The fine structure of a slender scalar plume in sheared turbulence

This chapter reports measurements of the fine structure of the turbulent concentration and velocity fields in the dye plume in USF. Results are presented in the form of the manuscript

> Vanderwel, C. and Tavoularis, S. (2014), "The fine structure of a slender scalar plume in sheared turbulence", Presented at the iTi (interdisciplinary Turbulence initiative) Conference on Turbulence, Bertinoro, Italy, September 21-24, 2014. Also under review for publication in Progress in Turbulence VI, Springer Verlag.

The measurements include probability density functions of the velocity, scalar, and scalar derivatives, as well as conditional expectations of the velocity and the scalar derivatives, conditioned upon the scalar fluctuations. Such results are particularly relevant to models of turbulent mixing that are intended to be used for solving the balance equation of the scalar pdf. Because of the strong intermittency of the present plume, the results differ qualitatively from measurements by previous researchers in less inhomogeneous scalar fields. We discuss these differences and their implications for turbulent mixing models.

# The fine structure of a slender scalar plume in sheared turbulence

Christina Vanderwel and Stavros Tavoularis

**Abstract** We present measurements of the fine structure of a passive scalar plume in uniformly sheared turbulence generated in a water tunnel. We report on the mixed velocity-scalar statistics of the plume, including the probability density functions of the velocity, scalar, and scalar derivatives, as well as conditional expectations of the velocity and the scalar derivatives, conditioned upon the scalar fluctuations. Such results are particularly relevant to models that are intended to be used for solving the balance equation of the scalar pdf. Specifically, we address the effect of having a highly intermittent scalar field, in which case the scalar pdf is highly skewed, the joint velocity and scalar pdfs are non-Gaussian, and conditional expectations of the velocity components are distinctly non-linear.

Details on the fine structure of turbulent mixing are particularly relevant for the modelling of chemical reactions and combustion. A popular approach for analyzing reactive flows is to consider the balance equation of the scalar probability density function (pdf) [1, 2, 3]. Although these equations have certain advantages over conventional Reynolds-averaged balance equations of velocity and scalar moments, they are complicated by the appearance of conditional expectations of the velocity and the scalar dissipation values, conditioned upon the scalar fluctuations. Most previous studies have focused on flows in which the velocity and scalar are nearly homogeneous and jointly-Gaussian, in which case these conditional expectations would be linear functions of the scalar value [2, 3, 4]; however, this would not necessarily be the case for inhomogeneous scalar fields as they would appear in industrial and environmental flows and even in many canonical flows, such as turbulent plumes, jets, wakes, and mixing layers.

C. Vanderwel · S. Tavoularis
University of Ottawa, Ottawa, Ontario K1N 6N5, Canada

Article submitted to the iTi Conference on Turbulence, Bertinoro, Italy, September 22-24, 2014

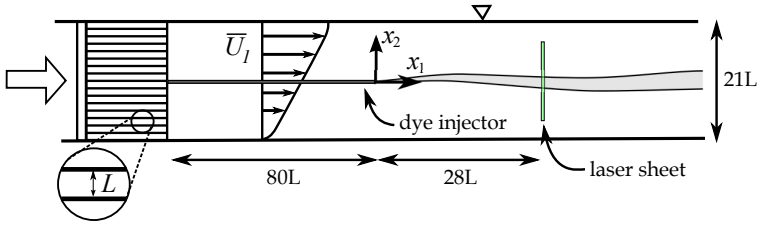


**Fig. 1** Schematic of the apparatus ($L = 25.4$ mm).

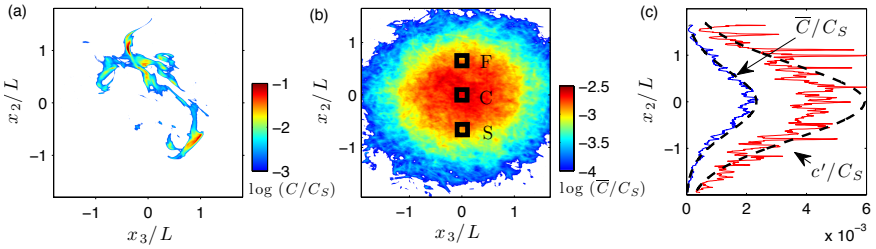


**Fig. 2** (a) Representative instantaneous concentration map at $x_1/L = 28$. (b) Mean concentration map at $x_1/L = 28$, with the three regions of interest indicated by squares. (c) Profiles of the mean concentration and the standard deviation of the concentration fluctuations; dashed lines represent Gaussian profiles.

The objective of the present study is to investigate experimentally the fine structure of a passive scalar plume of a solution of Rhodamine 6G dye injected from a fine tube in uniformly sheared turbulence generated in a water tunnel (figure 1). Measurements of the turbulent velocity and concentration fields in cross-sections of the plume were obtained simultaneously with the use of stereoscopic particle image velocimetry (SPIV) and planar laser induced fluorescence (PLIF). The present results complement previous reports of absolute and relative turbulent diffusion of the same plume [5, 6, 7], which have also documented the measurement procedure in detail.

**The scalar field** In the present flow, the turbulence was nearly homogeneous but strongly anisotropic [8]. The present plume was very slender by comparison to the dominant eddies of the turbulence; consequently, the scalar field was highly intermittent. A representative instantaneous concentration map, shown in figure 2a, illustrates the sinuous nature of the plume and its extensive meandering. At all points in the cross-section, the scalar intermittency factor $\gamma_c$, defined as the portion of time during which the concentration was non-zero, was lower than 0.4. Maps of the mean concentration had the shape of a 2D Gaussian function (figure 2b,c) and the standard deviation of the concentration fluctuations exceeded the mean concentration.

**Probability density functions** In the following, we will present representative measurements at three locations: on the axis of the plume and at two locations on either side of the axis and along the mean velocity gradient direction, near the two inflection points of the mean concentration profile (Points C, F and S, respectively).

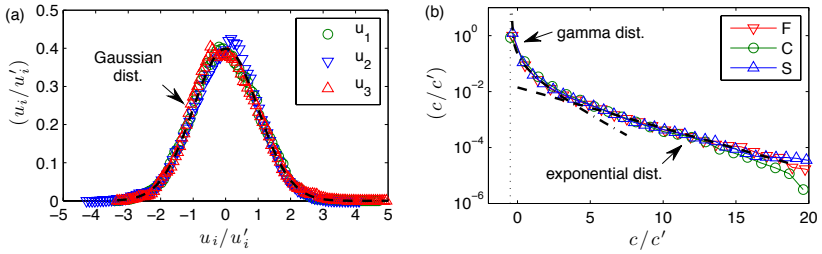


**Fig. 3** (a) Pdf of the velocity fluctuations; the dashed line represents a Gaussian distribution. (b) Pdf of the concentration fluctuations; the dotted line represents undyed fluid and the dashed lines represent fitted gamma and exponential distributions.

Unlike the pdfs of the velocity fluctuations (figure 3a), which were Gaussian, the pdf of the scalar fluctuations (figure 3b) were highly skewed and were bounded on the low side by the zero concentration and on the high side by a value that was significantly lower than the injected dye concentration $C_S$; these observations are consistent with previous measurements in thin plumes [9, 10]. At all three locations, the scalar pdf nearly coincided, although at the off-centre locations (F and S) the pdf had slightly higher values in the tails, which can be attributed to the peak generation of scalar fluctuations at the inflection points of the mean scalar field. For small concentration fluctuations ($c/c' < 4$), the scalar pdf could be described by a gamma distribution, whereas, the tails ($c/c' > 5$) were best described by an exponential distribution.

**Conditional expectations** The conditional expectations of the velocity components conditioned upon the scalar value in the present plume were distinctly non-linear (figure 4), unlike those in flows with homogeneous scalar fields in which the joint velocity-scalar pdfs were nearly Gaussian [2, 3, 4]. The variation of $\overline{u_2/u_2'|c/c'}$ illustrates that negative scalar fluctuations (*i.e.*, mostly undyed fluid) are associated with motions that originated outside the plume, whereas positive scalar fluctuations are associated with motions that originated largely in the core of the plume. Furthermore, the curves have steep vertical asymptotes on the negative side which are attributed to the fact that the scalar fluctuations are bounded on the negative size by the zero concentration. The variation of $\overline{u_1/u_1'|c/c'}$ had the opposite trends, which is consistent with the sign and strong magnitude of the Reynolds stress $\overline{-u_1u_2}$ in this shear flow [8]. As expected by considering the symmetry of the turbulence and the mean plume, $\overline{u_3/u_3'|c/c'}$ was zero at $x_3 = 0$.

**Scalar derivatives** Measurements of the scalar derivatives are particularly relevant as surrogates for the scalar dissipation rate [3]. The pdf of the transverse scalar derivative (figure 5) were highly peaked with long nearly-exponential tails, comparable to those measured in flows with less inhomogeneous scalar fields [3, 4, 11]. This is attributed to the small-scale intermittency of the scalar even in flows with Gaussian scalar pdf. The conditional expectations of the transverse scalar derivative at all measurement locations (figure 5b) were also distinctly non-linear functions of

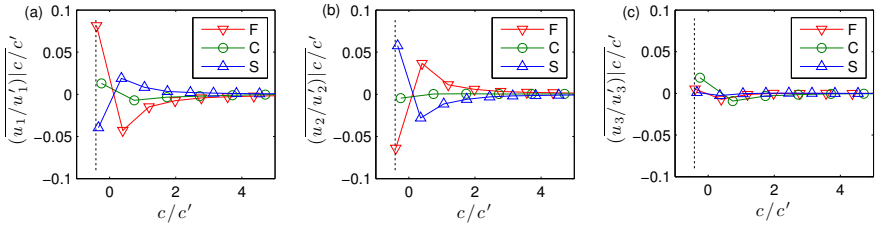


**Fig. 4** Conditional expectations of the velocity components, conditioned on the concentration fluctuation value; dotted lines represent undyed fluid.

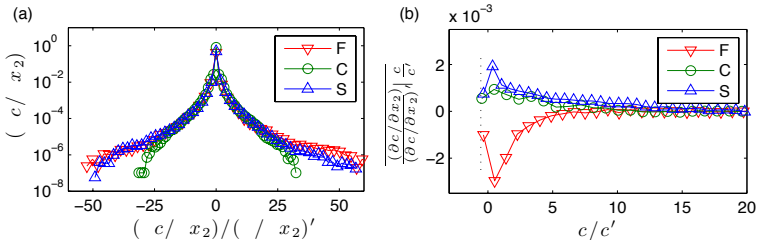


**Fig. 5** (a) Pdf of the transverse concentration derivative. (b) Conditional expectations of the transverse concentration derivative, conditioned on the concentration fluctuation value; the dotted line represents undyed fluid.

the scalar value, although their signs were consistent with the signs of the corresponding local mean scalar derivatives [12].

In summary, these results demonstrate that in a highly intermittent scalar field, the scalar pdf was strongly non-Gaussian and the conditional expectations of the velocity components and the scalar dissipation, conditioned upon the scalar value, were distinctly non-linear.

**Acknowledgements** Financial support by the Natural Sciences and Engineering Research Council of Canada (NSERC) is gratefully acknowledged.

## References

1. S. Pope, *Turbulent Flows* (Cambridge University Press, 2000)
2. L. Mydlarski, J. Fluid Mech. **475**, 173 (2003)
3. A. Behnamian, S. Tavoularis, in *Eighth International Symposium on Turbulence and Shear Flow Phenomena (TSFP8), Poitiers, France* (2013)
4. M. Ferchichi, S. Tavoularis, J. Fluid Mech. **461**, 155 (2002)
5. C. Vanderwel, S. Tavoularis, Phys. Rev. E **89**(4), 041005 (2014)
6. C. Vanderwel, S. Tavoularis, J. Fluid Mech. **754**, 488 (2014)
7. C. Vanderwel, S. Tavoularis, Exp. Fluids **55**, 1801 (2014)
8. C. Vanderwel, S. Tavoularis, J. Fluid Mech. **689**, 434 (2011)
9. S. Rahman, D. Webster, Exp. Fluids **38**(3), 372 (2005)
10. R. Lavertu, L. Mydlarski, J. Fluid Mech. **528**, 135 (2005)
11. Jayesh, Z. Warhaft, Phys. Fluids A **4**(10), 2292 (1992)
12. S. Tavoularis, S. Corrsin, J. Fluid Mech. **104**, 349 (1981)

# Chapter 8

## Scalar dispersion by coherent structures

This chapter explores the role of coherent structures on the turbulent dispersion of the dye plume in USF. Results are presented in the form of the manuscript

> Vanderwel, C. and Tavoularis, S. (2015), "Scalar dispersion by coherent structures", Under review for the Ninth International Symposium on Turbulence and Shear Flow Phenomena (TSFP9), Melbourne, Australia, June 30 - July 3, 2015.

In this study we apply new methods to investigate qualitatively and quantitatively the effect of coherent structures on turbulent dispersion. First, simultaneous velocity and concentration maps were used to investigate the correlation between the dye and vortex locations. Then, for the first time, a conditional eddy approach was applied to study scalar flux. Lastly, the correlation between the Reynolds stress and the scalar flux was documented. The results demonstrate that coherent structures are the main mechanism associated with large scalar flux events and are a dominant mechanism for scalar dispersion.

# SCALAR DISPERSION BY COHERENT STRUCTURES

**Christina Vanderwel**
Department of Mechanical Engineering
University of Ottawa
Ottawa, Canada

**Stavros Tavoularis**
Department of Mechanical Engineering
University of Ottawa
Ottawa, Canada

## ABSTRACT

We investigated the influence of coherent structures on the dispersion of a passive scalar by studying instantaneous measurements of a plume of dye released in uniformly sheared flow generated in a water tunnel. Measurements were performed using simultaneous stereo particle image velocimetry and planar laser-induced fluorescence to obtain instantaneous concentration and velocity maps in cross-sections normal to the flow direction. Coherent vortices were observed to effectuate scalar transport by inducing motions which displaced dyed fluid. Dye was observed to preferentially congregate within vortex cores and far away from vortices, whereas regions adjacent to vortices were less likely to contain dye. A conditional eddy analysis demonstrated that counter-rotating vortex pairs associated with hairpin vortices were responsible for both large Reynolds stress events and large scalar flux events. This observation was supported by the fact that the Reynolds stress was found to be correlated with the scalar flux.

## Introduction

Coherent structures are the recurring, dominant, vortical, large-scale flow patterns that are ubiquitous in turbulent flows. Previous experimental and numerical studies have shown that hairpin vortices are the predominant coherent structures in turbulent boundary layers (Adrian, 2007; Wu & Moin, 2010) as well as in other shear flows (Vanderwel & Tavoularis, 2011; Ghaemi & Scarano, 2011). The generation of such structures has been explained by the lifting and stretching of quasi-two-dimensional roller vortices. Coherent structures have been shown to be a primary mechanism for the generation of Reynolds stresses that dominate the transport of momentum, so that their control is essential for drag and noise reduction. As a corollary of Reynolds analogy, which connects heat and mass transport to momentum transport, one would expect that coherent structures should also be largely responsible for scalar transport. This connection has been demonstrated qualitatively by flow visualizations of scalar field patterns in turbulent boundary layers (Head & Bandyopadhyay, 1981; Kline *et al.*, 1967; Falco, 1977). More recently, Wu & Moin (2010) also observed hairpin vortices in isocontours of a scalar field examined by direct numerical simulations.

The effects of coherent structures on scalar transport are particularly important in the context of environmental flows. Katul *et al.* (1997) and Li & Bou-Zeid (2011) have noted that, in the atmospheric surface layer, the ejection and sweep motions that are typically associated with coherent structures are responsible for much of the land-surface evaporation, heat and momentum fluxes. Provenzale (1999) reviewed the impact of coherent vortices in quasigeostrophic flows in the ocean and the atmosphere and described how scalars seeded within vortices experience reduced dispersion compared to the free stream, and become, in a sense, islands of stability. Investigations of particle dispersion have also demonstrated that coherent structures are responsible for particle clustering, which has direct ramifications to reactive flows such as combustion as well as to droplet coalescence and the formation of clouds in the atmosphere (Shaw *et al.*, 1998; Rouson & Eaton, 2001). Better understanding of the role of coherent structures in scalar transport is also important for working towards the refinement of turbulent diffusion models to better be able to resolve their effects.

In view of the importance of scalar dispersion in many applications, it is rather surprising that the role coherent structures play on the dispersion of passive scalars has not yet been studied quantitatively and systematically in the laboratory. The goal of the present work is to investigate both qualitatively and quantitatively the influence of coherent structures on turbulent dispersion. We investigated a plume of dye released from a point source in uniformly sheared flow (USF) generated in a water tunnel. This turbulent field is nearly homogeneous but strongly anisotropic, and has a large-scale structure that is dominated by horseshoe/hairpin-shaped vortices (Vanderwel and Tavoularis, 2011), comparable to those found in turbulent boundary layers.

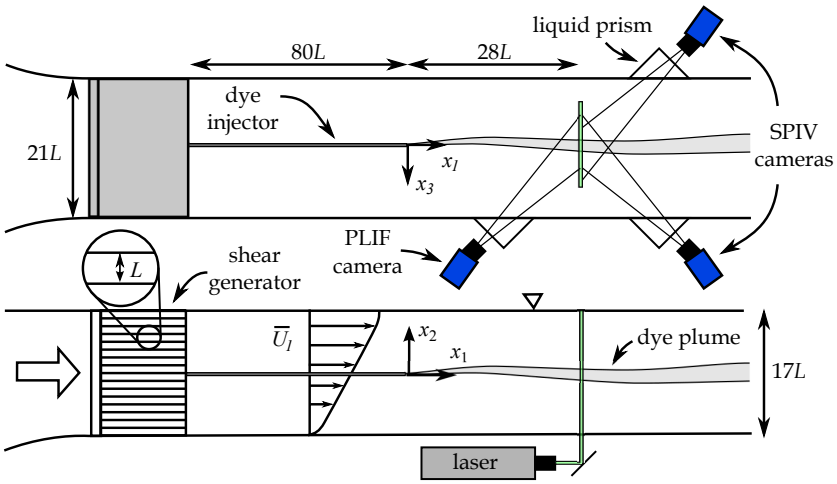


Figure 1: Top and side views of the experimental apparatus and main instrumentation in the water tunnel test section; $L = 25.4$ mm is the spacing of the shear generator.

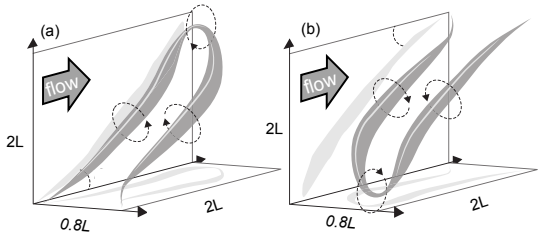


Figure 2: Sketches of (a) an upright and (b) an inverted hairpin vortex (adapted from Vanderwel & Tavoularis, 2011).

## Apparatus and Flow Conditions

A sketch of the experimental facility and main instrumentation is presented in figure 1. Uniform shear was generated with the use of a shear generator. The streamwise velocity at the centre of the channel was $U_c = 0.18$ m/s. The turbulence was nearly homogeneous on transverse planes and strongly anisotropic, and had a turbulence Reynolds number $Re_\lambda \approx 150$. The turbulence integral lengthscale, which was comparable to the shear generator spacing $L = 25.4$ mm, was much smaller than the dimensions of the flow domain. The mean and turbulent properties of the flow have been documented in detail by Vanderwel & Tavoularis (2011).

Previous measurements in this flow have documented the prevalence of horseshoe/hairpin-shaped vortices (Vanderwel & Tavoularis, 2011), having similar characteristics to those found in turbulent boundary layers at comparable $Re_\lambda$. In USF, both upright and inverted hairpins were observed, with idealised shapes as illustrated in figure 2, whereas, in turbulent boundary layers, the presence of the wall suppresses the development of inverted hairpin vortices. These coherent vortices were distributed evenly throughout the present flow.

Fluorescent dye (Rhodamine 6G) was released isokinetically from a fine tube in the fully developed region of the flow with a source concentration of $C_S = 0.3$ mg/$\ell$. Buoyancy effects were negligible and molecular diffusion was extremely weak, as this dye has a Schmidt number of 2500±300.

Simultaneous measurements of the instantaneous concentration and velocity maps were obtained in planes normal to the flow direction. Maps of all three components of the turbulent velocity were obtained via a two-camera stereoscopic particle image velocimetry (SPIV) system (FlowMaster, LaVision). Maps of the concentration were determined using the planar laser-induced fluorescence (PLIF) technique from dye fluorescence maps obtained with a third digital camera (PCO-Edge), synchronized with the SPIV system. Liquid prisms were used to prevent optical aberrations due to horizontal astigmatism associated with the oblique viewing angle into the test section. Details of the measurement procedure and the plume characteristics have been documented elsewhere (Vanderwel & Tavoularis, 2014*a*,*b*,*c*).

## Proximity of dyed fluid to coherent structures

As a first step for investigating the connection between the coherent structures and the scalar dispersion, we considered whether the locations of fluid marked by dye were correlated with or otherwise related to the locations of coherent structures. Two representative instantaneous velocity maps are presented in figures 3a,d. An algorithm (Vanderwel & Tavoularis, 2011) applied to these maps identified the cores of coherent vortices as regions of the flow where the swirling strength exceeded 25% of the maximum measured swirling strength; the cross-sectional area of each structure was subsequently determined by an area-growing algorithm as the region around each core in which the swirling strength exceeded 5% of the maximum. It was assumed that the cross-sections of the vortices had elliptical shapes and an ellipse with the minimum area was fit to the boundary of each vortex, as identified previously; then, the vortex centre was defined as the midpoint between the two foci of the ellipse and the vortex diameter was defined as the average of its major and minor axes. This method successfully distinguished neighbouring vortices, and especially vortex pairs, which were separated by regions of negligible swirling strength, corresponding to reversals of vorticity direction. Figures 3b,e indicate the locations of vortices identified by the algorithm in these examples, together with vector maps of the local relative

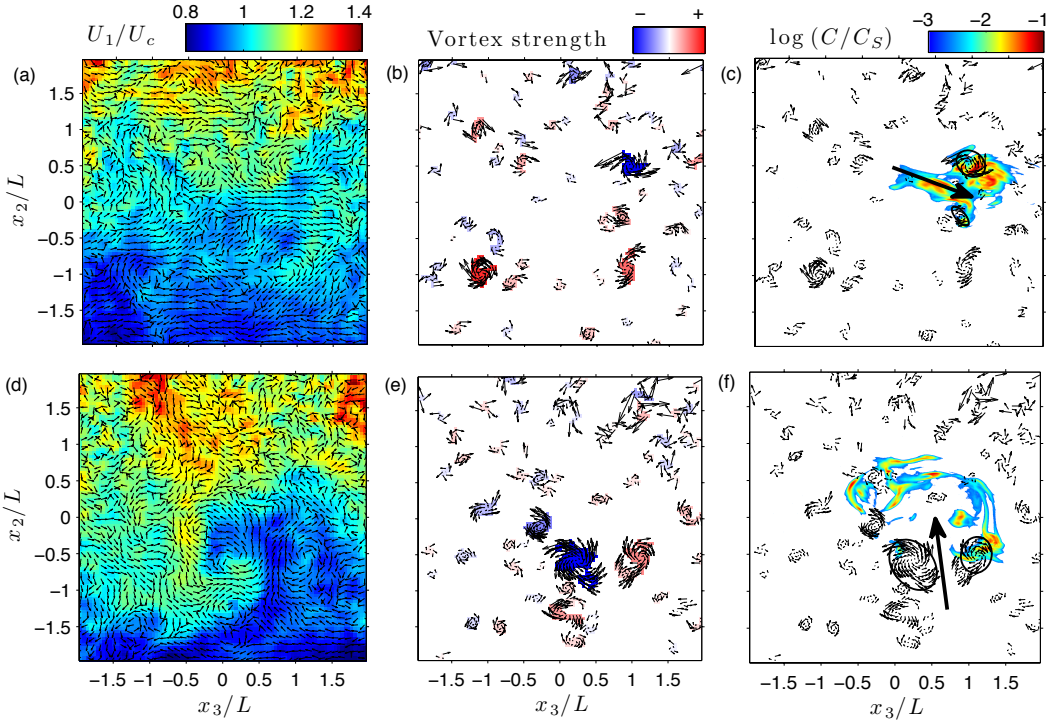


Figure 3: Two representative instantaneous sets of maps (a-c and d-f) illustrating the influence of coherent structures on dye transport. (a,d) transverse velocity vector maps with superimposed coloured contours of the streamwise velocity; (b,e) relative velocity vector maps within vortices, with coloured contours corresponding to vortex strength; (c,f) concentration maps superimposed on relative velocity vector maps within vortices. Pairs of relatively strong counter-rotating vortices, marked by ellipses, are seen to induce flows which displace dyed fluid.

velocities, which illustrate the direction and strength of local rotation. The vortices were roughly evenly distributed throughout the flow, as anticipated in view of the homogeneity of the turbulence. Several pairs of counter-rotating vortices are apparent, which are interpreted as cross-sections of hairpin vortices.

Representative instantaneous concentration maps, measured simultaneously with the corresponding velocity maps, are shown superimposed on the local relative velocity maps in figures 3c,f. Two different aspects of forceful scalar transport enacted by coherent structures can be seen readily in these figures: in figure 3c, a strong vortex pair induces a lateral flow between the two vortices, which transports dye between the pair and away from the plume centreline; in figure 3f, a similar vortex pair, presumably the cross-section of an upright hairpin vortex, induces an upward flow of undyed fluid, which in turn displaces dyed fluid further upwards. These examples clearly demonstrate an important point, namely that the fact that the locations of dye and coherent structures do not necessarily coincide does not mean that dye transport and dispersion are not connected intimately to coherent structure actions. This conjecture was supported by statistical analysis, which found no significant cross-correlation between concentration and vortex locations. Our investigation has demonstrated that the relationship between dyed fluid regions and coherent structures depends on their initial relative positions: if dyed fluid happens to be near the base of a vortex pair, it would be transported between the pair, but, if the dyed fluid happens to be initially on the other side of the pair, it would

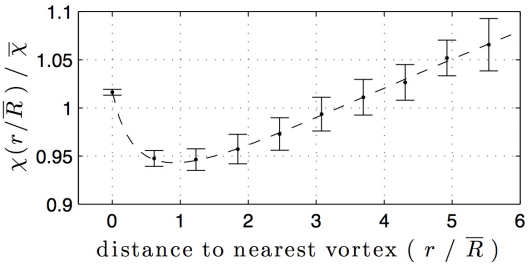


Figure 4: Variation of the normalized average local volume fraction of dye with normalized distance from the nearest vortex centre; uncertainty bars indicate the standard deviations of measurements at streamwise positions having $x_1/L = 20$, 28, and 35.

be pushed further away from it. In either case, the coherent structure would make a major impact on scalar transport.

To further investigate any possible relationship between the locations of regions containing dyed fluid and the locations of coherent structures, we calculated the average local volume fraction $\chi(r)$ of dyed fluid, as a function of distance $r$ from the nearest vortex centre. This property is deemed to indicate the likelihood of dye presence at the given distance. To calculate $\chi(r)$, we first identified the vortex that was nearest to each pixel in the measurement domain and then determined the distance between the pixel and the vortex centre. Finally, we computed the volume fraction as the ratio of the number of pixels with non-zero

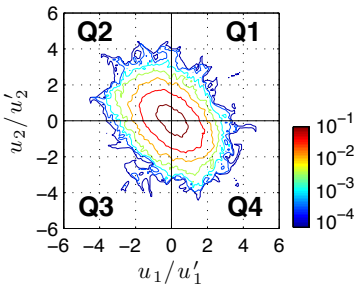


Figure 5: Contours of the joint pdf of $u_1$ and $u_2$ illustrating the predominance of Reynolds stress events to the Q2 and Q4 quadrants; primes indicate standard deviations.

concentration and the total number of pixels in annular regions with mean radius equal to $r$. We normalized $r$ by the mean vortex radius $\overline{R} = 0.07L$ and $\chi(r/\overline{R})$ by the overall volume fraction $\overline{\chi}$ in the entire measurement domain. The corresponding results are presented in figure 4. The likelihood of dye presence has a minimum near the periphery of the vortex; this indicates that there is some segregation of dye in the core of the vortex and a tendency for out-of-core dye to stay away from the core. The fact that the likelihood of dye presence in the vortex core is only slightly higher than elsewhere in the flow explains the observed lack of significant correlation between dye concentration and vortex location. The trend of dye volume fraction can be explained by the following conjecture: dye that was injected into the vortex core generally stayed in the core, whereas dye that was injected outside the core could be wrapped around it or pushed away by transverse motions induced by a vortex pair, without penetrating the vortex core. Lastly, dye appears to be segregated preferentially far away from vortices. We may speculate that these are regions with nearly uniform momentum, which appear between hairpin vortices in the flow (Vanderwel & Tavoularis, 2011).

## Conditional eddy analysis

In order to further investigate the influence of coherent structures on scalar transport, we applied a conditional eddy analysis, which is a method capable of reconstructing representative instantaneous flow patterns associated with the occurrence of significant flow events. The conditional eddy approach has been used by previous authors (Adrian & Moin, 1988; Adrian, 2007) to identify large-scale coherent structures in the turbulent boundary layer, as patterns that occurred when the nearby flow field met the condition of a large Reynolds stress in the Q2 quadrant ($u_1 < 0$ and $u_2 > 0$); reconstruction of the mean flow field resulted in a pattern that had the shape of a typical hairpin vortex.

In the present work, we first adapted conditional eddy analysis for vortex identification in USF and then extended it, for the first time, for identification of scalar transport events. As in turbulent boundary layers, in USF, the Reynolds stress tensor is anisotropic and the joint pdf of the streamwise and transverse velocity fluctuations (see figure 5) indicates a proclivity for events in the Q2 ($u_1 < 0$ and $u_2 > 0$) and Q4 ($u_1 > 0$ and $u_2 < 0$) quadrants, which is consistent with the negative correlation between $u_1$ and $u_2$. It is noted that, unlike turbulent boundary layers in which a one-sided orientation of hairpin vortices is imposed by the wall, USF has hairpins in both "upright" and "inverted"

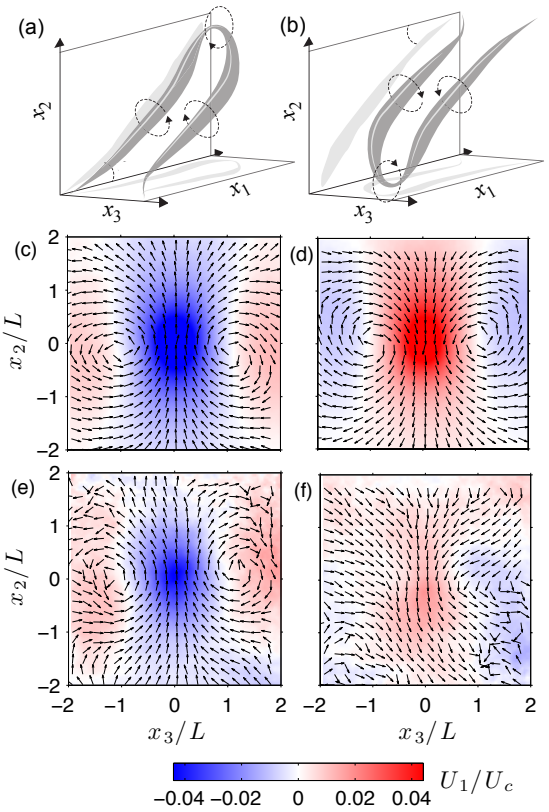


Figure 6: Conditionally averaged flow fields based on (c) large Reynolds stress events in Q2 and (d) in Q4 and (e) large scalar flux events having large positive values of $cu_2$ and (f) large negative values of $cu_2$, which indicate counter-rotating vortex pairs corresponding with the cross-sections of (a) upright and (b) inverted hairpin vortices.

orientations (Vanderwel & Tavoularis, 2011). For this reason, we identified large Reynolds stress events in both the Q2 and the Q4 quadrants as those that met the condition $|u_1 u_2| > 4u_1' u_2'$ (Antonia, 1981). Unlike previous studies which utilized a Linear Stochastic Estimation (LSE) to approximate the conditional flow field (Adrian, 1994), we determined the conditional flow field directly from the ensemble-average of the shifted instantaneous flow fields; reanalyzing the results using LSE yielded equivalent results without significant improvement. The corresponding mean flow fields in planes normal to the flow are shown in figures 6a,b. Both flow fields are cross-sections of pairs of counter-rotating vortices with sizes comparable to the characteristic lengthscale $L$ and consistent with the signatures of a hairpin vortex. Q2 events correspond to upright hairpin vortices (figure 6e), whereas Q4 events correspond to inverted hairpin vortices (figure 6f).

Subsequently, we determined the conditional eddies that met the scalar flux condition $|cu_2| > 4c'u_2'$, where $c$ is the dye concentration fluctuation. The resulting flow field associated with large positive $cu_2$ events (figure 6c) clearly indicates a pair of counter-rotating vortices corresponding to an upright hairpin vortex, which is also associated with large Reynolds stress events in the Q2 quadrant. The flow field associated with large negative $cu_2$ events (figure 6d) is consistent with the presence of inverted hairpin vortices, which are also associated with large Reynolds stress events

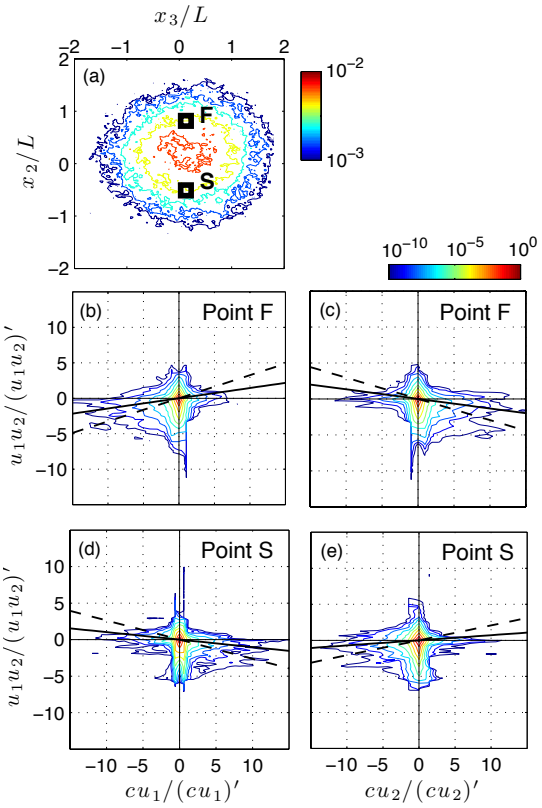


Figure 7: (a) Map of the mean concentration $\overline{C}/C_S$ with two regions of interest indicated by squares; (b-d) joint pdfs of the streamwise $cu_1$ and transverse $cu_2$ scalar fluxes and the Reynolds stress $u_1u_2$, measured at points F and S and normalized by the corresponding standard deviations; the solid line indicates the correlation coefficient whereas the dashed line indicates the correlation coefficient determined from values conditioned on $C>0$.

in the Q4 quadrant. The conditional eddies identified by the large scalar flux condition appear to be less distinct than those identified by the large Reynolds stress condition, because scalar flux events were restricted only within the present slender plume, whereas Reynolds stress events occurred in the entire flow domain. The results of this conditional eddy analysis clearly demonstrate that coherent vortices are a dominant mechanism for turbulent scalar transport.

In support of the previous assertion, we investigated the possible correlation between the Reynolds stress and the scalar flux. Such a correlation was also observed by Li & Bou-Zeid (2011), who studied the turbulent transport of heat and water vapour in the atmospheric surface layer. We present representative measurements at two locations on either side of the axis of the plume, along the mean velocity gradient direction, near the two inflection points of the mean concentration profile (points F and S, respectively, as indicated in figure 7a). The joint pdfs of the scalar fluxes and the Reynolds stress are presented in figure 7b-e. At point F, the joint pdf of $cu_1$ and $u_1u_2$ is clearly biased to the third quadrant, indicating a positive correlation between the Reynolds stress and the streamwise scalar flux. The joint pdf of $cu_2$ and $u_1u_2$ is clearly biased to the fourth quadrant, indicating a negative correlation. Similarly at point S, the

| Point | Scalar flux | $\rho$ | $\rho\|(C>0)$ |
|---|---|---|---|
| F | $cu_1$ | +0.14 | +0.33 |
| F | $cu_2$ | -0.13 | -0.30 |
| S | $cu_1$ | -0.10 | -0.26 |
| S | $cu_2$ | +0.07 | +0.21 |

Table 1: Values of the correlation coefficient between the scalar flux components and the Reynolds stress and the same correlation coefficient determined from values conditioned on $C>0$.

joint pdf of $cu_1$ and $u_1u_2$ is biased to the fourth quadrant, indicating a negative correlation, whereas the joint pdf of $cu_2$ and $u_1u_2$ is biased to the third quadrant, indicating a positive correlation. The change of sign of the correlations at points F and S is consistent with the change of sign of the mean scalar fluxes at these points. The fact that the correlations involving $cu_1$ and $cu_2$ have opposite signs is consistent with the fact that the streamwise and transverse scalar fluxes are negatively correlated at these locations (Vanderwel & Tavoularis, 2014*a*). The values of the correlation coefficients are presented in table 1 and are also indicated by lines in figure 7. The magnitudes of correlation coefficients were fairly low due to the fact that the present plume was particularly slender and the scalar signal was highly intermittent; therefore, correlation coefficients were also determined considering only values conditioned on dye being present ($C>0$). The resulting conditional correlation coefficients were significantly larger in magnitude than the unconditional ones, which further supports the conjecture that coherent structures simultaneously transport both mass and momentum.

## Conclusions

The influence of coherent structures on turbulent dispersion of passive scalars was qualitatively and quantitatively investigated from simultaneous measurements of the instantaneous concentration and velocity fields in a dye-marked plume. Despite the absence of a direct correlation between the scalar concentration and the locations of coherent structures, dye was found to segregate preferentially within vortex cores and away from vortices and less likely to be present in the periphery of vortices. A conditional eddy approach was applied to the study of scalar flux and the correlation between the Reynolds stress and the scalar flux was documented. These results demonstrate that coherent structures are the main cause of large scalar flux events and play a dominant role in turbulent diffusion.

Financial support by the Natural Sciences and Engineering Research Council of Canada (NSERC) is gratefully acknowledged.

## REFERENCES

Adrian, R.J. 1994 Stochastic estimation of conditional structure: a review. *Appl. Sci. Res.* **53** (3-4), 291–303.

Adrian, R.J. 2007 Hairpin vortex organization in wall turbulence. *Phys. Fluids* **19** (4), 041301.

Adrian, R.J. & Moin, P. 1988 Stochastic estimation of organised turbulent structure: homogeneous shear flow. *J. Fluid Mech.* **190**, 531–559.

Antonia, R.A. 1981 Conditional sampling in turbulence measurement. *Annu. Rev. Fluid Mech.* **13** (1), 131–156.

Falco, R.E. 1977 Coherent motions in outer region of turbulent boundary layers. *Phys. Fluids* **20** (124).

Ghaemi, S. & Scarano, F. 2011 Counter-hairpin vortices in the turbulent wake of a sharp trailing edge. *J. Fluid Mech.* **689**, 317–356.

Head, M.R. & Bandyopadhyay, P. 1981 New aspects of turbulent boundary-layer structure. *J. Fluid Mech.* **107**, 297–338.

Katul, G., Kuhn, G., Schieldge, J. & Hsieh, C.-I. 1997 The ejection-sweep character of scalar fluxes in the unstable surface layer. *Bound.-Lay. Meteorol.* **83** (1), 1–26.

Kline, S.J., Reynolds, W.C., Schraub, F.A. & Runstadler, P.W. 1967 The structure of turbulent boundary layers. *J. Fluid Mech.* **30** (04), 741–773.

Li, D. & Bou-Zeid, E. 2011 Coherent structures and the dissimilarity of turbulent transport of momentum and scalars in the unstable atmospheric surface layer. *Bound.-Lay. Meteorol.* **140** (2), 243–262.

Provenzale, A. 1999 Transport by coherent barotropic vortices. *Annu. Rev. Fluid Mech.* **31** (1), 55–93.

Rouson, D.W.I. & Eaton, J.K. 2001 On the preferential concentration of solid particles in turbulent channel flow. *J. Fluid Mech.* **428**, 149–169.

Shaw, R.A., Reade, W.C., Collins, L.R. & Verlinde, J. 1998 Preferential concentration of cloud droplets by turbulence: Effects on the early evolution of cumulus cloud droplet spectra. *J. Atmos. Sci.* **55** (11), 1965–1976.

Vanderwel, C. & Tavoularis, S. 2011 Coherent structures in uniformly sheared turbulent flow. *J. Fluid Mech.* **689**, 434–464.

Vanderwel, C. & Tavoularis, S. 2014*a* Measurements of turbulent diffusion in uniformly sheared flow. *J. Fluid Mech.* **(submitted)**.

Vanderwel, C. & Tavoularis, S. 2014*b* On the accuracy of PLIF measurements in slender plumes. *Exp. Fluids* **(submitted)**.

Vanderwel, C. & Tavoularis, S. 2014*c* Relative dispersion of a passive scalar plume in turbulent shear flow. *Phys. Rev. E* **89** (4), 041005.

Wu, X. & Moin, P. 2010 Transitional and turbulent boundary layer with heat transfer. *Phys. Fluids* **22** (8), 085105.

# Chapter 9

# Conclusion

## 9.1 Summary

This work investigated conclusively the turbulent diffusion of a point-source plume in uniformly sheared flow generated in a water tunnel. Simultaneous measurements of the concentration and velocity fields were performed using stereoscopic particle image velocimetry and planar laser-induced fluorescence. The instantaneous and statistical properties of the flow were documented in detail and allowed for the investigation of many facets of turbulent diffusion.

Significant developments to the planar laser-induced fluorescence measurement technique were accomplished, which allowed us to quantify the uncertainty of the technique and apply corrections to the present measurements. We evaluated the uncertainty caused by secondary fluorescence and concentration non-uniformity across the laser sheet, effects that had been hitherto neglected in previous applications of the PLIF technique. We developed correction procedures for the effect of secondary fluorescence in the calibration process and in the instantaneous concentration maps and identified criteria to quantify the importance of concentration non-uniformity across the laser sheet.

An analysis of the absolute diffusion of the plume was performed considering the ensemble-properties of the concentration and mixed concentration-velocity statistics in an Eulerian reference frame. The mean concentration maps were described well by Gaussian profiles, and the maximum mean concentration and the plume widths evolved downstream following power laws. The r.m.s. concentration maps were also Gaussian, without the double peaks that were observed by some previous researchers; this difference was attributed to the fact that the integral lengthscale of the present flow was much larger than the plume width. Maps of all three components of the

turbulent scalar flux vector were determined and related to maps of the mean concentration gradient through a first-order gradient transport model. For the first time, all components of the turbulent diffusivity tensor were measured directly. The normal components of the diffusivity tensor were consistent with the apparent diffusivities determined from measurements of the plume growth; however, the off-diagonal components were found to be large and the streamwise diffusivity was counter-gradient. These findings were explained by physical arguments and were compared with existing theoretical predictions. The measured diffusivities had the best agreement with the predictions by Tavoularis & Corrsin (1985). The strong anisotropy of the measured turbulent diffusivity tensor is in contrast with most diffusion models, which assume that the turbulent diffusivity tensor is constant and isotropic. The measurements were also used for the assessment of the importance of the individual terms in the advection-diffusion equation.

The analysis of the relative diffusion of the plume was performed using two different methods of analysis of the concentration maps. First, by constructing relative concentration maps by ensemble-averaging the instantaneous maps each shifted to a common centre-of-mass, and determining the relative plume width as the square root of the second central moment of the relative concentration distribution. Second, by analyzing the distance-neighbour function, constructed from the marginal pdf of two-dimensional autocorrelation maps of the concentration. The evaluation of the standard deviation of the distance-neighbour function was consistent with the evaluation of the relative plume width, both of which are measures of the r.m.s. particle separation. The evolution of the r.m.s. particle separation was also consistent with Richardson-Obukhov scaling, in which Richardson's constant was set to 0.35. Furthermore, Batchelor scaling was also consistent with a wide range of the results, which indicates that these two regimes overlap at moderate Reynolds number, in conformity with observations reported by recent particle tracking studies.

The fine structure of the concentration field and the mixed velocity-scalar statistics of the plume were documented. Unlike most previous studies, the scalar pdf was highly skewed and distinctly non-Gaussian as a consequence of the strong intermittency of the present plume. The measured conditional expectations of the velocity

components conditioned on the scalar value were strongly non-linear; their shapes were explained by considering the signs of the mean scalar flux and the anisotropy of the Reynolds stress in the flow. The scalar derivative pdf had long tails, consistent with other studies. The conditional expectations of the scalar derivatives, conditioned on the value of the scalar, were non-linear. These results clearly demonstrated the consequences of strong intermittency of the scalar field.

The effects of the individual coherent structures on scalar transport were also investigated by analyzing the instantaneous velocity and concentration maps. An algorithm was applied to identify the locations of coherent structures, however, these locations were found not to have any direct correlation with the scalar field. Maps of the mean velocity field conditional of the presence of large scalar flux events were consistent with the cross-sections of hairpin vortices, indicating the fact that hairpin vortices are the dominant mechanism for large scalar flux events. As a corollary to this result, we confirmed that the scalar flux was correlated with the Reynolds stress, which is also associated with the presence of hairpin vortices.

## 9.2 Main contributions

The present study reported high-quality measurements of a passive scalar plume in USF. To ensure the quality of the concentration measurements, a thorough analysis of the uncertainty of the PLIF technique was performed, investigating, for the first time, the effects of secondary fluorescence and concentration non-uniformity across the laser sheet. We identified criteria to quantify the importance of concentration non-uniformity across the laser sheet. We also developed an improved calibration procedure to account for secondary fluorescence and devised a novel method for removing the effect of secondary fluorescence from the instantaneous concentration maps.

The present study is the first time measurements of turbulent diffusion were obtained in USF in a water tunnel using SPIV and PLIF. This study reported extensive simultaneous measurements of the velocity and concentration, which contribute to the experimental database available in the literature. For the first time, it presented

full maps of the turbulent properties in cross-sections of the flow, as opposed to most previous studies, which reported point measurements obtained by LDA, hot-wires, cold-wires, and thermistors in wind tunnels. These measurements allowed for the determination of the velocity integral lengthscales in multiple directions, which had never been measured before. They also allowed for documentation of the mean and fluctuating concentration maps, as well as the mixed joint concentration-velocity statistics.

A significant contribution of this study is the measurement, for the first time, of all components of the turbulent diffusivity tensor at once. This was done by simultaneously fitting maps of the scalar derivatives to maps of the scalar flux, making use of the fact that the turbulence properties were homogeneous in cross-sections normal to the flow direction. The turbulent diffusivity tensor was found to be highly anisotropic, which highlights the shortcomings of most simplified diffusion models which assume a constant scalar value of the turbulent diffusivity or a diagonal turbulent diffusivity tensor. The contribution of each component of the tensor to the total diffusion was estimated and sophisticated physical arguments were made to explain the observed phenomena.

Analysis of the relative diffusion of the plume enabled us to investigate the shape of the distance-neighbour function and the evolution of the r.m.s. particle separation, for which the literature reports conflicting results, especially at moderate Reynolds number. The shape of the distance-neighbour function was found to be consistent with Richardson's predicted distribution, confirming previous observations by particle tracking but conflicting with other previous investigations of plumes. The r.m.s. particle separation remained in the inertial subrange and was consistent with Richardson-Obuhkov scaling with Richardson's constant set to 0.35, confirming that the Richardson-Obuhkov regime does manifest at moderate Reynolds number. We were also surprised to find that the Batchelor regime extended well beyond the Batchelor timescale, indicating that these two regimes overlap at moderate Reynolds number.

The fine structure of the turbulent mixing was also documented by measuring the pdf of the velocity and scalar, as well as the conditional expectations that appear in

the balance equation for the scalar pdf. We concluded that the strong intermittency of the plume was the cause for the strong skewness of the scalar pdf and the distinct non-linearity of the conditional expectations. These observations are in contrast with most previous studies and fill a gap in the literature.

The role of coherent structures in the turbulent diffusion of the plume was also investigated. Instantaneous measurements demonstrated that vortices in the flow induce motions in nearby fluid that effectuate scalar transport. For the first time, a conditional eddy analysis was adapted to investigate the conditional flow field around large scalar flux events, and the results demonstrated conclusively that hairpin vortices are the dominant mechanism for large scalar flux events. We were also the first to document the correlation between the scalar flux and the Reynolds stress, illustrating the link between coherent structures and scalar transport.

### 9.3 Recommendations for future work

Because of the thoroughness and high quality of the present measurements, further analysis of various facets of turbulent diffusion is still possible. Characteristics of turbulent diffusion that have been studied in previous literature that may be investigated with the present data include, among others, the fractal properties of the scalar interface (Prasad & Sreenivasan, 1989), the evolution of the expected mass fraction of the plume (Sarathi *et al.*, 2010), and an analysis with the perspective of plume tracing (Jackson *et al.*, 2007). These subjects were outside the scope of the current work but would be interesting to investigate in future work.

Further analysis of the anisotropy of the turbulent diffusivity tensor is also warranted, to confirm whether the measured magnitudes of the components of the turbulent diffusivity tensor are applicable to other turbulent shear flows, and to develop the results into useable models for numerical simulations. An interesting observation in the present plume was the fact that the streamwise diffusivity $D_{11}$ was initially positive, became negative, and continued to increase in magnitude downstream. It would be interesting to study the dependence of this component on the initial conditions and to follow its development farther downstream to see if it ever reaches an

asymptote.

A limitation that was encountered with the current plume was its relatively strong intermittency compared with plumes studies by other investigators. This was particularly exacerbated considering the extremely high Schmidt number of the dye in water, especially compared with the studies considering thermal plumes in air, which have Prandtl numbers close to 1. This meant that molecular diffusion was negligible in the present plume so that it remained very sinuous and slender throughout the entire measurement domain. The fact that the intermittency factor was lower than 0.5 at all measurement locations introduced a strong bias into the velocity-concentration correlation. A crude correction for these correlations was developed, but deserves a more thorough investigation. Additionally, it would be interesting to reevaluate some of these properties in a flow with a less intermittent scalar field, for example, a thicker plume, a jet, or a mixing layer.

# Appendix A

# Details of the Water Tunnel Facility

## A.1 Water tunnel design

The University of Ottawa's water tunnel was designed and built in the 1990s. It is a closed-circuit, recirculating facility capable of holding up to approximately 15,000 L of water. The flow velocity through the test section can be varied in the range of 0.05 to 0.4 m/s. Several rail systems, positioned along the four walls of the test section, allow for the positioning and traversing of laser Doppler velocimetry and particle image velocimetry measurement apparatus. In addition to these quantitative measurements techniques, the water tunnel has also been utilized for hydrogen bubble visualisation, lead-foil precipitation, and several kinds of dye visualisation.

In 2010, renovations of the water tunnel were completed (figure A.1), with designs by myself and Dr. Stavros Tavoularis. The objectives of these renovations were (1) to repair certain areas of the reservoir and test section that had developed leaks and (2) to replace the glass windows of the test section by longer ones, improving the optical access and preventing leakage.

The original water tunnel is presented in figure A.2. The original test section frame was composed of three separate sections that were bolted together. Between these sections, boundary layer suction hoses were installed, however these did not provide uniform suction and eventually became problematic due to leaks. The redesigned frame is welded as a single piece, removing the problematic frame members and increasing the viewing range. Drawings of the structural design of the new test section are provided in figure A.3. The inner dimensions and locations of the traversing carts remained the same as in the old tunnel with the exception of an added side traversing system along the second vertical wall.

The stress on the glass and frame due to the weight of the materials and the

Figure A.1: A SolidWorks model of the new water tunnel facility; model created by myself and Rachel Andersen.

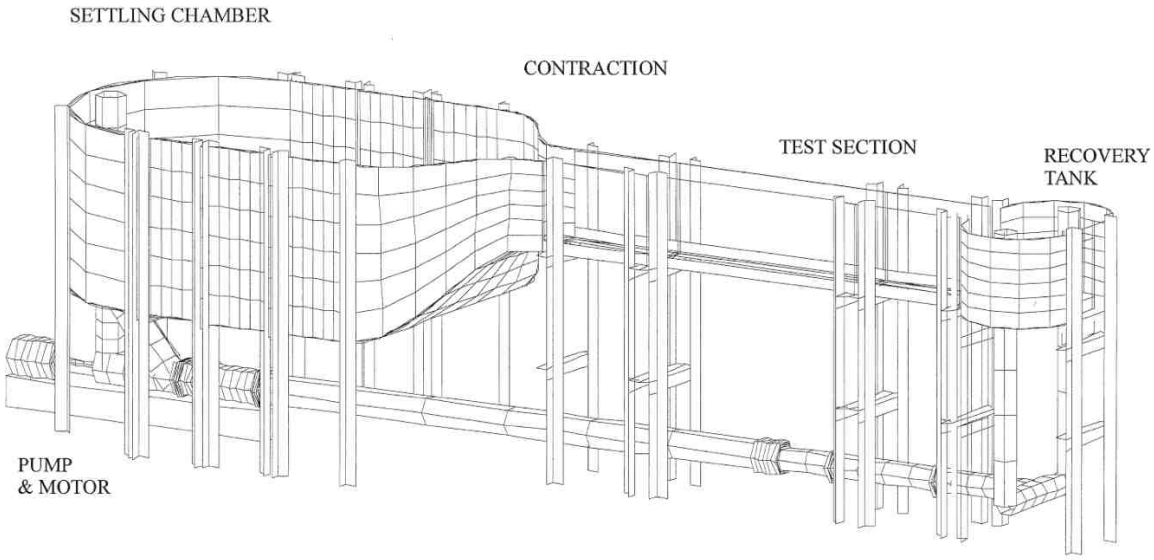


Figure A.2: Model of the old water tunnel facility (drawing by Ben Kislich-Lemyre).

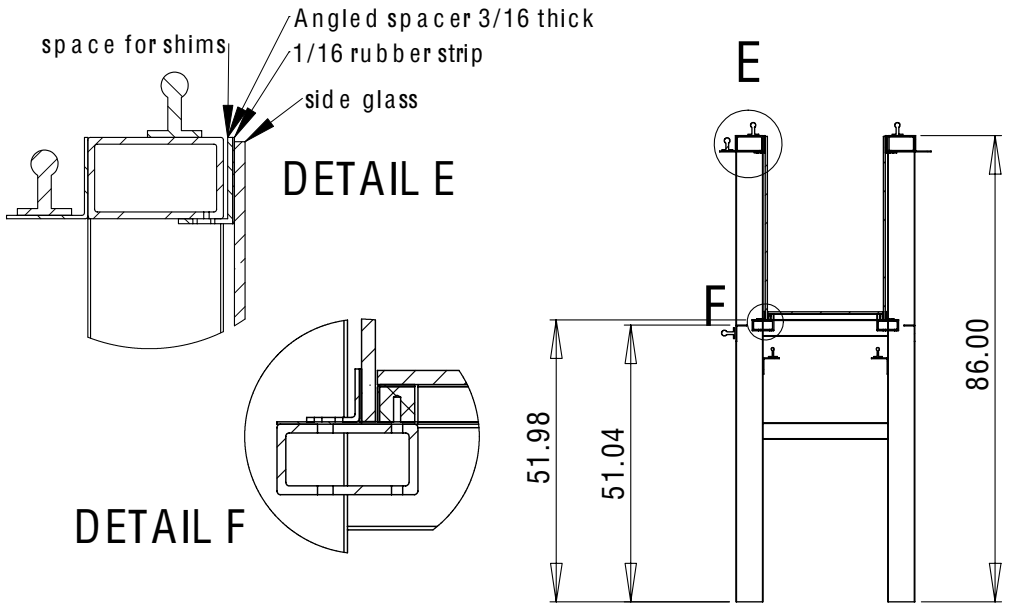


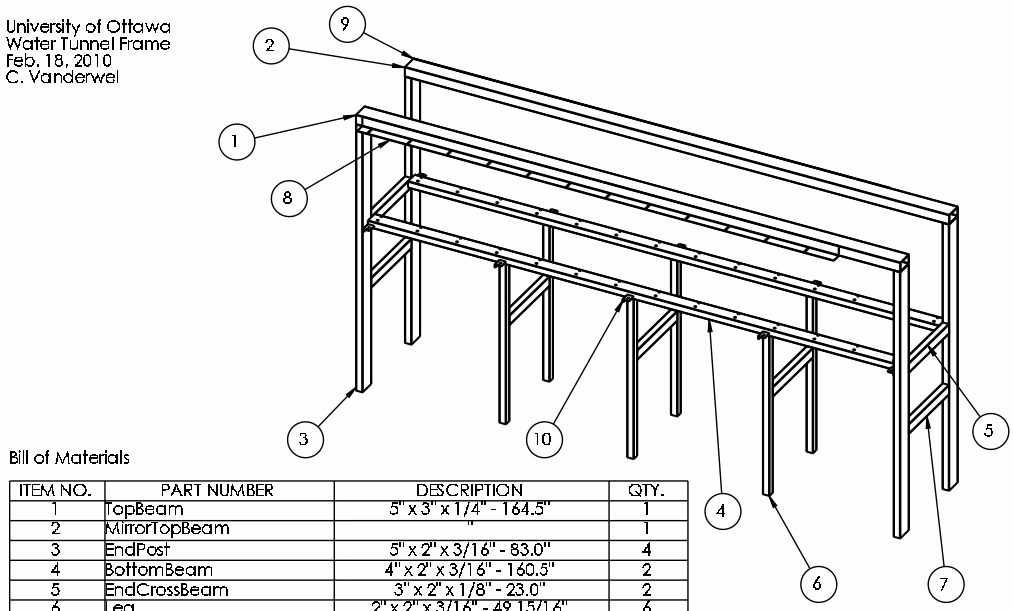


Bill of Materials

| ITEM NO. | PART NUMBER | DESCRIPTION | QTY. |
|---|---|---|---|
| 1 | TopBeam | 5" x 3" x 1/4" - 164.5" | 1 |
| 2 | MirrorTopBeam | " | 1 |
| 3 | EndPost | 5" x 2" x 3/16" - 83.0" | 4 |
| 4 | BottomBeam | 4" x 2" x 3/16" - 160.5" | 2 |
| 5 | EndCrossBeam | 3" x 2" x 1/8" - 23.0" | 2 |
| 6 | Leg | 2" x 2" x 3/16" - 49 15/16" | 6 |
| 7 | LowerCrossBeam | 3" x 2" x 1/8" - 23.0" | 5 |
| 8 | AngleForTopSideRail | Angle 3" x 3" x 3/16" - 144.0" | 1 |
| 9 | MirrorAngleForTopSideRail | " | 1 |
| 10 | SideRailSupport | Angle 2" x 1" x 3/16" - 2.75" | 5 |
| 11 | MirrorSideRailSupport1 | " | 5 |

12

Figure A.3: Drawings and bill of materials for the structural design of the new test section.

hydrostatic pressure was estimated using manual calculations as well as with the SolidWorks Simulation software (figure A.4). The factors of safety on the bottom glass and the side glass were approximately 10 and 4, respectively. The maximum outwards displacement of the test section frame when filled with water was about 2 mm.

In addition to the test section, the reservoir was refurbished to reduce leaking (figure A.5). Two of the three joints were welded together. On the last joint, a new gasket was installed to eliminate leaking. In addition to these changes, two additional screens were installed in order to help smooth and straighten the flow. The screens were placed in order of decreasing solidity and increasing mesh spacing towards downstream.

## A.2 Measurements in unobstructed flow

In order to characterize the flow in the water tunnel, measurements in the unobstructed test section were taken using Laser Doppler Velocimetry (LDV), with a water depth of 426 mm and with the pump speed controller set to 20.00 Hz. The measurements were taken to serve as a baseline for the turbulence properties in the channel.

Profiles of the mean velocity and r.m.s. velocity fluctuation are presented in figures A.6 and A.8. From the velocity profile of $U_1$, the boundary layer thickness is measured according to the table below. The boundary layer Reynolds number reached a value of approximately

$$Re_{x_1} = \frac{U_1 x_1}{\nu} = \frac{0.17\text{m/s} \times 3\text{m}}{1.5 \times 10^{-5}\text{m}^2/\text{s}} = 34000 \ . \tag{A.1}$$

As this is less than $5 \times 10^5$, this boundary layer is deemed to be be laminar, or at least not fully turbulent. According to the Blasius solution, a laminar boundary layer thickness is expected to vary with downstream position as

$$\delta = \frac{5.0 \ x_1}{Re_{x_1}^{1/2}} = 5.0 \ x_1 \left(\frac{\nu}{U_1 x_1}\right)^{1/2} = 5.0 \left(\frac{\nu}{U_1 x_1}\right)^{1/2} x_1^{1/2} \ . \tag{A.2}$$

A comparison of the measured boundary layer thickness to this solution is presented in figure A.7.

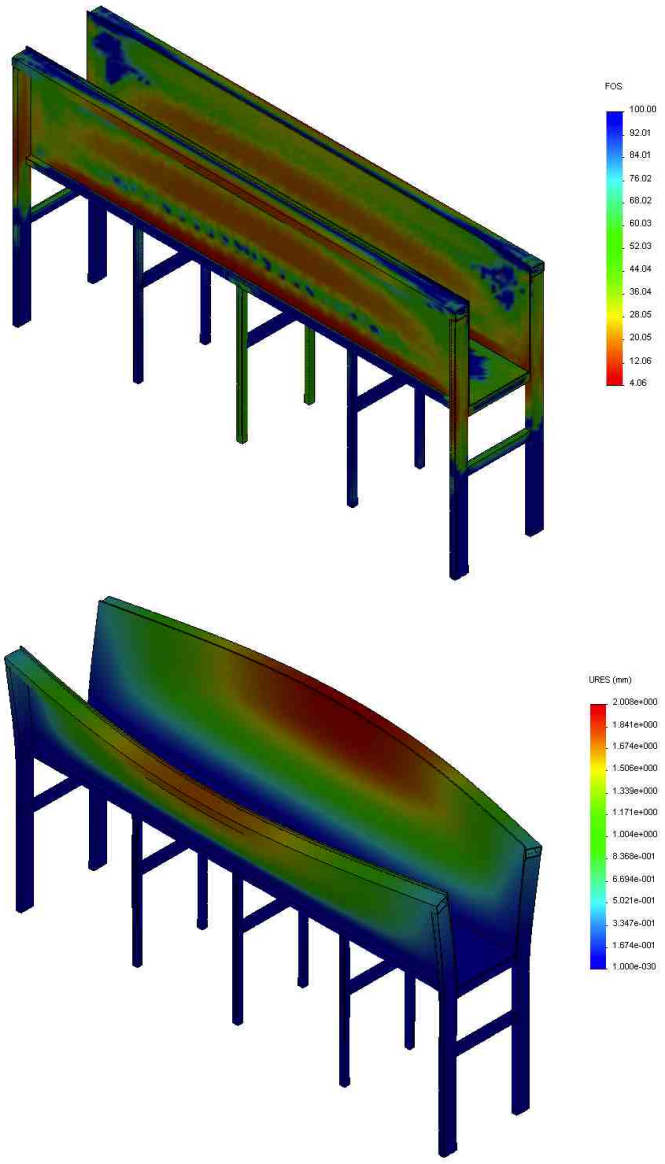


Figure A.4: SolidWorks Simulation calculating the factor of safety on the test section glass (top) and the displacement of the test section frame members (bottom).

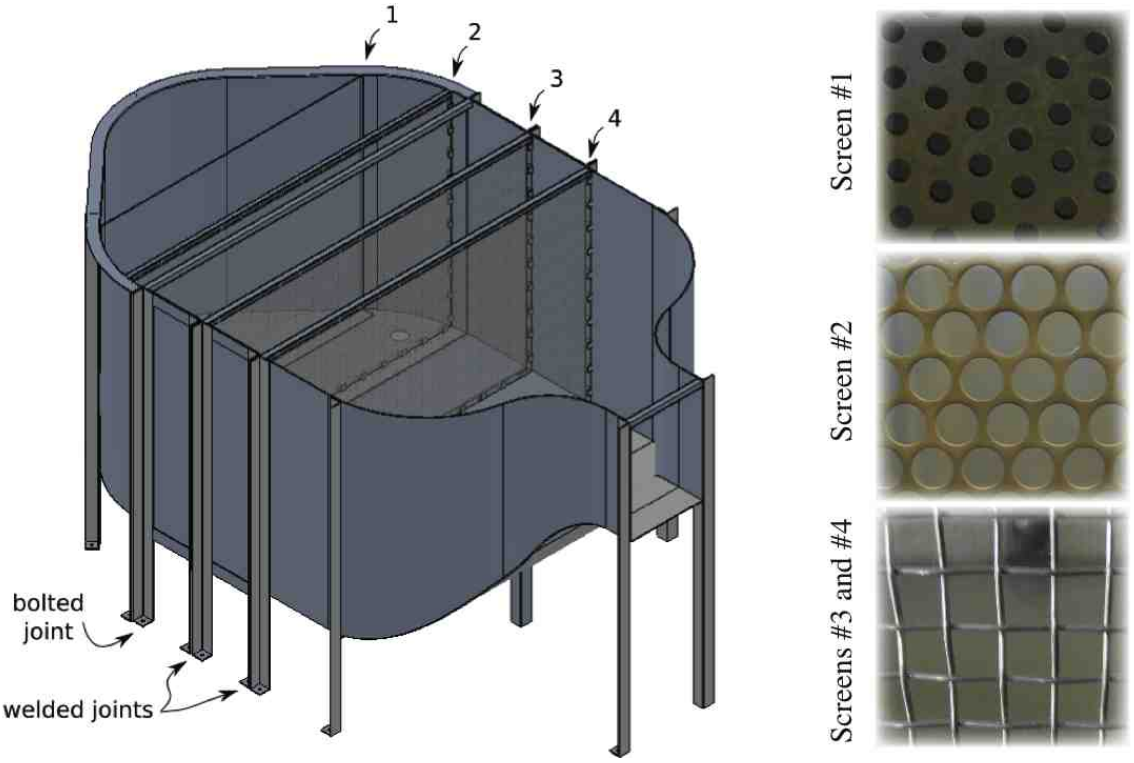


Figure A.5: Illustration of the reservoir construction and the installed screens.

Some inhomogeneities are present in the spanwise profiles of $U_2$ presented in figure A.8. These are attributed to weak streamwise vortices originating from the perforated cylinder connected to the pump and have the form sketched in figure A.9. Following this finding, an additional flow screen comprised of a 1.52 m by 2.44 m (5 ft by 8 ft) sheet of white pond filter media was added as a resistance in the reservoir at the outlet of the pump in order to further reduce the strengths of the streamwise vortices.

Open surface water tunnels are known to have low-frequency surface waves that effect the flow velocity. A video of surface waves shows their amplitude at about 1 mm (see figure A.10). The effect of these long surface waves on the flow velocity was investigated by analyzing a time history of $U_1$ at $x_1 = 2.000$ m, $x_2 = 250$ mm, $x_3 = 0$. These long waves were visible in the velocity signal and had an amplitude of about 0.0011 m/s and a frequency of 0.0849 Hz. I applied a lowpass filter with a cutoff of 0.3 Hz (three times the wave frequency), in order to remove the small fluctuations and isolate the long waves. A sample of the velocity signal and velocity spectrum

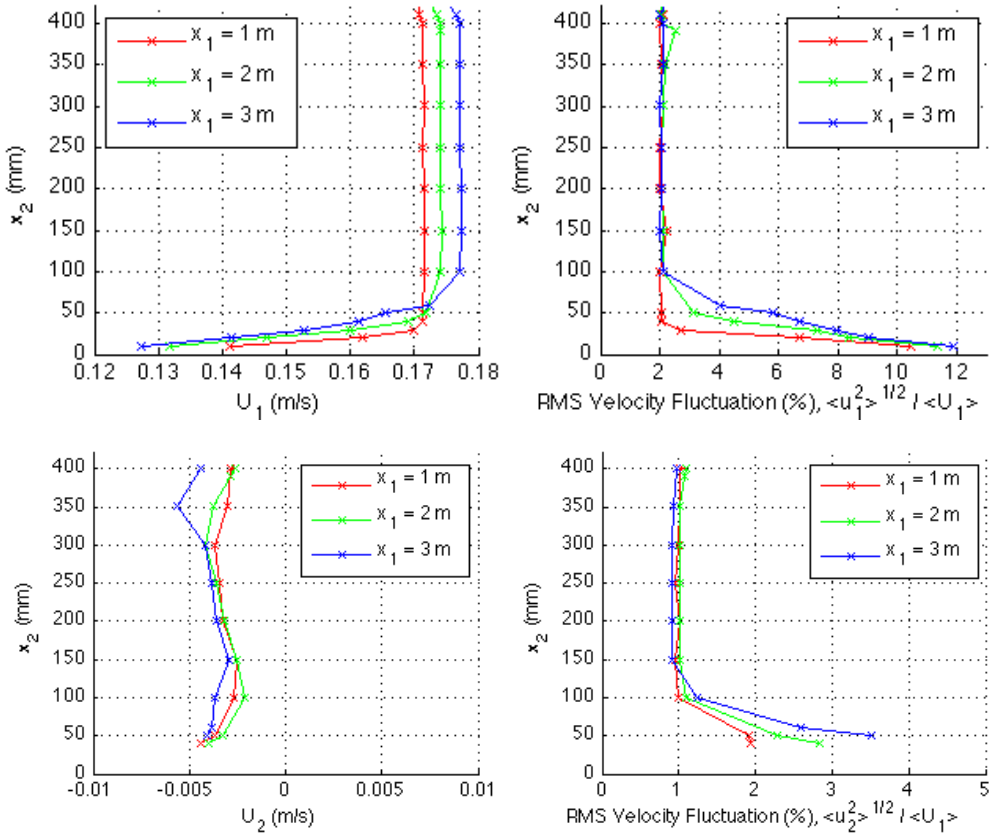


Figure A.6: Measurements of the mean (left) and standard deviation (right) of the streamwise (top) and vertical (bottom) velocity profiles in the centre of the tunnel ($x_3 = 0$) at $x_1 = 1$ m, 2 m, and 3 m.

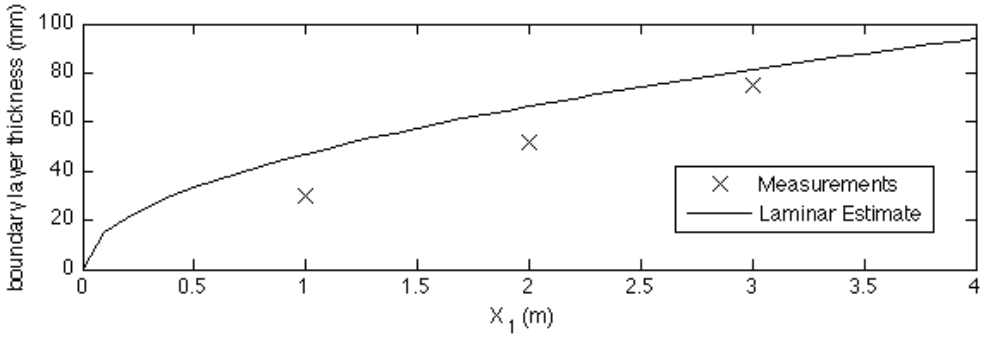


Figure A.7: Development of the measured boundary layer thickness compared to the laminar solution.

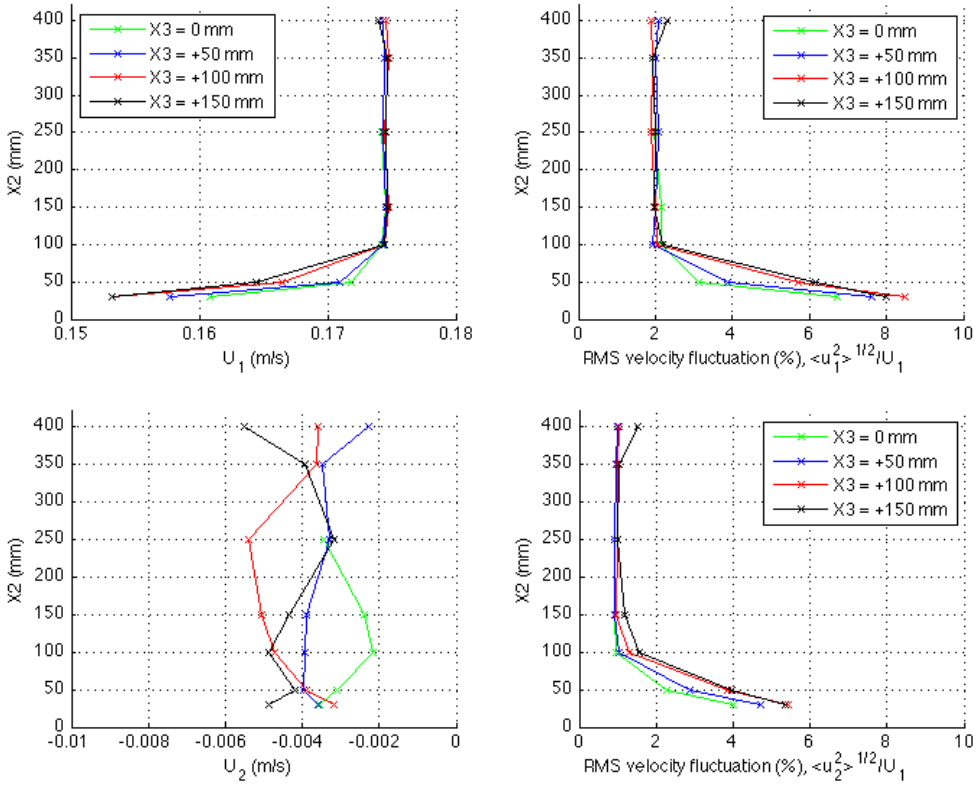


Figure A.8: Measurements of the mean (left) and standard deviation (right) of the streamwise (top) and vertical (bottom) velocities at several spanwise positions. The streamwise position is halfway down the tunnel ($x_1 = 2.000$ m). The water tunnel is 540 mm wide so $x_3$ extends to ± 270 mm. The LDV can reach from -126 mm < $x_3$ < +201 mm using the current traverse ($x_3 = 0$ in the centre).

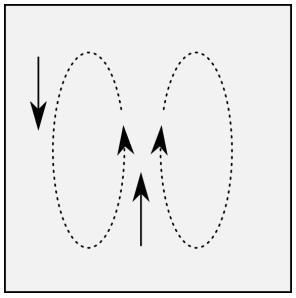

Figure A.9: The measurements of $U_2$ at several spanwise positions indicate that weak streamwise vortices are present in the tunnel having this approximate configuration.

before and after filtering are presented in figure A.11. The standard deviation of the filtered signal is 0.8% compared to 2.0% for the original data. Assuming that the waves and the small-scale fluctuations ("turbulence") are uncorrelated, their effects can be summed as:

$$\sigma^2_{total} = \sigma^2_{waves} + \sigma^2_{turbulence} \tag{A.3}$$

$$\sigma^2_{turbulence} = 2.0^2 - 0.8^2 = 1.8^2$$

The standard deviation of the turbulence without the waves (*i.e.*, the free stream turbulence intensity) is therefore estimated to be about 1.8%. For future measurements in the water tunnel, the low-frequency spectrum should be investigated for signs of long surfaces waves. If these waves are apparent, unless the low-frequency phenomena are of interest, the data should be high-pass filtered with a cutoff of between 0.1 and 0.3 Hz to remove any effect of the low-frequency surface waves before analyzing the velocity signal. However, it should be noted that I found that the low-frequency surface waves were partially suppressed by installing a plate at the height of the water level, spanning the whole width of the tunnel, inserted at the beginning of the test section; this is the case using the flow separator apparatus to generate uniformly sheared flow.

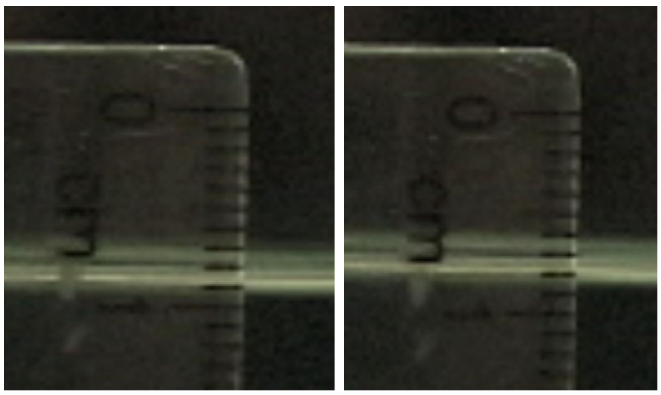

Figure A.10: Wave height in the test section measured using a video camera. Minimum (left) and maximum (right) water heights are shown, having a difference of nearly 1 mm.

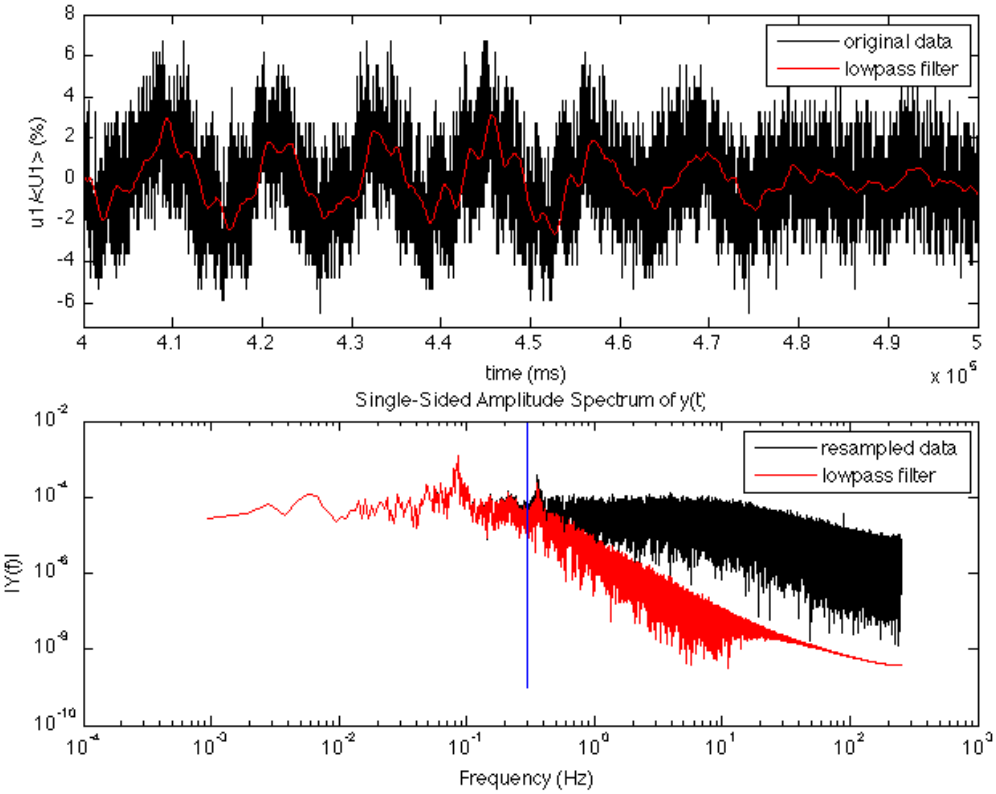


Figure A.11: Sample of the velocity signal (top) and spectrum (bottom) before and after low-pass filtering.

# Appendix B

## Additional Figures

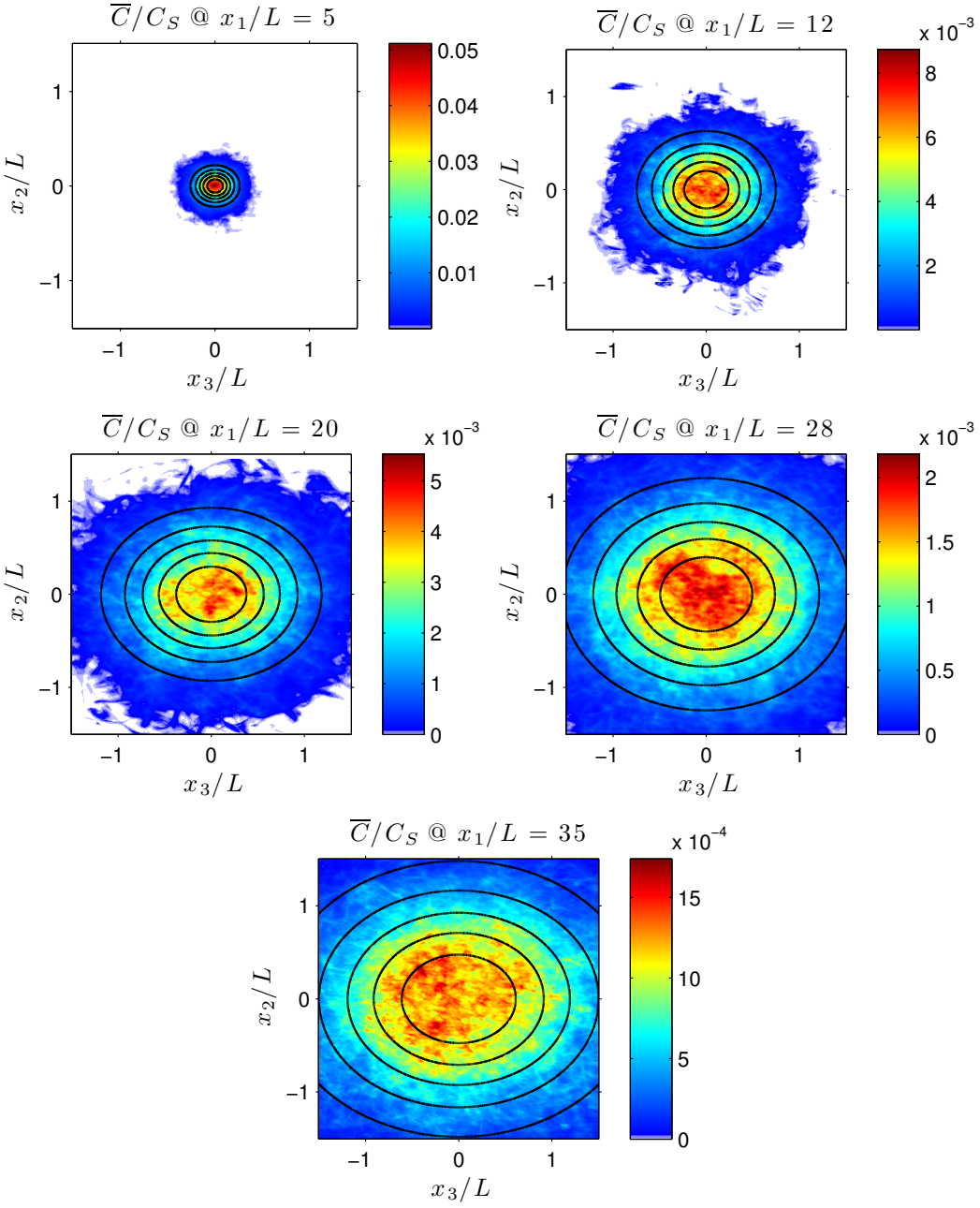


Figure B.1: Maps of the mean concentration; black ellipses indicate contours of fitted Gaussian functions.

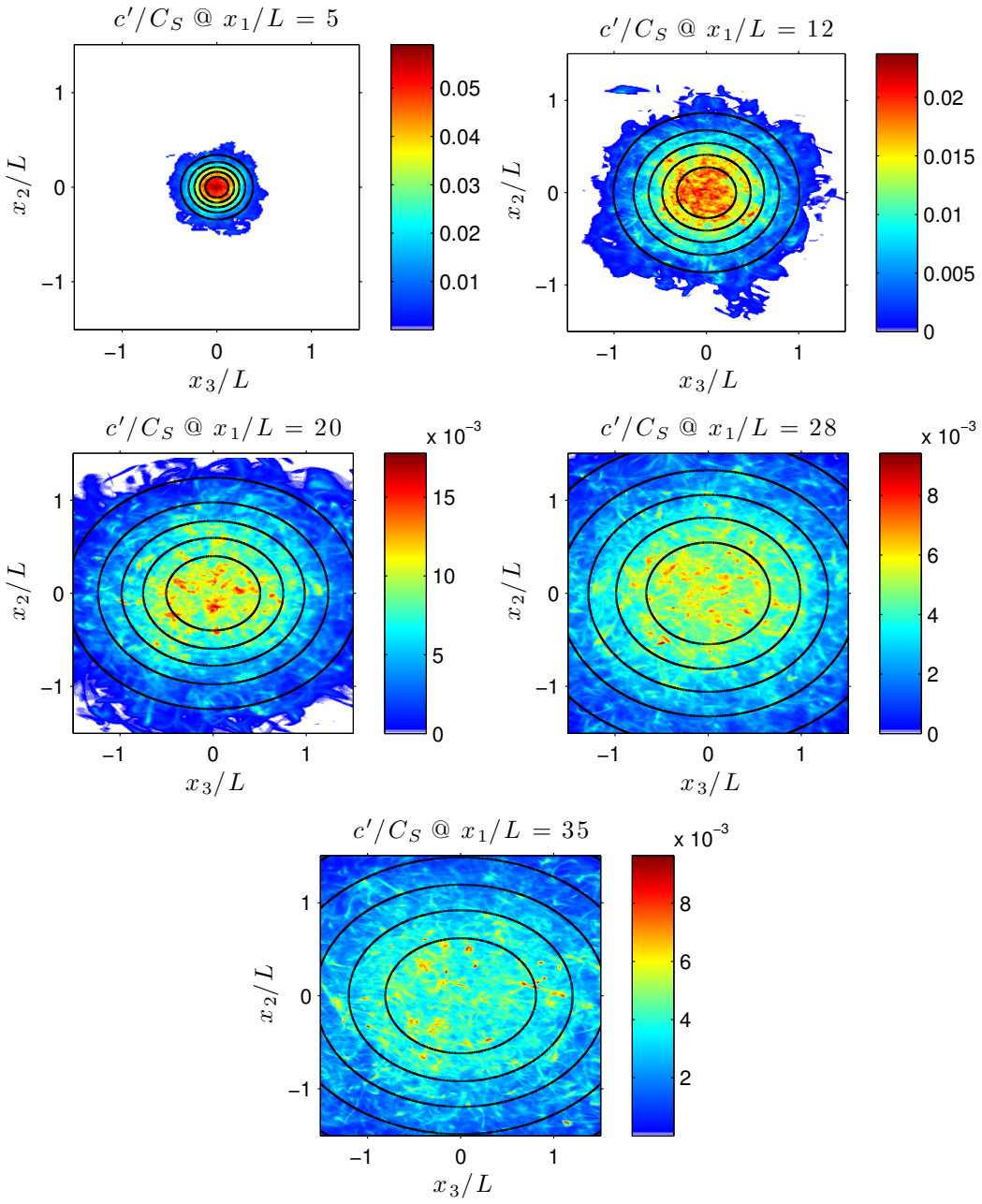


Figure B.2: Maps of the root-mean-square concentration fluctuations; black ellipses indicate contours of fitted Gaussian functions.

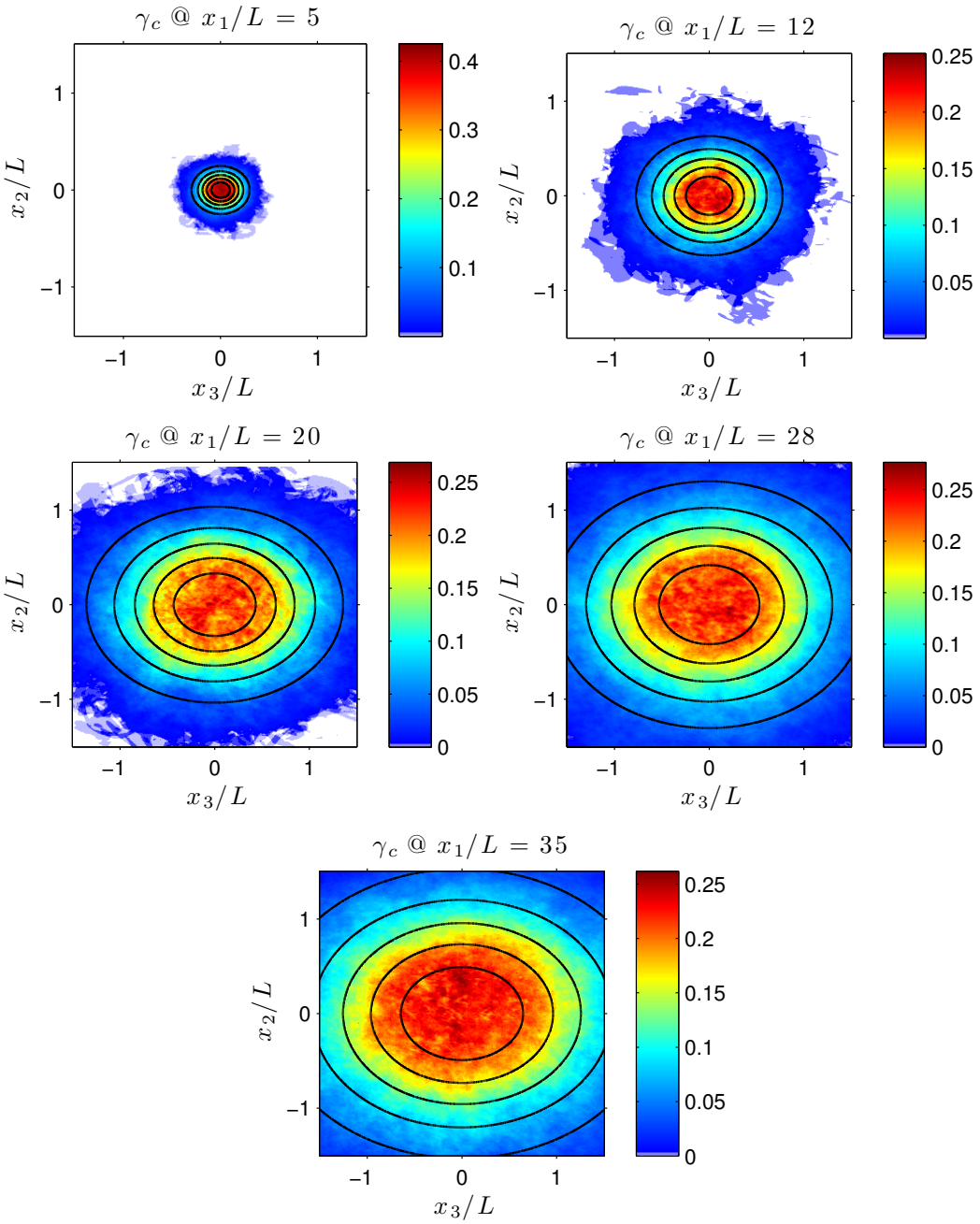


Figure B.3: Maps of the concentration intermittency factor; black ellipses indicate contours of fitted Gaussian functions.

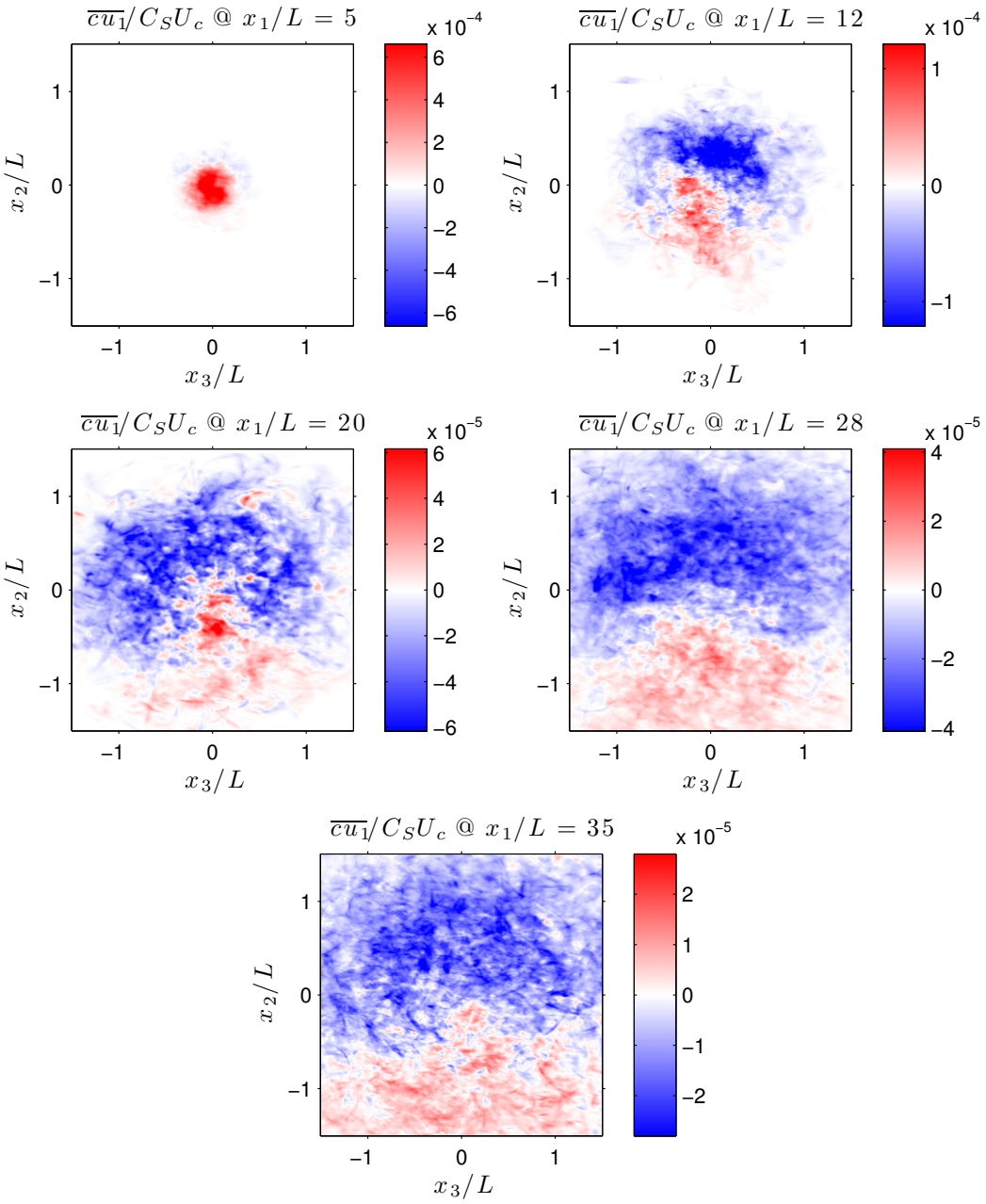


Figure B.4: Maps of $\overline{cu_1}/C_S U_c$.

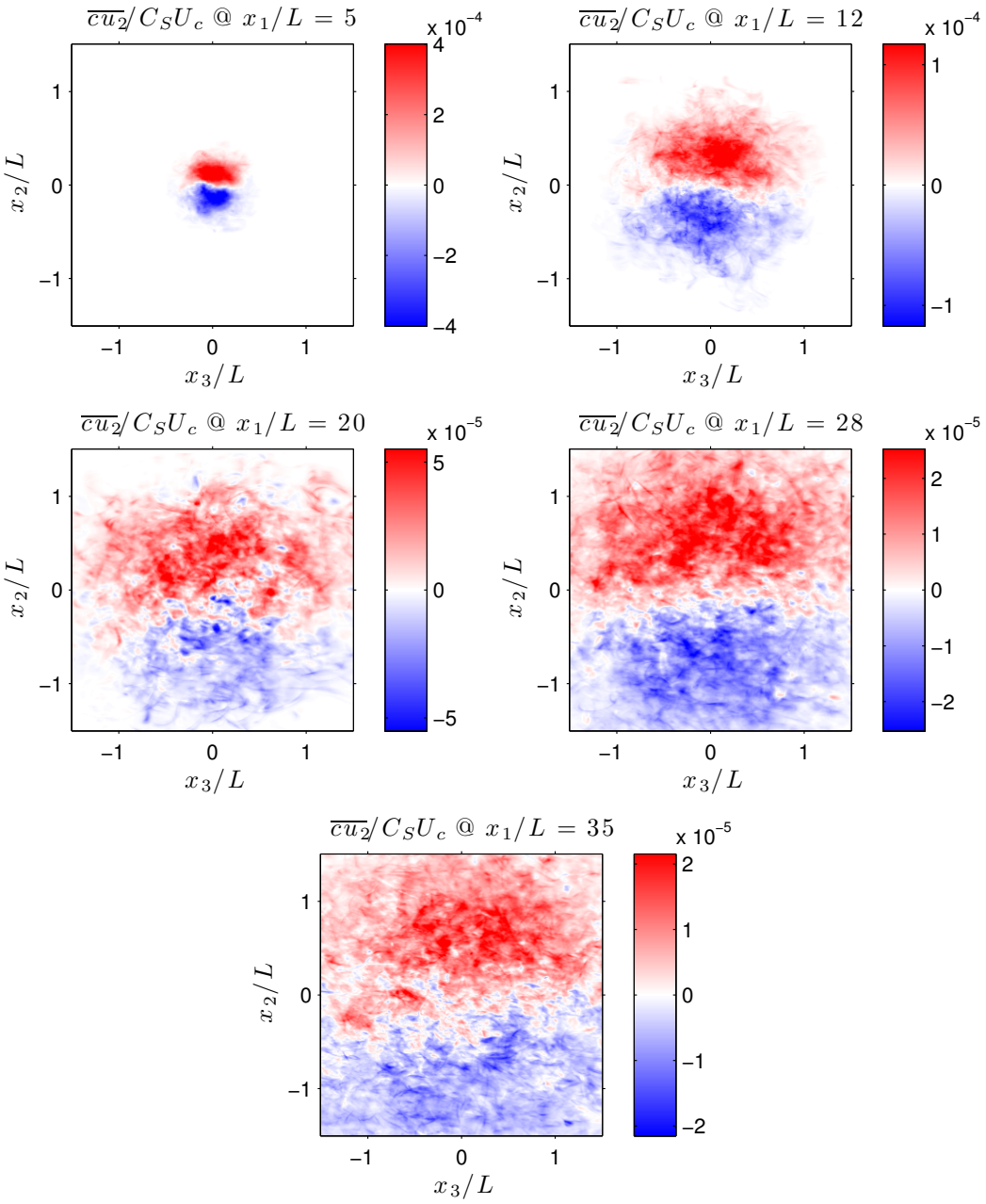


Figure B.5: Maps of $\overline{cu_2}/C_S U_c$.

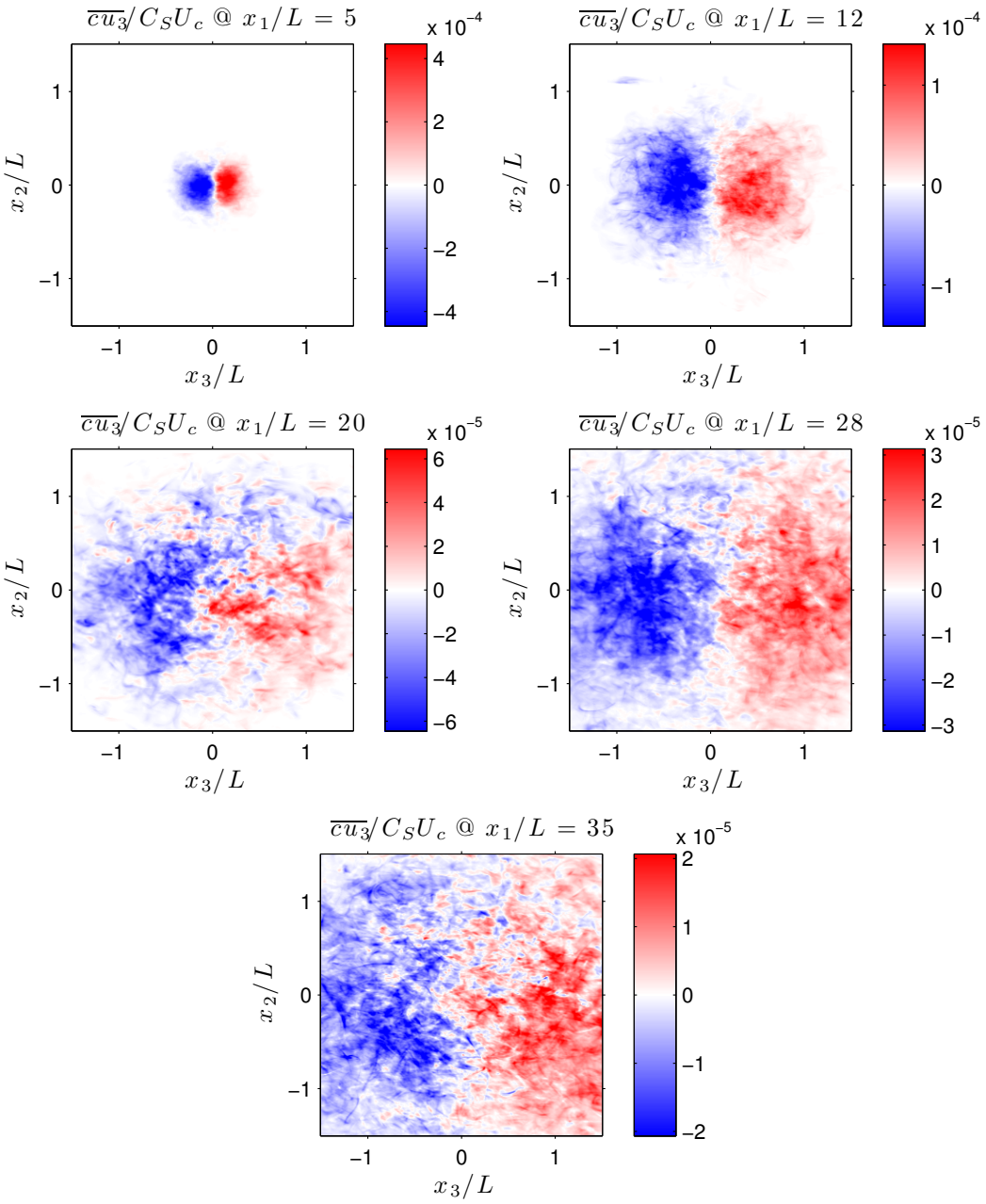


Figure B.6: Maps of $\overline{cu_3}/C_S U_c$.

## References


Adrian, R.J. 1994 Stochastic estimation of conditional structure: a review. *Appl. Sci. Res.* **53** (3-4), 291–303.

Adrian, R.J. 2007 Hairpin vortex organization in wall turbulence. *Phys. Fluids* **19** (4), 041301.

Adrian, R.J. & Moin, P. 1988 Stochastic estimation of organised turbulent structure: homogeneous shear flow. *J. Fluid Mech.* **190**, 531–559.

Adrian, R.J. & Westerweel, J. 2011 *Particle Image Velocimetry*. Cambridge University Press.

Anand, M.S. & Pope, S.B. 1985 Diffusion behind a line source in grid turbulence. In *Turbulent Shear Flows 4*, pp. 46–61. Springer.

Anaspec (Fremont, CA, USA) 2013 Rhodamine 6G Fluorescence Reference Standard [Online - Accessed September 2013]. Available from: http://www.anaspec.com/products/product.asp?id=28765.

Antonia, R.A. 1981 Conditional sampling in turbulence measurement. *Annu. Rev. Fluid Mech.* **13** (1), 131–156.

Arcoumanis, C., McGuirk, J.J. & Palma, J.M.L.M. 1990 On the use of fluorescent dyes for concentration measurements in water flows. *Exp. Fluids* **10**, 177–180.

Arya, S.P. 1999 *Air Pollution Meteorology and Dispersion*. Oxford University Press, New York.

Azzalini, A. 1985 A class of distributions which includes the normal ones. *Scand. J. Statist.* **12** (2), 171–178.

Batchelor, G.K. 1949 Diffusion in a field of homogeneous turbulence. I. Eulerian analysis. *Aust. J. Chem.* **2** (4), 437–450.

Batchelor, G. K. 1952 Diffusion in a field of homogeneous turbulence. *Math. Proc. Cambridge* **48**, 345–362.

Behnamian, A. & Tavoularis, S. 2013 Scalar-field probability density functions and conditional expectations in uniformly sheared turbulence. In *Eighth International Symposium on Turbulence and Shear Flow Phenomena (TSFP8), Poitiers, France*.

Berg, J., Lüthi, B., Mann, J. & Ott, S. 2006 Backwards and forwards relative dispersion in turbulent flow: An experimental investigation. *Phys. Rev. E* **74** (1), 016304.

Bilger, R.W. 1989 Turbulent diffusion flames. *Annu. Rev. Fluid Mech.* **21** (1), 101–135.

Borg, A., Bolinder, J. & Fuchs, L. 2001 Simultaneous velocity and concentration measurements in the near field of a turbulent low-pressure jet by digital particle image velocimetry–planar laser-induced fluorescence. *Exp. Fluids* **31** (2), 140–152.

Bourgoin, M., Ouellette, N.T., Xu, H., Berg, J. & Bodenschatz, E. 2006 The role of pair dispersion in turbulent flow. *Science* **311** (5762), 835–838.

Brier, G.W. 1950 The statistical theory of turbulence and the problem of diffusion in the atmosphere. *J. Meteorol.* **7** (4), 283–290.

Calef, D.F. & Deutch, J.M. 1983 Diffusion-controlled reactions. *Annu. Rev. Phys. Chem.* **34** (1), 493–524.

Catrakis, H.J. & Dimotakis, P.E. 1996 Mixing in turbulent jets: scalar measures and isosurface geometry. *J. Fluid Mech.* **317**, 369–406.

Chang, K.-A. & Cowen, E.A. 2002 Turbulent prandtl number in neutrally buoyant turbulent round jet. *J. Eng. Mech.-ASCE* **128** (10), 1082–1087.

Corrsin, S. 1974 Limitations of gradient transport models in random walks and in turbulence. *Adv. Geophys.* p. 25.

Cowen, E.A., Chang, K.-A. & Liao, Q. 2001 A single-camera coupled PTV–LIF technique. *Exp. Fluids* **31**, 63–73.

Crimaldi, J.P. 2008 Planar laser induced fluorescence in aqueous flows. *Exp. Fluids* **44**, 851–863.

Csanady, G.T. 1963 Turbulent diffusion in Lake Huron. *J. Fluid Mech.* **17** (03), 360–384.

Csanady, G.T. 1973 *Turbulent diffusion in the environment*. D. Reidel Publishing Company.

Davidson, P.A. 2004 *Turbulence - An introduction for scientists and engineers*. New York: Oxford University Press.

De Souza, F.A., Nguyen, V.D. & Tavoularis, S. 1995 The structure of highly sheared turbulence. *J. Fluid Mech.* **303**, 155–167.

Deardorff, J.W. 1966 The counter-gradient heat flux in the lower atmosphere and in the laboratory. *J. Atmos. Sci.* **23**, 503–506.

van Doorne, C. & Westerweel, J. 2007 Measurement of laminar, transitional and turbulent pipe flow using stereoscopic-piv. *Exp. Fluids* **42**, 259–279, 10.1007/s00348-006-0235-5.

van Dop, H. & Verver, G. 2001 Countergradient transport revisited. *J. Atmos. Sci.* **58** (15), 2240–2247.

Falco, R.E. 1977 Coherent motions in outer region of turbulent boundary layers. *Phys. Fluids* **20** (124).

Ferchichi, M. & Tavoularis, S. 2000 Reynolds number effects on the fine structure of uniformly sheared turbulence. *Phys. Fluids* **12** (11), 2942–2953.

Ferchichi, M. & Tavoularis, S. 2002 Scalar probability density function and fine structure in uniformly sheared turbulence. *J. Fluid Mech.* **461**, 155–182.

Ferrier, A.J., Funk, D.R. & Roberts, P.J.W. 1993 Application of optical techniques to the study of plumes in stratified fluids. *Dynam. Atmos. Oceans* **20**, 155–183.

Fukushima, C., Aanen, L. & Westerweel, J. 2000 Investigation of the mixing process in an axisymmetric turbulent jet using PIV and LIF. In *Laser Techniques for Fluid Mechanics* (ed. R.J. Adrian *et al.*), pp. 339–356. Springer, Berlin.

Gendron, P.O., Avaltroni, F. & Wilkinson, K.J. 2008 Diffusion coefficients of several rhodamine derivatives as determined by pulsed field gradient–nuclear magnetic resonance and fluorescence correlation spectroscopy. *J. Fluoresc.* **18** (6), 1093–1101.

Ghaemi, S. & Scarano, F. 2011 Counter-hairpin vortices in the turbulent wake of a sharp trailing edge. *J. Fluid Mech.* **689**, 317–356.

Guilbault, G.G., ed. 1990 *Practical Fluorescence*, 2nd edn. Marcel Dekker, Inc.

Hay, J.S. & Pasquill, F. 1959 Diffusion from a continuous source in relation to the spectrum and scale of turbulence. *Adv. Geophys.* **6**, 345–365.

Head, M.R. & Bandyopadhyay, P. 1981 New aspects of turbulent boundary-layer structure. *J. Fluid Mech.* **107**, 297–338.

Incropera, F.P. & DeWitt, D.P. 2002 *Fundamentals of heat and mass transfer*. John Wiley & Sons.

Jackson, J.L., Webster, D.R., Rahman, S. & Weissburg, M.J. 2007 Bed roughness effects on boundary-layer turbulence and consequences for odor-tracking behavior of blue crabs (callinectes sapidus). *Limnol. Oceanogr.* **52** (5), 1883–1897.

Jayesh & Warhaft, Z. 1992 Probability distribution, conditional dissipation, and transport of passive temperature fluctuations in grid-generated turbulence. *Phys. Fluids A* **4** (10), 2292–2307.

Jullien, M.-C., Paret, J. & Tabeling, P. 1999 Richardson pair dispersion in two-dimensional turbulence. *Phys. Rev. Lett.* **82** (14), 2872.

Karasso, P.S. & Mungal, M.G. 1997 PLIF measurements in aqueous flows using the Nd:YAG laser. *Exp. Fluids* **23** (5), 382–387.

Karnik, U. & Tavoularis, S. 1987 Generation and manipulation of uniform shear with the use of screens. *Exp. Fluids* **5**, 247–254.

Karnik, U. & Tavoularis, S. 1989 Measurements of heat diffusion from a continuous line source in a uniformly sheared turbulent flow. *J. Fluid Mech.* **202**, 233–261.

Karnik, U. & Tavoularis, S. 1990 Lagrangian correlations and scales in uniformly sheared turbulence. *Phys. Fluids A* **2** (4), 587–591.

Katul, G., Kuhn, G., Schieldge, J. & Hsieh, C.-I. 1997 The ejection-sweep character of scalar fluxes in the unstable surface layer. *Bound.-Lay. Meteorol.* **83** (1), 1–26.

Kline, S.J., Reynolds, W.C., Schraub, F.A. & Runstadler, P.W. 1967 The structure of turbulent boundary layers. *J. Fluid Mech.* **30** (04), 741–773.

Lavertu, R.A. & Mydlarski, L. 2005 Scalar mixing from a concentrated source in turbulent channel flow. *J. Fluid Mech.* **528**, 135–172.

Lavision GmbH 2012 Particle Image Velocimetry [Online - Accessed 2012]. http://www.lavision.de.

Lee, M.J., Kim, J. & Moin, P. 1990 Structure of turbulence at high shear rate. *J. Fluid Mech.* **216**, 561–583.

Lemoine, F., Wolff, M. & Lebouche, M. 1996 Simultaneous concentration and velocity measurements using combined laser-induced fluorescence and laser doppler velocimetry: Application to turbulent transport. *Exp. Fluids* **20** (5), 319–327.

Lepore, J. & Mydlarski, L. 2011 Lateral dispersion from a concentrated line source in turbulent channel flow. *J. Fluid Mech.* **678**, 417–450.

Li, D. & Bou-Zeid, E. 2011 Coherent structures and the dissimilarity of turbulent transport of momentum and scalars in the unstable atmospheric surface layer. *Bound.-Lay. Meteorol.* **140** (2), 243–262.

Liao, Q. & Cowen, E.A. 2010 Relative dispersion of a scalar plume in a turbulent boundary layer. *J. Fluid Mech.* **661**, 412–445.

Melton, L.A. & Lipp, C.W. 2003 Criteria for quantitative PLIF experiments using high-power lasers. *Exp. Fluids* **35**, 310–316.

Monin, A.S. & Yaglom, A.M. 1975 *Statistical Fluid Mechanics: Mechanics of Turbulence, Vol. 2*. MIT Press.

Mydlarski, L. 2003 Mixed velocity–passive scalar statistics in high-reynolds-number turbulence. *J. Fluid Mech.* **475**, 173–203.

Nakamura, I., Sakai, Y., Miyata, M. & Tsunoda, H. 1986 Diffusion of matter from a continuous point source in uniform mean shear flows (1st report). *B. JSME* **29** (250), 1141–1148.

O'Neill, P.L., Nicolaides, D., Honnery, D. & Soria, J. 2004 Autocorrelation functions and the determination of integral length with reference to experimental and numerical data. In *Proceedings of the Fifteenth Australasian Fluid Mechanics Conference. University of Sydney*.

Ott, S. & Mann, J. 2000 An experimental investigation of the relative diffusion of particle pairs in three-dimensional turbulent flow. *J. Fluid Mech.* **422** (1), 207–223.

Paranthoën, P., Godard, G., Weiss, F. & Gonzalez, M. 2004 Counter gradient diffusion vs "counter diffusion" temperature profile? *Int. J. Heat Mass Trans.* **47** (4), 819–825.

Pope, S. 2000 *Turbulent Flows*. Cambridge University Press.

Prasad, A.K. & Jensen, K. 1995 Scheimpflug stereocamera for particle image velocimetry in liquid flows. *Appl. Opt.* **34** (30), 7092–7099.

Prasad, R.R. & Sreenivasan, K.R. 1989 Scalar interfaces in digital images of turbulent flows. *Exp. Fluids* **7**, 259–264.

Provenzale, A. 1999 Transport by coherent barotropic vortices. *Annu. Rev. Fluid Mech.* **31** (1), 55–93.

Raffel, M., Willert, C. E. & Kompenhans, J. 1998 *Particle Image Velocimetry: A practical guide*. Springer.

Rahman, S. & Webster, D.R. 2005 The effect of bed roughness on scalar fluctuations in turbulent boundary layers. *Exp. Fluids* **38** (3), 372–384.

Richardson, L.F. 1926 Atmospheric diffusion shown on a distance-neighbour graph. *Proc. R. Soc. Lond. A* **110** (756), 709–737.

Riley, J.J. & Corrsin, S. 1974 The relation of turbulent diffusivities to Lagrangian velocity statistics for the simplest shear flow. *J. Geophys. Res.* **79** (12), 1768–1771.

Roberts, O.F.T. 1923 The theoretical scattering of smoke in a turbulent atmosphere. *Proc. R. Soc. Lond. A* **104** (728), 640–654.

Roberts, P.J.W. & Webster, D.R. 2002 Turbulent diffusion. In *Environmental Fluid Mechanics: Theories and Applications*. ASCE Press.

Rogers, M.M., Mansour, N.N. & Reynolds, W.C. 1989 An algebraic model for the turbulent flux of a passive scalar. *J. Fluid Mech.* **203** (1), 77–101.

Rogers, M.M. & Moin, P. 1987 The structure of the vorticity field in homogeneous turbulent flows. *J. Fluid Mech.* **176**, 33–66.

de Roode, S.R., Jonker, H.J.J., Duynkerke, P.G. & Stevens, B. 2004 Countergradient fluxes of conserved variables in the clear convective and stratocumulus-topped boundary layer: The role of the entrainment flux. *Bound.-Lay. Meteorol.* **112** (1), 179–196.

Rouson, D.W.I. & Eaton, J.K. 2001 On the preferential concentration of solid particles in turbulent channel flow. *J. Fluid Mech.* **428**, 149–169.

Salazar, J.P.L.C. & Collins, L.R. 2009 Two-particle dispersion in isotropic turbulent flows. *Annu. Rev. Fluid Mech.* **41** (1), 405–432.

Sarathi, P., Gurka, R., Kopp, G.A. & Sullivan, P.J. 2012 A calibration scheme for quantitative concentration measurements using simultaneous PIV and PLIF. *Exp. Fluids* **52** (1), 247–259.

Sarathi, P., Gurka, R., Sullivan, P.J. & Kopp, G.A 2010 Experimental measurements of expected mass fraction in a contaminant plume. *Bound.-Lay. Meteorol.* **137** (2), 167–185.

Sawford, B. 2001 Turbulent relative dispersion. *Annu. Rev. Fluid Mech.* **33** (1), 289–317.

Shan, J.W., Lang, D.B. & Dimotakis, P.E. 2004 Scalar concentration measurements in liquid-phase flows with pulsed lasers. *Exp. Fluids* **36** (2), 268–273.

Shaw, R.A., Reade, W.C., Collins, L.R. & Verlinde, J. 1998 Preferential concentration of cloud droplets by turbulence: Effects on the early evolution of cumulus cloud droplet spectra. *J. Atmos. Sci.* **55** (11), 1965–1976.

Slade, D.H., ed. 1968 *Meteorology and atomic energy. Report (United States Atomic Energy Commission)* 68-60097. U.S. Atomic Energy Commission, Division of Technical Information.

Specialist Committee on Uncertainty Analysis of 25th ITTC 2008 *Recommended Procedures and Guidelines - Uncertainty Analysis of Particle Image Velocimetry*. 25th International Towing Tank Conference.

Sreenivasan, K.R 1995 On the universality of the Kolmogorov constant. *Phys. Fluids* **7** (11), 2778–2784.

Sreenivasan, K.R., Tavoularis, S. & Corrsin, S. 1982 A test of gradient transport and its generalizations. In *Turbulent Shear Flows 3* (ed. Bradbury, Durst, Launder, Schmidt & Whitelaw), pp. 96–112. Springer Berlin Heidelberg.

Stapountzis, H., Sawford, B.L., Hunt, J.C.R. & Britter, R.E. 1986 Structure of the temperature field downwind of a line source in grid turbulence. *J. Fluid Mech* **165**, 401–424.

Sutton, O.G. 1932 A theory of eddy diffusion in the atmosphere. *Proc. R. Soc. Lond. A* **135** (826), 143–165.

Tavoularis, S. 2005 *Measurement in Fluid Mechanics*. Cambridge University Press.

Tavoularis, S. & Corrsin, S. 1981 Experiments in nearly homogeneous turbulent shear flow with a uniform mean temperature gradient. Part 1. *J. Fluid Mech.* **104**, 311–347.

Tavoularis, S. & Corrsin, S. 1985 Effects of shear on the turbulent diffusivity tensor. *Int. J. Heat Mass Trans.* **28** (1), 265–276.

Tavoularis, S. & Karnik, U. 1989 Further experiments on the evolution of turbulent stresses and scales in uniformly sheared turbulence. *J. Fluid Mech.* **204**, 457–478.

Taylor, G.I. 1921 Diffusion by continuous movements. *Proc. London Math. Soc.* **20** (2), 196–211.

Tennekes, H. & Lumley, J.L. 1972 *A First Course in Turbulence*. MIT press.

Vanderwel, C. 2010 Coherent structures in uniformly sheared turbulence. Master's thesis, University of Ottawa, Ottawa, Canada.

Vanderwel, C. & Tavoularis, S. 2011 Coherent structures in uniformly sheared turbulent flow. *J. Fluid Mech.* **689**, 434–464.

Vanderwel, C. & Tavoularis, S. 2013 Measurements of turbulent diffusion from a point source in uniformly sheared flow. In *Eighth International Symposium on Turbulence and Shear Flow Phenomena (TSFP8), Poitiers, France*.

Vanderwel, C. & Tavoularis, S. 2014*a* Measurements of turbulent diffusion in uniformly sheared flow. *J. Fluid Mech.* **754**, 488–514.

Vanderwel, C. & Tavoularis, S. 2014*b* On the accuracy of PLIF measurements in slender plumes. *Exp. Fluids* **55**, 1801.

Vanderwel, C. & Tavoularis, S. 2014*c* Relative dispersion of a passive scalar plume in turbulent shear flow. *Phys. Rev. E* **89** (4), 041005.

Veeravalli, S. & Warhaft, Z. 1990 Thermal dispersion from a line source in the shearless turbulence mixing layer. *J. Fluid Mech* **216**, 35–70.

Walker, D.A. 1987 A fluorescence technique for measurement of concentration in mixing liquids. *J. Phys. E: Sci. Instrum.* **20**, 217–224.

Warhaft, Z. 1984 The interference of thermal fields from line sources in grid turbulence. *J. Fluid Mech.* **144**, 363–387.

Warhaft, Z. 2000 Passive scalars in turbulent flows. *Annu. Rev. Fluid Mech.* **32** (1), 203–240.

Webster, D.R., Rahman, S. & Dasi, L.P. 2003 Laser-induced fluorescence measurements of a turbulent plume. *J. Eng. Mech.-ASCE* **129**, 1130–1137.

Webster, D.R., Roberts, P.J.W. & Ra'ad, L. 2001 Simultaneous DPTV/PLIF measurements of a turbulent jet. *Exp. Fluids* **30**, 65–72.

Wilson, D.J., Robins, A.G. & Fackrell, J.E. 1985 Intermittency and conditionally-averaged concentration fluctuation statistics in plumes. *Atmos. Environ.* **19** (7), 1053–1064.

Wu, X. & Moin, P. 2010 Transitional and turbulent boundary layer with heat transfer. *Phys. Fluids* **22** (8), 085105.

Würth, C., González, M.G., Niessner, R., Panne, U., Haisch, C. & Genger, U.R. 2012 Determination of the absolute fluorescence quantum yield of Rhodamine 6G with optical and photoacoustic methods–providing the basis for fluorescence quantum yield standards. *Talanta* **90**, 30–37.

Younis, B.A., Speziale, C.G. & Clark, T.T. 2005 A rational model for the turbulent scalar fluxes. *Proc. R. Soc. A* **461**, 575–594.

Zhu, Y. & Mullins, O.C. 1992 Temperature dependence of fluorescence of crude oils and related compounds. *Energ. Fuels* **6** (5), 545–552.